GROWTH AND EXTINCTION LIMITS: GROUND BASED TESTING OF SOLID FUEL COMBUSTION IN LOW STRETCH CONDITIONS IN SUPPORT OF SPACE FLIGHT EXPERIMENTS

by

MICHAEL C. JOHNSTON

Submitted in partial fulfillment of the requirements

For the degree of Doctor of Philosophy

Thesis Adviser: Dr. James T'ien

Department of Mechanical and Aerospace Engineering

CASE WESTERN RESERVE UNIVERSITY

January, 2018

Case Western Reserve University
We hereby approve the thesis[1] of

MICHAEL C. JOHNSTON

for the degree of

Doctor of Philosophy

Dr. James T'ien

Committee Chair, Adviser — Date
Department of Mechanical and Aerospace Engineering

Dr. Fumiaki Takahashi

Committee Member — Date
Department of Mechanical and Aerospace Engineering

Dr. Ya-Ting Liao

Committee Member — Date
Department of Mechanical and Aerospace Engineering

Dr. Hatsuo Ishida

Committee Member — Date
Department of Macromolecular Science

Dr. Sandra Olson

Committee Member — Date
National Aeronautics and Space Administration

Dr. Paul Ferkul

Committee Member — Date
Universities Space Research Association

[1]We certify that written approval has been obtained for any proprietary material contained therein.

Table of Contents

List of Tables

List of Figures

Nomenclature

α_s Solid thermal diffusivity

$\dot{m}_f$ Global burning rate

$\dot{m}''$ Surface pyrolysis rate, solid fuel local burning rate

$\dot{M}_{filteredwater}$ Mass of water filtered from combustion chamber

$\dot{Q}_f$ Radiation from flame to surface

$\dot{Q}_{flame}$ Heat generated by the flame

$\dot{Q}_{fuelinterior}$ Energy conducted into the solid interior

$\dot{Q}_{pyrolysis}$ Energy utilized by pyrolysis

ϵ Surface emissivity

γ Exponential curve fit parameter

λ_g Thermal conductivity of gas phase

λ_s Thermal conductivity of solid

ρ^* Characteristic gas density in the flame zone

ρ_f Density

σ Stefan-Boltzmann constant

τ Material thickness

A Area

a_b Buoyant stretch rate

a_f Forced convective flow rate

a_m Combined buoyant and forced stretch rate

$C_{cylinder}$ Volumetric oxygen concentration of the compressed gas cylinder

$C_{initial}$ Initial volumetric oxygen concentration of combustion chamber

C_{O_2} Volumetric concentration of oxygen

C_{target} Target volumetric oxygen concentration of combustion chamber

d Depth into solid material

D_o Molecular diffusion coefficient of oxygen into flame zone

g Acceleration due to gravity

H Measured flame height

H_{MMA} Heat of combustion of Methyl Methacrylate

L_v Latent heat of vaporization

M_f Molecular weight of fuel

M_{air} Molecular weight of air

M_{O_2} Mass of oxygen

$M_{satuation}$ Mass of water in the combustion chamber before condensation

n Direction normal to surface

$P_{Chamber}$ Pressure of combustion chamber

$P_{N_2Cylinder}$ Partial pressure of nitrogen from compressed gas cylinder

$P_{N_2Station}$ Partial pressure of nitrogen from space station supply

$P_{O_2Cylinder}$ Partial pressure of oxygen from compressed gas cylinder

P_{O_2} Partial pressure of oxygen

$P_{saturation}$ Partial pressure of water before condensation

P_{vent} Pressure vented

Pe Peclet number

Q Volumetric gas flow rate

R Characteristic radius of solid surface curvature

R Universal gas constant

s Stoichiometric ratio

T Temperature

T^* Characteristic flame temperature

T_∞ Ambient temperature, Freestream temperature

T_f Characteristic flame temperature

T_s Temperature of the pyrolizing solid surface

T_{bulk} Bulk material temperature. Ambient temperature unless otherwise noted

t_{burn} Burn time

$T_{Chamber}$ Combustion chamber ambient temperature

$T_{Pyrolysis}$ Surface pyrolysis temperature

U_∞ Freestream forced velocity

V Velocity

$V_{Chamber}$ Volume of combustion chamber

$V_{FilterLoop}$ Volumetric flow rate through CIR filtration loop

$V_{regression}$ Material regression rate

X_{H_2O} Molar mass of water vapor

X_{N_2} Molar mass of nitrogen gas

X_{O_2} Molar mass of oxygen gas

$Y_{ox,\infty}$ Oxidizer mole fraction

ACME Advanced Combustion in Microgravity Experiments

AWG American Wire Gauge

BASS Burning and Suppression of Solids

CIR Combustion Integrated Rack

ESA European Space Agency

GEL Growth and Extinction Limits

GRC Glenn Research Center

ISS International Space Station

LOI Limiting Oxygen Index

MDCA Multi-user Droplet Combustion Apparatus

MSG Microgravity Science Glovebox

NASA National Aeronautics and Space Administration

PMMA Poly(Methyl Methacrylate)

RITSI Radiative Ignition and Transition to Spread Investigation

SLM Standard Liters per Minute

SoFIE Solid Flammability, Ignition, and Extinction

SSCE Solid Surface Combustion Experiment

STS Space Transportation System

VVOT Vertical Variable Oxygen Tunnel

ZGRF Zero Gravity Research Facility

Acknowledgements

I am extremely grateful to Professor James T'ien for serving as my research advisor, dissertation committee chair, and mentor. His physical insight into the strange behavior of near limit flames was invaluable.

I would also like to thank Sandra Olson at the National Aeronautics and Space Administration and Paul Ferkul at Universities Space Research Association for serving on my committee and their input and technical support throughout my graduate career. Sandra served as my NASA mentor when on site and when attending NASA Space Academy, and Paul Ferkul servs as project scientist for the Solid Fuel Ignition and Extinction project, which this work is a part of.

Thank you to Professor Fumiaki Takahashi, Professor Ya-Ting Liao, and Professor Hatsuo Ishida for serving as faculty members of my dissertation committee.

I would also like to thank former doctoral graduate student Makoto Endo, who modeled the Burning and Suppression of Solids (BASS) sphere experiments upon which the GEL experiment is based, and for his considerable input and help throughout ground experiments including design and implementation of the GEL sample prototypes. Makoto still works tirelessly on his computer model long after his graduation as a personal hobby.

Thanks to ZIN Technologies for their design work on the SoFIE experimental apparatus, Mesiner Acrylic Casting for their work on the GEL samples, and Eric Neumann and the technicians at the NASA Zero Gravity Research Facility.

The primary source of funding for this research was provided by the National Aeronautics and Space Administration. A one year fellowship was provided by Underwriters Laboratories as the Underwriters Laboratories Fire Fellow.

Abstract

Growth and Extinction Limits: Ground Based Testing of Solid Fuel Combustion in Low Stretch Conditions in Support of Space Flight Experiments

Abstract

by

MICHAEL C. JOHNSTON

This work examines the effect of material preheating on the combustion and flammability of thermally thick poly(methyl methacrylate) (PMMA) solid fuel near the limits of low stretch oxidizer feed rate common in spacecraft. The in depth temperature rises as solid fuel is preheated causing a decrease in conduction away from the solid surface, freeing energy for increased fuel vaporization.

A 4 cm diameter PMMA sphere instrumented to measure in depth temperature and conduction was ignited and allowed to burn (preheat) in a low speed wind tunnel in the NASA Zero Gravity Research Facility drop tower. After reaching a specified temperature profile, the tunnel was dropped to cause a step change to microgravity for 5.18 seconds. The flammability boundary is mapped for independent parameters of heat loss to the solid interior and freestream velocity (stretch) near the low speed quenching branch at the near limit conditions of 17% oxygen concentration. Flame standoff distance decreased approximately linearly with increased conduction

to the interior. Flame quenching distance decreased with increased freestream velocity (stretch).

A second test series at similar stretch rates beneath a 21.8 cm diameter PMMA spherical shell served as a buoyant analog to microgravity tests. Conduction to the interior was held constant throughout each test by controlling the back surface temperature with an ice bath and varying shell thickness between 2.8-12 mm. A well defined surface area in the bottom stagnation zone was exposed to the flame and the remainder masked. Burning samples were suspended from a mass balance to measure global mass loss. Burning rate is expected to be spatially uniform near the stagnation region, therefore the first time derivative of global mass loss divided by exposed area gives local burning rate. Local burning rate as a function of oxygen concentration is presented for various heat losses.

This work supports the planned space flight experiment Growth and Extinction Limits (GEL) which is part of the Solid Fuel Ignition and Extinction (SoFIE) project aboard the International Space Station. Significantly longer duration microgravity is made available at the expense of increased experimental complexity. The challenges of chamber confinement and ignition are discussed.

1 Introduction

The combustion and flammability of solid fuel under microgravity conditions, where buoyancy forces are either small or non existent, can be quantitatively and qualitatively different than in Earth gravity. In normal gravity, the chemical heat release of the flame raises the local gas temperature and creates a density differential which accelerates hot products upwards and entrains fresh oxidizer into the flame zone in its place to perpetuate combustion. When gravitational forces are weak or non existent, this necessary pumping of products and oxidizer can only be carried out by molecular diffusion or convective flow forced by external means.

Humans have well over a thousand years of experience in how flames act in Earth gravity. Despite this, destructive fires devastating to human life and property are still common place. This bodes poorly for human occupied spacecraft where experience is limited to only a few dozen combustion and fire experiments under actual microgravity conditions. Only handful of these tests, reviewed in the next chapter, extend to the complexity of solid fuels.

Currently, the risk of spacecraft fire is mitigated by careful planning and restrictions on allowable materials. However, at the time of this writing, people have been living aboard the International Space Station (ISS) continually for nearly two decades.

What was originally a well planned out modular design, where every item was contained and separated within its designated rack, has become somewhat cluttered with new technology and upgrades, often necessitating safety waivers. Image 1.1 shows the Destiny module of the International Space Station. While many items are either made from low flammability materials, or protected with coverings such as Nomex or Teflon, many flammable solids have made their way into the environment; laptop computers, monitors, cameras, open books, loose paper, etc. are all vital to the ISS mission, but all present risk. Since there have only been a few actual cases of potential fires in spacecraft so far, these dangers are not well understood. As risk increases and the operational time line increases, the probability of a fire incident occurring increases dramatically. This should make clear the great need for further research in microgravity combustion from the standpoint of spacecraft fire safety.

Previous works, enumerated in the next chapter, have mapped solid fuel flammability onto an axis of oxygen mole fraction vs. oxidizer feed rate such as the solid line shown in Fig. 1.2. In normal gravity, the flame tends to extinguish due to Damkohler number related chemical quenching (blow off) as flow velocity becomes too high to anchor a flame. In microgravity conditions, flow speeds of lower magnitude are possible and materials can become flammable at lower than normal oxygen concentrations in the correct flow velocity range. Further decreasing flow velocity, extinction occurs due heat losses typically attributed to surface radiation. However, to better describe how thick solid fuels act over time as the flame heats the solid material, the flammability map shown as the Fig. 1.2 solid curve can be thought to expand outwards in time towards the dotted curves, increasing the flammable region as the heat loss to the solid interior decreases with increased material preheating.

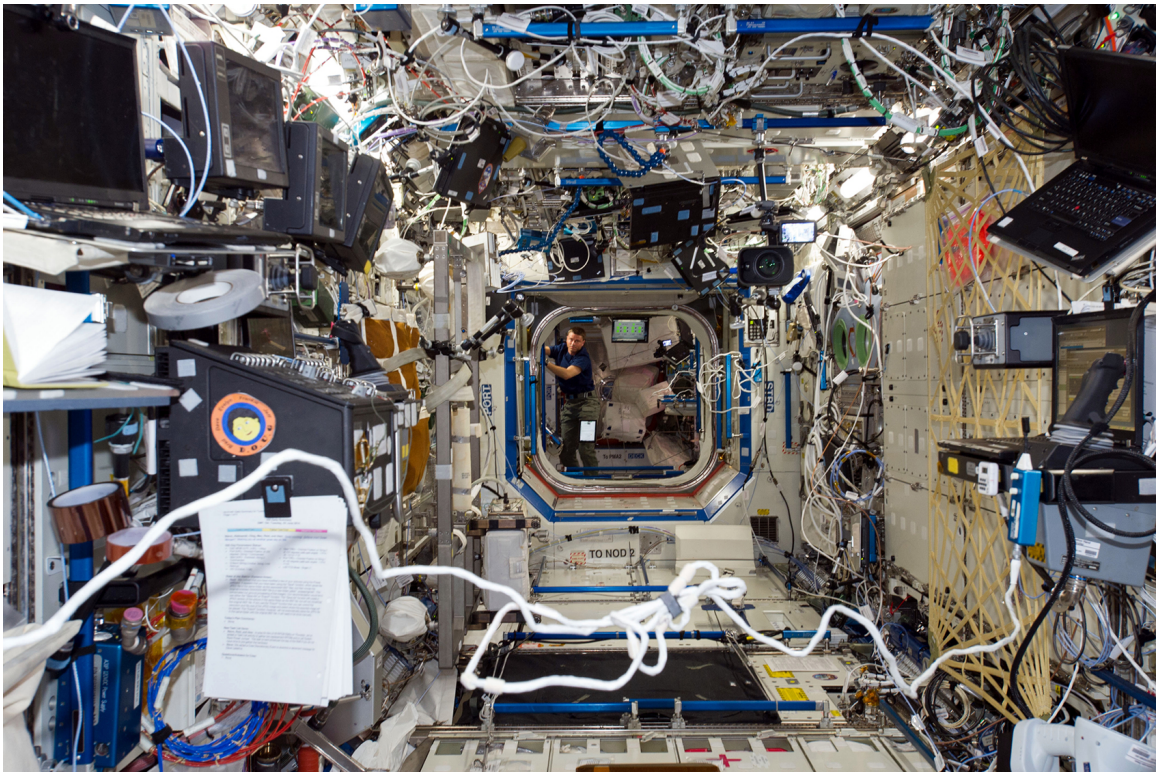

Figure 1.1. The Destiny module of the International Space Station. [ESA/NASA Photo ID-357925]

In this work, flammability experiments designed to explore the effect of solid fuel preheating (heat loss to the solid interior) under microgravity conditions are carried out on thermally thick poly(methyl methacrylate) (PMMA) solid fuel in a bottom stagnation geometry that simulates microgravity in buoyancy driven flow and in actual microgravity conditions in the NASA Zero Gravity Research Facility (ZGRF). This work will later be extended to longer duration microgravity times in the Growth and Extinction Limits flight experiment aboard ISS. The different experimental configurations require approaching the limit of flammability by different means. Each configuration also presents unique advantages for experimental measurement. These will be outlined next.

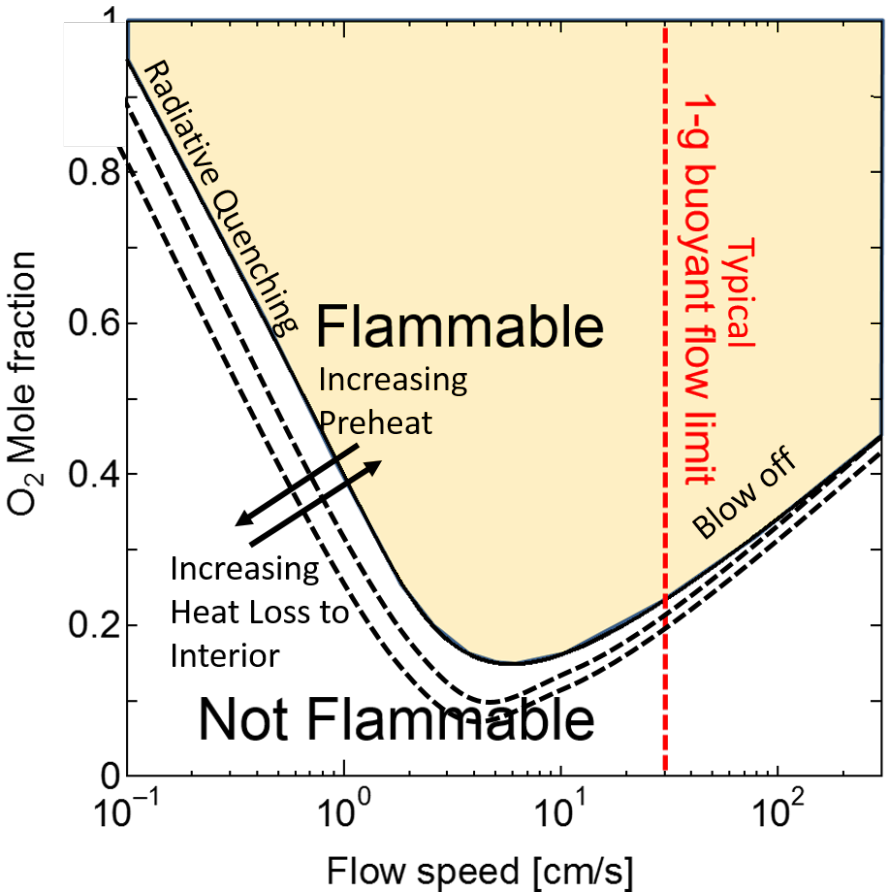

Figure 1.2. An example solid fuel flammability map with independent parameters of oxygen mole fraction and flow speed. As a material heats up, the flammable region expands to the dotted lines. [Diagram modified from [1]]

1.1 Research Concepts

A summary of the research approach on various experimental configurations is shown in the concept diagrams of Fig. 1.3. These are all presented in a flammability map layout similar to Fig. 1.2, where a flammability boundary is plotted on an axis of oxygen concentration and characteristic oxidizer velocity. The flammability boundary expands outward as the solid material heats up (becomes more flammable).

1.1.1 Low Stretch Flames on PMMA Spherical Shells

In a stagnation zone boundary layer flame, by use of a compressible boundary layer similarity solution, a correspondence between Earth gravity and purely forced flow microgravity combustion can be drawn. The founding principles of this will be discussed in the next chapter in reference to the work of previous investigators. In essence, characteristic flow speed outside the boundary layer is combined with sample curvature into a similarity variable called 'stretch rate' and allows direct comparison of small radius blunt body stagnation zones in low speed forced flow with large radius of curvature blunt bodies in higher characteristic speed buoyant flows.

In this work, low stretch rate flame experiments were conducted in Earth gravity in the bottom stagnation zone of 21.8 cm diameter spherical shells, which are on the same order of flame stretch rate as a 4 cm diameter sphere in slow purely forced flow described later. Shell thicknesses were between 2.8 and 12 mm with the back (inner) surface in contact with an ice bath. The constant temperature of the back surface combined with the relatively constant front surface pyrolysis temperature controls the heat conduction into the solid interior away from the surface where pyrolysis occurs. The solid fuel outside the stagnation zone was shielded from the flame with a non flammable masking and the exposed surface area was well defined. In a stagnation flame, the burning rate is uniform across the solid sample surface. By suspending the sample from a mass balance, the global mass loss was measured during combustion. The first time derivative of the mass loss divided by surface area gives local burning rate. Local burning rates were measured from 21% oxygen by volume down to the minimum oxygen extinction point for various shell thicknesses (heat loss to the solid interior).

In Fig. 1.3 Upper Left, the physical diameter of spherical shell (21.8 cm) controls the characteristic oxidizer velocity (stretch rate) in a buoyant field. Heat loss to the sample interior is controlled by shell thickness and held constant with an ice bath on the back surface. After the flame is established, the oxygen concentration is decreased until extinction is reached. The extinction oxygen concentration is dependent on the heat loss to the solid interior.

1.1.2 Growth and Extinction Limits (GEL) Prototype Samples in NASA Zero Gravity Research Facility (ZGRF)

A 4 cm diameter PMMA sphere with instrumentation capable of measuring the solid temperature profile near the forward stagnation zone is ignited and allowed to preheat in Earth gravity until a specified internal temperature (heat loss to the solid) is reached. The conditions are then suddenly step changed to microgravity in the ZGRF drop tower and the transient flame response is observed. The available 5.18 seconds of microgravity allow a snapshot of the flame behavior under the solid fuel preheat conditions and gas conditions. All tests in this series were conducted at an oxygen concentration of 17% by volume, near the limit of PMMA flammability. A flammability boundary was charted with independent parameters of heat loss to the solid interior and freestream velocity. The response of the stagnation zone flame standoff distance was measured and found to decrease approximately linearly with increasing heat loss to the solid interior, and a flame quenching distance boundary measured for extinguishing cases was charted against freestream velocity.

Figure 1.3 Upper Right, the flame is established on a 4 cm diameter sphere in buoyant conditions at a set oxygen concentration (black circle). After a step change

in gravity level, buoyancy driven flow ceases and characteristic oxidizer velocity is controlled externally by wind tunnel gas flow rate. The graph shows two discrete experiments. One test extinguishes, as it falls outside the flammable region (circle with X). The condition shown as the open circle depends on the solid fuel preheat level (heat loss to the solid interior), and may be flammable or may extinguish. The preheat level (heat loss to the solid interior) is measured throughout the test.

1.1.3 Growth and Extinction Limits (GEL) Flight Experiment

A future stage of the Growth and Extinction Limits (GEL) project will involve longer durations in actual microgravity conditions, 20-30 times longer than what is available in ZGRF. Flammability tests will be conducted on the instrumented 4 cm diameter PMMA sphere samples in the combined use Solid Flammability, Ignition, and Extinction (SoFIE) wind tunnel insert for the Combustion Integrated Rack (CIR) aboard ISS. The hardware, currently under construction, features a 10 cm x 10 cm square cross section wind tunnel with forced flow velocity between 0-80 cm/s. A concept drawing from ZIN Technologies, Inc. is shown in Fig. 1.4 and is more fully described in a later chapter.

Figure 1.3 Lower Left, a flame is established on a 4 cm diameter sphere in microgravity conditions with a characteristic oxidizer velocity (stretch rate) on the same order as the buoyant case. Flow velocity is then progressively decreased until extinction occurs (circle with X). Extinction velocity will depend on material preheat (heat loss to solid interior). The preheat value (heat loss to solid interior) will be measured throughout the test.

The same procedure can be used to measure high speed extinction (blow off) by progressively increasing characteristic oxidizer velocity. It is unknown whether (or where) the preheat dependent flammability boundaries will converge on the high speed size. While high flow rate experiments can be conducted on earth by supplementing buoyancy with additional forced flow, doing so in microgravity allows for the characteristic oxidizer velocity to be very well defined.

Figure 1.3 Lower Right, the GEL flight experiment can also approach the flammability boundary by depletion of oxygen within the closed combustion chamber of the CIR rack if supplemental oxygen addition is shut off. This is a slow process, in order to accurately set the preheat level at final extinction, the pre-extinction condition must first be approached by decreasing forced flow velocity to a value in the vicinity of the extinction curve then allowing oxygen to deplete at fixed velocity.

The GEL flight experiment has not begun, but some comments on the challenges of operating the experiment in the closed atmosphere combustion chamber are discussed in a later chapter for future reference.

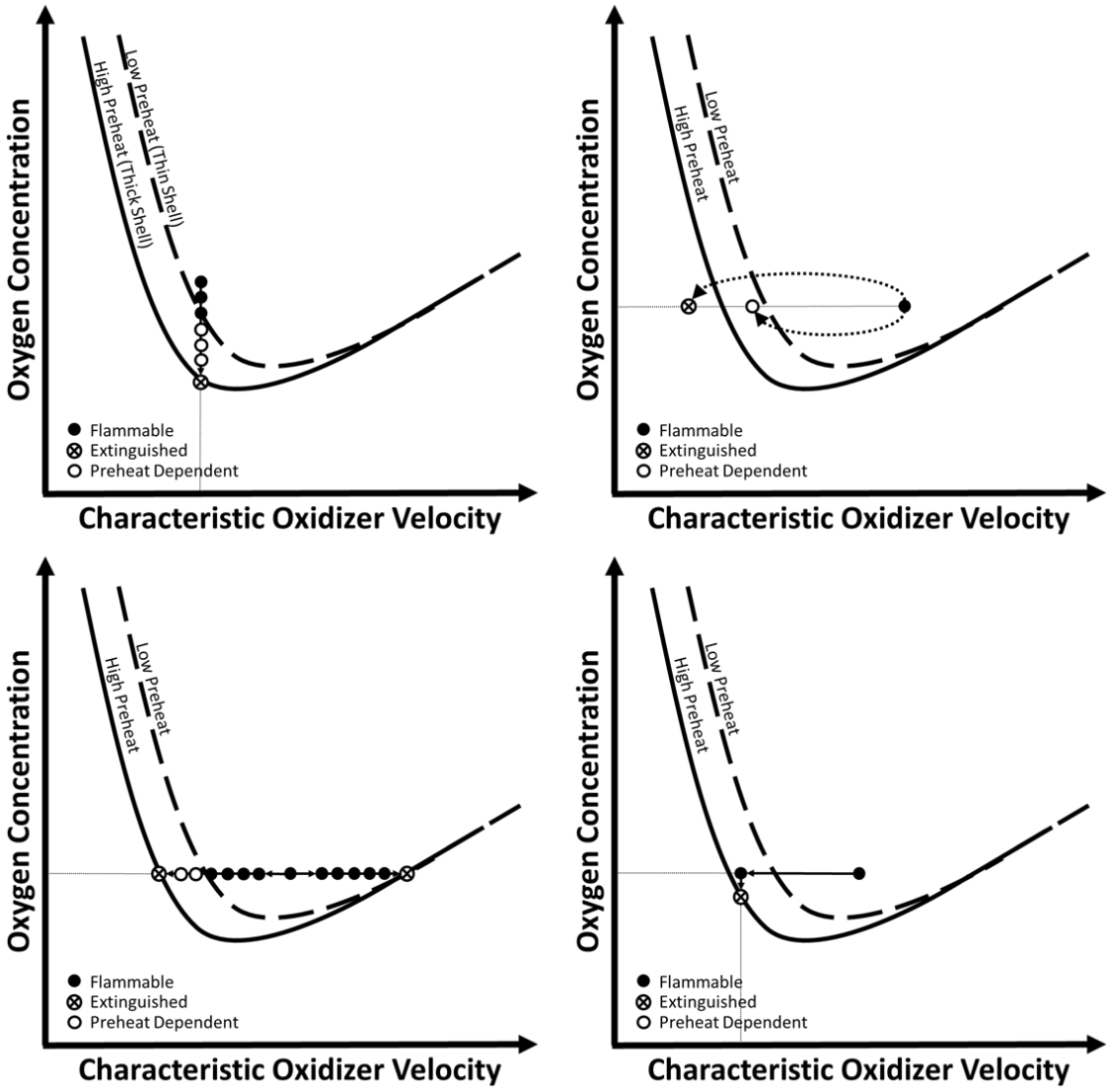

Figure 1.3. The experiment concept map utilizing the various configurations. Top Left: The bottom stagnation configuration on spherical shells. Characteristic oxidizer velocity is a constant value dependent on spherical shell diameter, ambient oxygen concentration is decreased progressively. Solid preheat is constant and chosen with shell thickness. Top Right: GEL sample in ZGRF. A step change to microgravity causes a sudden change from a buoyant characteristic velocity to low speed characteristic velocity. Preheat level is measured. Bottom Left: GEL flight experiment. The characteristic velocity is controlled completely by external fan flow. Velocity is decreased (or increased) until extinction. Preheat level is measured. Bottom Right: GEL flight experiment. Extinction can be approached by ambient oxygen depletion. The near limit conditions are first approached by velocity depletion.

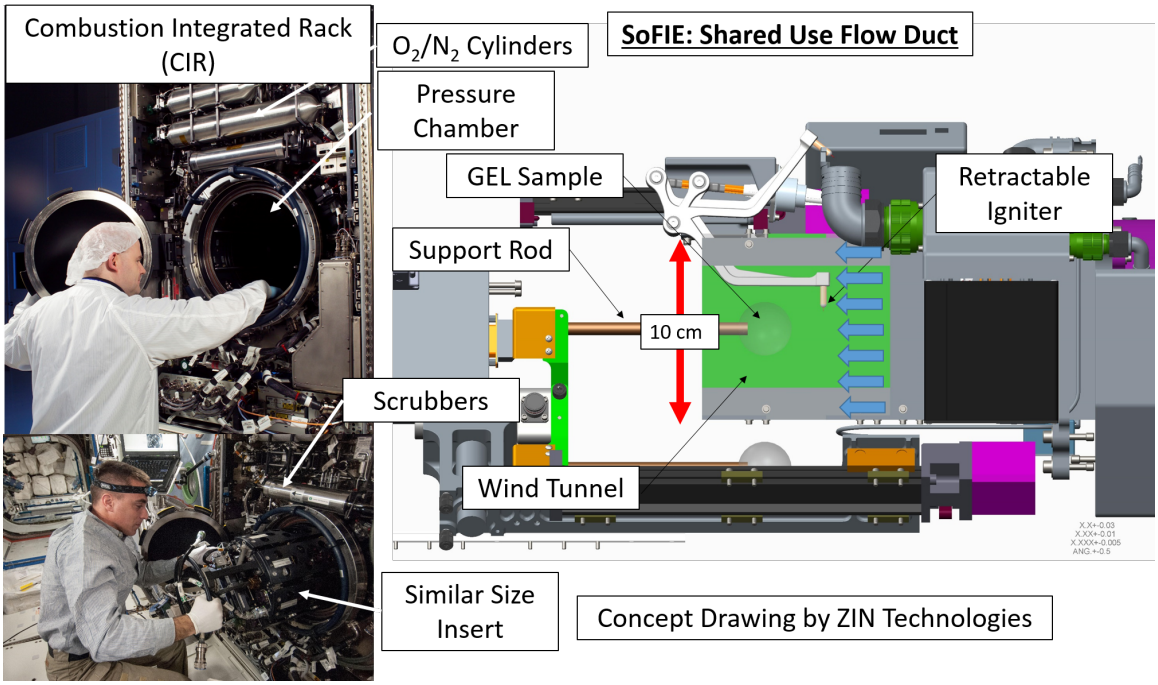

Figure 1.4. A concept drawing of the Growth and Extinction Limits (GEL) flight experiment. The Combined use Solid Flammability, Ignition, and Extinction duct is shown on the right with the GEL sample installed within the channel. The duct will be installed in the pressurized combustion chamber within the Combustion Integrated Rack (CIR) already aboard the International Space Station (ISS). Concept drawing from ZIN Technologies, Inc.

2 Literature Review

This chapter will provide an overview of the major relevant research in solid fuel combustion in microgravity, especially when related to thermally thick solid fuel, and the measurement of burning rate which motivates this work. It is not meant to be an exhaustive history.

2.1 Solid Fuel Combustion in Microgravity

The study of solid fuel combustion in microgravity has played an important role in understanding the flammability risk in human occupied spacecraft [3, 4], simplifying the complexity necessary to advance numerical combustion models [1, 5, 6], providing insight into fundamental combustion processes in the absence of the convolution of buoyancy driven flow [7], and in the future could help further the engineering capabilities of solid propellant reignition and chemical processing of in situ materials for long duration survival in space.

The progress of the field has been slow due primarily to the monetary expense of operating suitable facilities and time sharing (with other research fields) of what few facilities do exist. Cost and availability become increasingly limiting with duration and quality of microgravity required. Although the ultimate solution is to conduct

microgravity research within orbiting spacecraft, which this work leads up to, preliminary ground based experiments have always been critical in the planning and preparation for such an expensive enterprise.

Drop towers offer a relatively cost effective exposure to microgravity. A 2.2 second duration drop tower at NASA Glenn Research Center can support an entire test campaign within a few days. This amount of microgravity time has been successfully used to study the transient response of opposed flow flame spread after a step change in gravity on thermally thin solid fuels [8], but is more suitable for studying physics with shorter transient times such as gaseous fuel flames [9]. Similar duration drop towers exist at academic institutions and are readily accessible [10, 11].

The NASA Zero Gravity Research Facility (ZGRF) extends the microgravity time out to 5.18 seconds. Because the drop tower scheme depends on allowing true free fall, the facility requires a large amount of added complexity in reducing air drag by using a vacuum chamber, and substantially increasing the fall height. This significantly increases cost over smaller drop towers. ZGRF can handle up to two tests per day. This facility has been used to study flame spread on thermally thin solid fuels in both opposed flow and concurrent flow configurations [12–14]. It has also been used to study the gas phase flame transient during the step change in gravity on thermally thick solid fuels [15, 16], as will be continued as a part of this work.

A drop tower at the Japanese Microgravity Center was able to provide 10 seconds of microgravity, and has been used to study radiative ignition and subsequent transition to flame spread in microgravity [17] and psuedosteady flame spread on thin wire insulation [18] both of which were precursors to longer duration space flight experiments. Unfortunately, the facility has been discontinued.

Parabolic flight aircraft can offer around 25 seconds of microgravity or partial gravity for around ten times the price per test of NASA ZGRF, although around 40 parabolas are flown in a single session allowing multiple test points. This method has been successful in partial gravity testing of upward and downward flame spread on thin solid fuels [19, 20] and spheres of diameter 2 mm to 6.35 mm made from multiple polymers (including PMMA) in various oxygen concentrations and decreasing pressures [21]. Attempts have been made to study solid fuel combustion approaching microgravity, but the g-jitter on the order of the absolute g level from aircraft vibration and deviation from perfect parabolic flight trajectories can greatly influence the results [22, 23].

Longer duration parabolic flights can be carried out on sounding rockets, but are typically subject to the whims of the military surplus availability of rocket motors and are an order of magnitude more expensive than aircraft flights. Vietoris et al tested opposed flow over PMMA slabs at 40% oxygen at 5, 10, and 15 cm/s flow for 180 second flights [24]. Similar work was continued in DARTFire by Olson et al [25] studying flame spread over thermally thick PMMA slabs in microgravity times reaching 6 minutes while varying oxygen concentration, free stream velocity, and externally applied radiative heat flux. The European Space Agency (ESA) carried out a series of ignition and flame spread tests on cylindrical PMMA hollow rods in a sounding rocket campaign between 0-40% oxygen concentration by volume [26].

Orbiting spacecraft can offer very long duration microgravity times, subject only to scheduled orbit corrections and vibration from internal motors and human movement. A series of survey level solid fuel flammability tests were performed on the Skylab space station which included flame propagation on solid fuel, flame transfer to

adjacent surfaces, and extinguishment by depressurization, however the results were primarily qualitative in nature [27].

The Solid Surface Combustion Experiment (SSCE) aboard the Space Shuttle studied ignition and flame spread across 3 cm wide by 11 cm long thermally thin ashless filter paper in quiescent environments of 50% oxygen at 1 atm, 1.5 atm, and 2 atm, and at 35% oxygen at 1 atm and 1.5 atm [28]. A second phase of the experiment considered flame spread across thermally thick 2.54 cm long x 6.35 cm wide x 3.18 mm thick PMMA slabs in quiescent 50% oxygen at 1 atm, 50% oxygen at 2 atm, and 70% oxygen at 1 atm [29]. In such high oxygenated atmospheres, some of these flames were able to generate sufficient oxidizer flow by propagating into the unreacted atmosphere. But it was noted that thick fuel flames, without externally generated flow, will ultimately extinguish due to the slow flame propagation rate and heat loss due to radiation [30, 31].

A later experiment aboard the Space Shuttle named Radiative Ignition and Transition to Spread Investigation (RITSI), studied ignition of thermally thin solid fuel and transition to flame spread with added forced flow and externally applied radiative source, a preference of the flame to propagate upstream into the flow instead of downstream with 0 to 6.5 cm/s oxidizer velocity was noted [32]

Concurrent flame spread on 4.5 mm diameter rods of various polymers, including PMMA of direct interest to this work, was conducted onboard the Mir space station in velocities from 0 to 8.5 cm/s, however, the extruded variety of PMMA was inadvertently used which allowed the material to melt into flammable liquid before degrading into monomer vapor [33].

Very recently, the study of slow flow solid fuel combustion in microgravity has accelerated after the repurposing of a small wind tunnel originally designed to study co-flow gaseous fuel combustion in the Microgravity Science Glovebox (MSG) aboard the International Space Station [34–36]. The new series of tests, entitled Burning and Suppression of Solids (BASS) [37] studied ignition, subsequent flame spread in opposed and concurrent flow, and extinction through flow reduction or nitrogen suppression on flat samples of thermally thin cloth [38,39] and on millimeter thick PMMA slabs, which has yet to be published. Experiments also focused on ignition and flame spread from the forward stagnation point and the wake stagnation point of 1 cm and 2 cm diameter PMMA spheres which was the direct precursor to this work. Select data from the BASS sphere tests are published with accompanying computer model by Endo [1].

The success of BASS combined with the low cost of resupplying fuel samples lead to a reflight with significantly more sample geometries dubbed BASS-II, adding cylindrical and thick flat slab PMMA geometries [40–42].

The results are not yet published, but it will be noted that an international collaborative team recently conducted solid fuel ignition and flame spread experiments on a historically larger scale in primarily 20 cm/s concurrent flow aboard disposable Cygnus cargo spacecrafts after they completed their primary missions to resupply ISS. The spacecraft fire safety demonstration was dubbed Saffire [43]. Saffire flight 1 tested flame spread on one large 40.6 cm wide x 90.4 cm long thermally thin cotton/fiberglass fabric sheet of the same composition as used in BASS. Saffire 2 provided nine smaller samples which were 5 cm wide x 29 cm long made of: thermally thin cotton/fiberglass fabric, 0.8 mm and 1 cm thick PMMA (one of which had some surface

structure machined into it), thermally thin Nomex HT 90-40, and 0.27, 0.37, 0.61 and 1.03 mm thick silicone sheets.

2.2 Measurement of Local Burning Rate

The study of solid burning rates is important for a wide variety of fire and combustion fields: calibration and validation of combustion models, risk assessment of material flammability, estimation of heat release rates for industrial or commercial application, etc.

The recent proliferation of high precision analytical balances capable of measuring tiny weight changes in relatively heavy objects now presents the opportunity to take detailed time resolved weight measurements during combustion experiments.

The experimental studies available in literature thus far have only measured global burning rates on solid surfaces, that is, the total mass loss rate of the entire material sample. They lack either temporal resolution, spacial resolution, or both. The results are either published in their raw form, related to local burning rate, the global burning rate per unit surface area, in a crude approximation such as burning rate divided by surface area, or local burning rate is estimated with a distribution weighted by local regression.

As part of this work, the axisymmetric stagnation point configuration will be used to minimize the measurement uncertainty of local burning rate prevalent in the literature. The idealized axisymmetric stagnation flame is mathematically equivalent to a one dimensional flame and has been studied extensively in the past [5, 44–46]. It is suggested for detailed extinction studies by [47] since the entire flame is one

stabilization zone. Furthermore, although the flame edges may affect the results, they are minimized by the configuration and act in a symmetric manner about the axis of revolution. Some of the relevant works related to the experimental measurement of burning rate are summarized here.

Olson [48] studied low stretch rate flames beneath large cylindrical PMMA surfaces of various radii in air. Total mass loss was measured after the test. Local burning rate was inferred by relating the total average mass loss rate to the observed surface regression. Due to the physical two dimensional cylindrical nature of the configuration, an attempt was made to track the surface regression during the course of the test by measuring the location of vapor bubbles forming within the transparent solid viewed through the cylinder edge. Surface swelling and dripping made it unclear how accurately the instantaneous bubble layer depth relates to the instantaneous surface regression. The mass loss data is also limited by uncertainty due to dripping and the transient heat up and cool down periods which limit temporal precision. Real time precision mass data for such a heavy sample was likely unavailable during the tests due to technological constraints at the time. Despite hardware limitations, the long duration measurements show good agreement with this work.

Gollner [49] measured the burning rate on PMMA slabs at various angles of inclination extending the work of [46, 50]. Data was reported as mass loss rate divided by total surface area to compare to the previous works of similar configuration but different size and also presented by relating total mass loss to post burned cross sectional profile of the fuel for a selection of tests. It should be noted that the aerodynamic conditions beneath a flat sample are highly dependent on the edge conditions.

Pizzo et al [51] attempted an image tracking analysis originally proposed by Olson [2] for estimating local burning rate for upward flame spread on transparent PMMA slabs by tracking the depth of visible vapor bubble formation within the solid. However, this method was only capable of tracking the deepest bubble formations at the centerline of the fuel. Actual weight measurements were taken, but not reported in detail.

T'ien et al [44] measured burning rate on an upward facing stagnation point on PMMA under high stretch rate conditions. An apparatus capable of continuously feeding PMMA solid fuel into the combustion zone at a rate equal to the burning rate was devised. Burning rate is inferred directly from the fuel feed rate. Oxygen mole fraction and flow velocity (stretch rate) were changed to find the blow off limits (maximum burning rate). No attempt was made to chart the low flow stretch limits where buoyancy becomes important.

Ohtani et al [46] measured surface regression rate (closely related to burning rate) on the bottom surface of a burning cylinder and compared with their own similarity solution model. They compared the regression rates of various sample diameters (related to stretch rate) up to 13 cm but did not study the regression rates near low stretch extinction. Model results were also presented for the spherical stagnation point. The tests showed an inverse power dependence of flame temperature, heat flux, and fuel regression rate with diameter (stretch rate).

Drysdale [52] measured the critical mass flux for ignition of various materials in a configuration similar to [44] under various levels of externally applied radiation designed to simulate a flame. Unfortunately, mass flux at extinction for a real flame was not studied. [53] extended the study of critical mass flux for ignition to a wind tunnel

boundary layer configuration under various oxygen atmospheres and flow velocities. The boundary layer configuration was further studied by the addition of a pressure dependence by [54]. These studies were all conducted under artificial radiation conditions at ignition (i.e. representing ignition of a material in proximity to a larger nearby flame), and may not accurately represent the critical minimum burning rate for a fuel which is already burning under a real (but weak) gas phase flame which is near extinction.

It is difficult to measure local burning rate on upward spreading flames due to the large flame size, long transient periods during flame growth, and non uniformity across the sample surface. Honda and Ronney [55] suggest a maximum flame length for very wide flat samples which would result in a pseudo steady state flame and burning rate, however these flame sizes are larger than most practical laboratory experiments (on the order of a few meters). Rangwala [56] studied the fuel width effect on flame length for narrow width samples. It was found that short constant length flames could exist. However, as the sample becomes narrower, three dimensional flame effects become significant creating variation in local burning rate across the width of the sample.

Opposed flame spread experiments allow for shorter pseudo steady-state flames to exist making it attractive for detailed study. For relatively wide or cylindrical fuels, sample edge effects can be reduced. This is in fact the configuration of the Limiting Oxygen Index (LOI) device, typically used for polymeric materials, but becoming increasingly popular for fabrics [57–60].

As a precursor to this work, the measurement of local burning rate was attempted in the downward flat sample LOI configuration by adding a load cell. Complications arise when the uniformity of burning is broken as the flame tends to break up into

flamelets which are often observed near the flammability limit [61]. The breaking of the flame symmetry increases the effective oxygen feed rate into the flame zone, allowing the flame to survive at a lower oxygen concentration than possible with a two dimensional flame. In addition to the lower oxygen limit created by flamelets, the burning rate across the sample surface becomes non uniform, making local burning rate measurement difficult.

In an attempt to simplify flammability analysis, Drysdale [52], suggested measuring a critical minimum mass flux of volatiles for use in solid material flammability analysis in place of (or supplemental to) critical heat flux and critical surface temperature. The work suggests critical mass flux may be a more fundamental value in the combustion of condensed fuel. The maximum possible rate of heat generation from a burning condensed fuel must be directly proportional to the rate at which it vaporizes. The actual heat available can only be less due to added heat loss.

One of the objectives in this work is to measure the minimum critical burning rate in low stretch condensed fuel combustion. The experiments will be designed to coincide with the theoretical work of Foutch and T'ien [5] as closely as possible by using an axisymmetric stagnation point configuration, which under idealized conditions, exhibits a uniform burning rate across the stagnation region of the fuel surface enabling the calculation of local burning rate.

Most previous works have studied the critical mass flux for the flame ignition point, flash point, or ignition delay time under external radiation and various ambient oxidizer and pressure conditions. This work will attempt to measure the critical burning rate during extinction by beginning with a flame and reducing oxygen concentration until extinction is met. Thus far, this has only been performed in air by

reduction of stretch rate in a sequence of discrete experiments increasing diameter cylinders in buoyancy driven flow by Olson [2, 48].

It may be possible to approach either the quenching limit (left branch) or the blow off limit (right branch) while lowering oxygen concentration. During experiments, T'ien et al [44] ignored the effect of buoyancy and approached only the blow off extinction branch by independently controlling stretch rate via externally forced convection. The quenching branch caused by surface radiation was later explored in computer models [62] and again with gas phase radiation [45].

The only works to vary stretch rate at the low range in a gravitational field were by Olson [48] beneath cylinders and Ohtani [46]. Both of these tests were at 21% oxygen concentration by volume. Han et al [63] studied low stretch flames beneath a sphere, but controlled fuel mass injection using a porous burner.

2.3 Governing equations for axisymmetric stagnation point flames

The axisymmetric stagnation point flame is transformed into a pseudo one-dimensional configuration by the use of similarity solution. T'ien [44] recommended using a compressible boundary layer equation due to the large change in fuel density near the surface. The technique originally posed for purely forced flow conditions was extended to include free convection and mixed convection conditions by Foutch and T'ien [5]. The two dimensional partial differential governing equations can be mathematically contracted into one dimensional ordinary differential equations. Specifically, the flame which exists in three dimensions is mathematically pseudo one dimensional.

It is suggested in [5] to introduce the densimetric Froude number as referenced to a characteristic flame density ρ^*:

$$\phi = (\frac{\rho^* - \rho_e}{\rho_e}) \frac{g_x}{u_e \frac{du_e}{dx}} \tag{2.1}$$

Where $u_e = a_f x$ from the potential flow solution, $g_x = -gx/R$ and a_f is the forced convective stretch rate. The mixed stretch rate in terms of Froude number is approximated as:

$$a = a_f(1+\phi)^{1/2} = \sqrt{a_f^2 + a_b^2} \tag{2.2}$$

Where a_f and a_b are the pure forced flow stretch rate and pure buoyancy driven stretch rate components respectively. Specifically, a_f and a_b for an axi-symmetric blunt body will be referenced extensively later in this work in the form:

$$a_f = \frac{3}{2}\frac{u_e}{R} \tag{2.3}$$

$$a_b = \sqrt{\frac{T^* - T_\infty}{T^*}\frac{g}{R}} \tag{2.4}$$

In a_b, the gas density suggested by Foutch and T'ien is replaced by temperature using the ideal gas law for convenience of estimation as suggested by a continuation of the work by Armstrong et al [16]

2.4 The effects of preheating

The effect of sample preheat was studied numerically by [64] by introducing a heat sink term into the solid surface energy balance to represent various levels of internal temperature distribution. Olson [2] studied the effect of heat loss to the solid experimentally by adding a 0^oC ice bath to the back surface of cylindrical shells to sink heat away. In this case the heat sink term was altered with material thickness. Armstrong et al [16] used a similar method by adding a temperature controlled heater to the back surface of their samples. After reaching steady temperature profile, before significant material regression, the wall energy equation described by Foutch and T'ien [5] will apply.

In this work, heat loss to the solid interior will be controlled or measured based on the configuration. In spherical shell experiments, it will follow the method of [2] and in spherical samples, internal thermocouples will be used (described later) to measure the instantaneous internal solid temperature profile. Then the solid conduction term by [64] can be introduced as measured.

3 Solid Fuel Samples

The solid fuel samples used in this work will be described in this chapter. This includes cooled spherical shells used in ground experiments to allow the study of low stretch flames in Earth levels of gravity and instrumented 4 cm diameter samples intended to be used in the Growth and Extinction Limits space flight experiment.

3.1 Poly(Methyl Methacrylate) (PMMA)

Poly(methyl methacrylate) is a transparent plastic polymer commonly abbreviated as PMMA, and referred to as acrylic or by the trade names Plexiglas and Lucite. The material has been used extensively in scientific combustion and fire studies in normal Earth gravity and in space flight experiments (see chapter 2). It is manufactured by polymerization of methyl methacrylate (MMA) monomer and shaped by cell casting or extrusion. Samples shaped by extrusion are cheaper, have lower molecular weight and shorter polymer chain lengths than their cell cast counterparts. Cell cast PMMA has higher molecular weight, longer polymer chains ,and several burning properties which are desired for flight experiments; it tends to degrade directly from a solid polymer into methyl methacrylate monomer vapor following an Arrhenius pyrolysis law and it does not exhibit significant melting or dripping. Shape change is slow

due to material loss to the gas phase, but the bulk material does not change shape despite internal temperatures routinely rising above the glass transition temperature. Extruded PMMA has the capability of melting into methyl methacrylate monomer liquid and is therefore avoided in these tests.

PMMA tends to bubble if the internal temperature approaches the pyrolysis temperature,the in depth pyrolysis gives rise to vapor pockets internal to the bulk solid which can result in fuel jetting as the high pressure gas is expelled through the soft hot material [65]. This property intensifies under higher heating rates. It is undesired for the tests described in this work, but can not be avoided.

3.2 Spherical Shells

The shell method described here is an extension of the work by Olson [2] originally conducted on thick cylindrical PMMA shells. It was modified here to better match the GEL experiment and to restrict the burnable surface area for more accurate measurement of local burning rate in the Vertical Variable Oxygen Tunnel (VVOT). Spherical shells are manufactured from cell cast poly(methyl methacrylate) (PMMA) by heating disks past the glass transition temperature and pressing the hot disk between two spherical molds.

A circular PMMA disk is cut to the diameter of the smaller interior spherical mold with a scroll saw. A belt sander is used to fine tune the final disk shape and to smooth the edges. The disk is then placed on top of the inner spherical mold in the oven preheated to 125C for 5 minutes per 1 mm of thickness. The PMMA should be structurally softened as it passes the glass transition temperature.

A larger mold is then placed on top of the PMMA disk and forced downward so the material takes the shape of the two molds. A weight is placed on top to hold the molds in place. The oven is turned off and allowed to cool for about three hours.

After cooling, the actual radius of curvature achieved can be measured by image analysis. Taking a picture from the edge of the spherical shell with a scale or ruler in view, a circle with known coordinates can be superimposed onto the image of the sphere. The minimum equation to be solved is:

$$(x - x_o)^2 + (y - y_o)^2 = R^2 \tag{3.1}$$

Three positions on the shell are measured in the image (x_1, y_1), (x_2, y_2), (x_3, y_3) to give (x_o, y_o, R), where R, the measured radius of curvature is the desired value. A computer code was created in Matlab to accomplish this.

Three 1/16" holes are drilled 1/4" from the edge of the shell at equal intervals (120^o between). The shell is then completely covered in Kapton tape, which will act as a barrier to prevent PMMA vaporization. Black anodized aluminum foil is then wrapped over the taped spherical shell to act as a heat shield.

To expose the burnable area, the foiled shell is faced upward (convex) and a small diameter stainless steel mold is placed in the center of the shell. The outline of the mold is traced with a razor to score the foil and Kapton tape. Tape and foil in the stagnation zone are removed, exposing the PMMA surface. The amount of area exposed is controlled by the mold diameter chosen to remove the masking.

The shells throughout the manufacturing process are shown in Figure 3.1. The various diameter molds are on the far left, The precut circular disk blanks are on

the middle left. Shaped spherical shells are shown on the middle right, and masked spherical shells are shown on the far right.

A dental probe pokes through the 1/16" pre-drilled holes to punch the Kapton and aluminum foil. Copper wire is wrapped through each hole to suspend the shell from the precision balance in the Variable Oxygen Tunnel. The wires to each pre-drilled hole meet around a 1/4"-20 bolt in the center, from which the shell is hung. height and leveling is adjusted by twisting knots in each wire.

Shells can be manufactured in any size, thickness, shape. As part of this work, shells have been made in thicknesses of 12 mm, 7 mm, 2.5 mm and 1 mm and diameters of 4 cm, 6 cm, 7 cm, 8 cm, 9 cm, 10 cm, and 18 cm.

Figure 3.2 shows the spherical shell in the final test configuration. The back side of the shell is filled with an ice bath and the exposed surface is facing downward in the ceiling configuration. A flame is shown, blue in color, still developing and spreading across the surface of the exposed PMMA. The light is tinted green by colored LEDs illuminating through the transparent PMMA from above.

3.3 Cell Cast Instrumented Spheres

A special custom geometry PMMA solid fuel sample was designed for the Growth and Extinction Limits (GEL) experiment. The overall shape is a 4 cm diameter sphere similar, but larger than, the samples used in the prior Burning and Suppression of Solids (BASS) space flight experiment. The spheres are instrumented with thermocouples which are embedded in the cell cast polymerization process. A 4 cm diameter circular disk insert is laser cut from a sheet of cell cast PMMA, and the

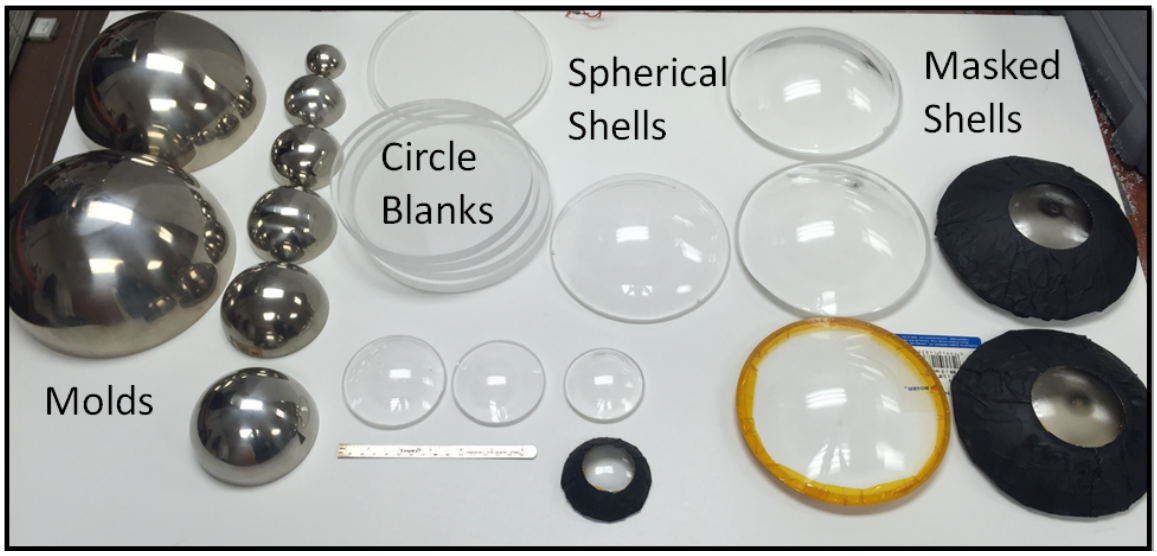

Figure 3.1. The components for making spherical PMMA shells. From left to right, the various sized spherical molds, circular PMMA disks, shaped PMMA spherical shells, and masked shells with controlled exposed surface area.

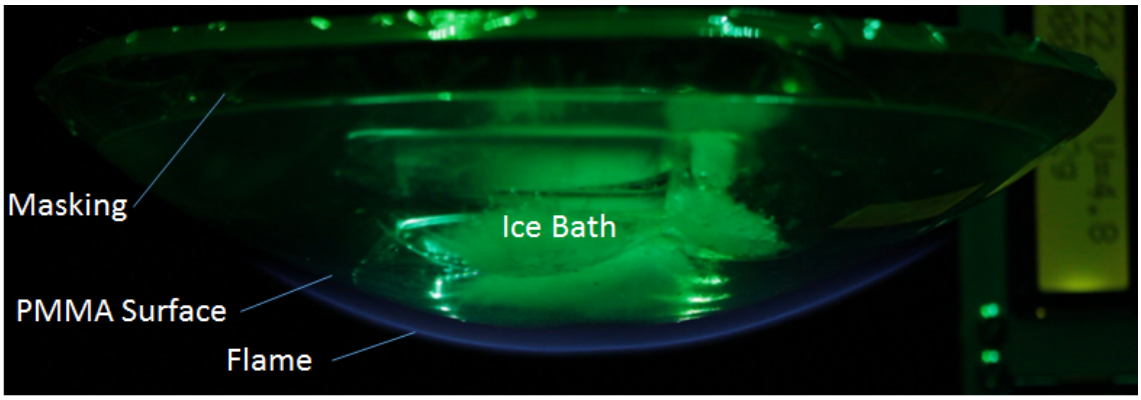

Figure 3.2. A spherical shell with a flame developing across the exposed surface. The burning surface faces in the downward ceiling configuration. The back surface is in contact with an ice bath. The ice is visible as bright green lens reflections through the transparent PMMA material.

tips of fine wire thermocouples are melted into the disk's surface at various strategic positions. As the melt location cools and resolidifies, the thermocouple junction is held in place after the plate material resolidifies. A 1/8" diameter, .028" thick wall, 304 stainless steel tube, Mcmaster-Carr model number 8457K21, is glued to a 1/8"

cutout in the PMMA disk. The support rods are currently 6 inches long, but can be cut to any length to accommodate the wind tunnel designed for the flight experiment. The thermocouple wires are routed through the support rod for mechanical and thermal protection. The thermocouples are K-type 40 gauge (.0787 mm diameter) fine wire with PFA insulation, Omega model number 5TC-TT-K-40-36. K-type miniature thermocouple plugs are mechanically attached to the fine wire thermocouples after feeding the leads through the support rod. The instrumented disk assembly is shown in Fig. 3.3 Left.

After assembling the thermocouple plate with support rod attached, the samples are packaged and sent to Meisner Acrylic Casting. Custom molds were machined out of metal in the shape of two half spheres. The instrumented plate is placed in the center of the molds and the two halves are closed like a clamshell. The support rod protrudes through a casting spew hole. Mesiner's MMA monomer slurry is poured into the mold through the spew port for cell cast polymerization. The conditions the mold undergoes and the composition of the slurry are corporate recipes and unknown to us before the completion of the polymerization. A fully polymerized sample is currently undergoing chemical analysis and has been tested for thermogravimetric analysis. The instrumented sphere can be seen in Fig. 3.3 Right.

A cylindrical shape made of PMMA extends beyond the sphere in the wake region along the support rod. This is a result of the spew port used during the cell casting process. The first prototype of instrumented sphere positioned this excess material in the forward stagnation region where it was planned to be machined down until only the sphere remained. This proved difficult in practice. The current design positions

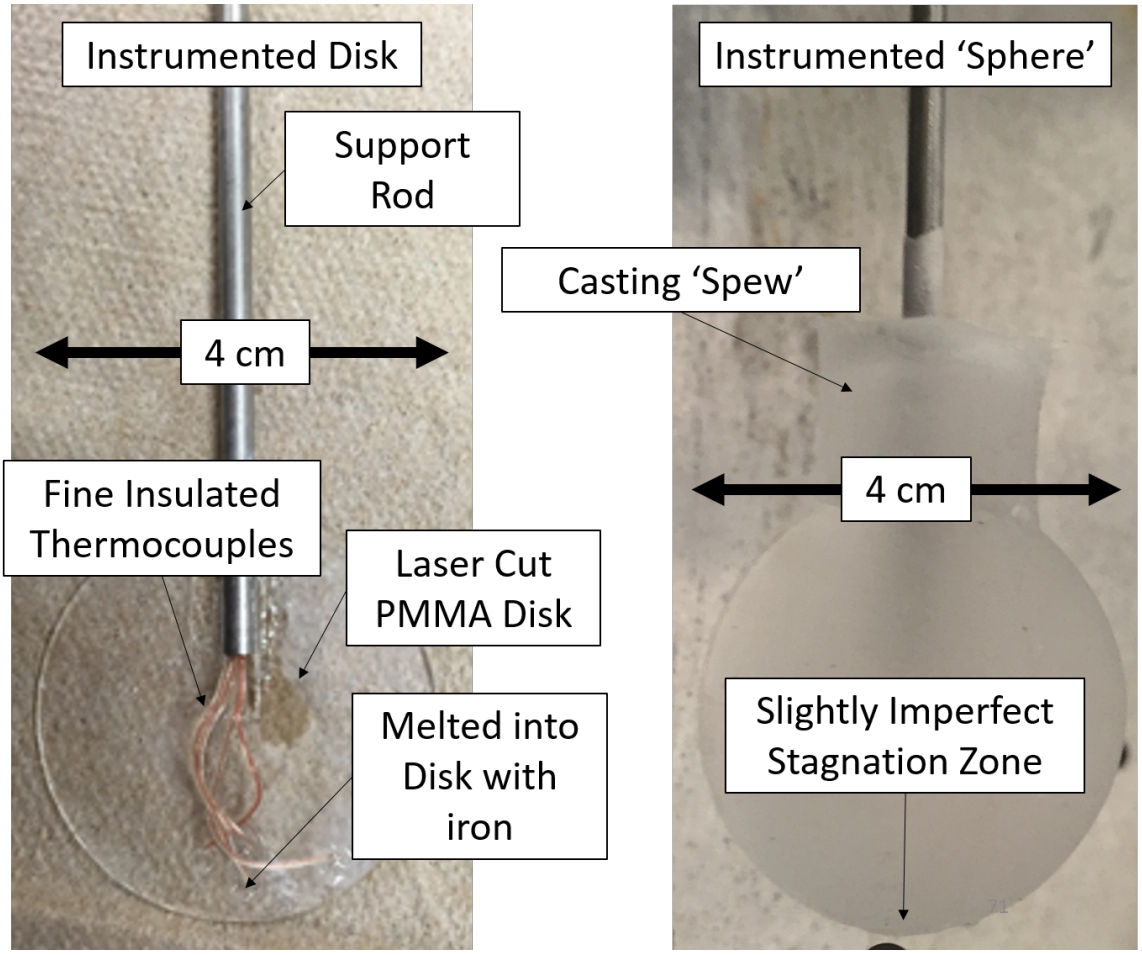

Figure 3.3. Left: A 1 mm thick, 4 cm diameter disc is instrumented with strategically placed thermocouples melted into the surface. Thermocouple lead wires are routed through the support rod. Right: The instrumented disc is cell cast into 4 cm diameter a PMMA sphere.

the spew in the wake along the rod, leaving it intact to help protect the support rod and internal wiring from the heat of the flame.

3.4 Computed Tomography

Three dimensional Computed Tomography (CT) x-ray scans are used to measure thermocouple distances and positions relative to the solid surface after the polymerization process. The sphere samples can be routinely rescanned after ground testing to measure the amount of solid fuel surface regression and bubble formation. If down mass from the ISS is available at the time of testing, surface regression could also be measured after flight tests, though this is not expected and has not been listed as a science requirement.

CT scans are carried out with a Siemens Inveon PET-CT machine capable of about 21 micron resolution. Only the Computed Tomography function of the machine is utilized.

The maximum scan field size is around six inches. The device is shown in Figure 3.4. The lead glass window is opened to access the specimen bed. 3.5 shows the GEL sample loaded onto a carbon fiber sample tray. Masking tape is used to secure the wiring, as any movement will destroy the scan. The sample tray is translated under the x-ray generator and sensor which will travel a 360 degree arc around the sample during scanning.

Most of the x-ray electrons easily penetrate the acrylic polymer and reflect off the nearly opaque thermocouple probes which are made of alumel and chromel metal alloys. A CT scan of a GEL sphere after a drop test in the NASA Zero Gravity Research Facility is shown in Fig. 3.6. Higher density material is shown as light in color, as it reflects more electrons from the X-ray source back to the sensor. The outline of the sphere is clearly visible in the scan. After a drop test, there is a low density region near the surface of the sphere, this is the bubble layer, which penetrates in a few mm

in this case. The thermocouple wires and support rod are displayed as bright white curves. The inset in the lower right of the figure shows just the instrumentation which was embedded in the sphere by thresholding out the PMMA density voxels (volumetric pixels). The inset in the upper right shows the measurement distance of the first thermocouple to the sphere surface (2.150 mm). Distances are measured by taking thin planar slices of the scan, where the thermocouple bead will appear as a bright circle.

Figure 3.7 shows a 3D reconstruction of the same CT scan bound within a rectangular Region of Interest (ROI) to about 4 mm depth into the stagnation zone of the sphere. This stagnation zone is shown in the upper left photograph. On the right hand side of the figure, the 3D ROI is marked out as a rectangle in orthogonal views of the sphere. In the picture to the left, the original circular plate, upon which the thermocouples are mounted, appears to be a higher density than the rest of the sphere. The production of bubbles in depth varies depending on the material properties of the specific PMMA used, the difference in bubble density and bubble sizes are clearly visible in the CT scan for plate and bulk material.

The distances of each thermocouple to the sphere surface between each ground test are charted in a later section.

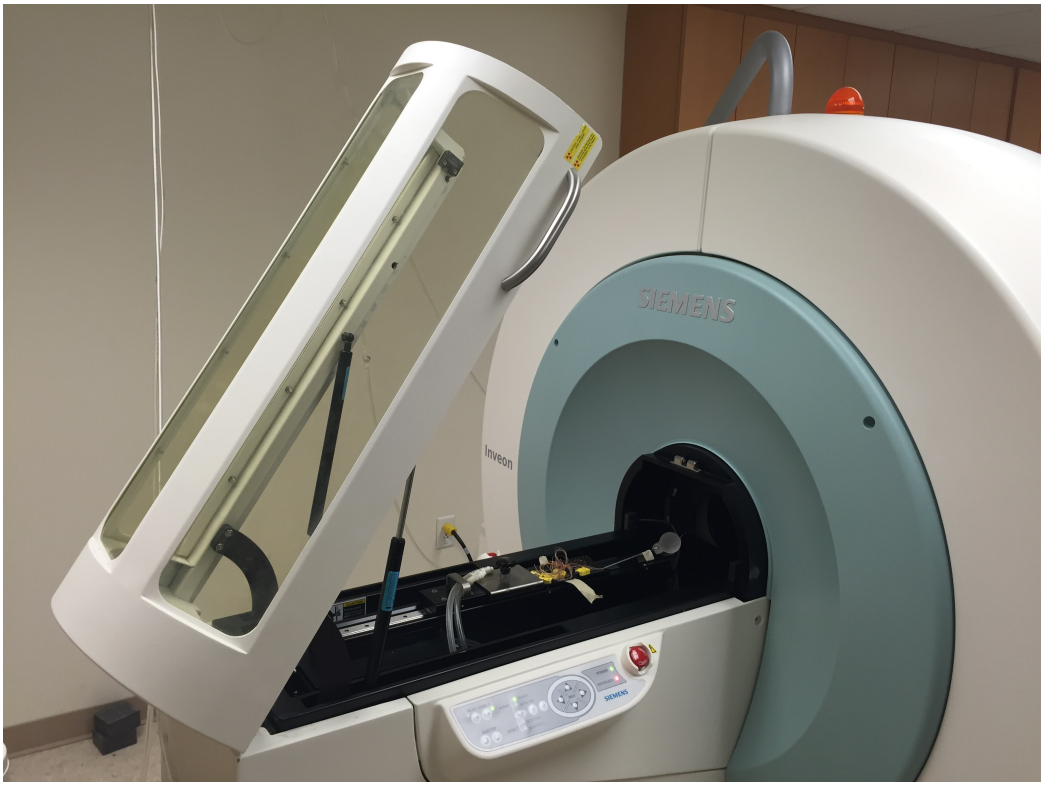

Figure 3.4. Siemens Inveon CT/PET scanner with lead glass canopy open and sample installed.

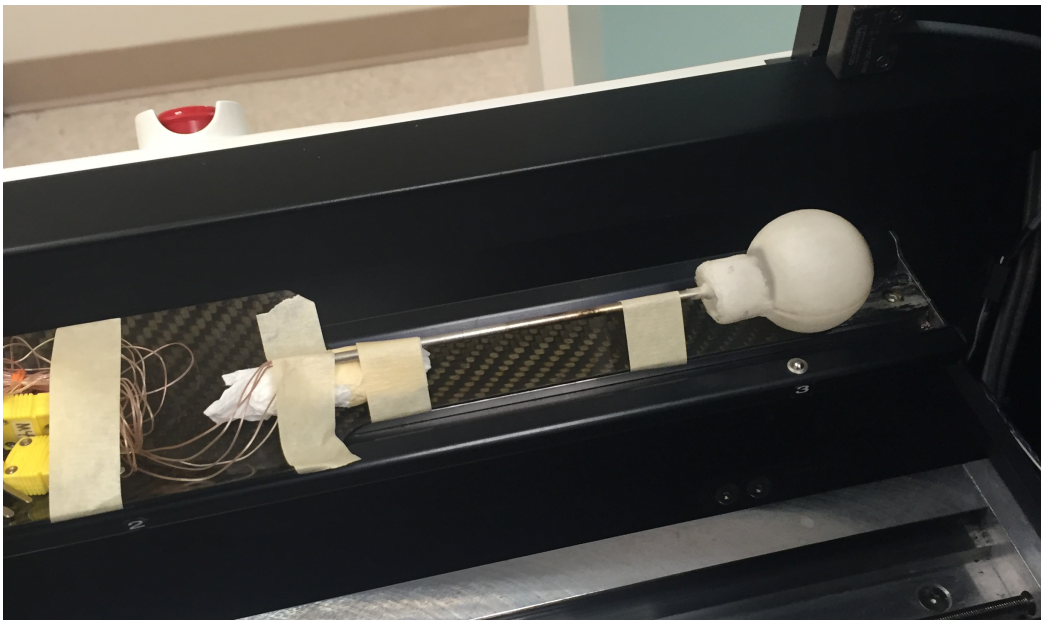

Figure 3.5. A GEL sample is loaded into the CT scanner on a carbon fiber sample tray.

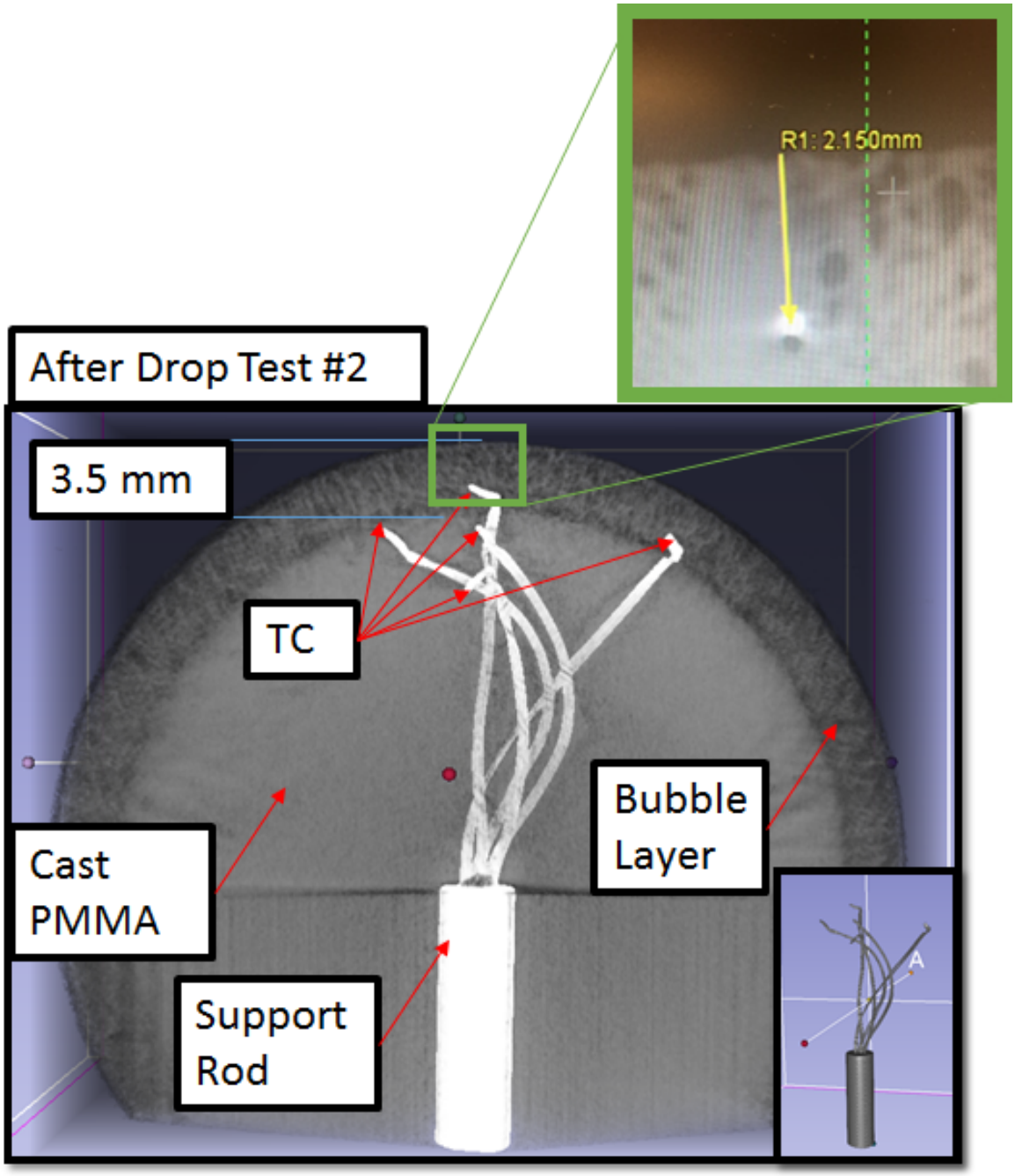

Figure 3.6. A 3D Computed Tomography reconstruction of the GEL sphere after Drop Test #2. The bubble layer penetration depth, thermocouple locations, and support rod are visible within the sphere.

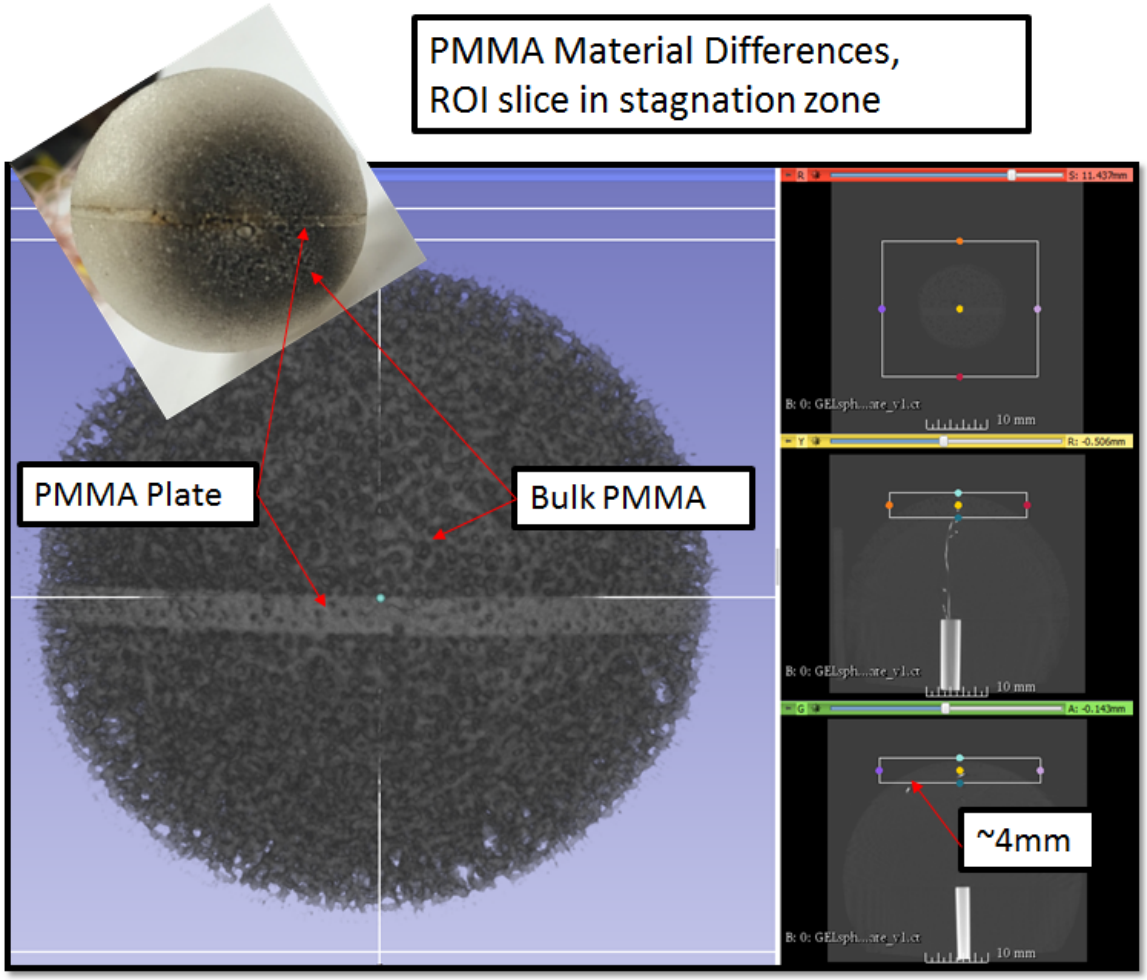

Figure 3.7. A rectangular Region of Interest (ROI) reconstruction of the CT scan showing material density differences and bubbles in the stagnation region.

4 Vertical Variable Oxygen Tunnel

This chapter describes the construction and validation of a Vertical Variable Oxygen Tunnel (VVOT) that was used for measuring limiting oxygen index in predominantly buoyant flow and burning rates as a function of oxygen percentage which will be discussed in a later chapter. The validation of the gravimetric analysis component by using ethanol tea lamps will be discussed here. There is also an interesting case of limit cycle oscillation in ethanol tea lamps at the end of the chapter. Some of this chapter has been published in the Fire Safety Journal [66].

4.1 Design and Construction

Figure 4.1 shows the experimental setup. The photo on the left hand side is the overall setup. The main component is a square glass walled flow tunnel, often used as just a nozzle. The cross section has a dimension 10 cm x 10 cm and the length can either be 20 cm (one section as shown) or 40 cm (two sections stacked). The square shape is designed to be similar to the SoFIE experiment duct and to help imaging the sample and flame without optical distortion. A custom flow blend of oxygen and nitrogen can be supplied entirely by compressed cylinders or shop air supplied from a breathing air quality compressor and industrial drier then modified with added

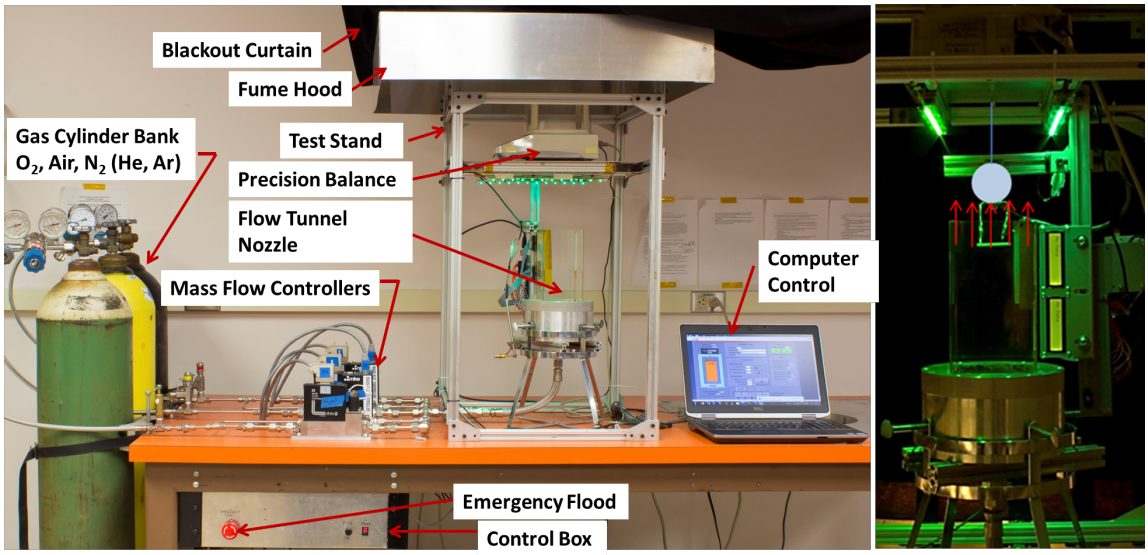

Figure 4.1. Variable oxygen tunnel/nozzle setup with precision mass balance. Left: overall set up. Right: close-up of the flow tunnel/nozzle with a PMMA spherical sample hanging above the nozzle exit.

nitrogen or pure oxygen from cylinders. The rate of mixture flow and its proportion are adjusted by mass flow controllers. The control can either be pre-programed by computer script or controlled manually in real time and recorded throughout the test. An A&D FX-500i precision mass balance capable of 1 mg precision is placed above the tunnel exit. The test sample (e.g. a PMMA sphere is shown) is suspended from the mass balance as shown on the right-side photo in Fig. 4.1. The burning sample can be placed inside the flow tunnel or, for larger samples, in the immediate exit of the tunnel which acts as a nozzle.

Figure 4.2 shows a schematic of the gas flow system. It can be run with any three gases desired, but typical configuration uses high purity nitrogen, compressed breathing air, and high purity oxygen. Nitrogen runs through computer controlled mass flow controllers shown as items (1) coarse control up to 50,000 SCCM and (2) fine control up to 1,000 SCCM. Compressed breathing air comes from a SCUBA

tank compressor and runs through item (3) coarse control up to 50,000 SCCM mass flow controller. Compressed oxygen is routed through the third branch mass flow controller item (4) fine control up to 1,000 SCCM and (5) coarse control up to 50,000 SCCM. Safety relief valves are shown as items (7), (8), (9). Item (6) is an outlet with a quick disconnect fitting which allows a hose to connect to the mixing section of the flow tunnel. A complete list of flow system parts and devices is available in Appendix 8 for future reference and maintenance.

Careful precautions were taken to ensure smooth laminar flow through the tunnel section. Gas is combined in the piping upstream upstream and flows through a 1/2" diameter stainless steel hose into a mixing chamber upstream of the tunnels section. At maximum designed flow rate of about 154,000 cm^3/min, flow through the piping can be quite fast, but well below choked speeds:

$$V_{inletpipe} = Q/A_{inlet} \tag{4.1}$$

$$V_{inletpipe} = \frac{154,000 SCCM}{\pi(1/8)^2 in^2} = 81 m/s \tag{4.2}$$

Upstream of the open tunnel, a flow conditioning system was designed to reduce the possibility of gas momentum disrupting the flow field. A gas mixer section is shown in Fig. 4.3. The bottom is angled downward with a circular counter bore to fit a gas injector. The injector is a combination impactor with lateral gas ports to stop high speed gas from entering straight into the tunnel section as seen in Fig. 4.4. Mounted on top of the impactor/injector is a screen seen in Fig 4.5. Copper BBs are loaded above the internal screen to create a pressure drop. This helps even the

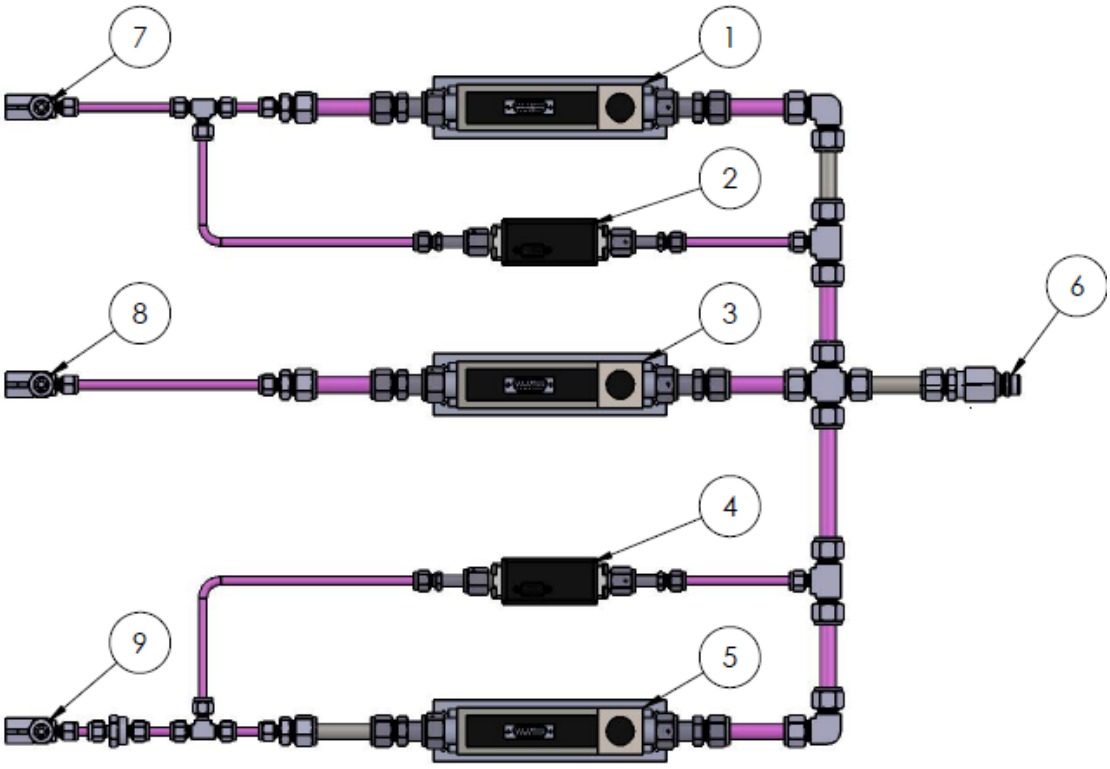

Figure 4.2. The computer controlled flow system is shown. Typically configured as follows: 1.) Nitrogen 50,000 SCCM mass flow controller, 2.) Nitrogen 1,000 SCCM mass flow controller, 3.) Air 50,000 SCCM mass flow controller, 4.) Oxygen 1,000 SCCM mass flow controller, 5.) Oxygen 50,000 SCCM mass flow controller, 6.) Quick disconnect to outlet hose, 7.) Safety relief valve, 8.) Safety relief valve, 9.) Safety relief valve.

flow across the downstream tunnel, and increases mixing in the free section upstream of the BBs 4.6. Figure 4.7 shows a second screen between the mixing section and tunnel section to help protect the mixer from dripping and charring samples during combustion tests.

The set up resembles that of the limiting oxygen index (LOI) apparatus with added mass balance. Most of the LOI devices have a cylindrical tube for the flow

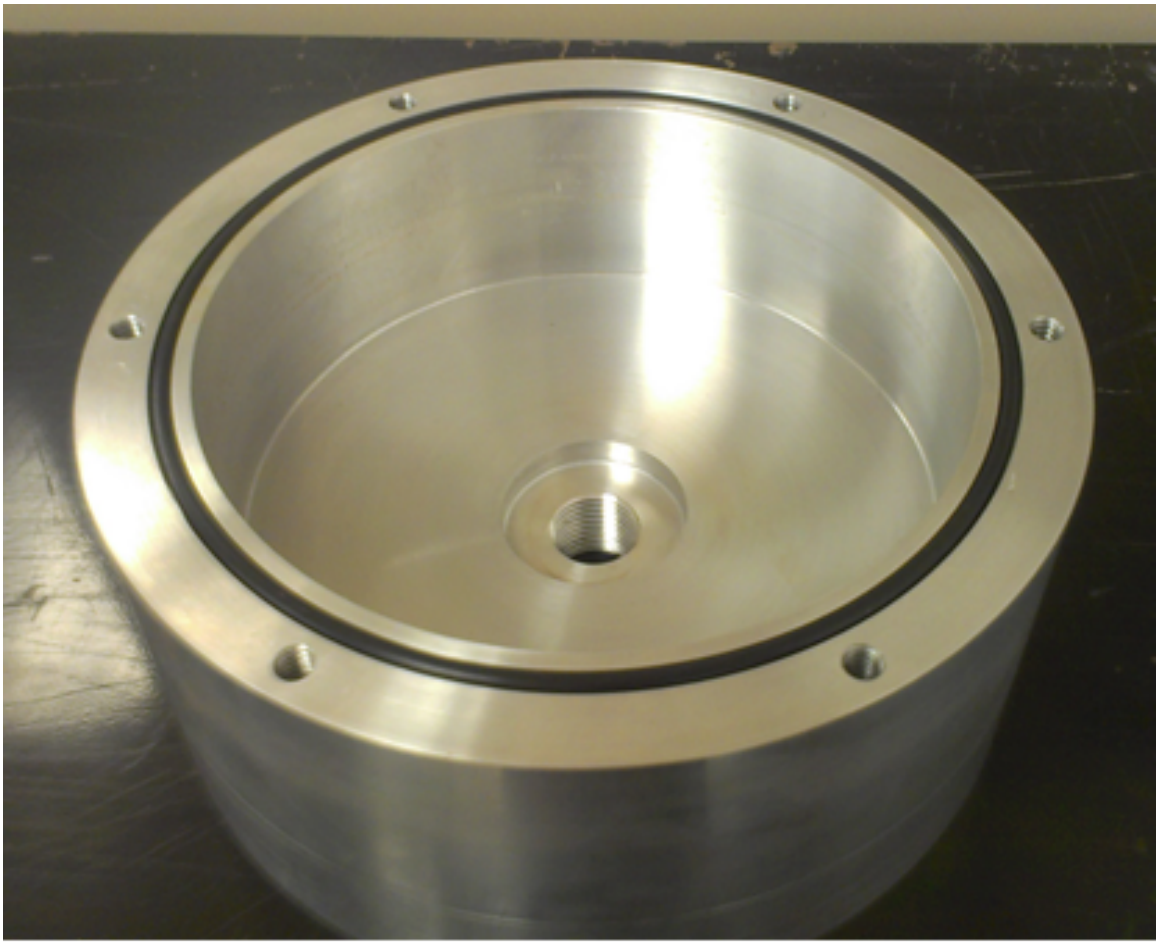

Figure 4.3. The mixing section. The counter bore cut out for the impactor can be seen in the center. A gasket groove is cut around the outside where the lid attaches. A high oxygen service compatible gasket is used and is sealed with six bolts around the diameter

section, although other tunnel shapes have been allowed by the standard. The square tunnel is chosen here to facilitate optical measurement without distortion. Note that a square cross sectional LOI device with the present dimension has been extensively studied numerically in [57]. This square section also matches well with the current SoFIE designs. The mixture flow velocity can be varied and controlled via computer. Typically, a low flow speed between 3-10 cm/s was used during testing. [57] discussed the influence of flow speed in detail. All tests reported in this work have oxygen

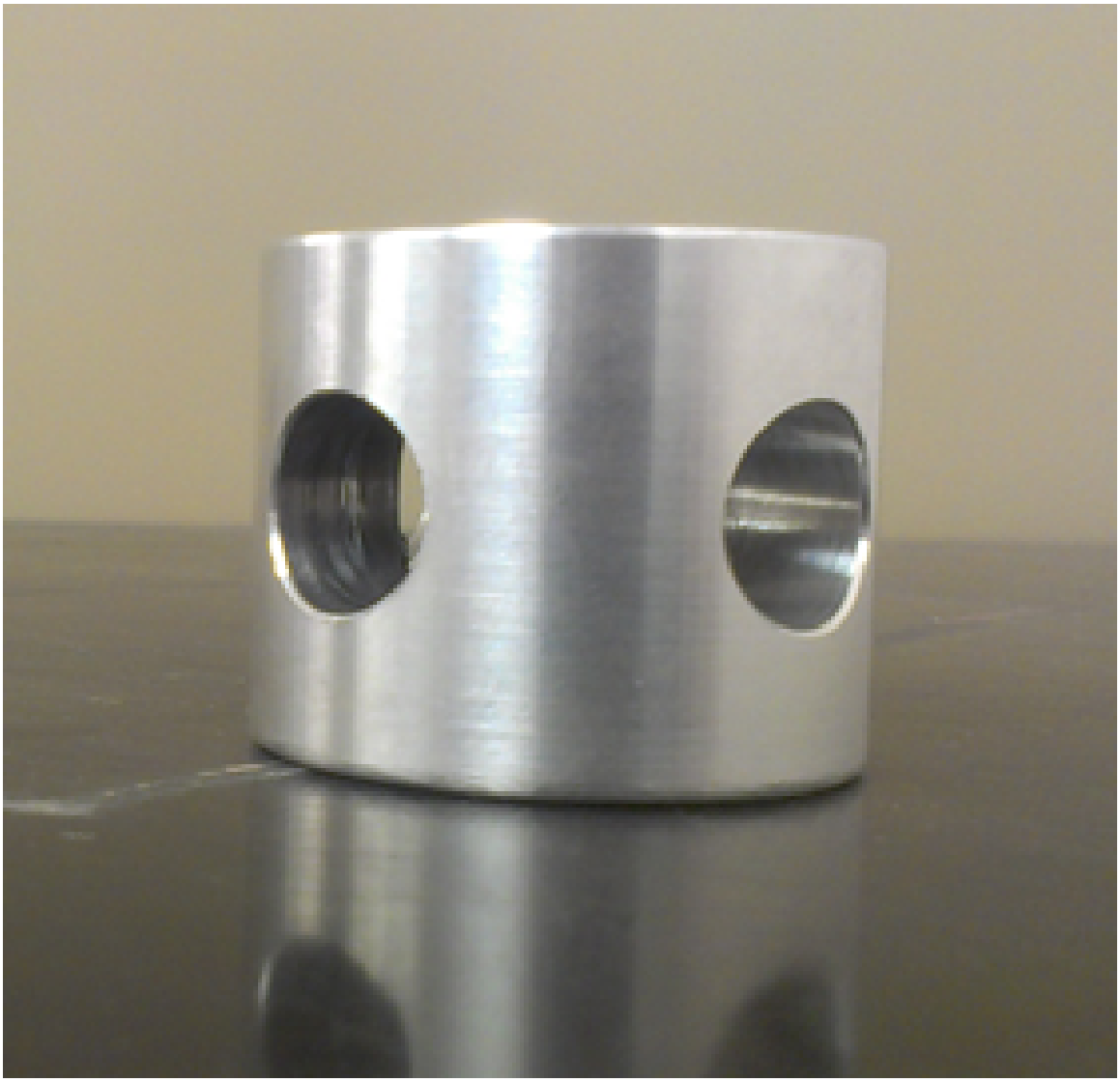

Figure 4.4. The impactor nozzle reduces momentum driven flow through the center of the tunnel. gas enters from the bottom and is injected radially.

between 14% and 21% by volume, although the device has been used by other researchers with elevated oxygen when testing fire protection materials such as Nomex fabric [67] and flame retardant additives in polyurethane foam (proprietary results). Unless otherwise noted, in the tests to be reported, the flow speed through the tunnel

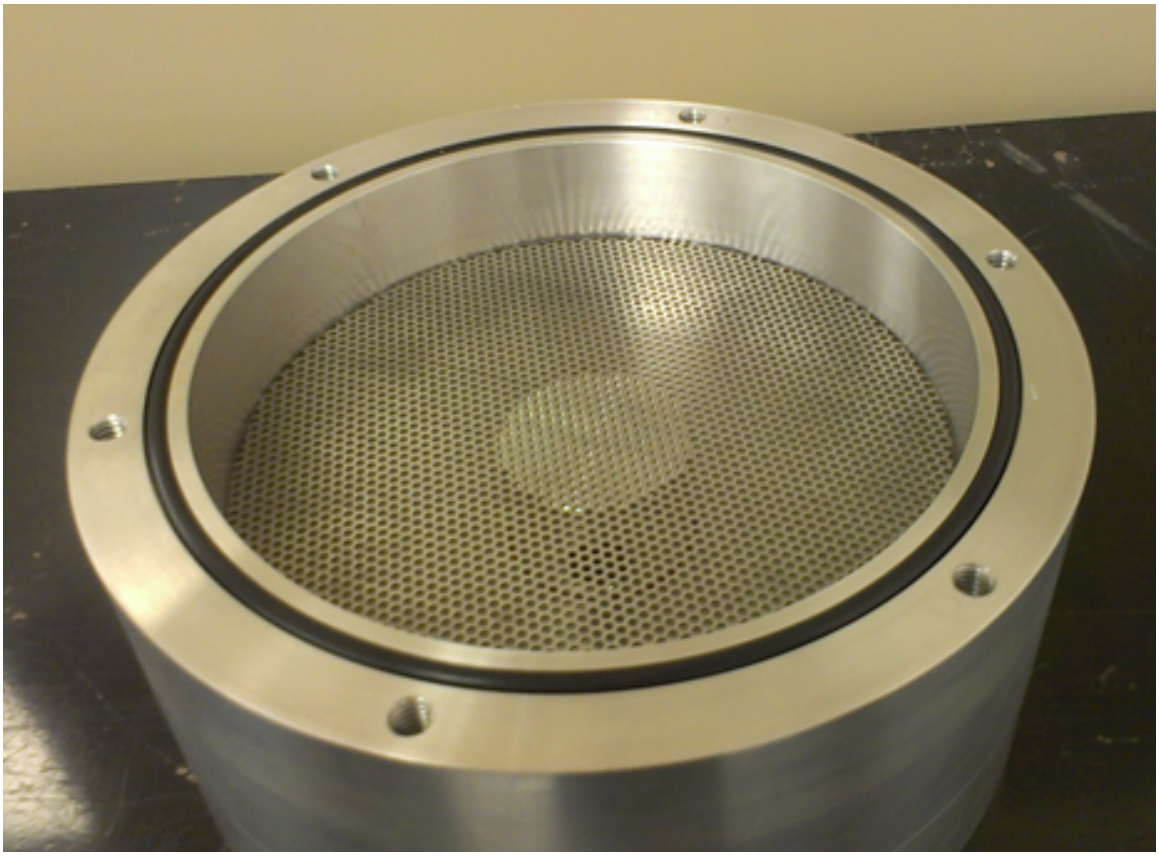

Figure 4.5. A screen mounted above the impactor separates the open mixing section from the tunnel section. The screen will hold copper BBs to create a pressure drop between the free space below and the tunnel section above.

is set at 5 cm/s to minimize forced convective effects while supplying adequate oxidizer to the flame's buoyant entrainment field in accordance with the modeling work [57] and the specifications of Limiting Oxygen Index standards [68].

Wiring is routed through a rack mounted electronics panel seen in Fig. 4.8 listed as follows: 1.) On/Off switch, 2.) Fuse, 3.) Emergency stop switch, 4.) Panel rack mounts, 5.) 12 Volt DC power supply, 6.) +/- 15 Volt DC power supply, 7.) Wire terminals. All power, sensor, and data acquisition data moves through this panel. A detailed wiring chart can be found in Appendix 8 for future improvements and repair.

Figure 4.6. Copper BBs are packed above the screen to create a large pressure drop to encourage mixing and smooth flow.

The emergency stop button listed above as item #3 in Fig. 4.8 electrically disconnects gas flow setpoints from the computer controlled mass flow controllers and flushes the flow tunnel with inert nitrogen gas at maximum flow. This is designed as a safety feature, or to end a combustion test suddenly as necessary. Activation is recorded by computer to mark the end of a test. Any malfunction of this safety system will stop and prevent the flow of oxidizer.

A National Instruments cDAQ-9174 data acquisition chassis holds modules for analog output for mass flow controller setpoints (NI-9264), analog input for mass flow controller flow rates (NI-9201), Thermocouple and radiometer inputs (NI-9213),

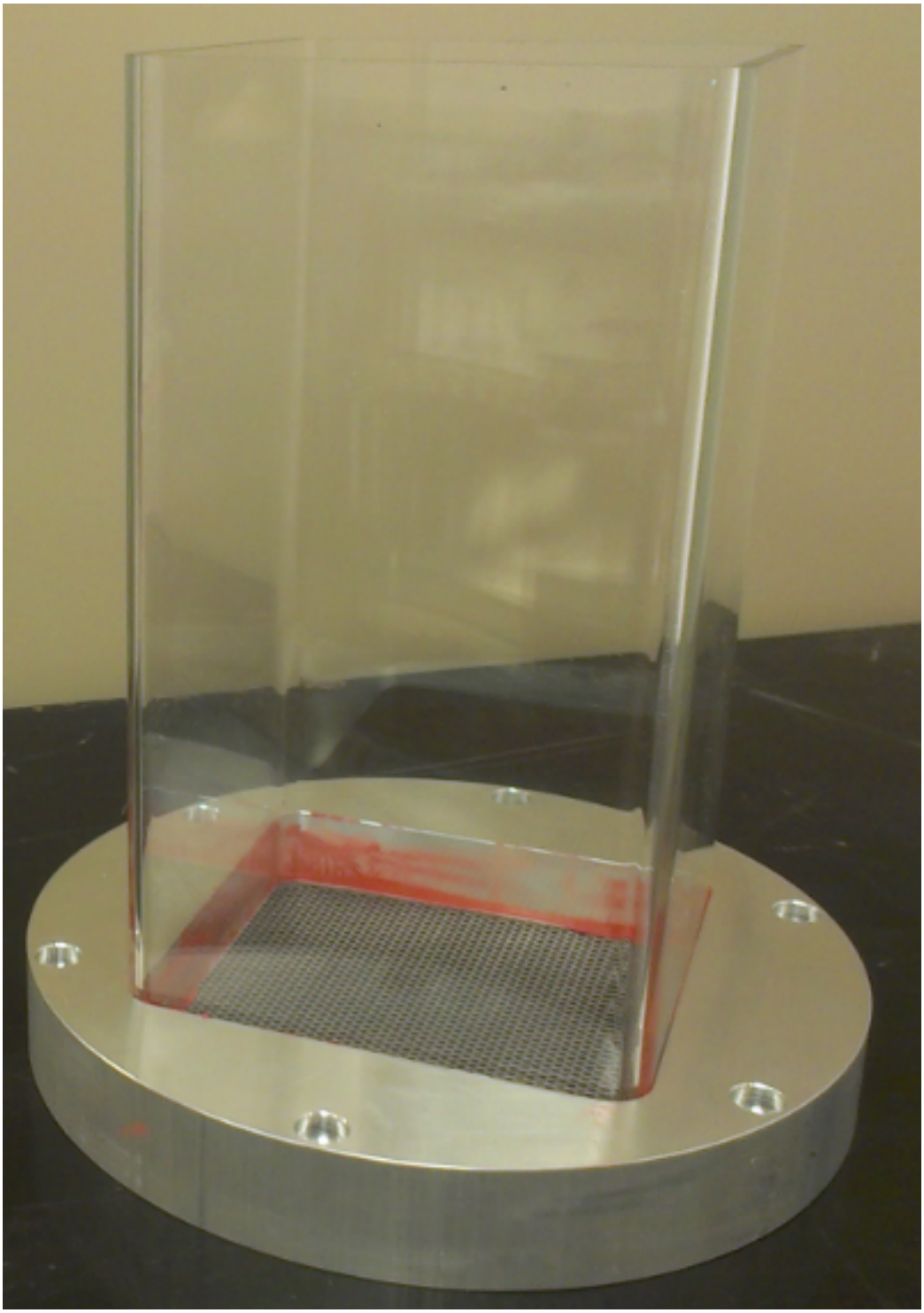

Figure 4.7. The borosilicate glass flow duct is mounted to an interchangeable lid. It is sealed around the edges with silicone sealant. A screen separates the flow section from the copper BBs to help prevent samples from contaminating the interior of the mixing chamber.

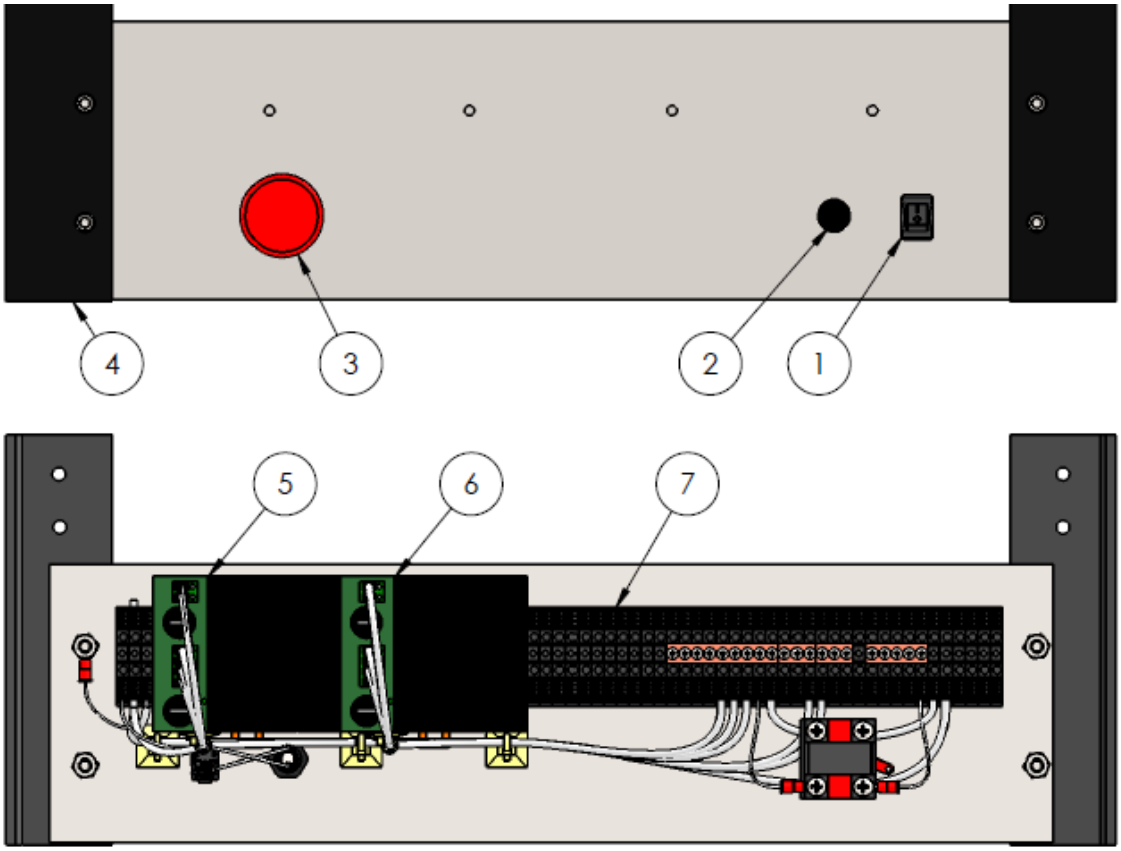

Figure 4.8. Electronic control panel. 1.) ON/OFF switch, 2.) Fuse, 3.) emergency stop switch, 4.) panel rack mounts, 5.) 12 Volt DC power supply, 6.) +/- 15 Volt DC power supply, 7.) wire terminals.

and relay control for lights and igniter power (NI-9481). These devices are capable of faster than necessary data acquisition and control.

Physical toggle switches allow for the manual over ride of relay controlled items, igniter retraction, igniter on/off, and lights on/off can all be set manually and over rides are recorded by the spare input channels on the analog input module (NI-9201).

Video recordings are synchronized with the computer recorded data by use of a liquid crystal display (LCD) module. An LCD controller was made with custom software written to an Arduino Uno circuit board to interpret information from the computer control software sent via RS-232 serial communications. The Arduino Uno

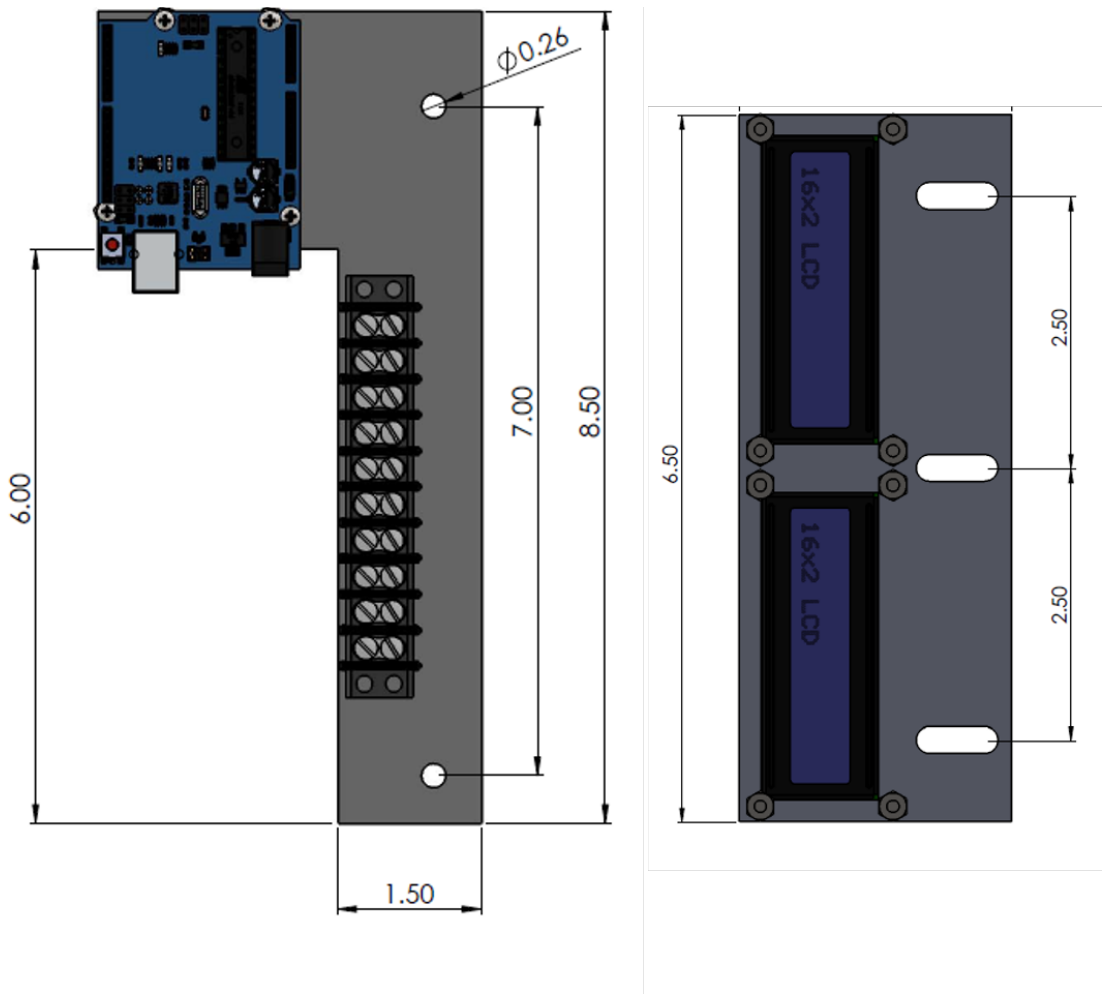

Figure 4.9. Left: Liquid Crystal Display (LCD) controller and interpreter. The board mount is cut to stay out of the camera view. Right: Liquid Crystal Display (LCD) panel display which can be mounted in view of the camera. LCDs are connected with a ribbon to the controller.

is mounted to a panel with a wiring terminal block seen in Fig. 4.9 Left. Two 16 character x 2 line LCDs are necessary to display the relevant information: Experiment number and title, oxygen percentage, flow velocity, and elapsed time, Fig. 4.9 Right. LCD and control unit are mounted separately and connected with a ribbon so the LCD location is adjustable within the camera view.

Sample mass and gaseous flow rates were recorded at 10 Hz throughout the test by computer. Images were recorded throughout the test with a high resolution digital camera typically set on intervalometer mode, 1 frame per minute was typical for the slow changing psuedosteady flames. High Definition video was taken for some tests to capture flame oscillations near the extinction limits or flame steadiness. Images are synchronized with computer recorded data via LCD display which shows experiment time. Green lighting is used in some tests to illuminate the surface of the test specimen while reducing contamination of the predominantly blue flame images.

4.1.1 Computer Control Software

The variable oxygen tunnel is controlled by custom software written in the National Instruments LabView programming environment. It is a graphical computer language designed for use with the National Instruments data acquisition and control hardware. Several custom made independently coded control blocks run simultaneously on parallel processor threads.

To the typical end user of the Vertical Variable Oxygen Tunnel (VVOT), input data of oxygen percentage, flow velocity, igniter on time, experiment title, and test number are required. Preset oxygen and/or velocity ramping parameters can also be input. Displayed on the screen are set flow rates, measured flow rates, oxygen percentage, sample mass, igniter state and elapsed time. For advanced users, a secondary control tab allows for the gasses to be changed and recalibrated. A maximum oxygen limit is hard coded into the control software to prevent accidental creation of a potentially dangerous high oxygen environment when none was intended. A software

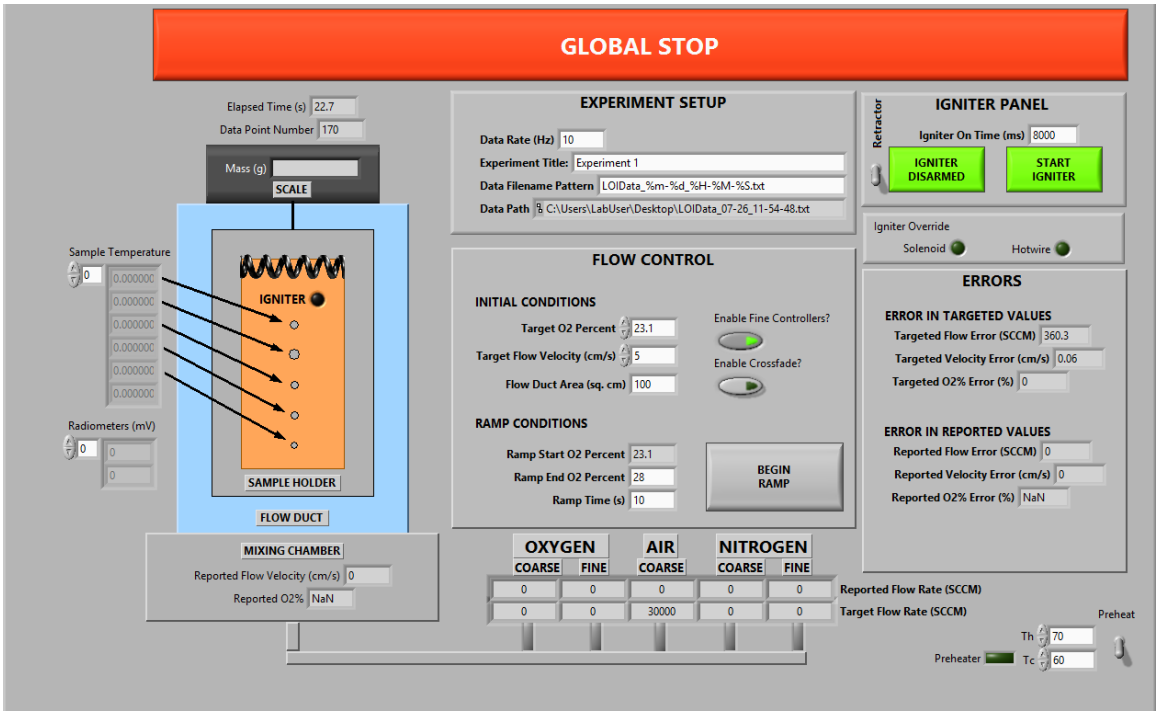

Figure 4.10. The main graphic user interface of the variable oxygen tunnel

override switch, when high oxygen is intended, is available to capable programmers in the advanced settings tab.

All data input by the user and displayed on the interface is recorded to a csv file on the control computer desktop. The default filename is labeled with the time and date for later access.

Figure 4.10 shows the main graphical user interface to control the Variable Oxygen Tunnel. The main functions of the interface will be described here for future reference.

A *GLOBAL STOP* button is very prevalent at the top of the interface. This will stop all flow and end a test. This can be used in an emergency in addition to the physical emergency shut down button that is available to the user. This button will stop the flow of oxygen, flush the chamber with a small amount of nitrogen to

extinguish the flame, and ensure the data has been saved to the hard drive. For continued nitrogen flushing, the physical emergency stop button should be pressed.

The *Elapsed Time* and *Data Point* numbers are shown in the upper left. This elapsed time corresponds to the time visible on the LCD display which is described in the next section. This allows the synchronization of video data with data recorded by the computer.

Below the *Elapsed Time* is the sample *Mass* in grams, *Sample Temperatures* from thermocouples (if available), and *Radiometers* radiometer values in mV (if available). The elapsed time and mass data will also be displayed on the physical LCD readout.

In the bottom left, the *Mixing Chamber* module displays the *Reported Flow Velocity* in cm/s and *Reported O2%* oxygen percentage measured by the thermal flow meters contained inside the mass flow controllers. Depending on hardware tuning, there can, and will be some deviation from the intended set point values. These actual measurements are recorded to the disk.

In the center top, the *Experiment Setup* module allows the user to change the *Data Rate* in Hertz, the *Experiment Title*, the auto generating *Data Filename Pattern*, and the *Data Path* where the file is saved on the computer is displayed. The experiment title is displayed on the physical LCD. A data filename is calculated from the pattern and suggested based on the start time of the experiment. It is recommended that the default filename be used for consistency.

The *Flow Control* section in the center of the GUI will be manipulated throughout a test in the VVOT. The *Initial Conditions* are set at the top of the module with *Target O2 Percent* between 0 and 100, *Target Flow Velocity* in cm/s, and the *Flow Duct Area* in cm^2. *Enable Fine Controllers* is turned ON by default. The *Target O2*

Percent and *Target Flow Velocity* can be manipulated in real time during testing to change the flow conditions within the chamber.

At the bottom of the *Flow Control* module, a *Ramp Conditions* feature allows smooth proportional ramping of gases. The *Ramp Start O2 Percent* is the value referenced from the *Initial Conditions* and is not accessible to the user in this section, the *Ramp End O2 Percent* is the desired final oxygen percentage, and the *Ramp Time (s)* is the length of time the oxygen change should take, in seconds. The *Begin Ramp* button will start the ramping sequence.

The flow controller raw data is shown at the bottom center of the GUI. The first row displays the measured flow rates in standard cubic centimeters per minute (SCCM) for the coarse and fine oxygen control, the coarse air control, and the coarse and fine nitrogen control. The bottom row displays the targeted set points for each controller in SCCM.

The *Igniter Panel* in the upper right controls the igniter circuit via software. The igniter can also be controlled manually from the physical control panel. Ignition will be recorded on the computer regardless of how the igniter is operated. The switch on the left of the module enables and disables the igniter retractor, which is available when installed. The *Igniter ON time* box sets how long the igniter is energized in milliseconds. Toggling *Igniter Disarmed* to *Igniter Armed* will allow the *Start Igniter* button to be activated. The disarm prevents accidental ignition. After pressing *Start Igniter*, the button will toggle to a *Stop Igniter* mode which can cancel ignition.

The *Igniter Override* module below the *Igniter Panel* indicates whether the positioning solenoid or hotwire have been manually activated on the physical control panel. These values are recorded in the data file.

The *Errors* panel attempts to estimate the error in flow rates based on the fundamental principles of the mass flow controllers and thermal mass flow sensors used. It should be noted that this represents a minimum error, as other errors such as improper gas purity, miscalibration, leakage, etc could conceivably be present.

In the lower right of the graphic user interface is a *Preheat* circuit. This allows the igniter circuit to be used as a preheater. When toggled ON, the igniter will turn ON when thermocouple channel 1 reads lower than the value in Tc (in Celsius), and will turn OFF when thermocouple channel 1 reads higher than the value in Th (in Celsius).

Figure 4.11 shows the advanced settings for the VVOT. The advanced settings allow for the basic control hardware to be changed, and provides a large amount of debugging data to ensure proper function of the device. This menu is chosen from the tab in the upper left labeled *Setup and Configuration*. It is broken down into various modules: The *MFC Channels* module sets the input and output data acquisition channels of the mass flow controllers. If the analog input and/or analog output National Instruments data acquisition hardware modules are changed, it is more practical to rename the new hardware modules LOI_AnalgoOut and LOI_AnalogIN to correspond with the settings that are used in the graphic user interface. This can be done from the National Instruments Measurements and Automation Explorer driver controller which is installed with this GUI.

The module labeled *Scale Connection Settings* sets the serial communication protocols between the computer and the A&D digital precision scale. Note that these settings must correspond to those programmed into the scale.

LCD String shows the raw data which is sent to the LCD control module which is described below. This string is a combination of parsing characters and relevant data and is meant for debugging problems with the LCD controller. In the lower left corner, *Igniter State*, *Voltage Reported by Controller*, *Voltage Written to Controller*, and *Voltage Adjustment (Manual Zeroing)* give raw data for debugging possible software calculation errors and hardware errors with the VVOT.

The *MFC Calibration* module allows the user to change the settings of each individual mass flow controller. These mass flow controllers are intended to be swappable. If a new mass flow controller is installed, the hardware specifications need to be updated here. These values can be found in the user's manual of the mass flow controllers to be installed.

The *Igniter Relay* module sets the data acquisition hardware module and channels that will control the hotwire power and the positioning solenoid power. The *Solenoid Override Input* and *Hotwire Override Input* set the data acquisition module and channels which read a signal from the manual override switches on the physical control panel.

Radiometer In sets the data acquisition channels for radiometers, if installed.

In the upper right, the *LCD Display Settings* controls the data communication protocols to the LCD display hardware module. These can not be changed without reprogramming the firmware on the LCD's integrated circuit. The LCD is enabled by selecting *Enable LCD Panel*.

The *Thermocouple* module in the lower right sets the data acquisition hardware module and channels of the thermocouples.

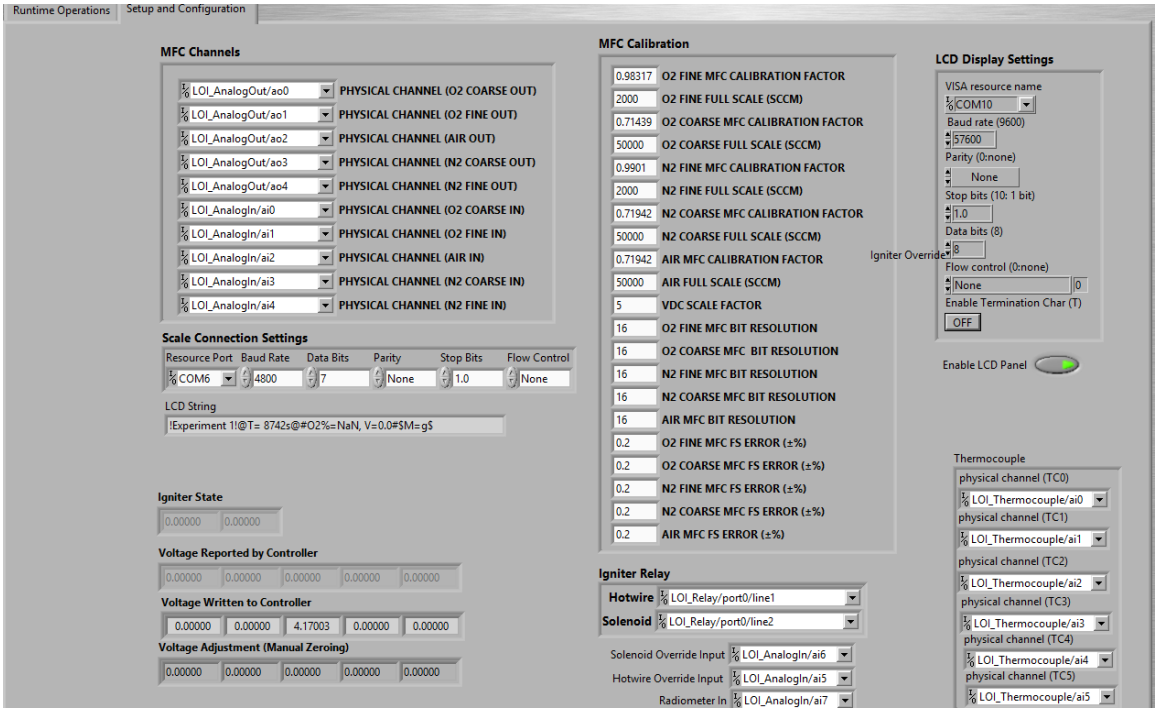

Figure 4.11. Advanced preferences menu for the variable oxygen tunnel

Parsing Character	Destination
!	! LCD 1 Line 1!
@	@ LCD 1 Line 2@
#	# LCD 2 Line 1 #
$	$ LCD 3 Line 2 $

Table 4.1. LCD serial communication data parsing scheme

An independent code block sends pertinent data from the computer to the LCD controller as discussed above. Each LCD Data string is sent via RS-232 serial communication and is parsed with special characters as listed in table 4.1. The firmware created for the LCD controller will know how to interpret these lines. Each information string can be 16 characters long and is sent in any order as fast as new information is available. The LCD controller firmware is set to operate at the serial speed and settings listed in Table 4.2. A duplicate of this device was also built for use in [69].

Setting	Parameter
Baud	57600
Parity	None
Data Bits	8
Stop Bits	1
Flow Control	None

Table 4.2. LCD serial communication settings

4.2 Validation with Ethanol Tea Lamps

Since mass burning rate is obtained from the time derivative of mass loss $\Delta m/\Delta t$, within the period Δt, the mass loss needs to be nearly constant to be meaningfully referred to as the instantaneous rate. To test steadiness of the burning sample and to validate the mass measurement technique, the ethanol-fueled tea lamp is chosen shown in 4.12. The fiberglass wick used is short enough so that there is no liquid dry out at the tip and the supply of ethanol flow from the liquid fuel bottle through capillary action is expected to be constant.

Figure 4.13 shows a typical fuel mass loss (blue line) of the ethanol tea lamp with a 7 mm long wick (3 mm diameter) at constant oxygen percentage of 23.1% by mass (21% by mole fraction i.e. air) throughout a test spanning approximately 1.25 hours. Burning rates every 100 seconds are shown by the brown dots. They are computed from a linear fit of mass loss curve ($\Delta m/\Delta t$) using a $\Delta t = 100s$. As shown the figure, the instantaneous mass burning rate is seen to be very constant throughout the test ranging from 3.823 mg/s to 3.820 mg/s, consistent with the mass loss curve being a straight line.

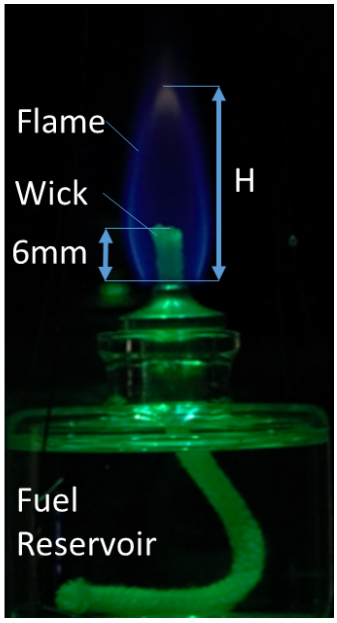

Figure 4.12. Photograph of ethanol tea lamp specimen. The green color is tinted illumination to reduce interference with analysis of the blue flame.

Effect of Wick Length. Having demonstrated that the device can measure burning rate with good accuracy, a systematic investigation of the effect of the wick length was made.

Figure 4.14 shows the effect of wick length on burning rate. Note that at zero wick length, the flame is sustained by the fuel vapor from the top surface (burning area $= \pi(D_{wick}/2)^2$ where D_{wick} is the wick diameter). The burning rates then increase with wick length almost linearly. The slight non-linearity is thought to be due to the contribution of the wick top surface which may not be exactly constant with wick length and the interaction of the lower portion of the wick with the metal wick holder. Note also at 10 mm length, the wick approaches the fuel transport limit. In an ordinary commercial candle, wick burnout may occur and self-trim. In the present case, a non-combustible fiberglass wick is used. So the 12 mm data is marked *wick burn out*.

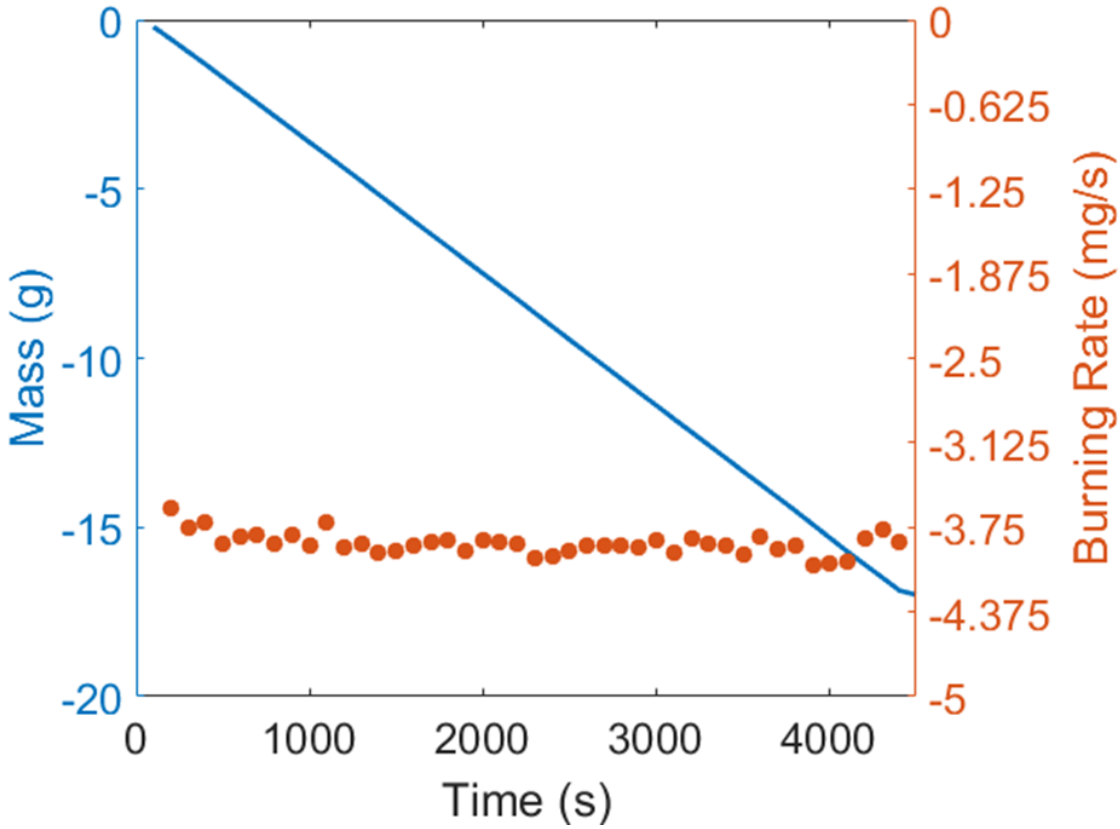

Figure 4.13. Mass loss of the ethanol tea lamp with a 7 mm long wick at constant oxygen percentage of 23.1% by mass (21% by mole, air).

Effect of Oxygen Concentration on Burning Rate. Figure 4.15 shows the effect of oxygen concentration on burning rate. The wick is still 3 mm diameter, and now 5 mm in length. The effect of oxygen concentration appears linear for all but the lowest oxygen percentage at 17.28% by mass. This drop off is due to a limit cycle oscillation which yields a much reduced average burning rate. This limit cycle oscillation will be discussed in a later section.

When the ambient oxygen percentage increases, the observed flame length also increases. Although more sophisticated numerical model can compute this variation e.g. [70, 71], a paper by Sunderland [72] opted to use the simpler analytic expression by Roper [73, 74] to compare their candle flame data. Note that Ropers work is based

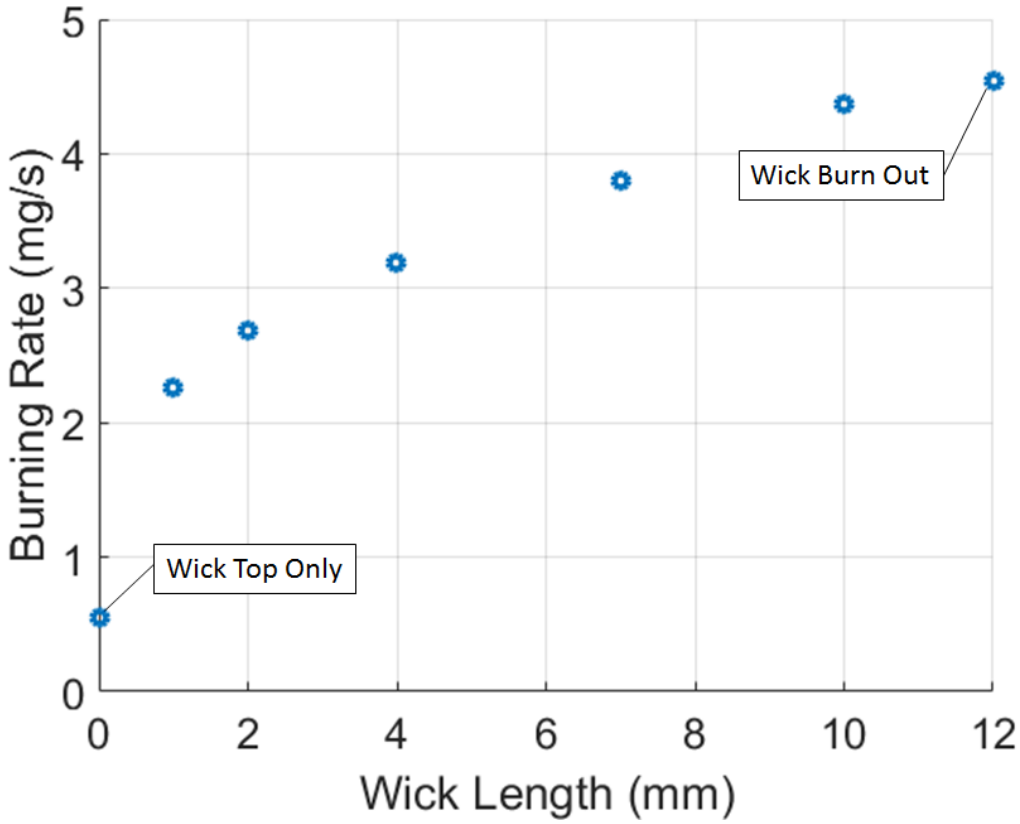

Figure 4.14. Ethanol tea lamp mass burning rate vs. wick length in air (3 mm diameter wick)

on buoyant co-flow gaseous flames so this may stretch beyond its original scope. To compare with the mass burning rate, the Roper model [73] yields an expression for fuel burning rate from experimentally measured flame height H as follows:

$$\dot{m_f} = \{(\frac{1}{4\pi D_o}(\frac{T_\infty}{T_f})^{.67})^{-1}\rho_f \frac{M_{air}}{M_f}\frac{1}{s}\}Y_{ox,\infty}H \tag{4.3}$$

where D_o is the molecular diffusion of oxygen into the flame zone, T_∞ is the ambient temperature, T_f is the characteristic flame temperature, ρ_f is the density, M_{air} is the molecular weight of air, M_f is the molecular weight of fuel, s is the

stoichiometric ratio, $Y_{ox,\infty}$ is the oxidizer mole fraction, and H is the measured flame height, which Roper's model was originally proposed to predict.

Using this equation with experimental flame height measurements, the burning rate vs. mass oxygen percentage is shown by brown dots in 4.15. The trend follows the experimental data except at high oxygen (likely due to increased soot) and near the extinction limit. Note mass burning rate is proportional to the flame height, a basic prediction from Burke-Schumann analysis assuming mass diffusion controlled flames. Prediction of extinction limit at the low oxygen limit is not expected from the fast kinetic model. But more interestingly, we have observed near-limit self-sustained flame oscillation (limit-cycle) in this wick flame configuration.

Limit-Cycle Oscillations Near the Oxygen Extinction Limit. Near limit flame oscillation for a wick stabilized flame has been reported previously e.g. [75, 76]. In these experiments, extinction limits were reached by a gradual depletion of oxygen due to burning in a sealed chamber. During the oscillation, the flame bottom retreats downstream then flashes back with increasing amplitude until extinction is reached. Since oxygen is decreasing continuously in these experiments, it is not clear whether an oscillation once initiated will always lead to extinction or if a limit-cycle constant amplitude motion can be sustained. Since in the present setup, we can keep the oxygen at constant level near the limit with a very high precision, this question is explored.

We have found constant amplitude near limit oscillations in this work. The oxygen range for this to occur is very narrow and needs to be approached carefully. Starting from a steady flame and reducing oxygen, the flame base will first have small amplitude vertical fluctuation along the side of the wick. This progresses until the flame

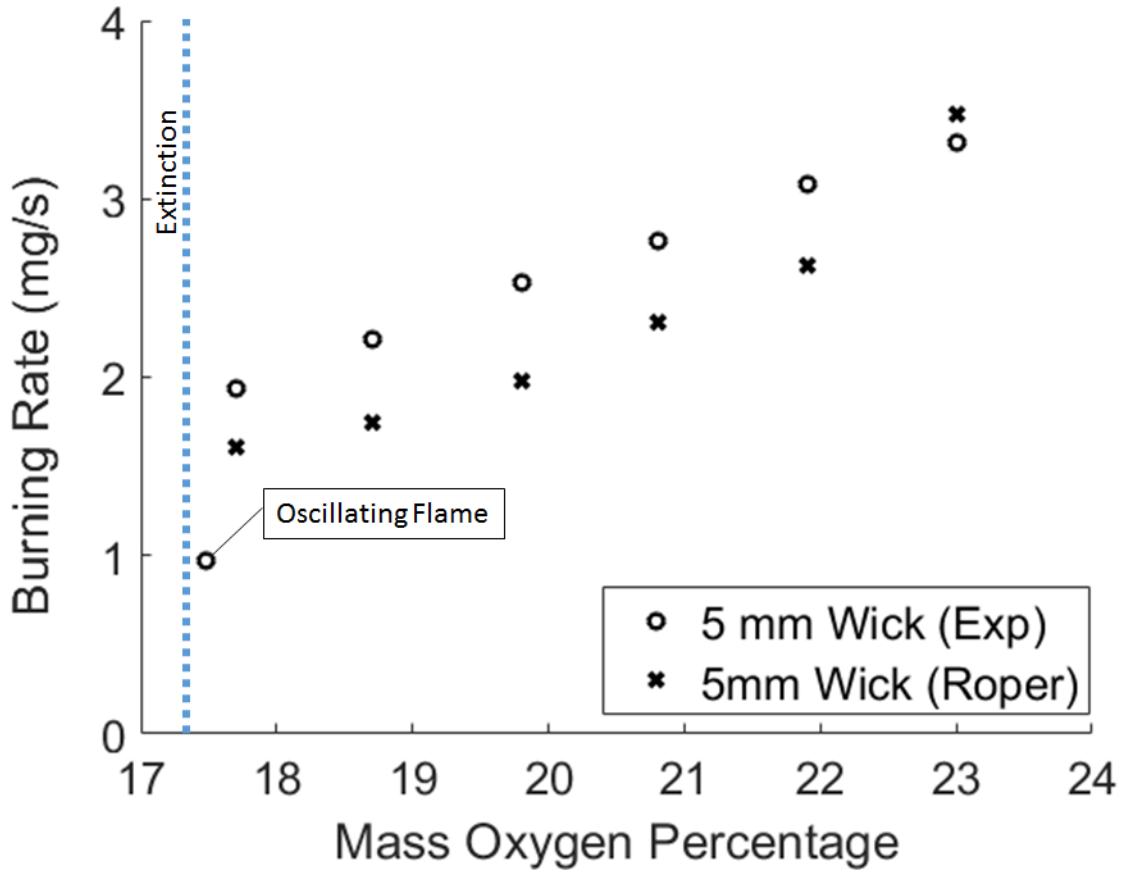

Figure 4.15. The effect of oxygen on burning rate for an ethanol tea lamp with (3 mm diameter x 5 mm length wick). Circles are measured mass loss rates, x's are calculated using a measured flame height.

base is lifted off from the side of the wick to a location above the wick. The flame becomes very small in size but it then flashes back toward the base of the wick. This cycle repeats and can last for many minutes or even hours depending on the initiation process. Note that with a stabilized wick flame, the ethanol in the container receives heat from conduction from the flame base through the container wall. If a steady flame is maintained for a long period, the liquid equilibrium temperature can be 2-3^oC higher than that of the ambient (measurement from an inserted thermocouple). With the beginning of oscillation, the heat feedback from the flame to the container is reduced and the liquid reservoir temperature slowly decreases. The flame

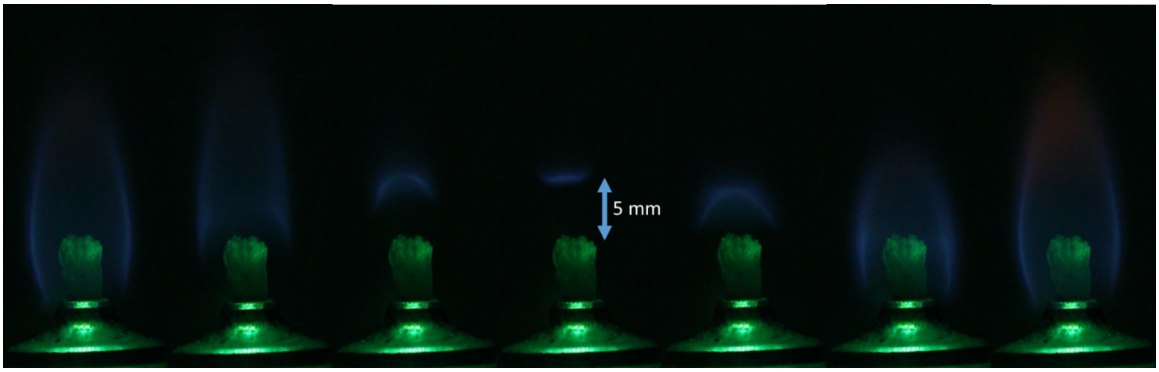

Figure 4.16. A typical oscillation cycle consisting of the lift off of flame base from the side of the wick and the flashback of shrunk flame at the top of the wick. O2 = 17.28% oxygen by mass. Each frame is 1/30th of a second

may become extinguished after several minutes of oscillations. However, by careful adjustment of oxygen, a regime of pseudo-steady state oscillation in ethanol tea lamps can last for hours with a frequency between 5 to 6 Hz. Fig. 4.16 shows the flame size and position relative to the wick in one cycle. Videos are provided as supplemental materials with the original publication [66], but not with the dissertation.

While there are a number of theoretical analyses on near limit diffusion flame oscillation [77, 78], most are linear and are not suitable for finite amplitude limit cycles. It is not clear whether the observed oscillation is the result of this particular wick configuration or something more general. For example, flame front flickering has been observed in flame spread over liquid pools. Its occurrence and characteristics are sensitive to the pool temperature [79]. We would also like to mention that a steady state numerical investigation of a thick solid slab burning in a limiting oxygen device in the candle configuration predicted the existence of hysteresis of two solutions: one, a side stabilized flame and the other, a wake stabilized flame [80]. In contrast, here we observed two flames oscillating between these two locations. Because of the oscillation, the cycle average mass burning rate is reduced. As can be seen in Fig.

4.15, the average burning rate of the oscillatory flame is about one half of the value of the steady flame at the nearest steady conditions.

5 Low Stretch Flames on PMMA Spherical Shells

The spherical shell samples of various sizes are described fully in the samples section of this document. The spherical shells are filled with about 50% ice and 50% water to cool the back surface. This ensures the back of the shell is always held near 0^oC (temperatures of 10-20^oC were typical in practice due to boundary layer effects in the ice bath). The ice content of the ice bath and back surface temperature are monitored throughout testing to make sure there is still a significant amount of ice left at the end of the combustion test. Mass loss measurements would be invalid if the ice bath has been significantly heated due to mass transfer from evaporation.

The shells are suspended from the precision balance above the Vertical Variable Oxygen Tunnel (VVOT). Because of the large size of the spherical shells, the VVOT is used as a nozzle instead of a flow tunnel. The shell is hung approximately 4 cm above the tunnel outlet. Because of the close proximity of the sample to the tunnel exit, it is expected that the oxygen concentration in the flame zone is the same as in the tunnel itself.

To ignite the shell during testing, an igniter wire slides on rails into the symmetry position below the sphere. The igniter is 28 gauge Kanthal A-1 powered with 3.8 A constant current. The flame is overdriven past ignition then the igniter is turned off and retracted.

Figure 5.1 shows a side view of the exposed section of the PMMA shell after ignition. The ignited flame spreads over the exposed surface until overlapping the aluminum foil masking. The internal temperature within the shell material is allowed to reach a steady state profile.

Because the front surface pyrolysis temperature is nearly constant during steady state burning, and the back surface is held near 0^oC, the heat flux into the solid interior is constant, no matter the external conditions of oxygen concentration, stretch rate, nozzle velocity, etc. Figure 5.2 shows a schematic of the solid with ice bath back surface. Temperatures on front and back are confirmed with fine wire k-type thermocouple wires for many, but not all of the tests. In this case, the heat flux is based entirely on material thickness, which is varied as a parameter throughout the testing campaign. The lower right of Fig 5.2 summarizes how heat flux relates to material thickness.

With the steady state solid temperature profile, and therefore heat flux into the solid interior held fixed, all excess energy from the flame will either blow off downstream or be used to pyrolyze excess fuel from the surface. The flame will respond nearly instantly to changes in flow condition of oxidizer or velocity.

Material regression is assumed to be near zero over the course of a test (the Peclet Number $Pe \approx 0$). This can be confirmed with mass loss measurements from the precision balance or by image analysis before and after each test.

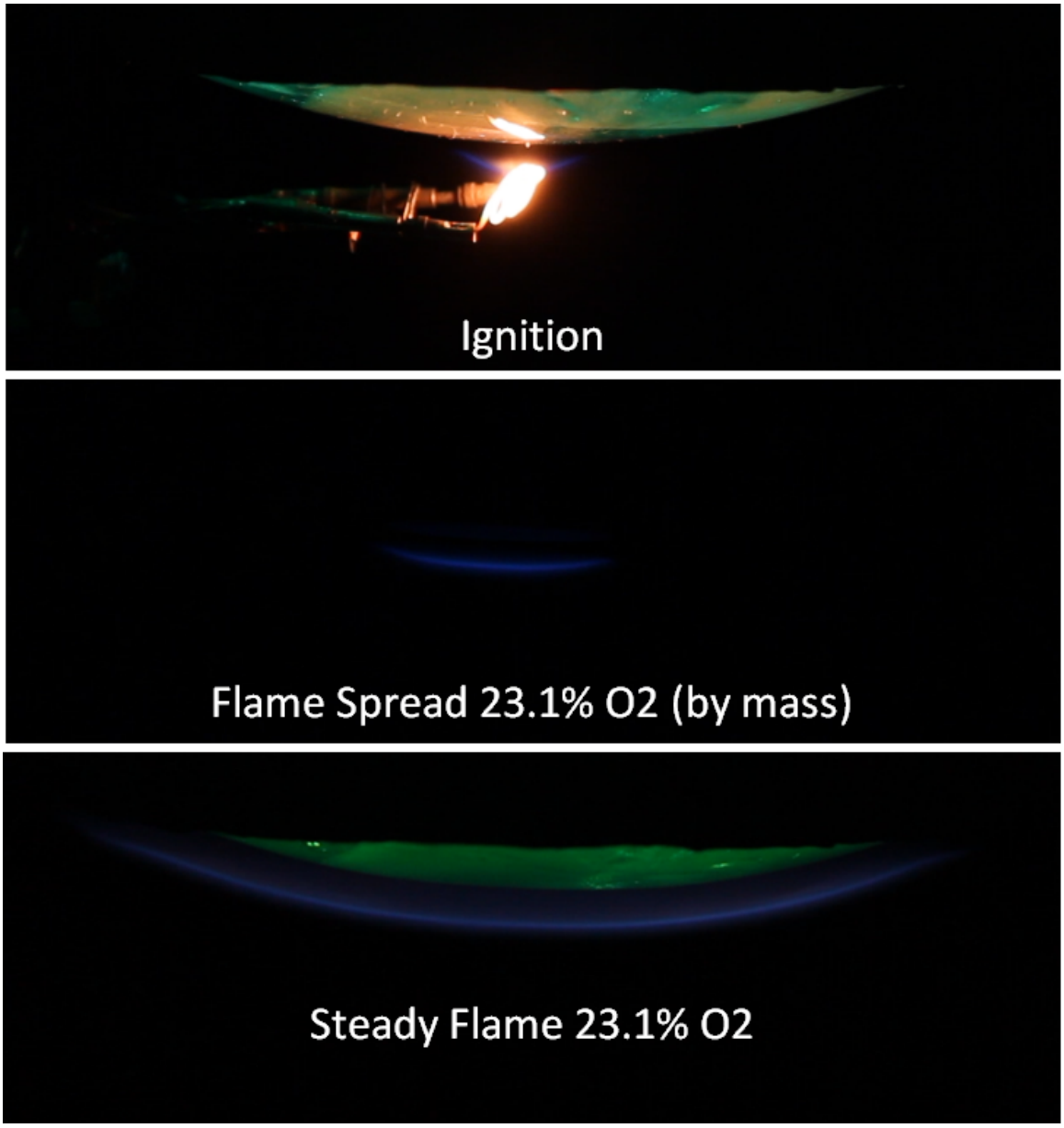

Figure 5.1. Flame spread across the exposed area of a spherical shell. Ignition, flame spread with the igniter retracted, and the psuedo steady state flame. The exposed PMMA appears green due to colored illumination from above the transparent sample, the low soot flame is blue in color.

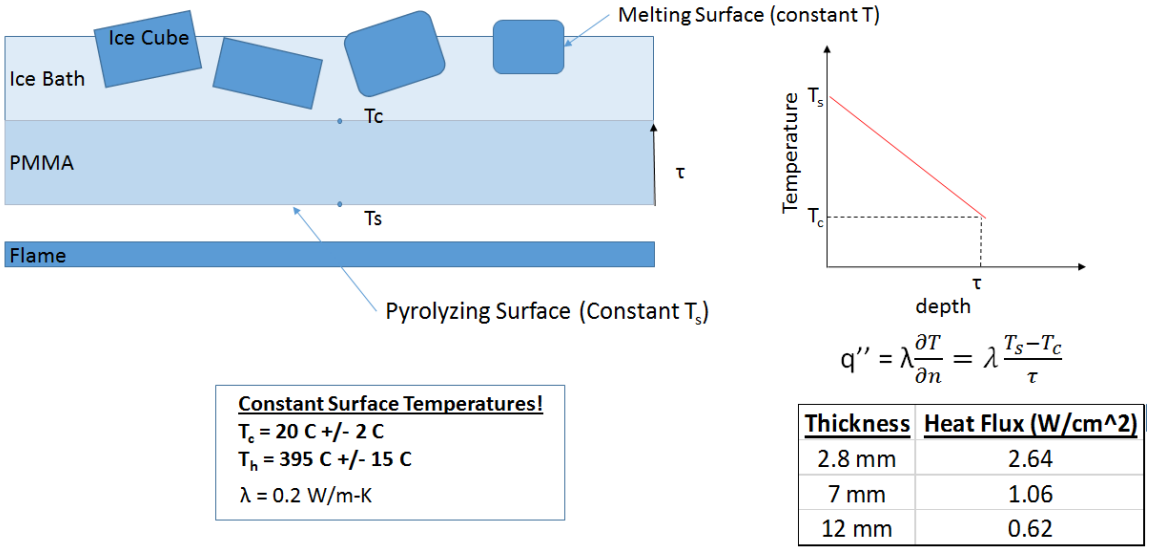

Thickness	Heat Flux (W/cm^2)
2.8 mm	2.64
7 mm	1.06
12 mm	0.62

Figure 5.2. Summary of heat transfer through spherical shells. The back surface is held near constant with an ice bath. The front surface temperature is at the poly(methyl methacrylate) pyrolysis temperature during steady burning. The solid internal temperature will reach a steady state profile and is controlled only by the material thickness.

5.1 Local Burning Rate Measurement

Mass measurement of the sample with the precision balance only yields the total burning rate or global burning rate. On the other hand, if we have spacially uniform burning across the sample surface, then the local burn rate is just the measured total burning rate divided by the burning area. As discussed previously, it is known that the flame in the stagnation region of a blunt body is nearly one-dimensional with uniform standoff distance as seen in the bottom of Fig. 5.1. In a mixed buoyant and forced flow, conditions near the stagnation region can be characterized by a densimetric mixed flow stretch rate [5]:

$$a_m = (a_b^2 + a_f^2)^{1/2} \tag{5.1}$$

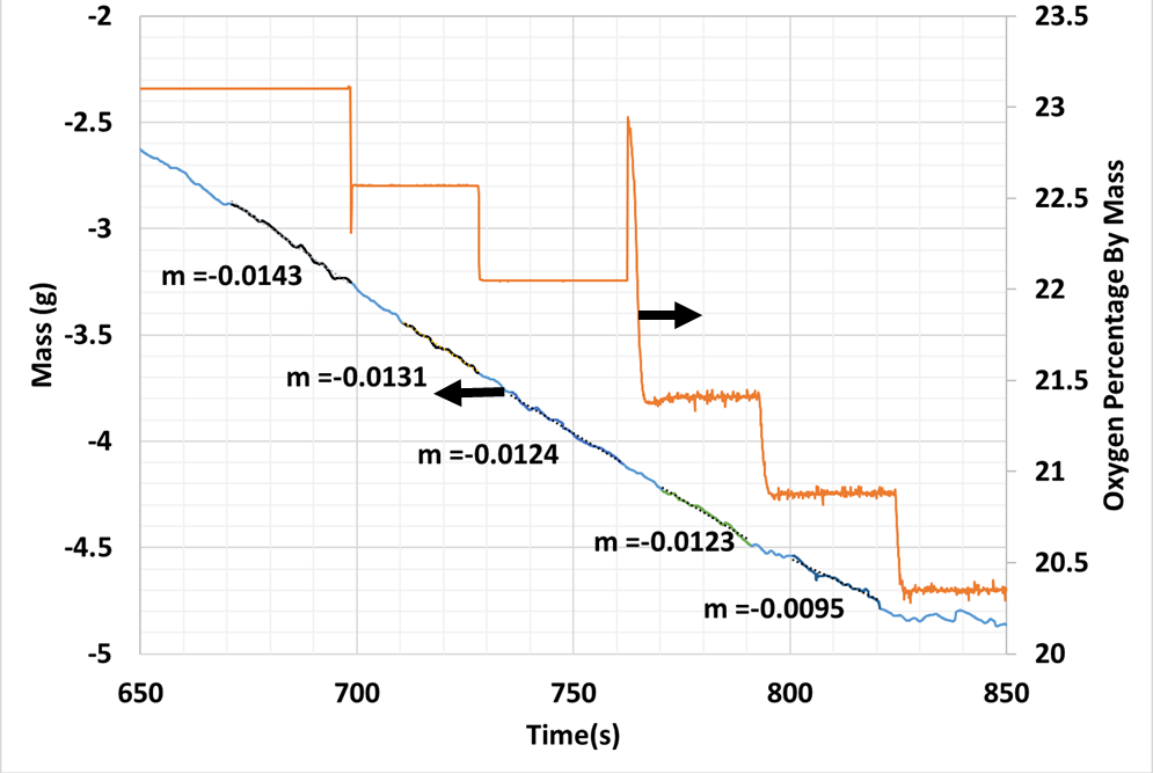

Figure 5.3. Mass loss of stagnation burning of a 7 mm thick PMMA shell subject to multiple step decreases in oxygen concentration. The slope of the mass is the burning rate. Stretch rate is 7.86 s^{-1}.

The buoyant stretch rate $a_b = \sqrt{\frac{T_f^* - T_\infty}{T_f^*}\frac{g}{R}}$, the forced flow stretch rate $a_f = \frac{3}{2}\frac{U_\infty}{R}$, where R is the radius (of curvature) of the spherical shell, T_f^* is the characteristic flame temperature, T_∞ is the ambient temperature, g is the gravitational force, and U_∞ is the free stream forced velocity.

In this work, spherical shells of three different thicknesses were fabricated with radius of curvature R=10.4 cm. For a forced flow velocity of 5 cm/s and normal Earth gravity, $a_f = 0.72s^{-1}$, $a_b = 7.86s^{-1}$ and $a_m = 7.89s^{-1}$. The radius of curvature is chosen to be large enough to yield a small a_m comparable to space flight test geometries of interest, but not too large to impair the function of the nozzle. The

shell thicknesses were used to vary the amount of heat loss from the flame to the solid interior.

The surface energy balance in the gas-solid interface can be expressed by:

$$\dot{m}_f L_v = \lambda_g \frac{\partial T}{\partial n}|_g + \dot{Q}_f - \epsilon\sigma(T_s^4 - T_\infty^4) - \lambda_s \frac{\partial T}{\partial n}|_s \tag{5.2}$$

Where $\dot{m}L$ on the left side of the equation is the rate of heat used for pyrolysis, the four terms on the right hand side of the equation are respectively, heat conduction from the flame to the solid, the net rate of gas radiation to the surface, radiation loss from the surface, and heat conduction into the solid interior. Since solid heat up is a slow process compared with gas phase transient, the conduction into the solid is slowly varying. During the slow heat up process, the gas phase flame can be considered as quasi-steady with heat conduction into the solid as a loss to the solid. In [64], the ratio of solid heat loss to gas phase heat feedback is treated as a parameter to determine the solid flammability. The extinction boundary was found to be a strong function of the heat loss parameter and includes both the blow off and quenching branches of the flammability map.

In the present work, we use the different shell thicknesses with an ice bath back surface to control the rate of heat loss to the solid. An estimate is given in Table 5.1. This follows Eq. 5.3 It is expected that heat loss should affect the oxygen extinction limit. The critical burning rates corresponding to these limits is measured.

$$q_c = \lambda_s \frac{\partial T}{\partial n}|_s = \frac{\delta T}{\tau}\lambda_s \tag{5.3}$$

Shell Thickness (mm)	Heat Loss to Solid (W/cm^2)
2.8	2.64
7	1.06
12	0.62

Table 5.1. Estimated heat loss to the solid interior for ice cooled PMMA shells.

$$q_c = \frac{380K}{.003m}(0.2\frac{W}{mK}) = 25,333\frac{W}{m^2} \tag{5.4}$$

Because the surface temperature of the solid is relatively steady during burning, surface radiation stays steady no matter the conditions and follows:

$$Q_{rs} = \epsilon\sigma(T_s^4 - T_\infty^4) = (0.86)(5.67x10^{-8}\frac{W}{m^2K^4})((65.3K)^4 - (300K)^4) \tag{5.5}$$

$$Q_{rs} = 0.85\frac{W}{cm^2} \tag{5.6}$$

The amount of energy lost from the solid by pyrolysis can be calculated, if the mass loss rate is known. In the Variable Oxygen Tunnel, this value can be measured. For this example case, $\dot{m}'' = 0.0013g/cm^2 - s$ is a reasonable value. Actual measured results will be shown elsewhere in the document.

$$Q_L = L_v\dot{m}'' \tag{5.7}$$

$$Q_L = (1000J/g)(0.0013g/cm^2 - s) = 1.3W/cm^2 \tag{5.8}$$

A picture of a 7 mm thick PMMA shell with a blue flame adjacent to the bottom surface is shown in the bottom of Fig. 5.1. Water is filled inside the bowl of the shell

with small ice cubes to control the back side temperature. A thermocouple is placed on the water-solid interface. To control the burning area and confine the flame to the uniform burning region, the periphery of the shell bottom surface was covered with black anodized aluminum foil and Kapton tape. Only the center region of PMMA is exposed with area 39.53 cm^2. In the bottom of Fig.5.1, the blue flame is quite uniform and extended over and just beyond the exposed surface (excess pyrolyzate effect) [81]. The inconsistent appearance of the sample surface is a lens distortion of ice water inside the shell.

During burning, the measured water-PMMA interface temperature remained at 20 ± 2^oC. The PMMA pyrolysis temperature is estimated to be 395 ± 15^oC. Assuming a linear solid temperature distribution (thin shells), the rate of heat losses can be determined (using solid heat conductivity 0.2 w/m-K).

Figure 5.3 shows an example of one test run for the 7 mm spherical shell with limited exposed surface area $39.53cm^2$ ignited at 23.1% oxygen by mass and allowed to reach steady state. The oxygen level is lowered every 30 seconds (shown in orange). The mass of the solid is measured during the test (shown in blue). The burning rate of the sample is calculated by calculating the slope after the flame reaches the quasi-steady state after each step down in oxygen. Since the temperature boundary conditions of the solid are fixed, the system responds very quickly to changes in gas conditions with just a delay from flow system residence time.

Figure 5.4 shows the measured local burning rate for different plate thicknesses (hence different heat loss to the solid interior) as a function of mass oxygen percentage. For 2.8 mm thick shell, the heat loss is too large, the flame could not self sustain without the additional energy from the igniter. For a given loss, lowering O_2% yields a

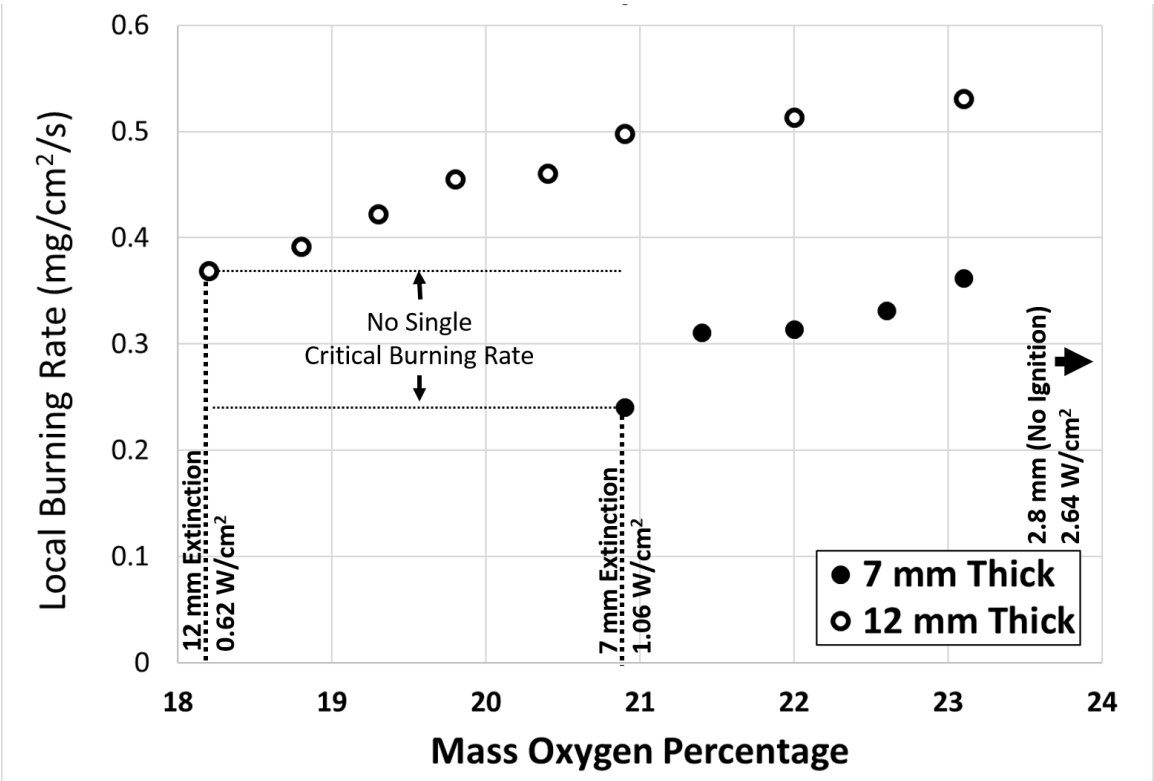

Figure 5.4. The local burning rate of two PMMA shells, 7 mm and 12 mm thick, as a function of oxygen concentration. There is significant difference between the oxygen limit and the critical burning rate. Stretch rate is 7.86 s^{-1}.

smaller burning rate as expected. Comparing the 7 mm and 12 mm shells, greater heat loss results in a smaller burning rate. The 7 mm shell has a heat loss of $1.06 W/cm^2$, the oxygen extinction limit is 20.8% by mass and the critical mass burning rate is $2.4x10^{-4} g/cm^2/s$. The 12 mm shell has a heat loss $0.62 w/cm^2$, the oxygen extinction limit is 18.2% by mass and the critical mass burning rate is $3.69x10^{-4} g/cm^2/s$. The two local mass burning rates at the different limits for the same material are not the same. The difference is more than 50%. The critical burning rate at the extinction limit is not a function of the material alone.

Figure 5.5 provides additional data on local burning rate in air at the stagnation region of PMMA extending to lower stretch rate from Olson [2]. The data for 7

mm and 12 mm shells are from the present work. All of the data were obtained in normal gravity. The data points at different stretch rates were obtained using shells of different radius of curvatures: 10.4 cm, 5 cm and 4 cm. Burning rate in [48] was estimated by visual regression over a long time period compared to overall mass loss during the entire test.

The local burning rates in these tests are direct instantaneous measurements made during steady state. Only the stretch rate 3 s^{-1} is near the extinction limit and the burning rate is $1.8x10^{-4}g/cm^2/s$. This is lower than those in Fig. 5.4. So in addition to heat loss, the critical burning rate is also a function of flow parameters (e.g. flow strain rate or flame stretch rate) and possibly others.

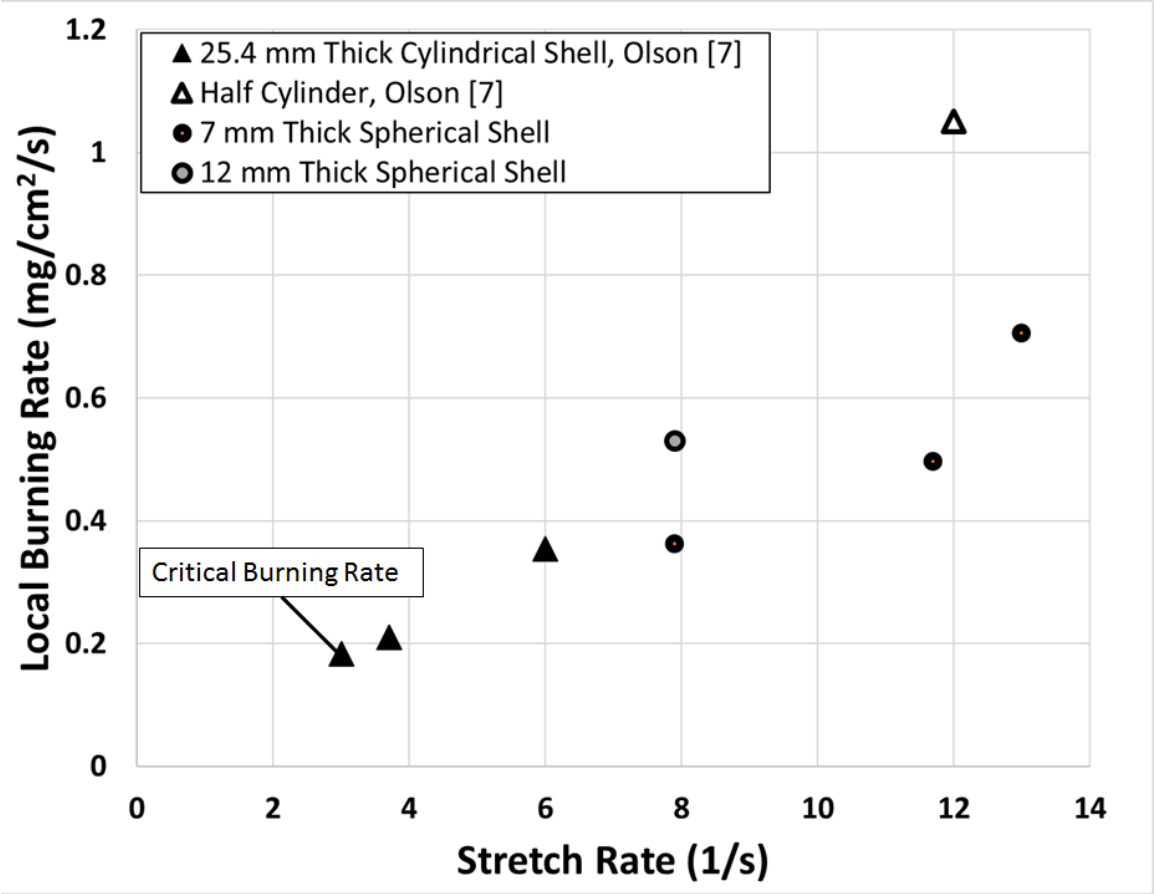

Figure 5.5. New data for PMMA spherical shells plotted with cylinders from Olson [2]. The burning rate decreases with decreasing stretch rate.

6 GEL Prototype Ground Testing in the NASA Zero Gravity Research Facility

6.1 Description of NASA Zero Gravity Research Facility and Combustion Tunnel

The NASA Zero Gravity Research Facility (ZGRF) is a 5.2 second drop tower at Glenn Research Center which was used to study the flame transition of a burning GEL sample in a step change from normal Earth gravity to microgravity. The sample is ignited in the forward stagnation region in a trickle flow of air (21% oxygen concentration by volume) and then changed to the desired test oxygen concentration and flow velocity after the flame is well established across the surface and the material is preheated to the desired level by the flame. The thermocouple embedded closest to the surface within the GEL sample is monitored in the control room in real time before the drop. At the moment the desired internal temperature is reached, the drop is triggered, causing the test apparatus to transition to microgravity.

The 5.2 seconds of microgravity are produced by dropping a torpedo shaped vehicle (Fig. 6.2) with a self contained wind tunnel about 430 feet through a vertical vacuum shaft, decelerated at the bottom in a bucket of polystyrene beads (Fig. 6.1. The internal configuration of the drop vehicle used, named the Combustion Tunnel is shown in Fig. 6.2 (CENTER, RIGHT). The Combustion Tunnel can provide two independently controlled gas mixtures and velocities, chamber pressure control, electronic power from batteries, two orthogonal view high resolution video cameras, and thermocouple data acquisition. The wind tunnel section is pressurized, typically to 1 atmosphere, and vents into the drop shaft vacuum. After deceleration, the tunnel section is vented to vacuum, ensuring flame extinguishment.

Ignition is with a 28 gauge Kanthal A-1 resistive hotwire shaped as a three turn coil powered with a constant current power supply set to 4.1 amps. The igniter is energized remotely from the control room and monitored on video stream. After ignition, the igniter wire is retracted by a rotating solenoid to move it out of the way of flame and gas flow. Igniter configuration is shown in Fig. 6.3.

Fig. 6.4 shows the overall configuration of the sample holder. The GEL sphere is cantilevered into the flow field from down stream by holding the sample support tube through which the thermocouple lead wires are routed. The igniter wire approaches the sample from the side to minimize flow disturbances.

Gas concentration is set by drawing from one of the two separate compressed gas cylinders onboard the drop vehicle. The cylinders can be filled independent gas blends. For the tests performed as part of this work, one gas cylinder is filled to 21% oxygen by volume to facilitate ignition in a reasonable amount of time with minimal regression of solid material, and the other is filled with the test blend of interest, 17%

by volume for all tests presented here. The gas is switched during deployment with solenoid valves. Flow velocity through the tunnel section is controlled by a critical flow orifice and upstream pressure regulator set prior to the experiment. Tunnel pressure is regulated with a downstream feedback controlled pressure regulator.

Because of the limited amount of microgravity time available in ground based test facilities (including NASA ZGRF), only the gas phase transition to microgravity can be studied. The solid material and internal temperature profile will not have time to respond in such a short amount of time. The temperature profile can therefore be set in 1 g by preheating the solid either by an external heat source or with the 1 g flame. The thermal profile at time zero will persist to good approximation through the entire drop. Because of this, the desired conditions and test matrix can be predicted and mapped for the long duration tests aboard ISS, but the ZGRF can not substitute for the space flight experiment. The main goal for this test campaign is to narrow down the initial test conditions to save sample mass and crew time in the flight experiment. The secondary goal is to begin to populate a flammability map of heat loss to the solid vs externally forced flow velocity (or stretch rate).

Figure 6.1. A Stock photograph of the NASA Zero Gravity Research Facility vacuum drop shaft. The decelerator is shown in red on the right. In the center a drop vehicle is being recovered with a crane from above. [NASA Stock Photo GPN-2000-001454, 1966]

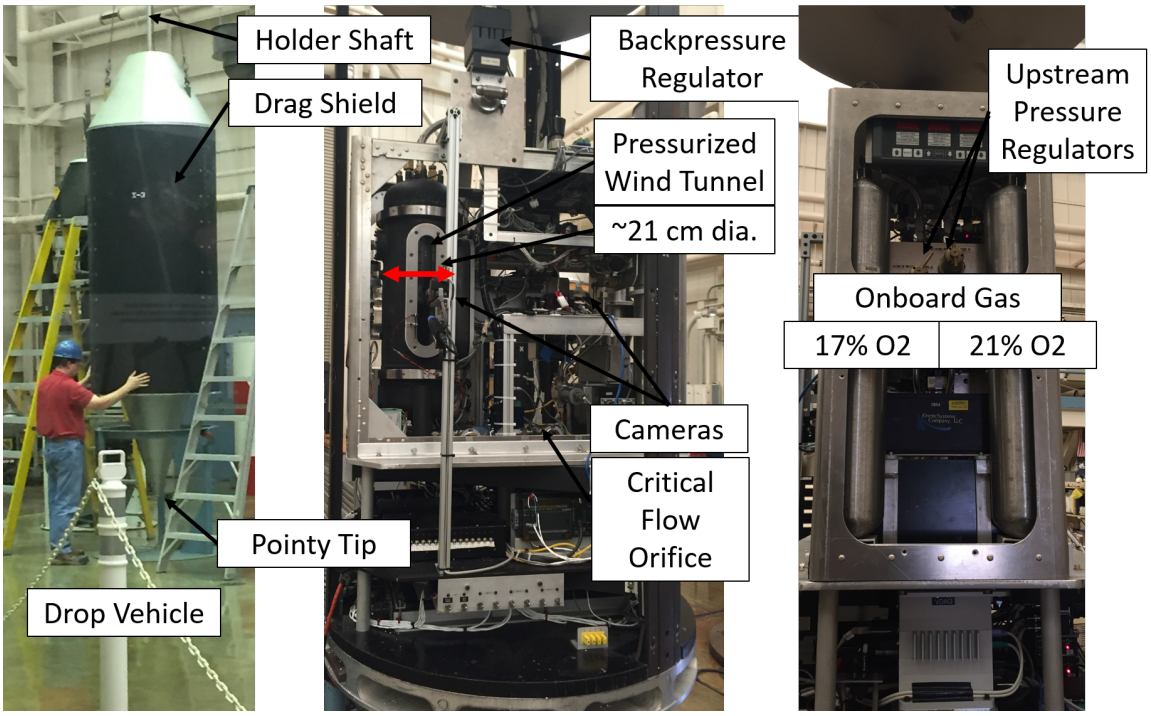

Figure 6.2. Left: The X-model ZGRF drop vehicle containing the Combustion Tunnel with outer drag shield installed. A crane is reinstalling the vehicle onto a holder to be reset for the next test. Center: The Combustion Tunnel with the drag shield removed. The 21 cm diameter combustion tunnel is installed left of the centerline. High resolution cameras image from orthogonal views. Tunnel pressure is controlled at the exhaust by a back pressure regulator valve, and gas is fed into the tunnel at the bottom through with flow rate controlled by a critical flow orifice. Right: Gas is provided by two independently controlled onboard gas cylinders filled to the desired oxygen concentrations. Pressure to the flow system is set by pressure regulators for each cylinder.

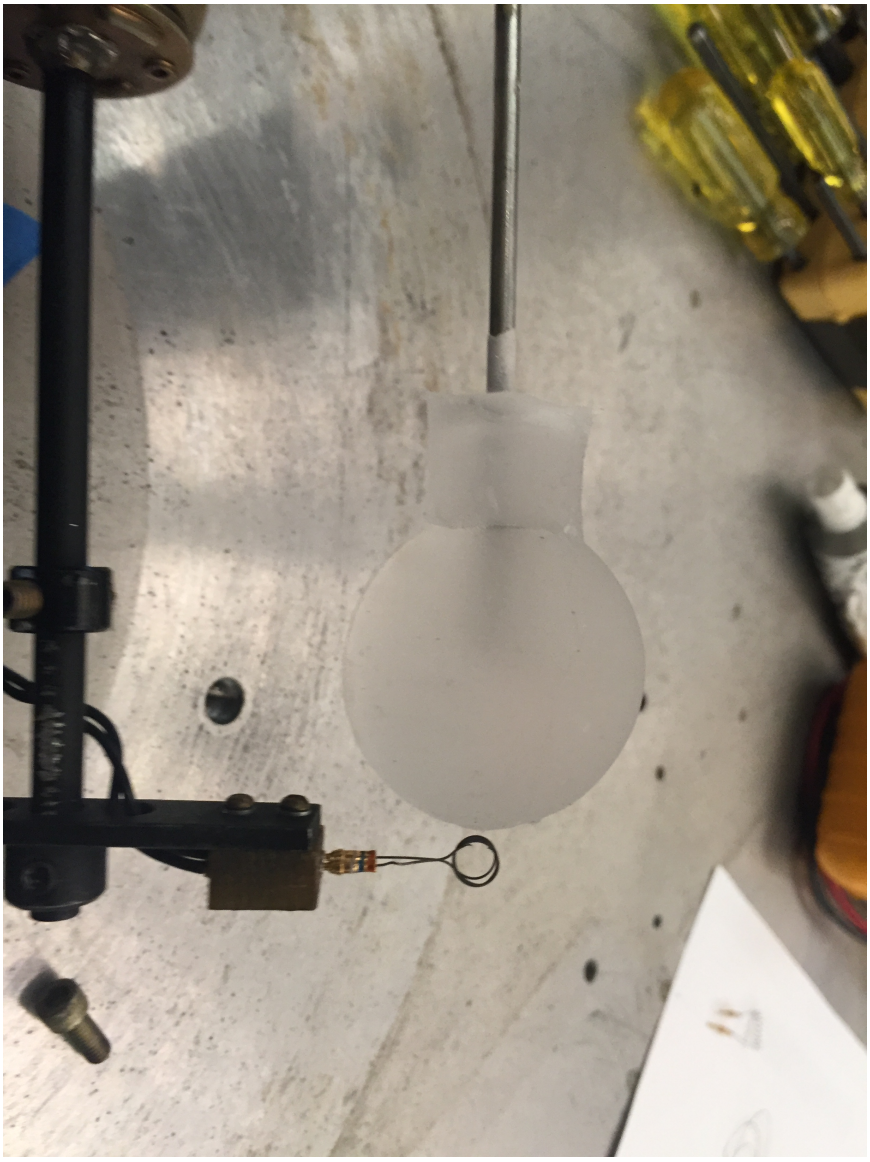

Figure 6.3. Igniter configuration for GEL testing in the ZGRF

Figure 6.4. Combustion Tunnel sample holder modified for use with the GEL sphere samples

6.2 Methods

The methods used in data analysis of the experiments in the NASA ZGRF are described here. This includes curve fitting the measured temperature profiles and estimating heat transfer to the solid fuel interior along with a description of the measurement of flame stand off distance, which is defined as the distance between the flame sheet and solid surface.

6.2.1 Temperature Profile Fit and Heat Transfer Estimates

The heat loss to the solid fuel interior is a primary measurement and experimental parameter of this study. An accurate and repeatable estimate is vital to the success of the experimental campaign. In depth temperature curves are fit from point measurements using a least squares fit of equation 6.1 where d is the depth into the solid in mm and γ is the fit parameter calculated by a least squares fit. This equation perfectly fits a one dimensional semi infinite solid with a constant surface temperature, and will remain a valid approximation for a sphere if the in depth bulk temperature does not increase appreciably. Specifically, the deep interior remains at 22 degrees Celsius, which is the starting temperature of the solid, unless otherwise noted. If the interior solid temperature rises, then a transient fit based on spherical harmonics would become necessary.

The fit curves are plotted with the measured data at the time of drop for each test case in the results section below. The heat flux into the solid is estimated by calculating the first spacial derivative of the fit curve with respect to depth, evaluated at the solid surface at the time of the drop trigger, multiplied by the estimated solid heat transfer coefficient k. This heat flux value is expected to remain relatively

constant throughout the drop since the solid response time is slow compared to the gas phase response time and the drop duration of 5.18 seconds. The heat flux at the surface, the first spacial derivative of the fit curve times the thermal conductivity of the material is shown in equation 6.2.

$$T(d) = (T_{Pyrolysis} - T_{bulk})e^{-\gamma d} + T_{bulk} \tag{6.1}$$

$$q(0) = -k\frac{dT}{dx}|_{x=0} = k(T_{Pyrolysis} - T_{bulk})\gamma \tag{6.2}$$

The heat transfer coefficient is estimated in this work to be a constant value k=0.20 W/m*K. Although this value may change based on temperature, exact chemical composition, polymer chain length, thermal history, and bubble formation, it is commonly estimated as a constant value in literature due to lack of better information. In the future, this value should be investigated in detail at the wide array of conditions expected during flight tests especially considering the changing bubble layers at the solid surface.

A temperature profile fit based on Peclet number as the fitting parameter from Olson [2, 42] is also included and shown in equation 6.3. This arrangement gives theoretical insight into the pyrolysis process at the expense of slightly increased equation complexity. The Peclet number is defined as the ratio of the heat in the solid convecting towards the surface due to surface regression vs the solid conduction away from the solid surface into the solid interior. Here, Peclet number is related to surface regression as in equation 6.4.

$$T(d) = (T_{Pyrolysis} - T_{Bulk})\frac{e^{\frac{-Pe*d}{k}} - e^{-Pe}}{1 - e^{-Pe}} + T_{Bulk}; \tag{6.3}$$

$$Pe = \frac{V_{regression}R}{\alpha_s} \tag{6.4}$$

This expression relating Peclet number to regression rate, also mentioned in [42] is extremely simple. It can be validated by solving for $V_{regression}$ and integrating over burn time as in Eq. 6.5. This can then be compared to the CT scans of the sphere which measure surface position before and after each test. If accurate, this means the burning rate can be deduced in real time by in depth thermocouple measurements.

$$\Delta x = \int_{t_1}^{t_2} \frac{\alpha_s Pe}{R} dt \tag{6.5}$$

Here, Δx is the amount of surface regression, proportional to solid fuel burning rate.

6.2.2 Standoff distance measurements

The flame standoff distance is a primary controlling factor of the convective and conductive heat transfer from the gas phase flame to the solid surface. In the stagnation region, it is a result of the incoming oxidizer impinging towards the solid surface vs. the vaporizing fuel mass flux from the surface pyrolysis. A stronger external flow pushes the flame closer to the surface. Higher vaporization rate (hotter surface) pushes the flame away from the surface.

For the predominantly blue flames expected during the GEL experiments, the flame sheet standoff distance is tracked by measuring the number of pixels along the

stagnation streamline from the solid surface to the point of furthest blue which is twice the intensity of the sensor noise floor. This point of furthest blue is a repeatable representation of the flame sheet. Other representations can be taken, such as the point of brightest blue. Fig. 6.5 shows the intensity of each pixel in the separate red, green, and blue color channels along the stagnation streamline, starting from the solid surface (corresponding to 0 on the abscissa) and pointing in the upstream direction. The solid surface would correspond to the point marked in 6.5 (Left). In Fig. 6.5 (Right), starting at the solid surface, the intensity of the blue is predominant, as expected by looking at the blue appearance of the flame, red and green are also prevalent, likely due to cross sensitivity of the camera's consumer grade sensor. From the solid surface, the colors increase in intensity peaking around 30 pixels, the intensity values drop off steeply and reach the electrical noise floor of the camera sensor at around 45 pixels. The pixel measurements can be converted to metric units by using a scale factor ratio of pixels to mm, measured from a photograph of a ruler in the same field of view at the point of focus.

Although the point of brightest blue intensity may better represent the location for the flame sheet, it is easily fooled when soot is present. Soot is typically recorded on the sensor as white light, which contains a large amount of blue. At the expense of the x-axis distance measurement bias between the *outer blue* and *peak blue* points shown in 6.5, tracking the outer blue is more robust when unexpected soot and vapor jetting are present.

It should be noted that the intensity value is only of interest when compared relatively to other measurements in the same image frame. Due to the limited dynamic range of the imaging sensor, the intensity value compared in time is meaningless since

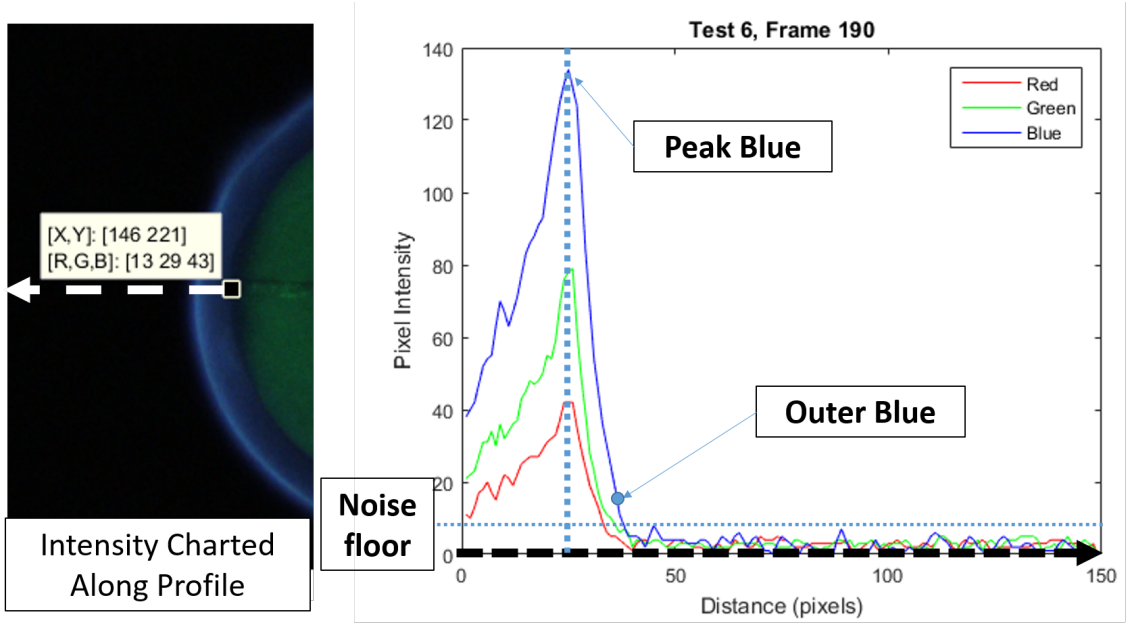

Figure 6.5. Left: The location of the solid surface along the stagnation streamline. Right: Pixel Intensity of the separate red, green, and blue channels measured from the solid surface to the upstream along the stagnation streamline and centerline axis of symmetry

the camera gain and shutter speed vary to keep the sensor from saturating. Specifically, to gain any insight from flame intensity, a radiometer or specialized calibrated camera should be used.

6.3 Results

This section shows the results of each GEL experiment conducted in the NASA ZGRF. The conditions and major results of each test are described. Plots are presented for temperature measurement, chamber pressure and tunnel operation, thermocouple locations before and after each test, flame standoff distance at the stagnation point, a time sequence of video frames of interest, and the temperature curve fit at the time of the drop.

Pre Drop Test #1 thermocouple locations	
TC1	0 mm on axis
TC2	2 mm on axis (monitored)
TC3	4 mm on axis

Table 6.1. Thermocouple locations for Drop Test #0.

The experiments spanned a variety of flow velocities from 2-25 cm/s. An initial attempt was made to constrain the test series to two preheat levels which were often referred to as 'low preheat' and 'high preheat'. After analysis of post drop thermocouple locations and using the heat flux estimates from Eq. 6.2, this was not achieved in practice. Towards the end of testing, this strategy was abandoned as flammability boundaries of heat flux vs flow velocity developed. The flammability boundaries will be presented in the discussion section.

Drop Test 0

A preliminary practice test was performed in 1 G only within the Combustion Tunnel hardware to work out the test procedures because of the expense of operating the ZGRF. A significantly depleted instrumented GEL sphere was used which had been previously burned with a large amount of surface regression and shape change in the laboratory's variable oxygen tunnel. The sample was lopsided and no longer spherical, the thermocouple closest to the stagnation zone was exposed due to material regression. The surface was charred and pocked with bubbles.

The sample was analyzed with computed tomography before testing to measure the thermocouple locations. This was not necessary for this sample since TC1 was just barely exposed at zero depth, the relative positions should therefore be known.

Test Conditions.

- 2 cm/s forced flow, $a_b \approx 19s^{-1}$
- Ignition in 21% oxygen by volume for 20 seconds at t=-57.7 s
- Switched to 17% oxygen by volume after t=-14.2 s
- 17% Oxygen reaches sample around $t \approx 5s$
- Tunnel vented shortly after impact

Results. A flow rate of 2 cm/s was used with ignition at 21% oxygen by volume. The goal was to change to 17% oxygen by volume when thermocouple TC2 reached 80^oC. Due to dead pixels on the touchscreen interface, the gas was not switched in time. Combined with the tunnel residence time delay of nearly 20 seconds for 2 cm/s flow, the 17% oxygen gas reached the sample late when TC2 reached 170^oC. The flame was exposed to 17% oxygen for very little time before the chamber was vented to vacuum.

The temperature measurements are shown in Fig. 6.6. The igniter ON time is represented as a square wave shown in light blue. Because thermocouple TC1 (shown in dark blue) is at the surface of the solid, it heats up very quickly when exposed to the energized igniter. As the igniter turns off, the temperature of TC1 drops quickly due to surface radiation and conduction to the solid interior and then begins heating up again as the flame continues to add heat energy the surface. Thermocouples TC2 at 2 mm depth (shown in red) and TC3 at 4 mm depth (shown in green) take longer to respond to the flame since they are located deeper within the solid. At 5.18 seconds after what would be the drop trigger in an actual test, at the 0s mark, the chamber vents to vacuum. The in depth thermocouples continue heating up slightly as the temperature heat wave is still propagating in depth. After some delay, the temperatures begin to fall.

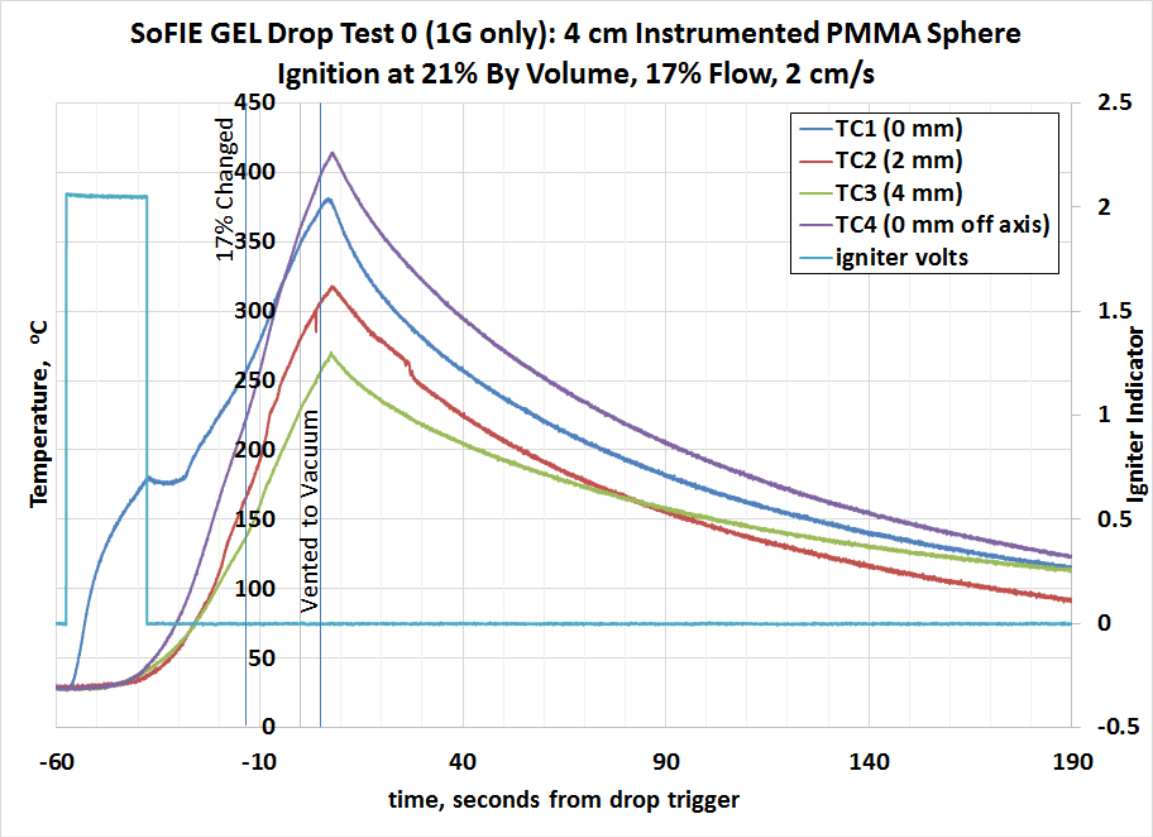

Figure 6.6. Drop Test 0 thermocouple temperature measurements

Drop Test 1, X-16-128

This was the first drop test and used a newly cast unburned instrumented sphere. The sphere was analyzed with computed tomography before the test to measure the original thermocouple locations which are shown in Table 6.2. The test was ignited for 20 seconds in 21% oxygen flowing at 2 cm/s. The gas was switched to 17% oxygen by volume before the drop. The drop was triggered when the 3 mm thermocouple indicated 100^oC. The sphere extinguished 4.236 seconds after the transition to zero gravity at a purely forced flow stretch rate of $a_f \approx 1.46s^{-1}$.

Pre Drop Test #1 thermocouple locations	
TC1	3.07 mm on axis
TC2	5.07 mm on axis
TC3	7.07 mm on axis
Post Drop Test #1 thermocouple locations	
TC1	3.07 mm on axis
TC2	5.07 mm on axis
TC3	7.07 mm on axis

Table 6.2. Thermocouple locations for Drop Test #1.

Test Conditions.

- 1.95 cm/s forced flow, $a_b \approx 19s^{-1}$, $a_f \approx 1.46s^{-1}$
- Ignition at 21% oxygen by volume for 20 seconds starting at t=-39.553s
- Switched to 17% oxygen by volume 13.7 seconds after the start of ignition at t=-25.853 s
- dropped when TC1 read 105^oC (with the target drop at 100^oC).
- The sphere extinguished at t=4.236 s after the drop
- Heat loss to the solid at the time of drop is estimated to be $3.78W/cm^2$

Results. After the switch to 17% oxygen, the flame shrunk slightly with the flame tips retreating upstream in response to the gas change, then continued to grow towards an envelope flame in 1G. The flame was slightly lopsided with one flame tip extending just past the sample's equator, and the opposite side extending to the downstream edge of the sphere at the time of the drop. Some vapor jetting was visible at the stagnation zone but the flame remained predominantly blue in color except in the downstream region and in the intermittent jets which emanate from the surface.

The transition to microgravity caused a significant increase in standoff distance from 1.30 mm to a maximum of 3.16 mm as the incoming flow changes from a stretch rate of $a_b \approx 19s^{-1}$ in 1G to $a_b \approx 1.46s^{-1}$ in 0 g. The transition was somewhat

turbulent with pockets of bright orange swirls throughout the stagnation region. The flame tips open up and retreat significantly in the first few milliseconds and the stagnation region standoff distance relaxes back towards the solid as heat feedback to the material surface decreases. The standoff distance is shown in the Fig. 6.8. Pockets of holes and flame flickering towards the stagnation region occurs near extinction with pulsing rate starting around 4 Hz and slowing down in time to about 2 hz while increasing in oscillation magnitude before the eventual quenching extinction. Extinction is 4.234s after the drop.

Fig. 6.7 shows the temperature measurements and Combustion Tunnel flow parameters throughout the test. Ignition begins at the left edge of the graph, and the temperature recorded by thermocouple TC1 located 2.77 mm below the surface shows a delay of about 5 seconds before the temperature begins increasing at that depth. Thermocouples TC2 at 4.77 mm and TC3 at 6.77 mm show increasingly longer delays before the temperature begins to rise even deeper in the solid. The peak temperature experienced by all of the thermocouples this far in depth does not occur until after the flame has been extinguished.

Fig. 6.9 shows image frames throughout the test, gas flow is from bottom to top. Frame 1 in the upper left starts just before the drop at t=-0.0333 s. The flame starting condition at the start of the drop is lopsided. It is unknown if this is caused by an unsymmetric ignition or an unsymmetric flow condition within the Combustion Tunnel. Frame 2 at t=0.0333 seconds after the drop shows the flame standoff distance increasing and the flame tip on the right hand side retreating back upstream. Ripples can be seen in the flame sheet caused by vapor jetting from the material surface. Frame 3 at t=0.2 s shows increased sooting and the flame tips begin to open up due

to the lack of buoyant upward acceleration and lack of buoyancy induced entrainment from the sides. Frames 4 and 5 show a continuation of the increased sooting and flame tip response up until about t=0.7 s. Between this point and frame 7 at t=3.97 s, the flame tips shrink towards the stagnation zone. Although the gas mixture can not support combustion away from the stagnation region, some pyrolysis continues and fuel mixes with the incoming oxidizer to form a flammable mixture. Flashing begins to occur at t=4.033 seconds until the last frame, when the the flame extinguishes.

Figure 6.10 shows the in depth temperature measurements for the thermocouples TC1, TC2, and TC3 at the time of the drop. The exponential curve fits used to calculate the heat loss to the solid interior are shown.

Surface regression was minimal with very little charring of the material surface. The originally frosted surface was somewhat flame polished after the test.

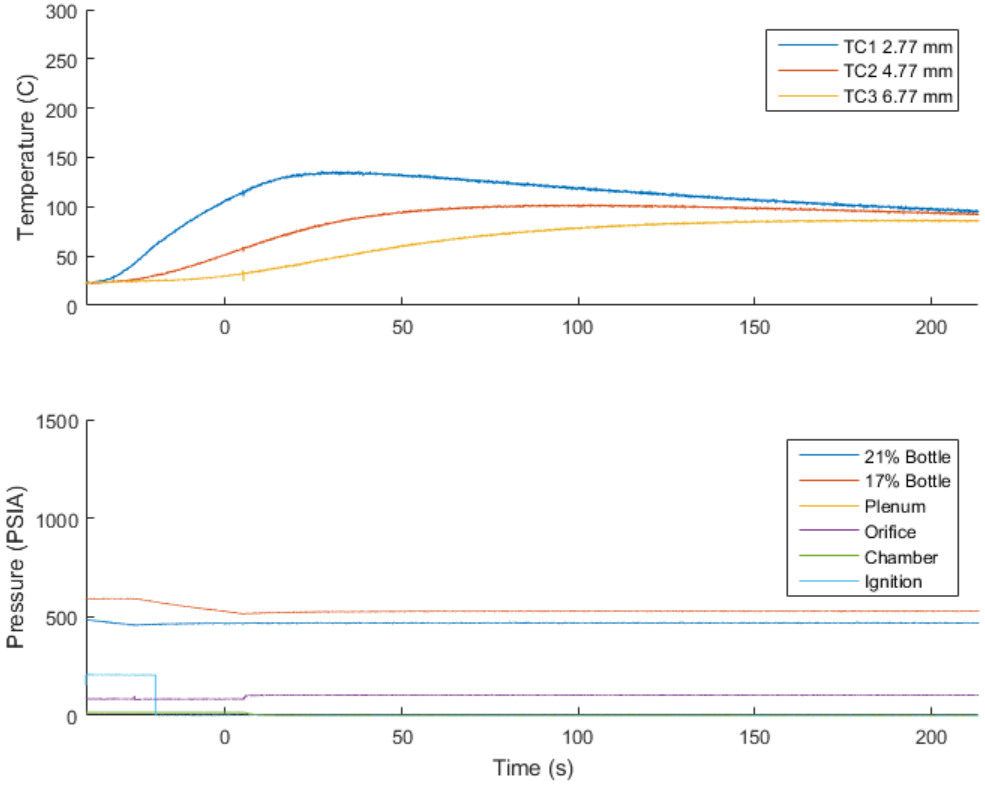

Figure 6.7. Drop Test 1 thermocouple temperature measurements and Combustion Tunnel control parameters.

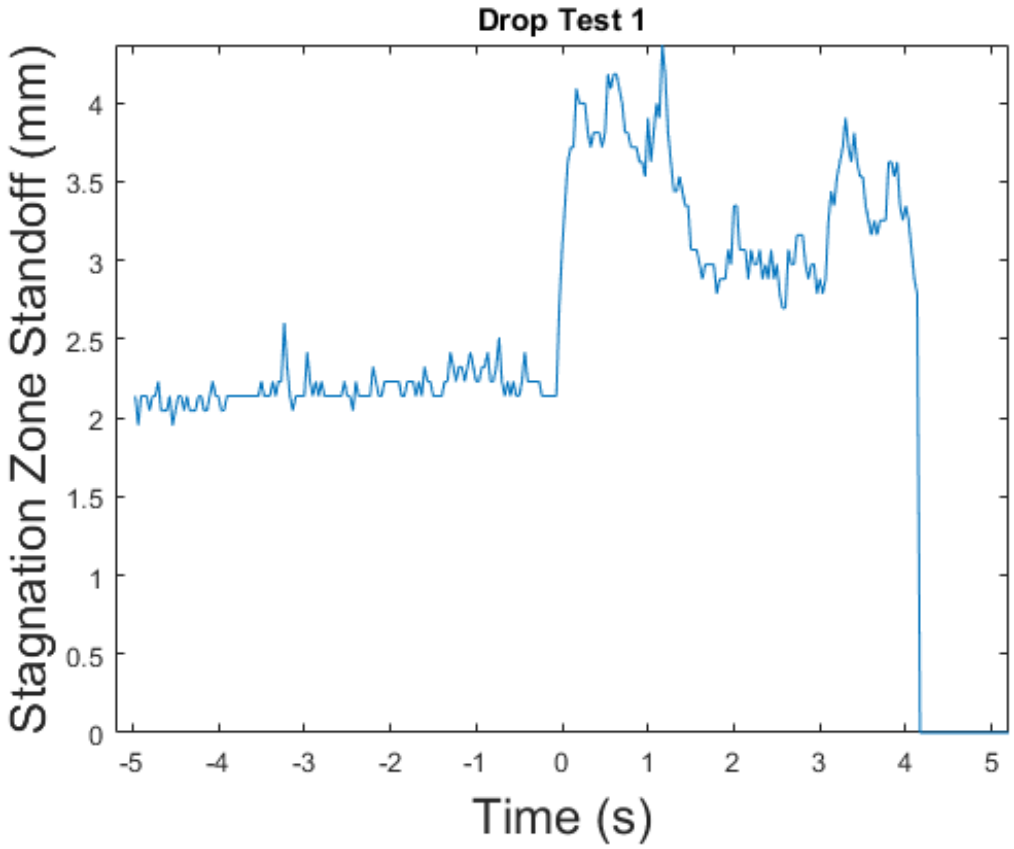

Figure 6.8. Drop Test 1 flame standoff distance and flame sheet thickness.

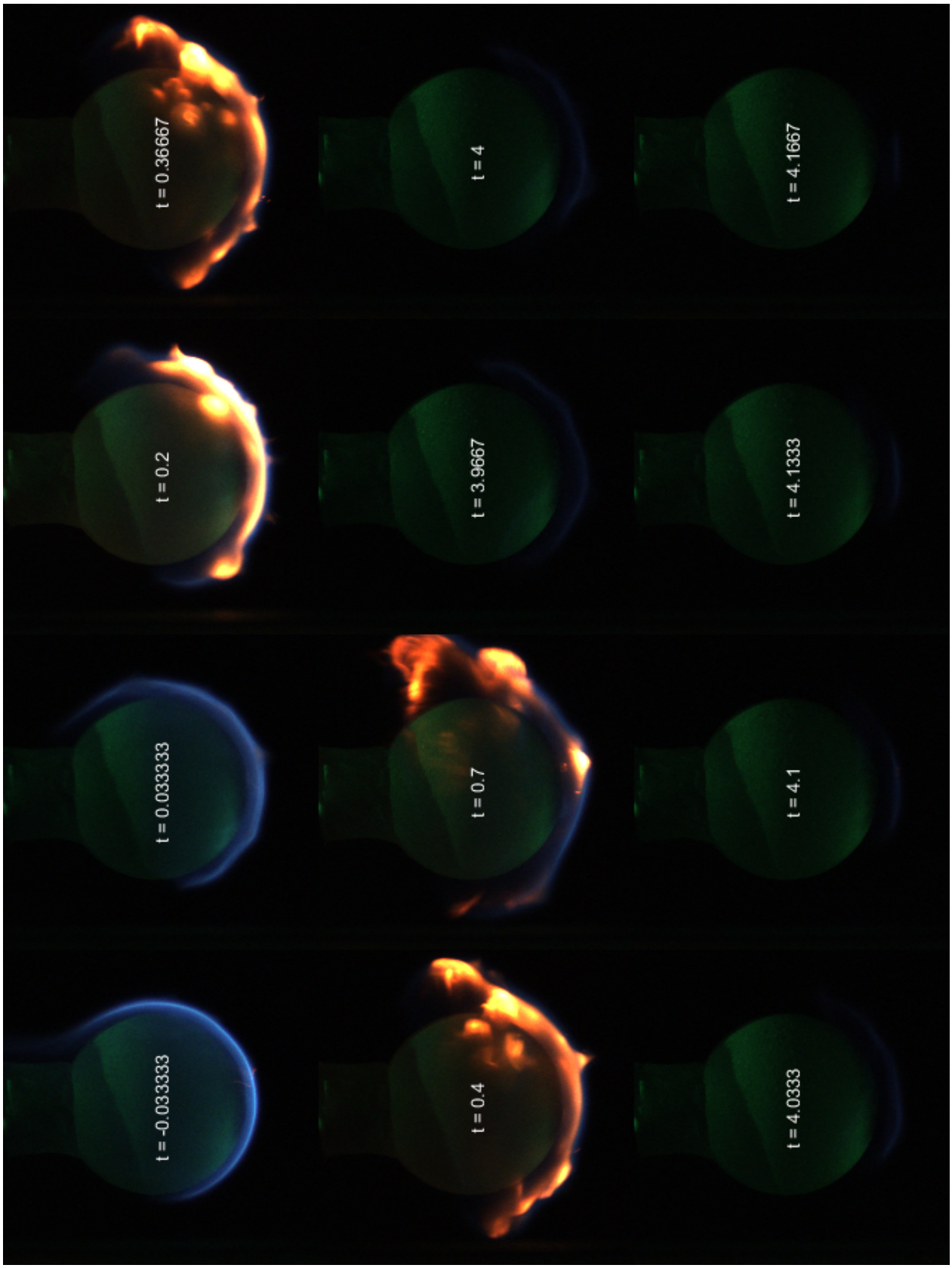

Figure 6.9. Drop Test 1 significant image frames

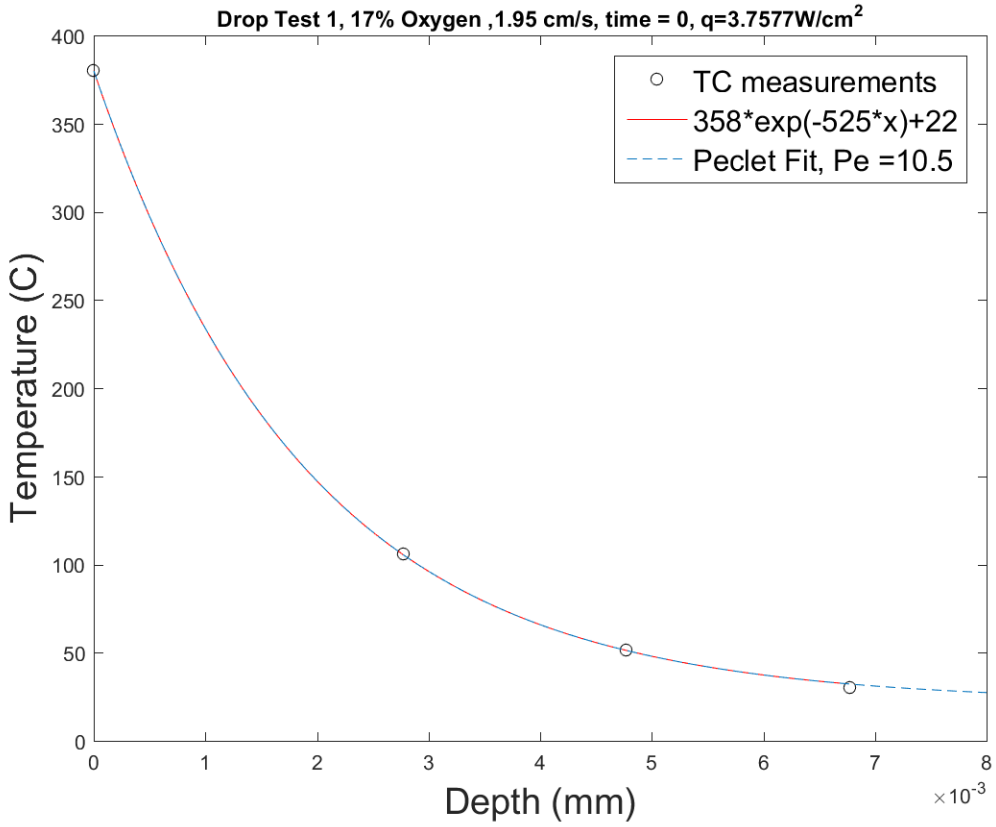

Figure 6.10. Fit of temperature profile at the time of the drop.

Drop Test 2, X-16-129

This was the second drop test, intended to be run at the same conditions as Drop Test 1 with a higher level of preheating. It was originally hoped that this test would survive the drop with less heat loss to the solid interior. Computed tomography was unavailable between tests 1 and 2. The thermocouples were estimated to be in the same locations since sphere regression was so minimal during test 1. In hindsight this was a mistake since it would have been beneficial to have a record of the bubble layer penetration depth. The test was ignited for 20 seconds in 21% oxygen by volume.

Pre Drop Test #2 thermocouple locations	
TC1	3.07 mm on axis
TC2	5.07 mm on axis
TC3	7.07 mm on axis
Post Drop Test #2 thermocouple locations	
TC1	2.1 mm on axis
TC2	4.1 mm on axis
TC3	6.1 mm on axis

Table 6.3. Thermocouple locations for Drop Test #2.

The gas was switched to 17% oxygen and flame allowed to stabilize before the drop. The drop occurred when thermocouple TC1 read 200^oC. The flame extinguished in microgravity 4.476 s after the drop.

Test Conditions.

- 1.95 cm/s forced flow, $a_b \approx 19s^{-1}$, $a_f \approx 1.46s^{-1}$
- Ignition at 21% oxygen by volume for 20 seconds starting at t=-120.73s
- Switched to 17% oxygen by volume 17.3s after ignition starts at t=-103.57s
- 17% oxygen reaches sample about 10 seconds after the end of ignition
- dropped when TC1 read 200^oC
- Sphere extinguished at t=4.476 s after drop.
- Heat loss to the solid at the drop time is estimated at $2.19W/cm^2$

Results. This test was preheated too long and some of the thermocouples were damaged by the intense heat generated and stopped functioning correctly in future tests. The flame color remained very blue during 1 g burning except at the tips of the full envelope flame, despite the intense heat. Vapor jetting in the stagnation zone was minimal. The transition from 1 g to 0 g was exceptionally smooth with an orange glowing soot layer forming between the flame sheet and material surface as the stagnation distance increased from 1.39 mm in 1 g to a maximum overshoot of 5.20

mm in zero g before the soot dissipated and the flame standoff relaxed back towards the material surface as heat feedback to the surface decreased. Stretch rate in 1 g is estimated at $a_b \approx 19s^{-1}$ and stretch rate in 0 g is estimated at $a_b \approx 1.46s^{-1}$. The flame tips retreat smoothly towards the stagnation region with some ripples caused by surface jetting. The flame extinguished at the stagnation region in microgravity 4.476 seconds after the drop.

The temperature measurements and flow parameters are shown in Fig. 6.11. Thermocouple TC1 located at 2.15 mm shows an increase in temperature after a short delay after ignition, the temperature increase slows down after the igniter turns off and again after the gas is switched to 17% oxygen at -103.6 seconds. Spikes in the temperature curves start occurring first for TC3 (shown in yellow) before the drop, then TC1 (shown in blue) after the test is over. The insulation around each wire within the sample support tube has melted off due to high temperature and the wires begin shorting to the rod and to each other. This becomes a recurring problem in the high preheat drop tests.

Figure 6.12 shows the stagnation zone flame standoff distance measurements for 5 seconds before and after the test. In 1-g, the stand off distance is very constant at about 1.5 mm. After the drop, the standoff increases for about 0.7 seconds and then begins to relax back towards the surface until extinction at 4.476 s.

Figure 6.13 shows the significant image frames throughout the test. In Frame 1 at t=-0.033 seconds, a full envelope flame is already established. The flame is predominantly blue in the 17% oxygen flow with slightly orange soot visible in the wake region. The flame has barely responded to the change in gravity level by t = 0.033 seconds in Frame 2. In frame 3, the tips have opened up, the stand off

distance has increased, and orange sooting between the flame sheet and solid surface has increased significantly. Frame 4 shows further increase in the soot brightness. In Frame 5 at t=0.7 s, the flame sheet has reached maximum standoff distance and the sooting begins to dim. The flame standoff then relaxes back towards the surface and the tips retreat towards the stagnation region. Frames 6-12 show a continuation of the flame retreating process until the off axis extinction at 4.476 s.

Fig. 6.14 shows the exponential temperature curve fit plotted against the in depth temperature measurements.

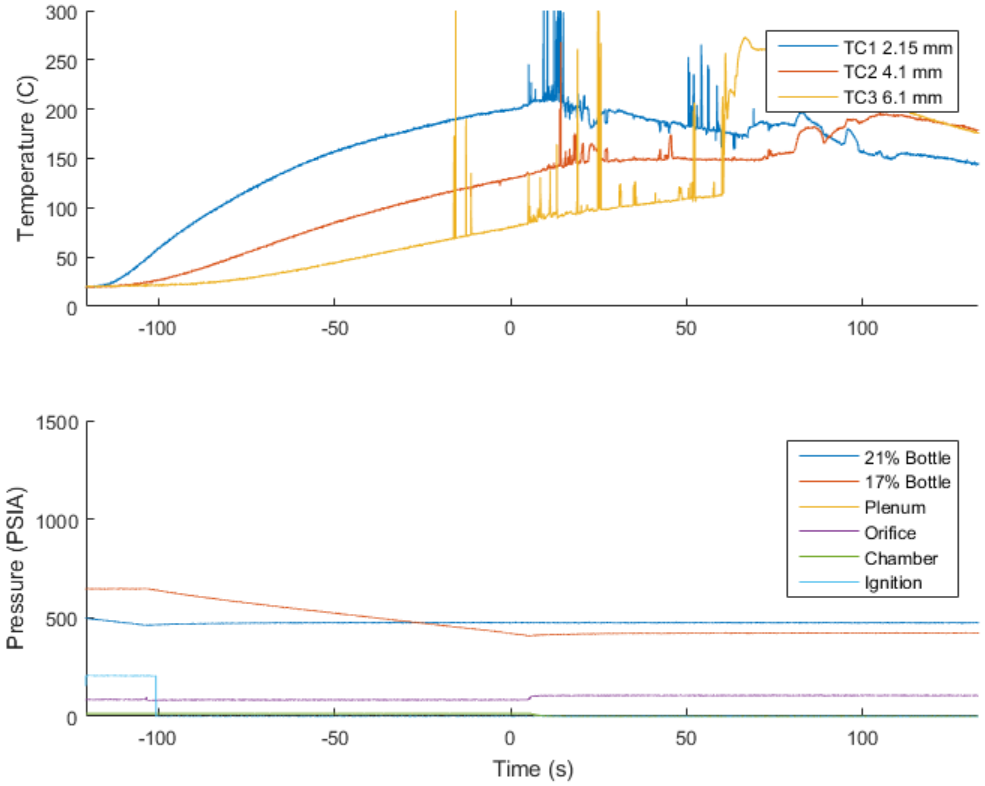

Figure 6.11. Drop Test 2 thermocouple temperature measurements and Combustion Tunnel control parameters.

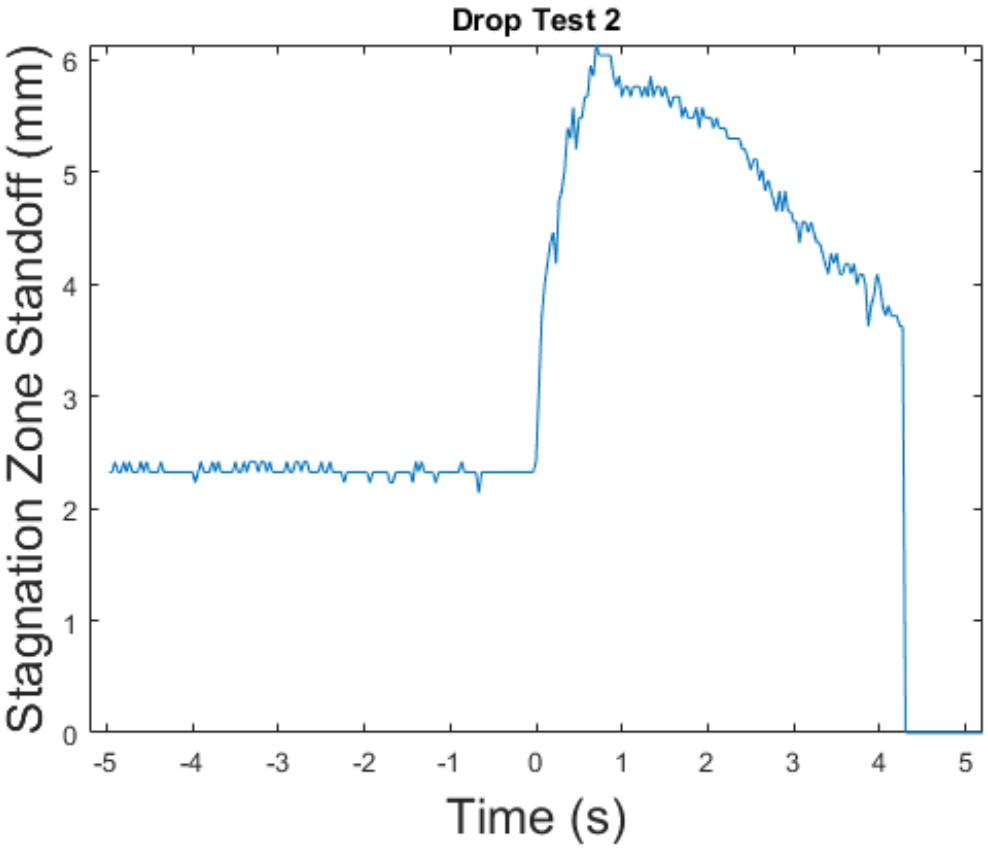

Figure 6.12. Drop Test 2 flame standoff distance.

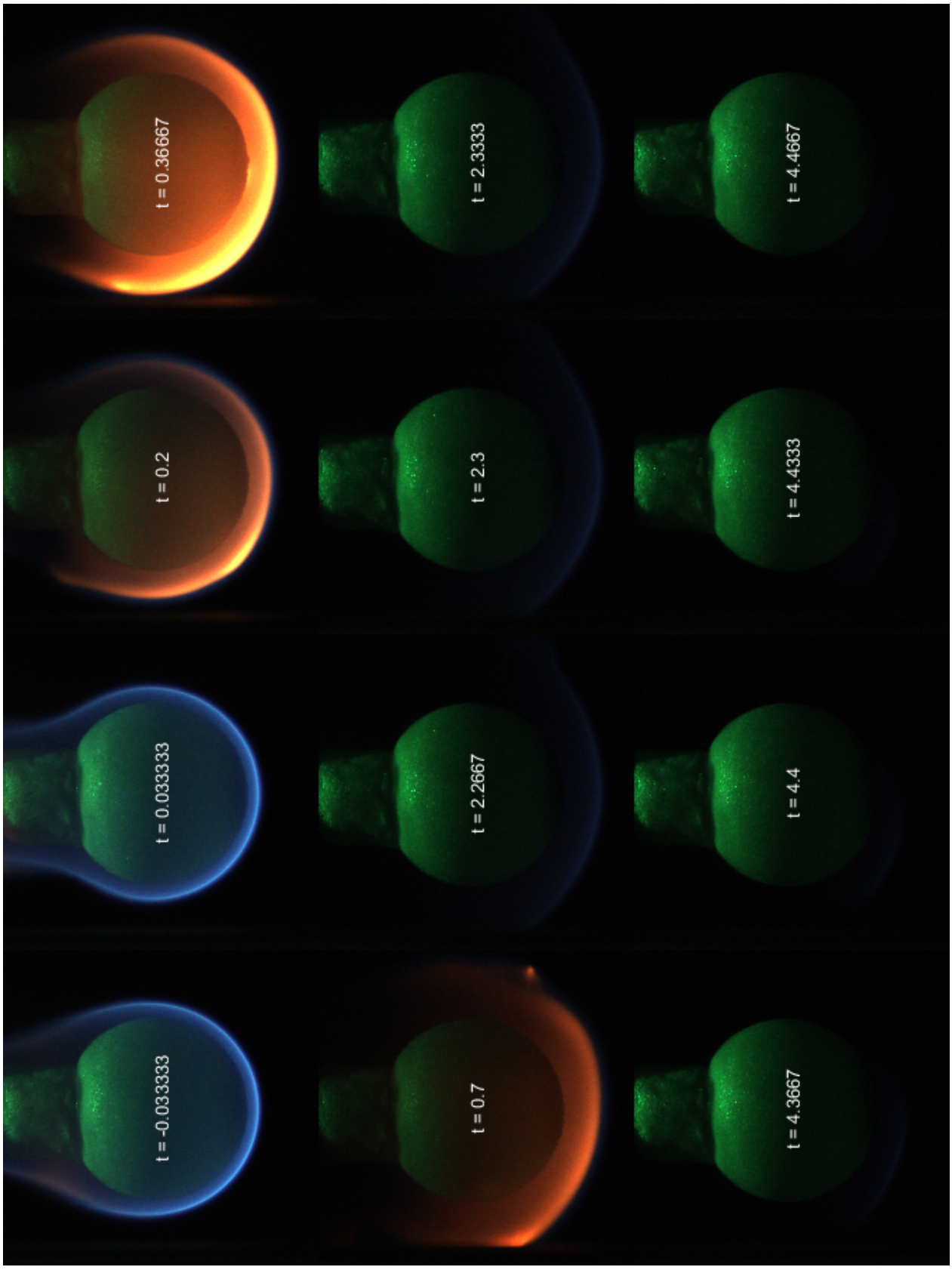

Figure 6.13. Drop Test 2 significant image frames

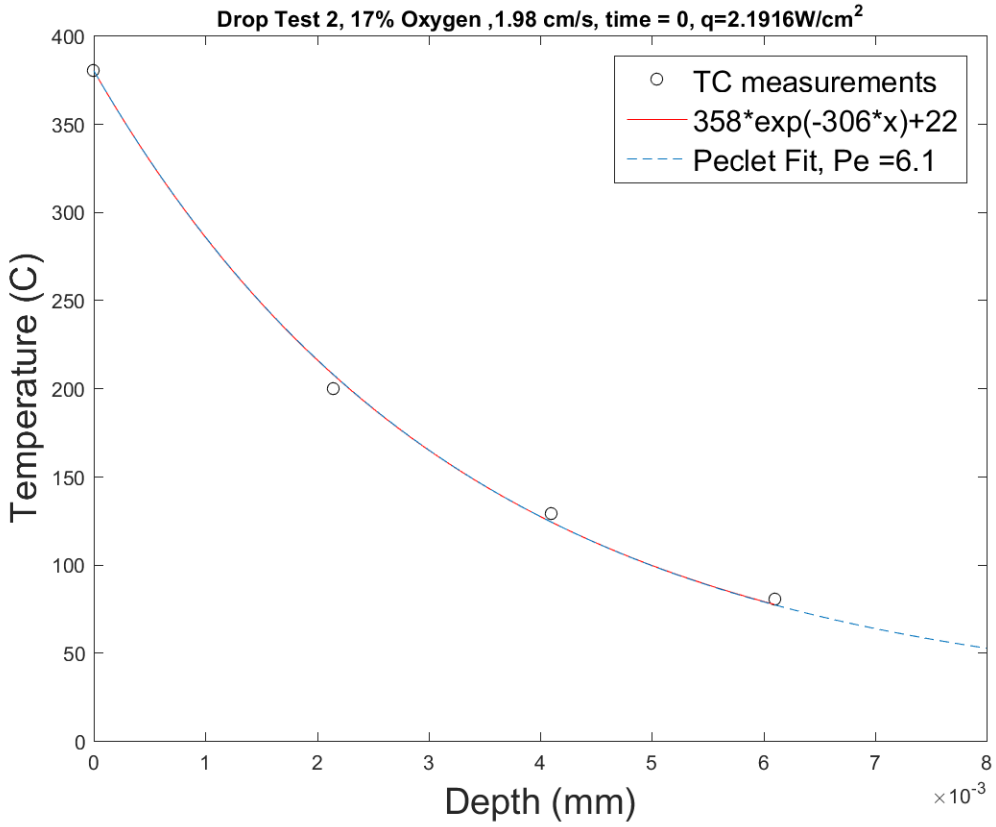

Figure 6.14. Fit of temperature profile at the time of the drop.

Drop Test 3, X-16-131

This test was intended to be run at the same conditions as Drop Test 1 with a faster freestream velocity. The flame extinguished unexpectedly after the switch to 17% oxygen in 1 g and was reignited a second time. The sphere was CT scanned before the test and thermocouple locations are shown in Table 6.4. Thermocouple TC3 broke during Drop Test 2 and the data was discarded in the temperature curve fit and heat loss estimate in Figure 6.18.

Test Conditions.

Pre Drop Test #3 thermocouple locations	
TC1	2.1 mm on axis
TC2	4.1 mm on axis
TC3	6.1 mm on axis
Post Drop Test #3 thermocouple locations	
TC1	1.339 mm on axis
TC2	3.146 mm on axis
TC3	5.759 mm on axis

Table 6.4. Thermocouple locations for Drop Test #3.

- 3.8 cm/s flow, $a_b \approx 19s^{-1}$, $a_f \approx 2.85s^{-1}$
- Ignition at 21% oxygen by volume for 20 seconds at t=-54.96 s
- Switched to 17% oxygen by volume 17.7s after ignition starts at t=-37.32 s
- 17% oxygen reaches the sample about 7 seconds after the end of the ignition
- The flame extinguished in 1g unexpectedly
- Re-ignition in 17% oxygen for 20s longer starting at t=-24.99s
- Dropped when TC1 read 187^oC
- Extinction at t=2.428 seconds after the drop.
- Heat loss to the solid at the drop time is estimated at $3.72W/cm^2$

Results. After the 20 second ignition in 21% oxygen by volume, the flame retreated back towards the stagnation point and extinguished after igniter retraction and had to be reignited. This appeared to be a typical thermal flame quenching case. It is not clear why extinction occurred, but was probably due to poor igniter placement. This is a critical factor as an igniter too close to the solid surface will cause unwanted material erosion, and an igniter too far from the surface will need much higher ignition energy from either increased power or longer ignition duration. After moving the igniter back into position and reigniting, the sample was able to support a growing

flame after the additional 20 seconds. The energy from the double ignition eroded a lot of the forward stagnation region of the sphere, flattening the shape .

Figure 6.17 shows the significant image frames. At t=-0.033 s before the drop, displayed in Frame 1, the flame tip reaches the sphere equator on one side and has extended past the sphere's downstream edge on the opposite side. The flame was still growing in 1 g. After the drop, Frames 2, 3, and 4 show a smooth transition with increase in standoff distance and sooting in the stagnation zone. The flame tips open up and start to retreat towards the stagnation region after Frame 5 at t=0.7 s, as the flame standoff distance relaxed back towards the surface. The flame quenched at the surface slightly off center towards the side of the sphere where the flame was stronger. Extinction was 2.529 seconds after the drop.

Figure 6.15 shows the temperature measurements and flow conditions. Thermocouple TC1 (blue) shows increasing temperature shortly after the start of ignition. The rate of temperature increase slows down after the flame unexpectedly extinguishes. The rate increases again during re-ignition. Thermocouple TC3 (shown in yellow) is seen to follow TC2 (red) closely, it has has short circuited and the data is discarded.

Figure 6.16 shows the flame standoff distance in the stagnation zone. Before the drop, the flame stand off is very steady, with spikes in the graph displaying some pixel noise. After the drop, the standoff distance spikes to about 3.25 mm, then relaxes back to about 2.25 mm before extinguishing.

The exponential temperature profile curve fit is shown Fig. 6.18. The temperature measurement from TC3 located at 5.759 mm is discarded when fitting the curve.

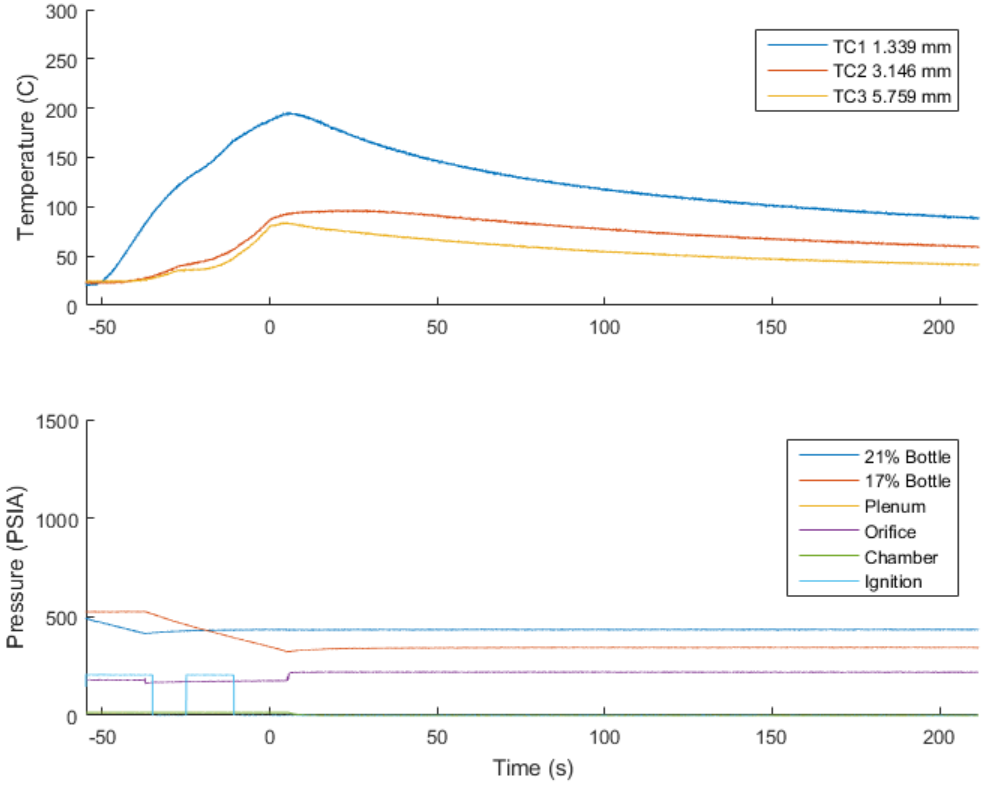

Figure 6.15. Drop Test 3 thermocouple temperature measurements and Combustion Tunnel control parameters.

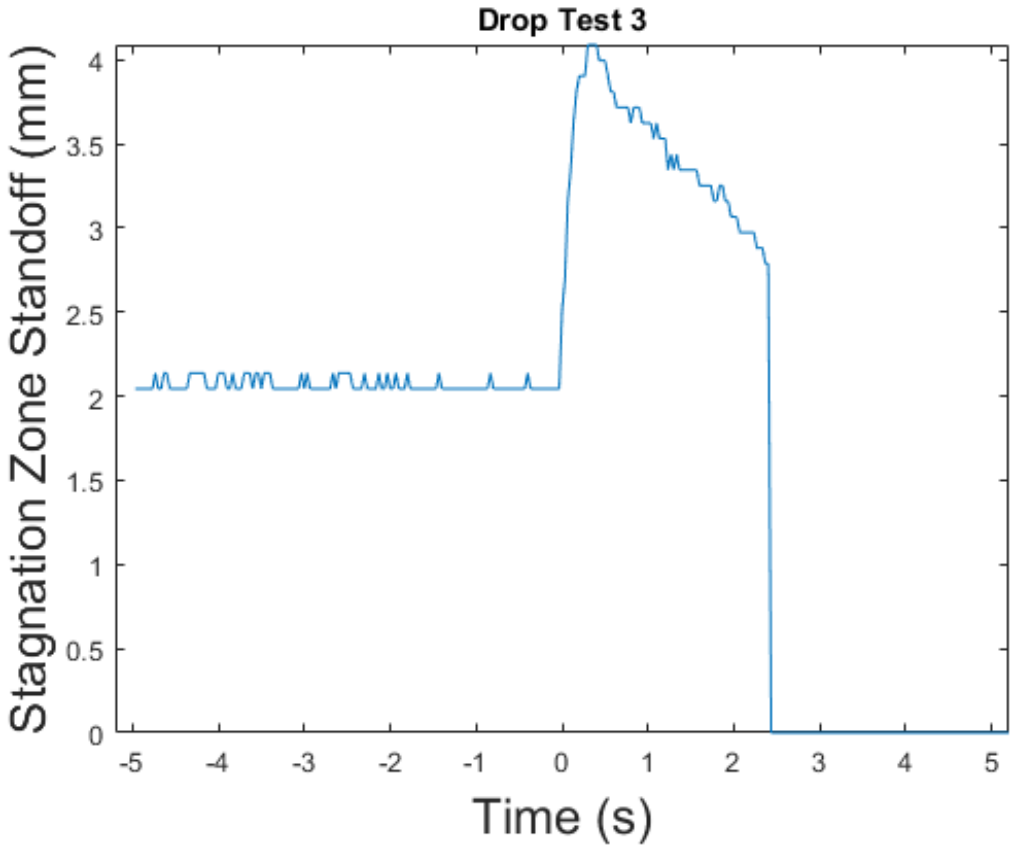

Figure 6.16. Drop Test 3 flame standoff distance and flame sheet thickness.

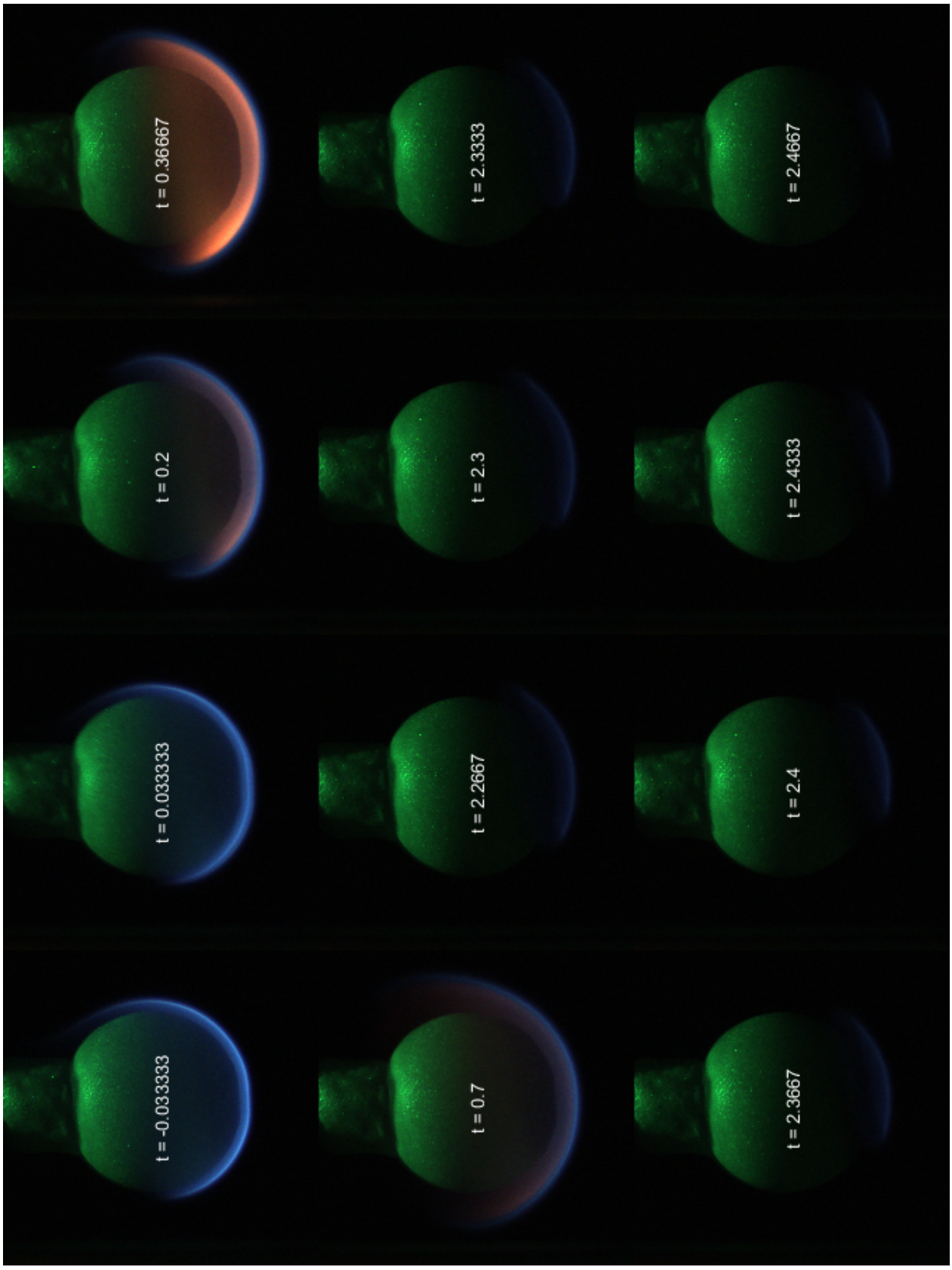

Figure 6.17. Drop Test 3 significant image frames

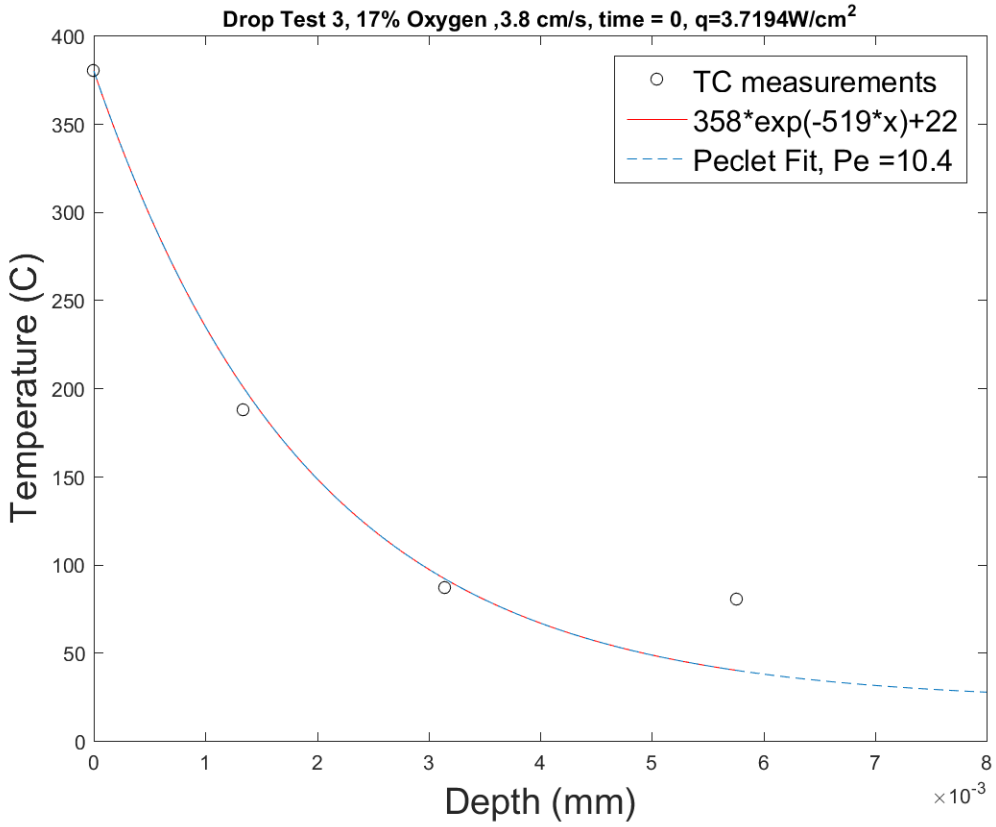

Figure 6.18. Fit of temperature profile at the time of the drop.

Drop Test 4, X-16-133

Drop Test 4 was conducted at 17% oxygen with forced flow velocity of 6 cm/s at a low preheat value with the same sphere sample as drop tests 1, 2, 3. The thermocouple positions from the CT scans are shown in Table 6.5. Ignition was for 20 seconds at 21% oxygen by volume with an actual average forced flow velocity of 5.9 cm/s. The gas was switched to 17% oxygen by volume and the flame allowed to stabilize and begin growing before the drop. The drop was triggered when the temperature of thermocouple TC1 reached 244^oC.

Pre Drop Test #4 thermocouple locations	
TC1	1.339 mm on axis
TC2	3.146 mm on axis
TC3	5.759 mm on axis
Post Drop Test #4 thermocouple locations	
TC1	0.837 mm on axis
TC2	2.676 mm on axis
TC3	5.436 mm on axis

Table 6.5. Thermocouple locations for Drop Test #4.

Test Conditions.

- 5.9 cm/s flow, $a_b \approx 19s^{-1}$, $a_f \approx 4.43s^{-1}$
- Ignition at 21% oxygen by volume for 20 seconds at t=-57.21 s
- Switched to 17% oxygen by volume after ignition starts at t=-27.81 s
- 17% oxygen reaches the sample about 3.5 seconds after the end of the ignition
- The flame was growing in 1g 17% oxygen
- Dropped when TC1 read 244^oC
- Extinction at t=3.934 seconds after the drop.
- Heat loss to the solid at the drop time is estimated at $3.72W/cm^2$

Results. Figure 6.21 Frame 1 shows a symmetric full envelope flame established on the sphere at t=-0.0333 s before the drop. The sample surface is still noticeably flattened in the stagnation zone from the double ignition in Drop Test 2. After the drop, the flame responded in manner similar to Drop Test 3, with increasing standoff distance and sooting between the flame sheet and sample surface in Frames 3,4, and 5. The flame tips begin to open up and the wake appears to grow larger for a short time as the glowing soot blows off downstream. After t=0.7 seconds, the flame tips retreat upstream towards the stagnation region as the flame sheet relaxes back towards the

sample surface. The flame quenches at t=3.934 seconds, slightly off center of the axis of symmetry.

Figure 6.19 shows the thermocouple measurements and flow controls of the Combustion Tunnel. Thermocouple TC1 (shown in blue) increases in temperature quickly during ignition, because of the close proximity to the sample surface, there is a decrease in rate of temperature increase just after the igniter is retracted. The rate increases again as the flame grows. A second decrease in rate occurs again after the change to 17% oxygen. Thermocouple TC3 (shown in yellow) was known to be broken from Drop Test 2. Thermocouple TC2 has an unexplained glitch just before the drop, which is likely due to short circuiting to another thermocouple wire.

As in Drop Test 3, thermocouple 3 was ignored when fitting the temperature curve used in the analysis of the heat loss to the solid. This can be seen in the fit at the time of drop in Fig. 6.22. Although the temperature reading of thermocouple TC2 located at 2.676 mm is suspicious, the exponential temperature profile fits well with the experimental data whether this data point is used for the fit or not.

Figure 6.20 shows a standoff distance of about 1.25 mm in 1G, increasing to a maximum of about 3.5 mm, and then relaxing back towards the surface until extinction at 3.934 seconds.

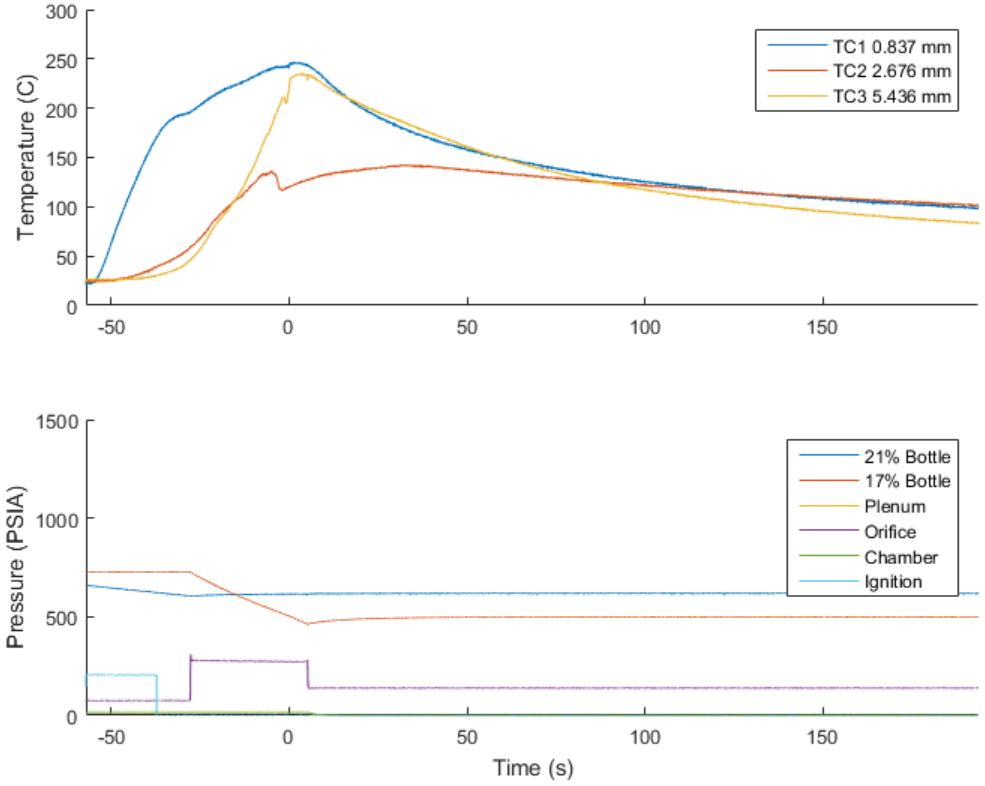

Figure 6.19. Drop Test 4 thermocouple temperature measurements and Combustion Tunnel control parameters.

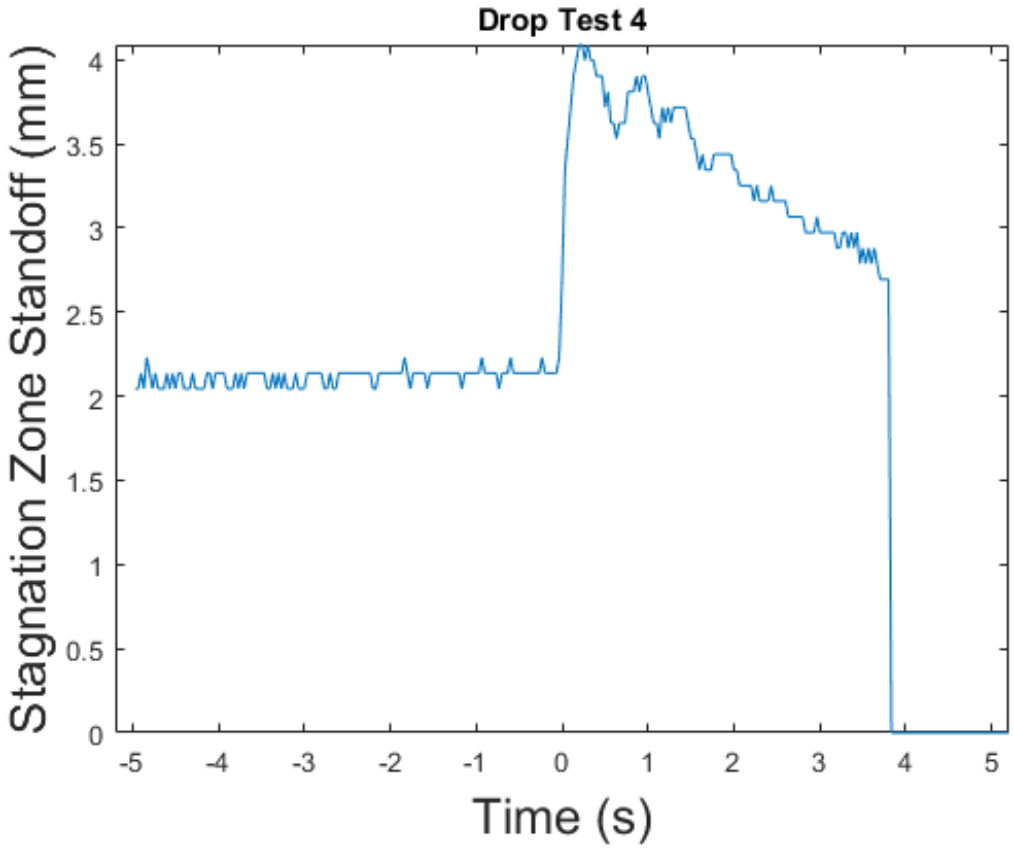

Figure 6.20. Drop Test 4 flame standoff distance and flame sheet thickness.

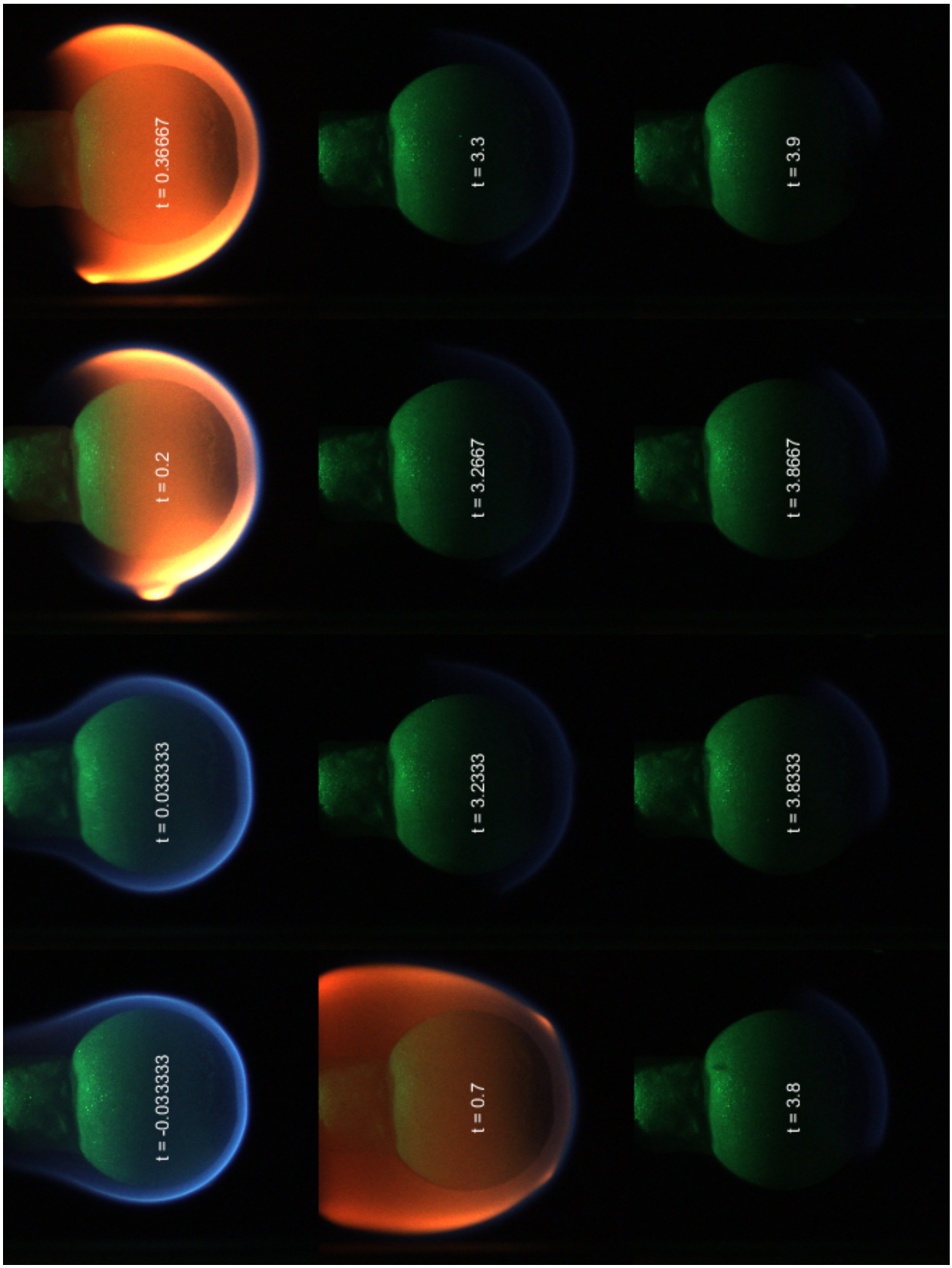

Figure 6.21. Drop Test 4 significant image frames

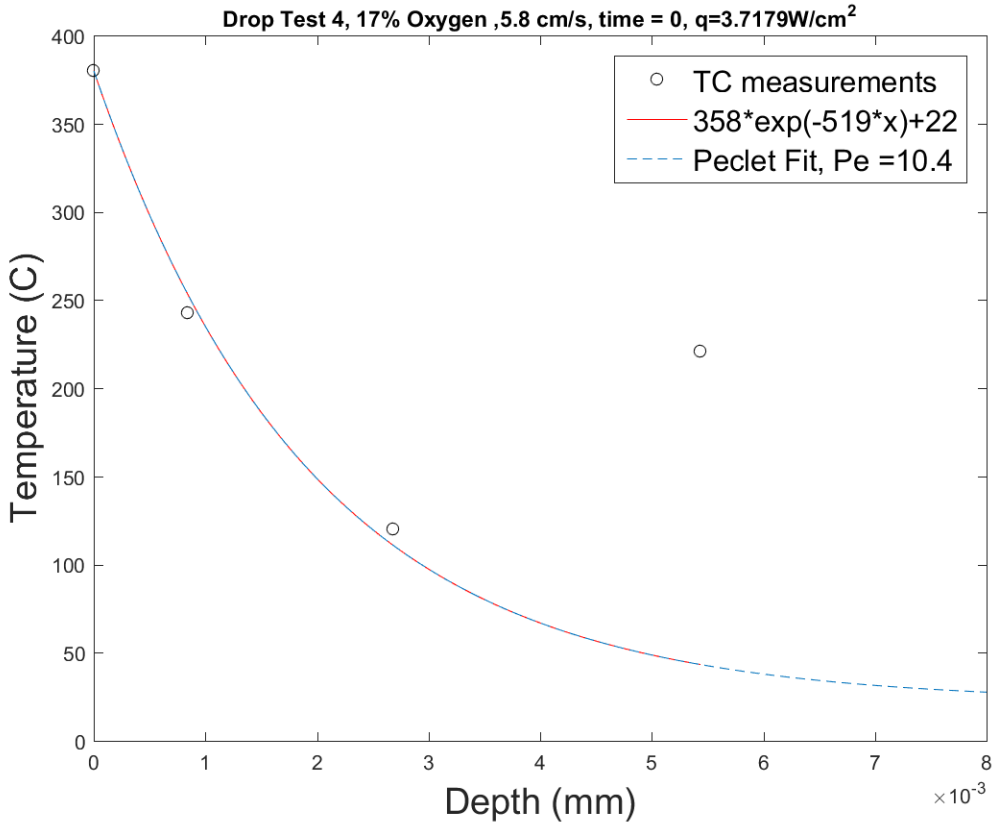

Figure 6.22. Fit of temperature profile at the time of the drop.

Drop Test 5, X-16-142

Drop Test 5 is conducted at 17% oxygen concentration and an freestream velocity of 25 cm/s. The forced flow stretch rate was $a_f \approx 19s^{-1}$ to match the estimated stretch rate of pure buoyancy flow in the stagnation region. The flame tip appearance is very different in the purely forced case due to the lack of upward acceleration to counteract the outward blowing from the solid surface and the lack of entrainment from the sides in the wake region, but the stagnation region is expected to have similarity according to stagnation flame theory.

Pre Drop Test #5 thermocouple locations	
TC1	2.769 mm on axis
TC2	2.991 mm on axis
TC3	4.839 mm on axis
Post Drop Test #5 thermocouple locations	
TC1	2.469 mm on axis
TC2	2.991 mm on axis
TC3	4.839 mm on axis

Table 6.6. Thermocouple locations for Drop Test #5.

The flow rate for Drop Test 5 was near the limits of capability of the Combustion Tunnel due to maximum compressed gas cylinder pressure and volume. Because of this, the sphere was ignited in quiescent 21% O_2 by volume to conserve gas and the flame was allowed to spread. The 25 cm/s flow was then turned on before the quiescent chamber oxygen depleted and was then changed to 17% oxygen by volume before the drop. The drop was triggered when thermocouple TC1 read 122 degrees Celsius.

The sphere for this test was newly cast Sphere0002. The stagnation zone was slightly non symmetric from casting with a small peak to one side of the axis of symmetry. The internal thermocouples shifted during the casting process and positions are shown in Table 6.6. Thermocouple 1 and 2 are at nearly identical positions at 2.769 mm and 2.991 mm from the surface, and thermocouple 3 shifted off axis. Thermocouple 4 was damaged and had a circuit fault so was not used for measurements.

Test Conditions.

- 25 cm/s flow, $a_b \approx 19s^{-1}$, $a_f \approx 19s^{-1}$
- Ignition in quiescent 21% oxygen by volume for 20 seconds at t=-50.46 s
- 25 cm/s 21% oxygen flow starting at t=-19.53 s.
- 17% oxygen by volume after t=-12.63 s

- Dropped when TC1 read 122^oC
- No extinction
- Heat loss to the solid in the stagnation zone the drop time is estimated at $3.62W/cm^2$

Results. Figure 6.25 Frame 1 shows a robust full envelope flame at t=-0.033 s, which was established before the drop with an added freestream velocity of 25 cm/s at 17%. Some vapor jetting was present and visible in the video recording, but the flame remained predominantly blue throughout, including in the wake region. A clear bright flame sheet was visible in the stagnation zone. Immediately after the drop, just after Frame 2 at t=0.033 s until Frame 4 at t=0.367 s, a large amount of bright soot develops in the downstream region. The flame tips open up and the standoff distance increases slightly. The blue flame in the stagnation zone dims in the video images due to the camera's automatic shutter speed response to the bright downstream soot. The video camera shutter speed goes from a nominal imaging integration time of 33333 microseconds per image to a minimum imaging integration time of 2505 micro seconds. The camera shutter speed overshoots as the downstream portion appears very dim and the soot begins do disappear as in previous tests.

As the flame responds to the new conditions, some vapor jetting continues to cause ripples in the stagnation zone, with some waviness continuing in the downstream flame. Frames 6 through 12 exhibit little change in the flame. The flame survived the duration of the drop at the low preheat value, and appears as if it would survive indefinitely.

From Fig. 6.24, the standoff distance in purely forced flow was measured at 1.67 mm. The nearly pure buoyant standoff distance measured from the Drop Test #1

experiment before the zero g drop was measured at 1.30 mm. This is a difference of approximately one flame thickness. It is unclear why there is so much difference in stagnation flame standoff but this may indicate that the buoyant stretch rate estimate needs modification. This is discussed later.

Figure 6.23 shows the thermocouple temperature measurements and flow conditions within the Combustion Tunnel. Thermocouples TC1 and TC2 were in nearly identical locations with TC1 located at 2.469 mm and TC2 located at 2.566 mm. These read nearly identical temperature values, which are displayed in the chart. Thermocouple TC3 was located deeper at 4.8 mm and takes a very long time to respond to the flame. The temperature is still rising 50 seconds after the flame is extinguished at the end of the drop.

The temperature curve fit used to estimate the heat flux into the solid interior is shown in Fig. 6.26. The fit is in very good agreement with the known temperatures.

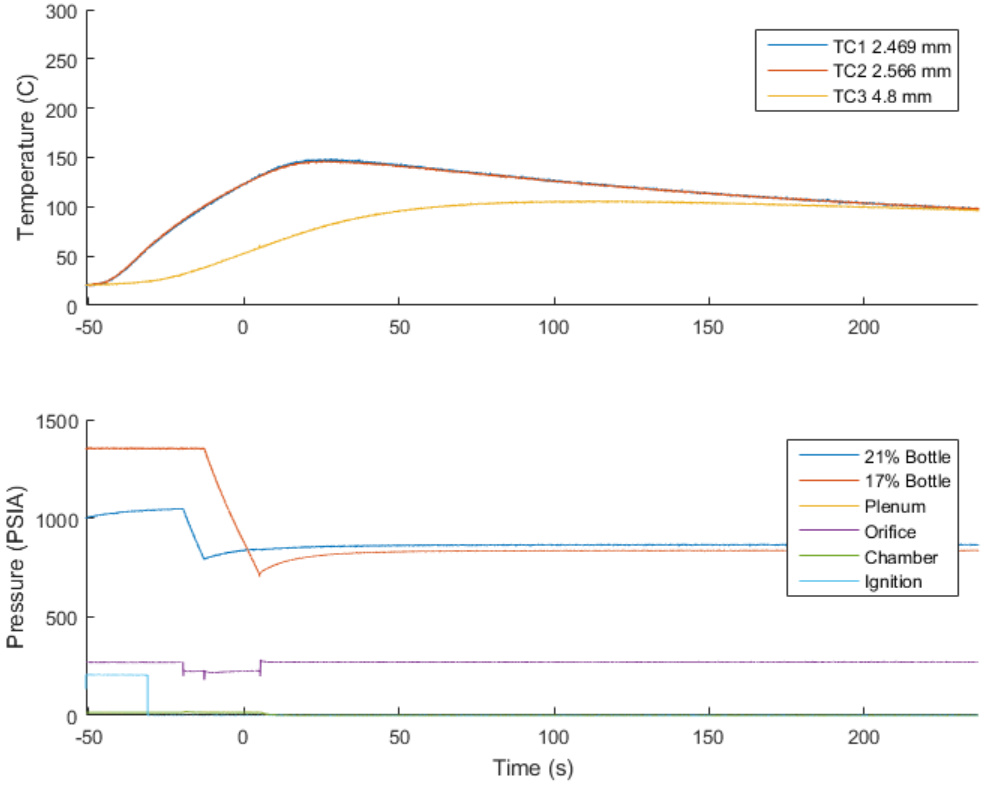

Figure 6.23. Drop Test 5 thermocouple temperature measurements and Combustion Tunnel control parameters.

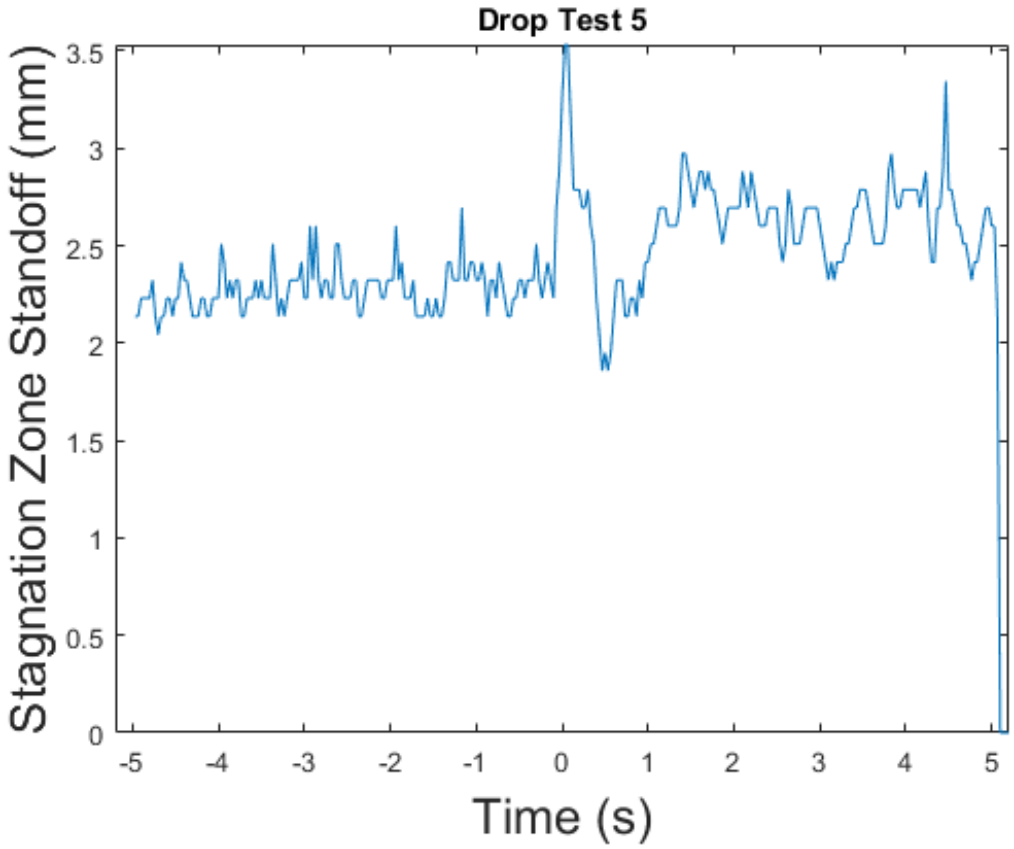

Figure 6.24. Drop Test 5 flame standoff distance and flame sheet thickness.

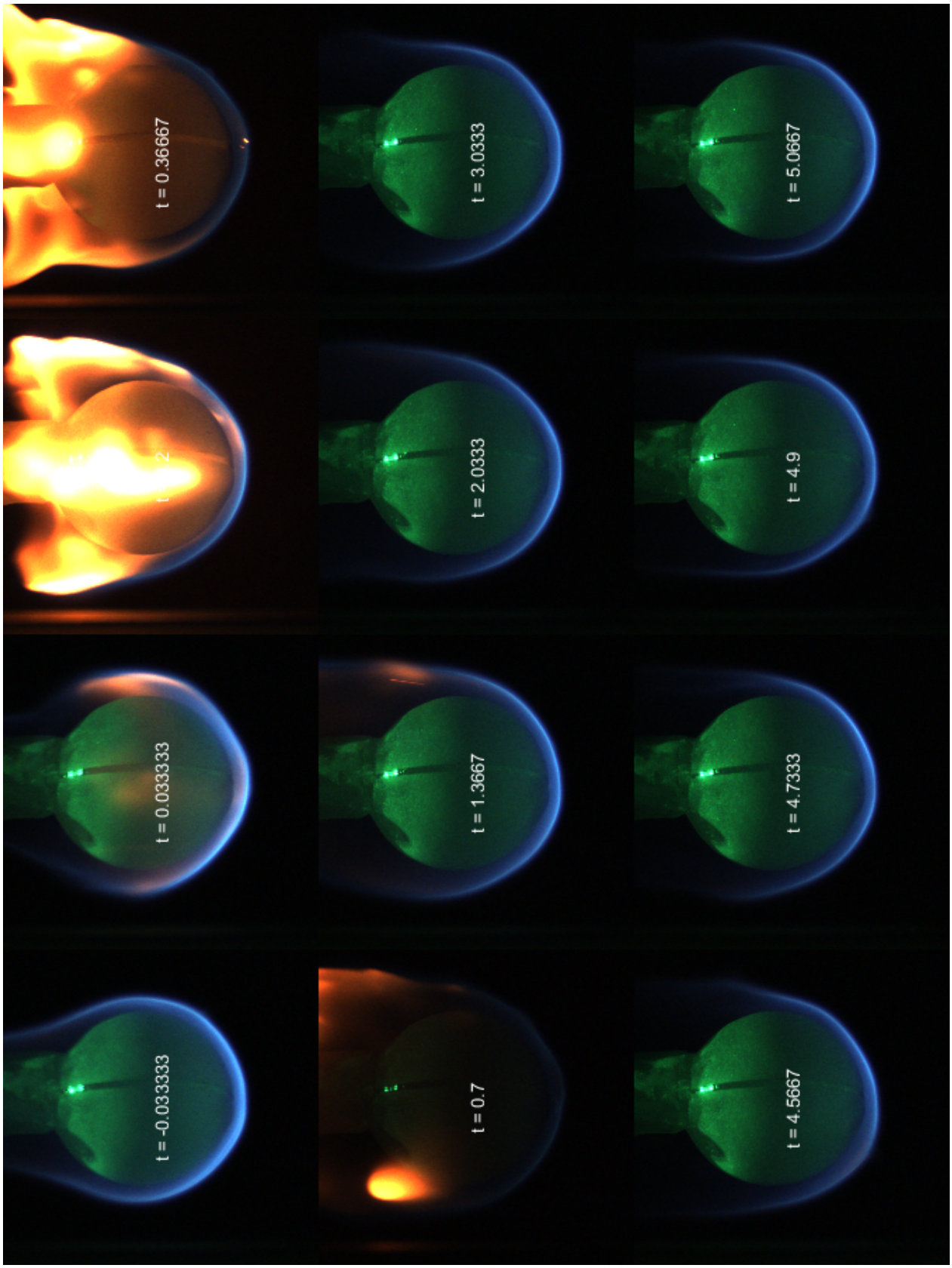

Figure 6.25. Drop Test 5 significant image frames

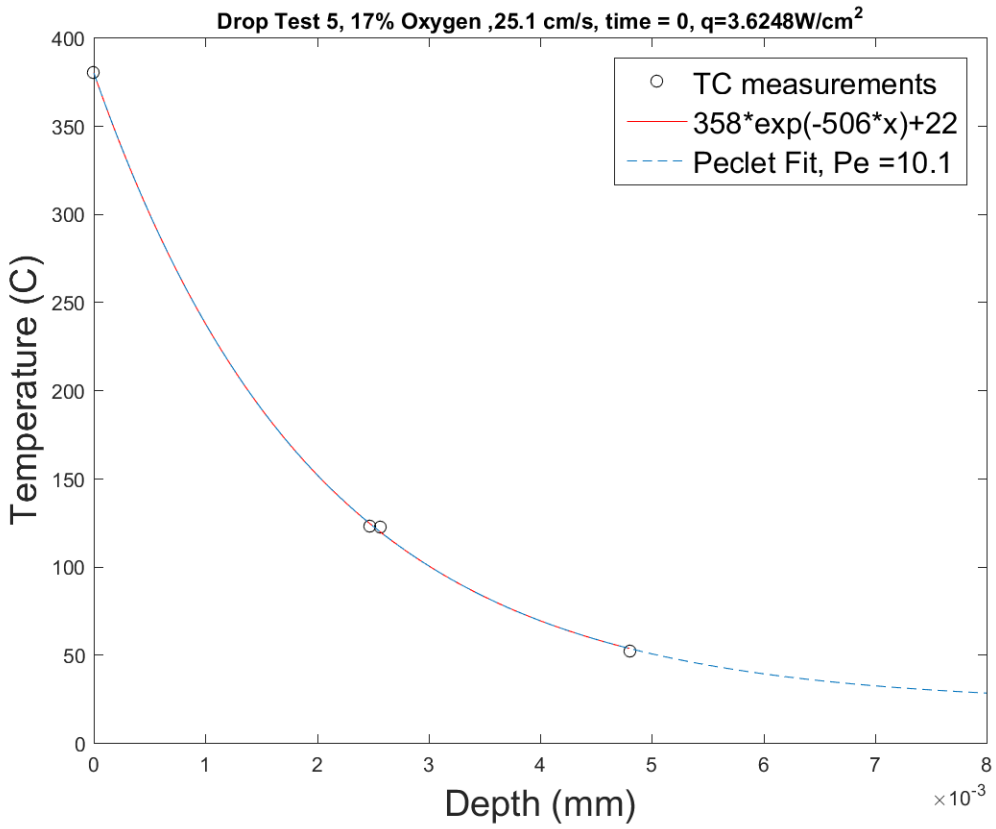

Figure 6.26. Fit of temperature profile at the time of the drop.

Drop Test 6, X-16-143

Drop Test 6 was run at a freestream velocity of 14.5 cm/s and 17% oxygen by volume. Ignition was for 20 seconds in quiescent 21% oxygen. The 14.5 cm/s flow was turned on and switched to 17% oxygen before the drop. The drop was triggered when the stagnation point thermocouple TC1 read 138^oC.

The sample was newly cast as Sphere0003. Thermocouple locations from CT scans before and after the test are shown in Table 6.7.

Test Conditions.

Pre Drop Test #6 thermocouple locations	
TC1	2.557 mm on axis
TC2	5.205 mm on axis
TC3	6.773 mm on axis
Post Drop Test #6 thermocouple locations	
TC1	2.214 mm on axis
TC2	4.870 mm on axis
TC3	6.493 mm on axis

Table 6.7. Thermocouple locations for Drop Test #6.

- 14.5 cm/s flow, $a_b \approx 19s^{-1}$, $a_f \approx 11.3s^{-1}$
- Ignition in quiescent 21% oxygen by volume for 20 seconds starting at t=-47.86 s
- 14.5 cm/s 21% oxygen flow starting at t=-19.60 s.
- 17% oxygen by volume after t=-17.79 s
- Dropped when TC1 read 138^oC
- Extinction at t = 3.497s
- Heat loss to the solid in the stagnation zone the drop time is estimated at $3.58W/cm^2$

Results. Figure 6.29 Frame 1 at t=-0.033 seconds before the drop shows a symmetric envelope flame established over the spherical sample. After the drop, Frame 2 shows the right side of the flame flashing before the left side, but it reestablishes before frame 3 at t=0.2 seconds. The typical sooting and increase in stagnation flame standoff distance occurred. After frame 5 at t=0.7 seconds, most of the soot has blown downstream into the wake region, some vapor jetting continues to cause sooty spots in the stagnation zone. Flame flashing then occurred, with holes developing in the flame and propagating throughout the flame zone until extinction 3.497 seconds after the drop.

Figure 6.27 shows the recorded temperature from thermocouples and the flow conditions within the Combustion Tunnel. The exponential fit temperature profile at the time of the drop is shown with the recorded data in Fig. 6.30. The fit shows good agreement with all of the known temperatures.

The standoff distance is displayed in Fig. 6.28 The buoyant standoff distance is about 1.5 mm and increases to a peak of about 3 mm after transition to microgravity before relaxing back towards the surface and extinguishing at approximately 1.75 mm at 3.497s.

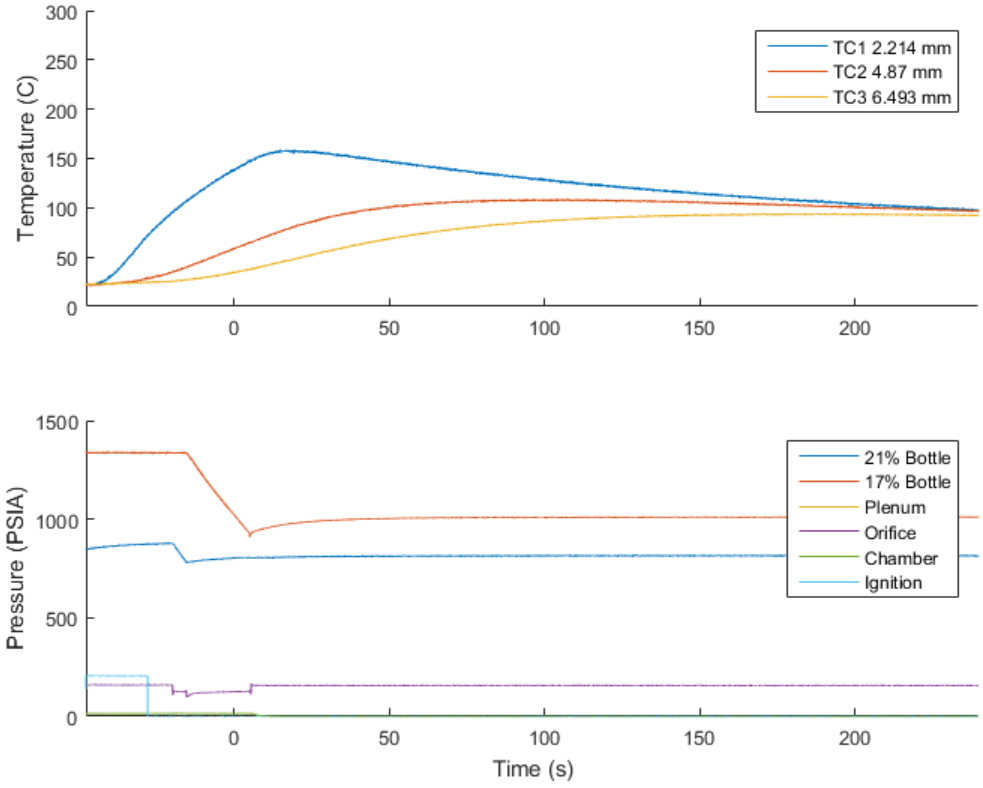

Figure 6.27. Drop Test 6 thermocouple temperature measurements and Combustion Tunnel control parameters.

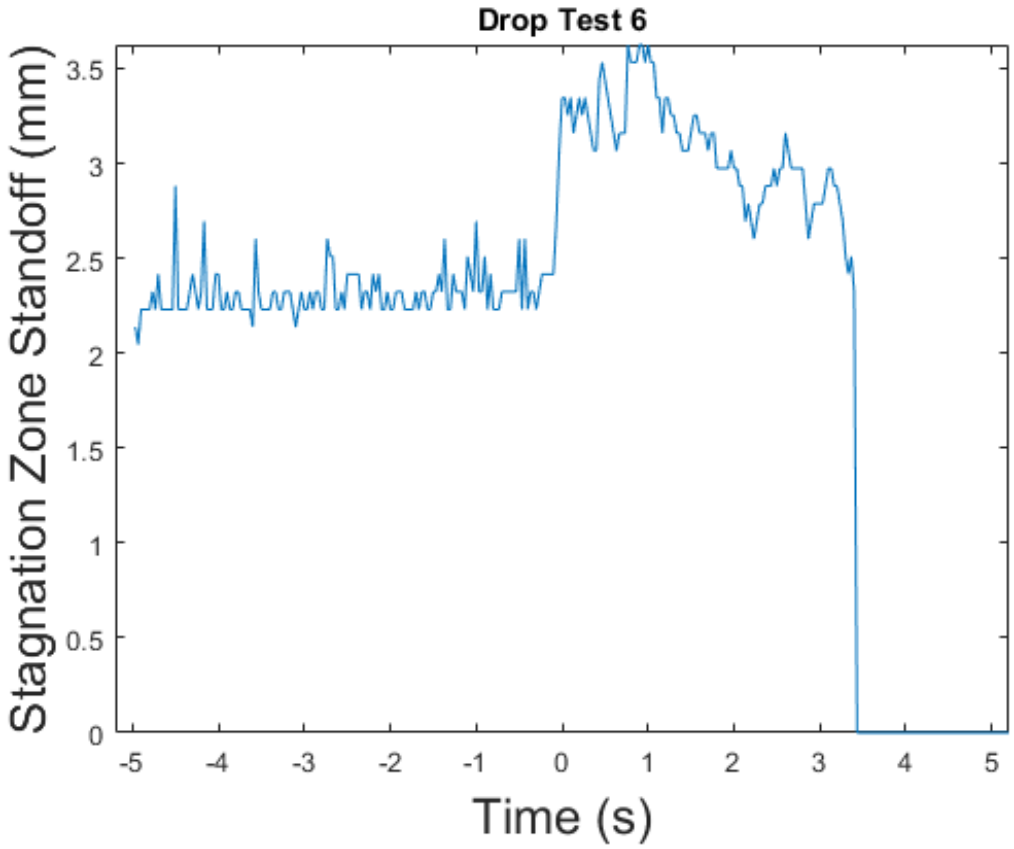

Figure 6.28. Drop Test 6 flame standoff distance and flame sheet thickness.

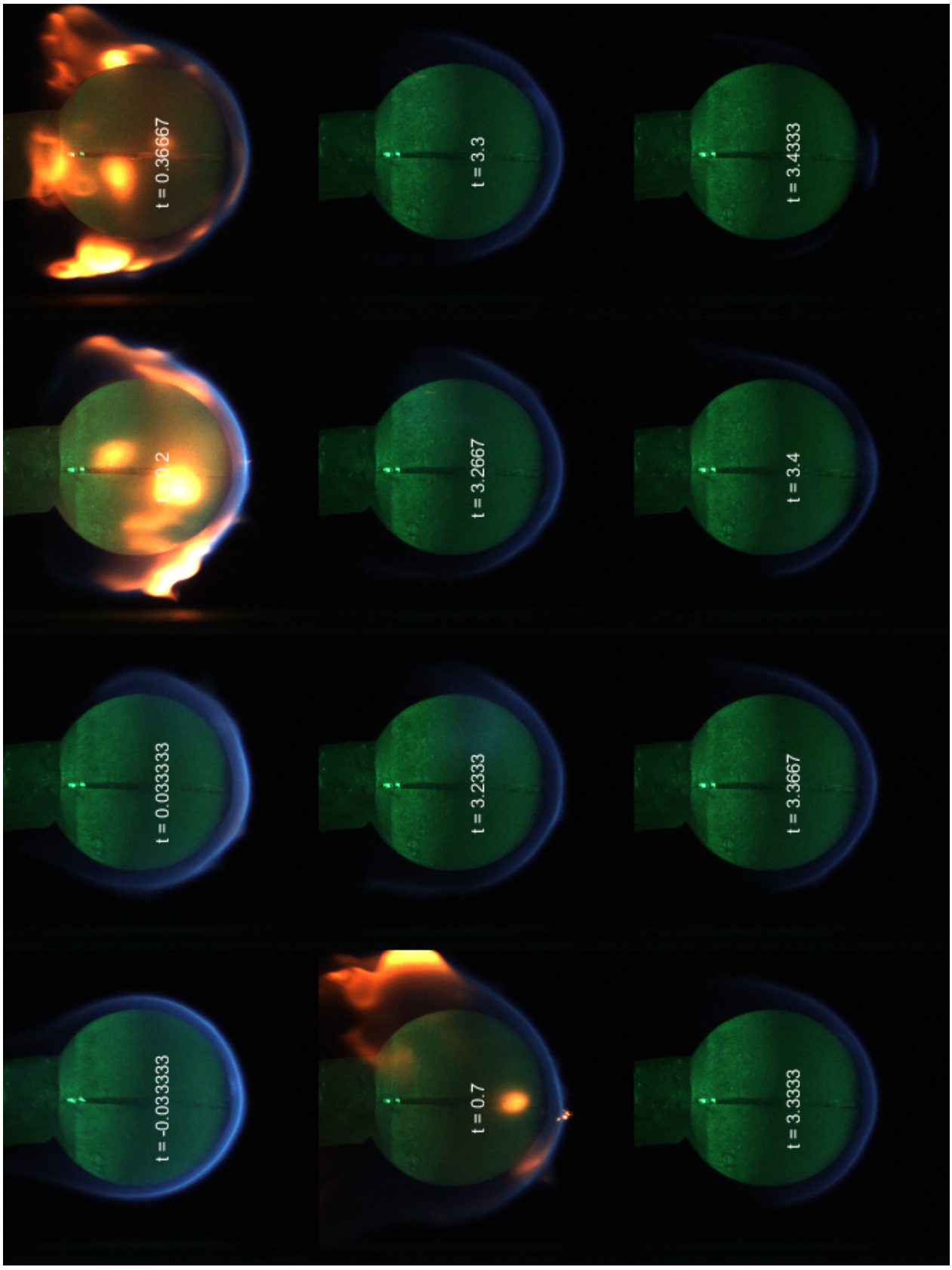

Figure 6.29. Drop Test 6 significant image frames

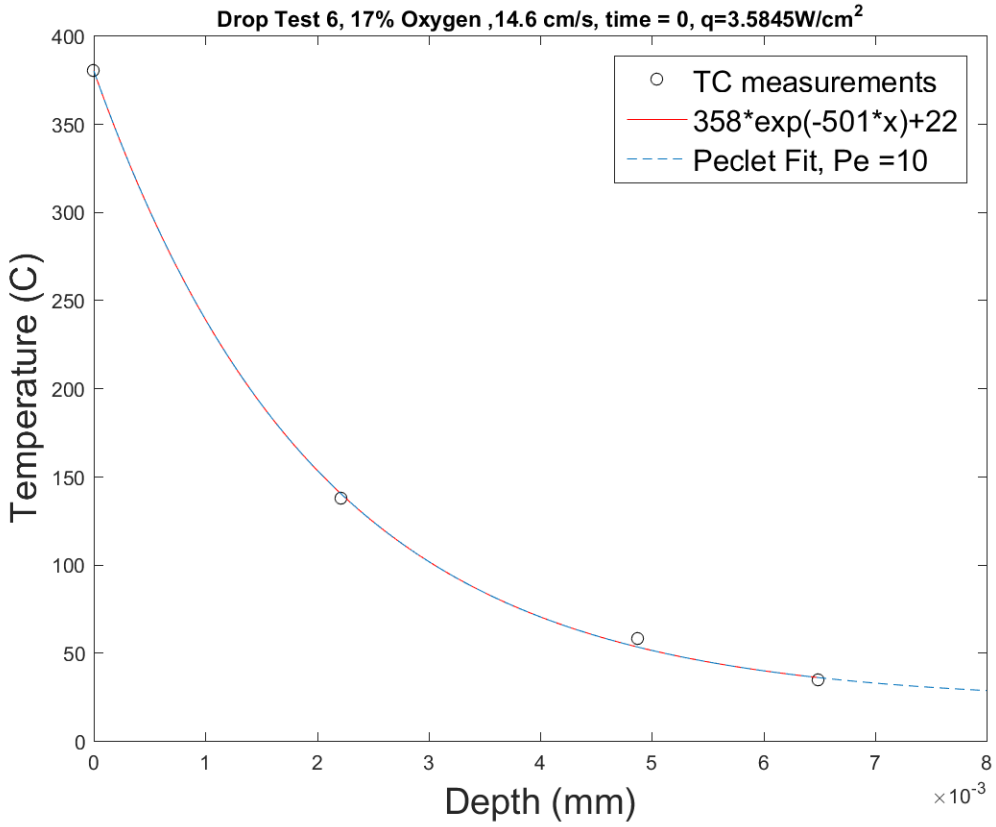

Figure 6.30. Fit of temperature profile at the time of the drop.

Drop Test 7, X-16-144

Drop Test 7 was conducted at velocity conditions between Drop Tests 5 and 6 at 17% oxygen concentration and 20 cm/s. Ignition was for 20 seconds in quiescent 21% oxygen by volume. Flow was started from the 21% oxygen cylinder at 25.9 cm/s. The intended speed was 20 cm/s. Ignition of the sample surface was not symmetric. When the gas was changed to 17% oxygen by volume at 19.5 cm/s the flame extinguished. The 17% oxygen flow was turned off to conserve gas and the igniter was moved back into position and renergized for 20 seconds in the quiescent 17% oxygen. The igniter

Pre Drop Test #7 thermocouple locations	
TC1	2.942 mm on axis
TC2	4.896 mm on axis
TC3	7.331 mm on axis
Post Drop Test #7 thermocouple locations	
TC1	2.016 mm on axis
TC2	4.006 mm on axis
TC3	6.354 mm on axis

Table 6.8. Thermocouple locations for Drop Test #7.

was removed and 19.5 cm/s flow was resumed after the flame was re-established. The drop was triggered when thermocouple 1 reached 149^oC

The sample was newly cast as Sphere0005. The front stagnation zone was not perfectly spherical as can be seen in the pictures. The casting spew port and support tube was not centered and was off axis.

Test Conditions.

- 20 cm/s flow, $a_b \approx 19s^{-1}$, $a_f \approx 15s^{-1}$
- Ignition in quiescent 21% oxygen by volume starting at -73.29 s
- Started 25.9 cm/s (20 cm/s was intended) 21% oxygen flow at -45.39 s
- Started 19.5 cm/s (20 cm/s was intended) 17% oxygen by volume at -41.05 s
- Reignited in 17% quiescent flow starting at -30.35 s
- Restarted 17% oxygen flow at 19.5 cm/s before drop
- Dropped when TC1 temperature is 149^oC
- Heat loss to the solid in the stagnation zone the drop time is estimated at $3.34W/cm^2$

Results. As with Drop Test #3, the cause of the unsymmetric ignition and subsequent extinction is unknown. Although every effort was made to place the igniter in

the stagnation zone, the samples have an inherent non symmetry due to manufacturing error. This sample in particular had a significant spew defect that was not symmetric around the axis of rotation. The ignition process is obstructed by the bright glow of the igniter and can not be monitored in real time. This will also be a problem present in the GEL space flight experiment.

Figure 6.33 Frame 1 shows the flame before the drop was triggered, the flame tip on one side of the sphere fully enveloped past the downstream spew towards the support tube. The other side of the flame enveloped the sphere but not the spew. After the drop, the typical increase in flame stand off distance along with sooting between the flame sheet and material surface occurred and the flame tips opened up between Frames 3 and 5. The soot blows off downstream just after Frame 5 and the flame tips begin retreating towards the stagnation region. Frame 6 shows one side of the flame continues past the boundary layer separation point until the end of the drop, the other side retreated upstream of separation, due to the reduced preheating in that region which was caused by the unsymmetric ignition. There was no extinction during the 5.18 second drop.

The thermocouple temperature data and flow conditions within the Combustion Tunnel are shown in Figure 6.31. The two ignitions can be seen in the bottom graph as a light blue square wave. The temperature data looks smooth with no anomalies. Figure 6.34 shows the exponential temperature profile fit plotted against the known temperature values. The poor fit is likely caused by the extinction and re-ignition of the flame which departs from the ideal case of constant boundary conditions. Specifically, a non exponential fit would need to be used for non constant boundary conditions.

Figure 6.32 shows the flame standoff distance of about 1.2 mm in 1g and 2 mm in purely forced flow.

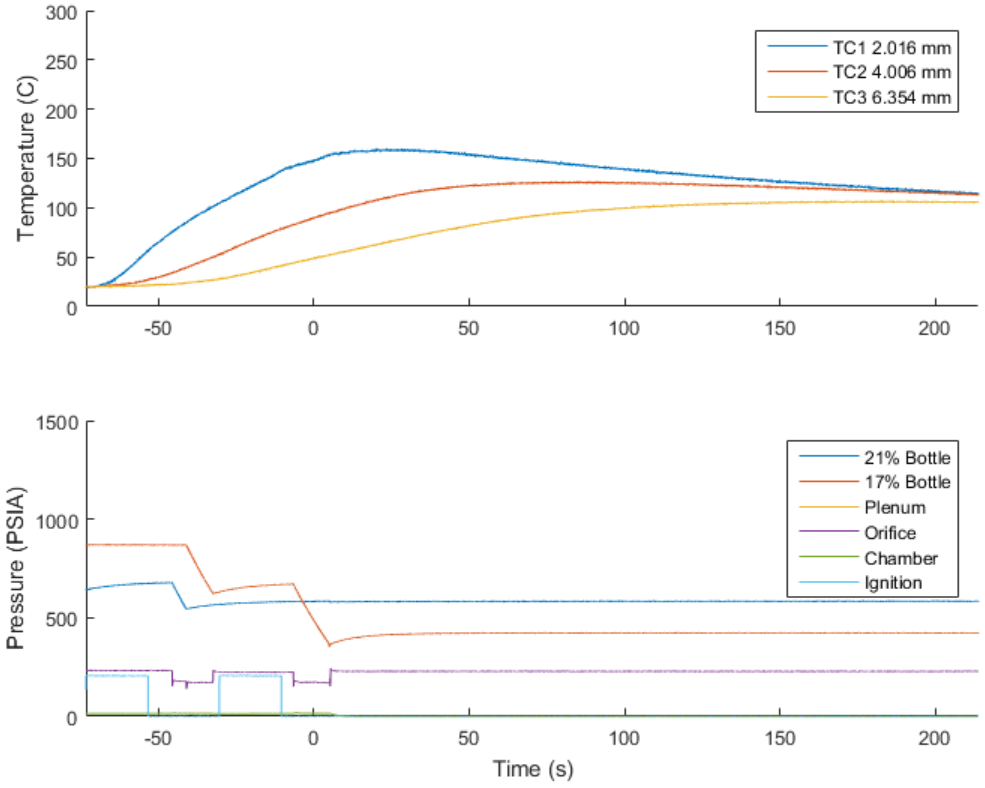

Figure 6.31. Drop Test 7 thermocouple temperature measurements and Combustion Tunnel control parameters.

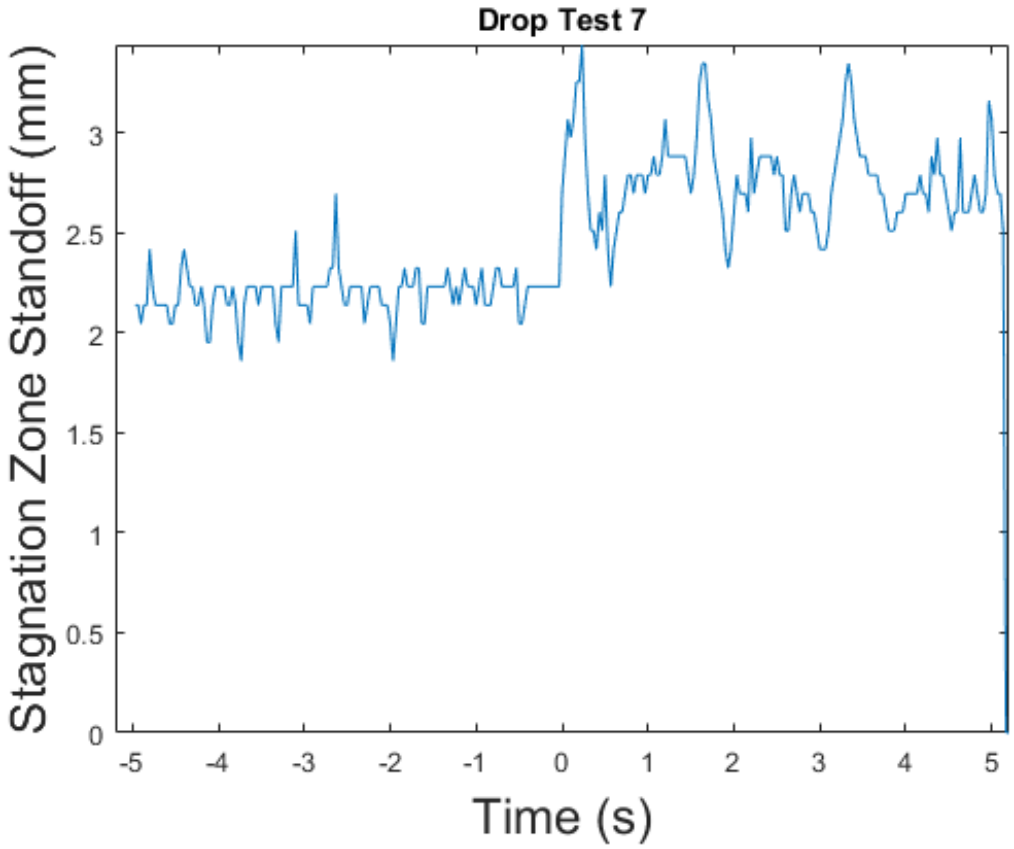

Figure 6.32. Drop Test 7 flame standoff distance and flame sheet thickness.

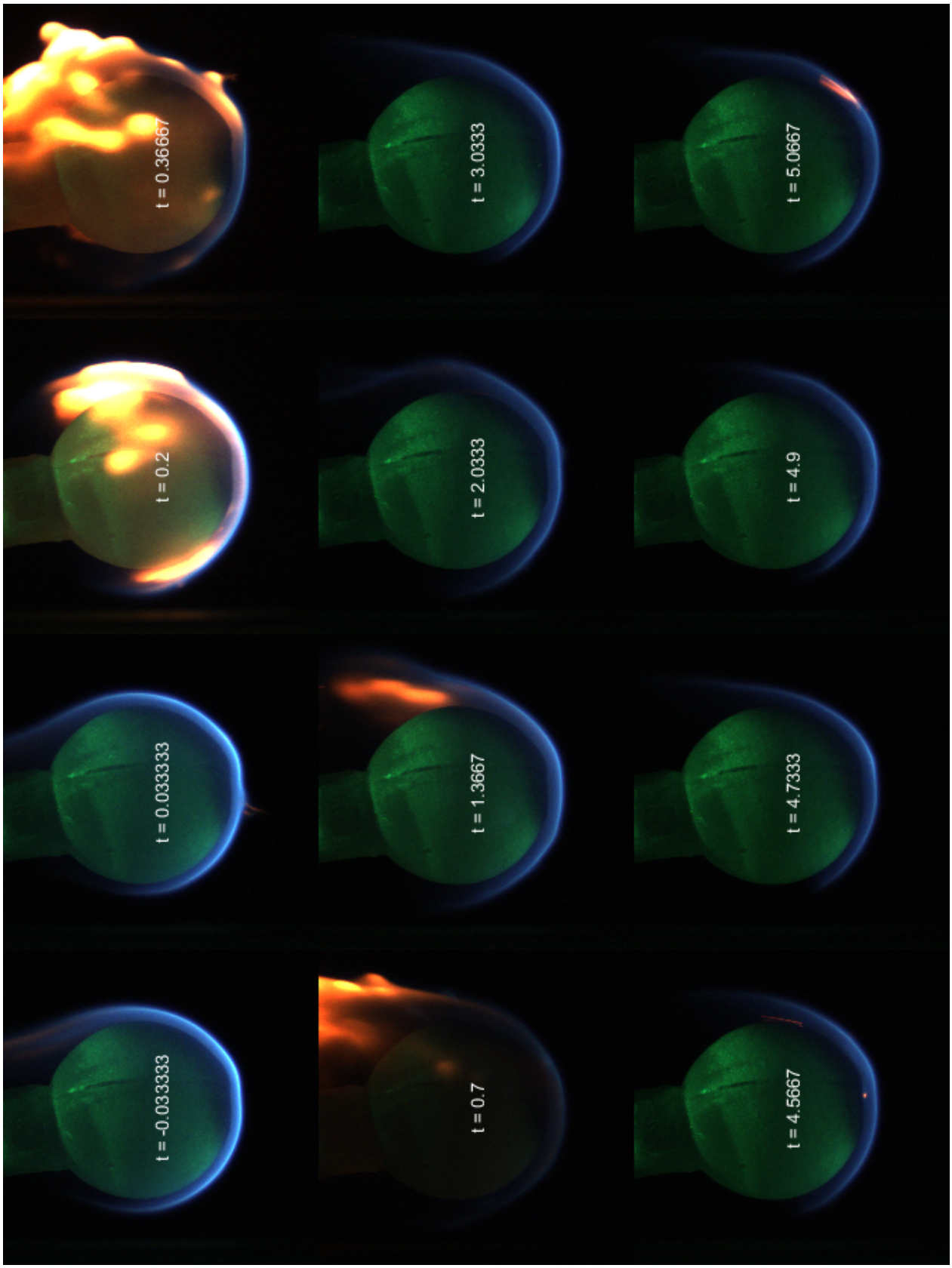

Figure 6.33. Drop Test 7 significant image frames

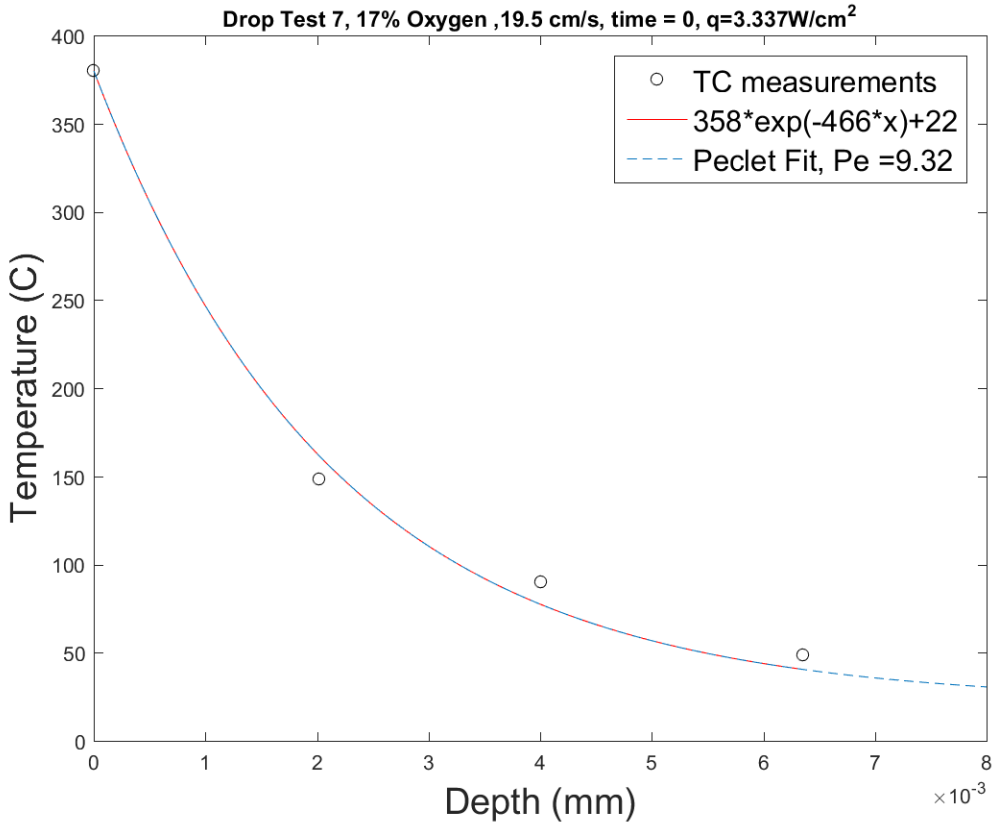

Figure 6.34. Fit of temperature profile at the time of the drop.

Drop Test 8, X-16-145

Drop Test 8 was run at the same conditions as Drop Test 7 with a lower level of preheating to help establish the flammability boundary. Ignition was for 20 seconds in quiescent 21% oxygen by volume. The gas was switched to 19.6 cm/s 17% oxygen concentration by volume before the drop. The drop was triggered when thermocouple 1 read 165^oC.

The test reused sample sphere0003 which was CT scanned before and after testing. The thermocouple locations are shown in Table 6.9.

Pre Drop Test #8 thermocouple locations	
TC1	2.214 mm on axis
TC2	4.870 mm on axis
TC3	6.493 mm on axis
Post Drop Test #8 thermocouple locations	
TC1	1.579 mm on axis
TC2	4.166 mm on axis
TC3	5.826 mm on axis

Table 6.9. Thermocouple locations for Drop Test #8.

Test Conditions.

- 20 cm/s flow, $a_b \approx 19s^{-1}$, $a_f \approx 15s^{-1}$
- Ignition in quiescent 21% oxygen by volume starting at -50.00 s
- Started 20 cm/s (20 cm/s was intended) 21% oxygen flow at -11.40 s
- Started 19.6 cm/s (20 cm/s was intended) 17% oxygen by volume at -8.73 s
- Dropped when TC1 temperature is 165^oC
- Extinction at 2.53 s
- Heat loss to the solid in the stagnation zone the drop time is estimated at $3.98W/cm^2$

Results. Figure 6.37 shows ignition was unsymmetrical with one side of the flame extending beyond the spew and the other side extending just beyond the sphere's equator. Before the drop (not shown), a hole developed in the forward stagnation zone towards the strong side of the flame (right side in image). This propagated downstream as a flash. This hole and flash were likely due to a large vapor jet creating a condition too fuel rich for combustion. The flame recovered because of continued burning on the weak side. After the drop was triggered, the flame stand off distance increased between Frames 2 and 5, but excess sooting was minimal compared to previous tests. What little soot was present blew off downstream just after Frame

4. The flame stand off distance relaxed between Frames 4 and 5 and the flame tips retreated. Flashing extinction occurred with holes developing near the stagnation region and the average flame tip distances extending just beyond the boundary layer separation point. The flame was completely extinguished at 2.596 seconds after the drop. The last visible flame in Frame 12 at t=2.5 s was not a stable quenching case, but the remnants of flashing extinction.

Figure 6.35 shows the recorded thermocouple measurements and flow conditions within the Combustion Tunnel. The exponential fit temperature profile is shown with good agreement with known temperature data in Fig. 6.38.

The standoff distance is displayed in Fig. 6.36. The 1g standoff was measured at approximately 1.3 mm, and the maximum overshoot around 2.5 mm before relaxing back to 1.75 mm before extinction. Note that this is a measurement in the stagnation region along the centerline, although the flame extinguished downstream.

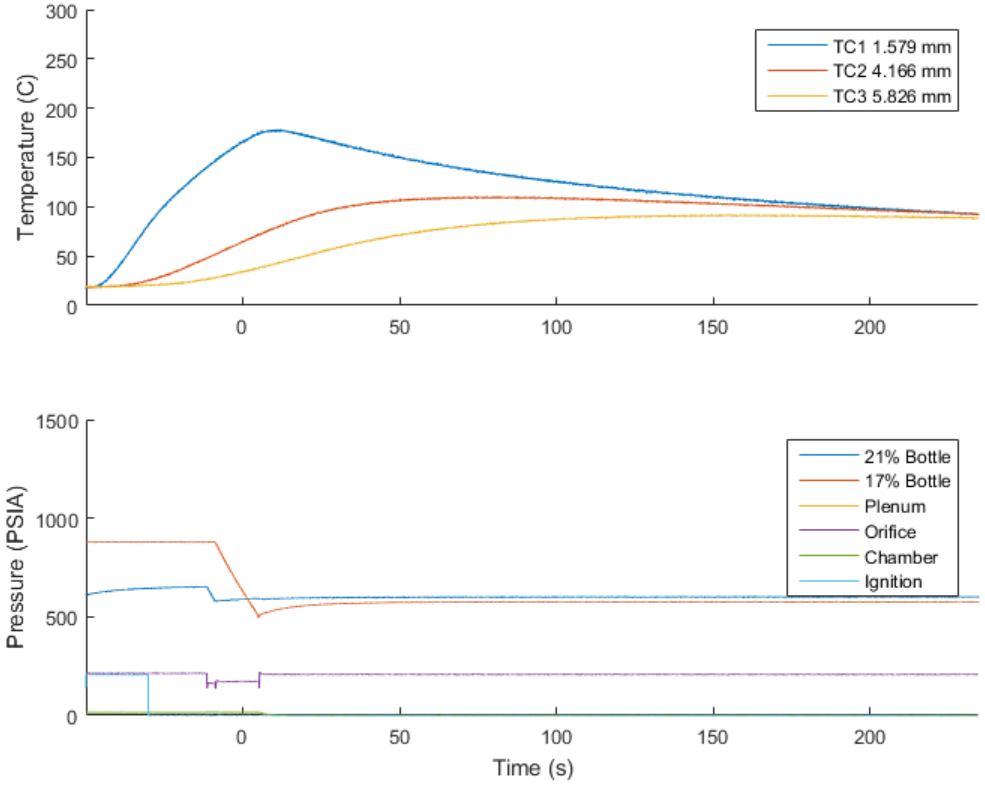

Figure 6.35. Drop Test 8 thermocouple temperature measurements and Combustion Tunnel control parameters.

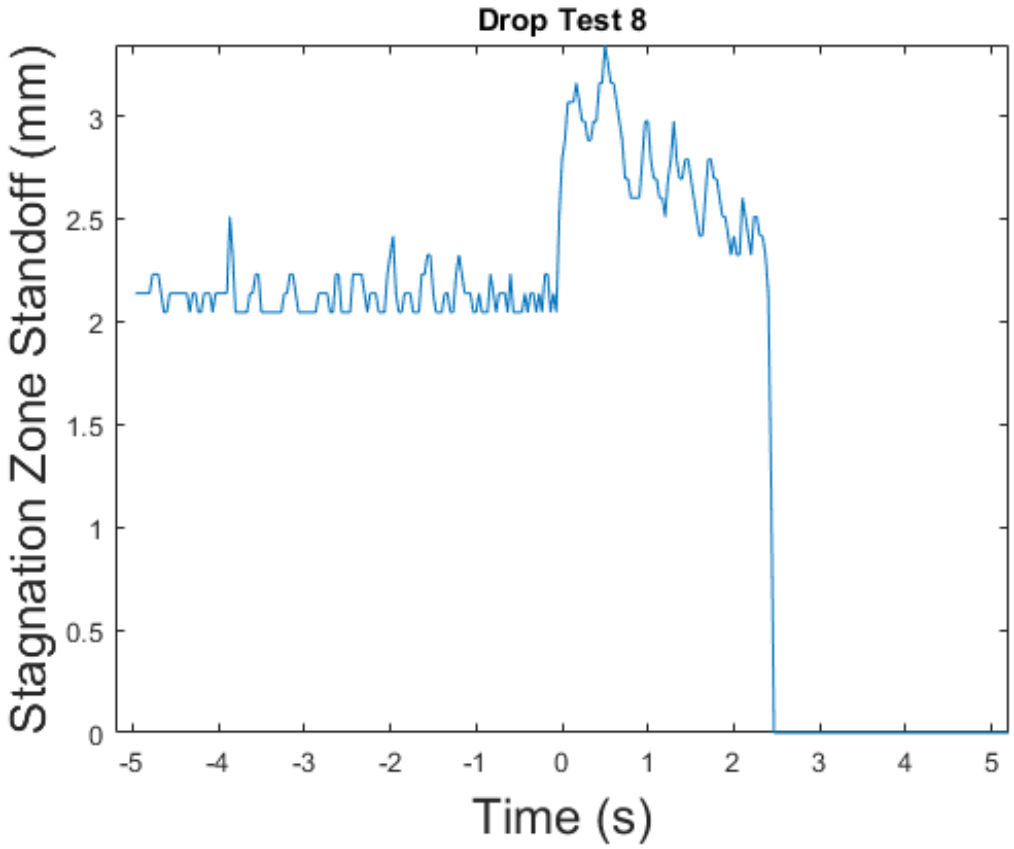

Figure 6.36. Drop Test 8 flame standoff distance and flame sheet thickness.

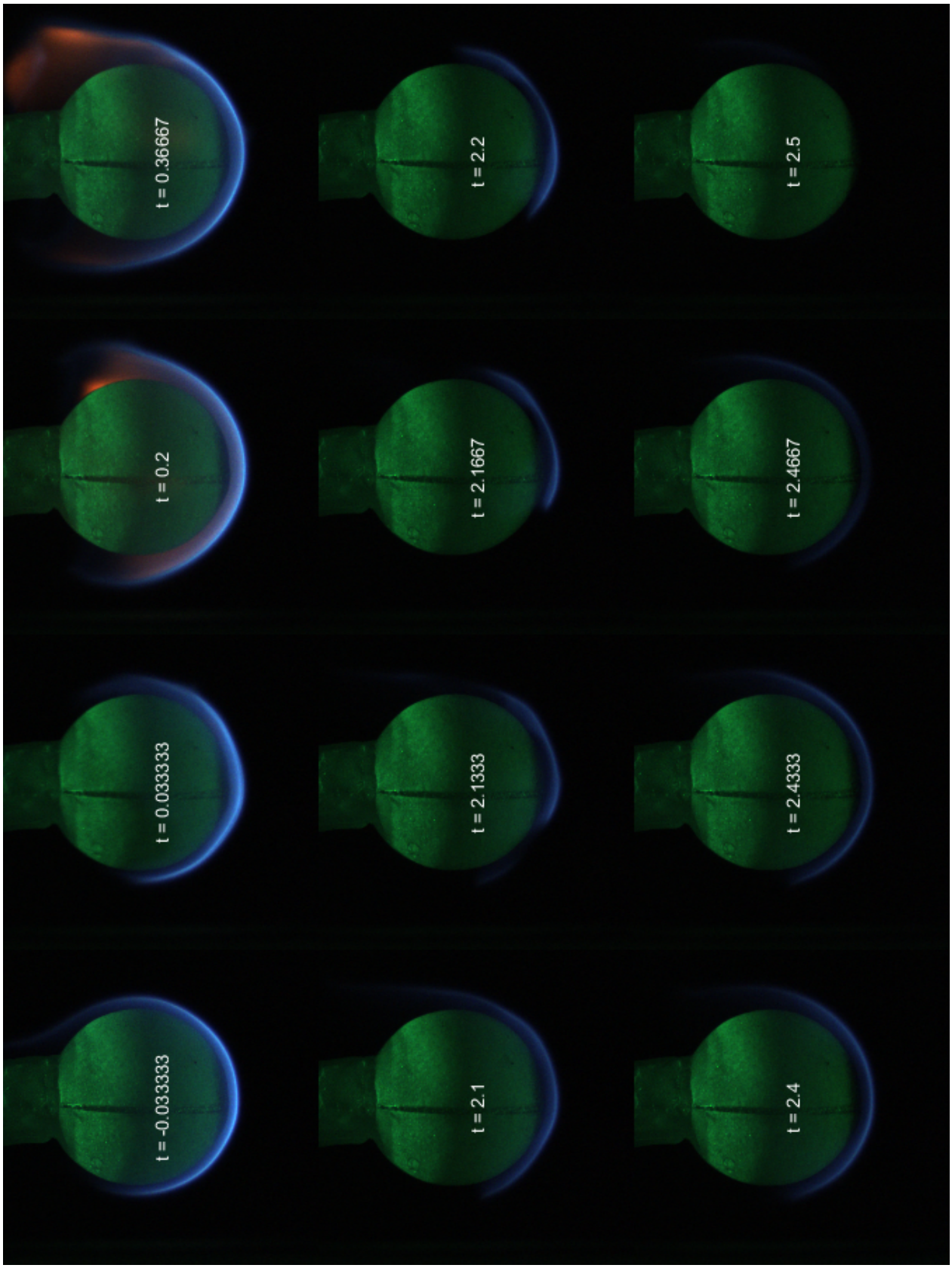

Figure 6.37. Drop Test 8 significant image frames

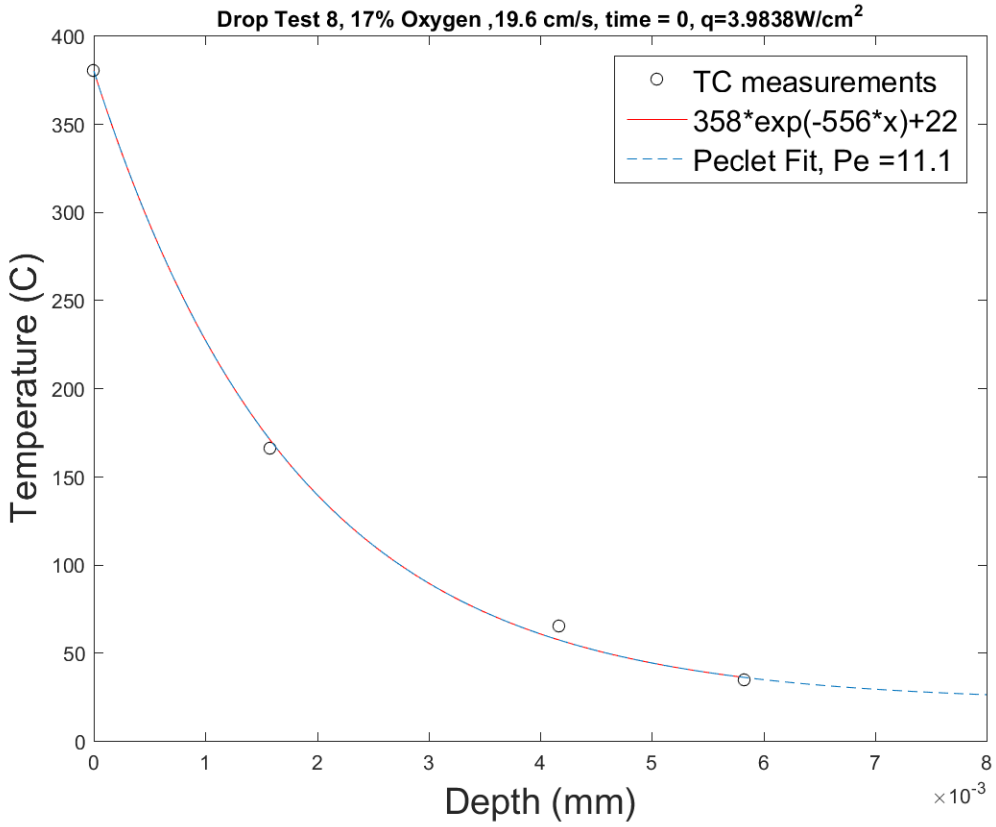

Figure 6.38. Fit of temperature profile at the time of the drop.

Drop Test 9, X-16-146

Drop Test 9 was conducted at the same conditions as Drop Test 6 with a higher level of preheat. Ignition was for 20 seconds in quiescent 21% oxygen concentration by volume. Fresh oxidizer was added to the chamber at 15 cm/s twice during preheating to counteract oxygen depletion in the relatively long preheat. The gas was switched to 17% oxygen by volume and 15 cm/s flow before the drop. The drop was triggered when thermocouple TC1 read 230^oC.

Pre Drop Test #9 thermocouple locations	
TC1	2.469 mm on axis
TC2	2.566 mm on axis
TC3	4.800 mm on axis
Post Drop Test #9 thermocouple locations	
TC1	2.169 mm on axis
TC2	2.266 mm on axis
TC3	4.500 mm on axis

Table 6.10. Thermocouple locations for Drop Test #9.

This test reused sample sphere0002. Thermocouple locations from CT scans are shown in Table 6.10

Test Conditions.

- 15 cm/s flow, $a_b \approx 19s^{-1}$, $a_f \approx 11s^{-1}$
- Ignition in quiescent 21% oxygen by volume starting at -109.39 s
- Started 15 cm/s 17% oxygen flow at -12.66 s
- Dropped when TC1 temperature is 230^oC
- Heat loss to the solid in the stagnation zone the drop time is estimated at $2.32W/cm^2$

Results. After the ignition and growth stage, the full envelope flame on the sphere sample dimmed slowly during preheating due to oxygen depletion in the otherwise quiescent chamber. When fresh oxygen was burped in twice, the flame became so bright it blinded the camera view which was visible in the control room until oxygen depletion allowed the flame to cool again and sooting subsided. When switching to the flow of 17% oxygen at 15 cm/s before the drop, the flame again became dimmer. The flame before the drop can be seen in Fig. 6.41, there is more soot in the downstream wake region of this test than was typically experienced, with more vapor jetting causing some sooting in the stagnation region. In Frame 2, t = 0.033

seconds after the drop was triggered, the flame stand off distance increases and the region between the flame sheet and surface and the downstream wake region between the flame tips became extremely sooty and spotted with very bright yellow regions in a predominantly orange wake because of the vapor jetting of the hot surface material. These bright sooty hot spots propagate downstream and blow off in the wake with the gas flow. The camera shutter speed decreases automatically in response to the bright soot, and Frame 4 and 7 appear dimmer than Frame 3. As heat feedback to the surface decreases in response to the new conditions, the flame becomes blue again by Frame at t=3.03 s. The flame survives the 5.18 second drop.

Figure 6.39 shows the temperature data recorded by the thermocouples and the flow conditions within the Combustion Tunnel. Because of the close proximity of TC1 and TC2, they read very similar temperatures. The thermocouples begin to break and short circuit just after the drop rig impacts the decelerator indicated by the sharp temperature spikes, ending the test. It is less obvious that thermocouple TC3 has also broken. This is more clear in Fig. 6.42 where it would be impossible to match an exponential fit with all of the temperature data points. TC3 data is discarded during the fitting procedure.

The stagnation zone standoff distance can be seen in Fig. 6.42. The stand off in 1 g is about 1.5 mm, and the standoff before extinction is about 2.1 mm.

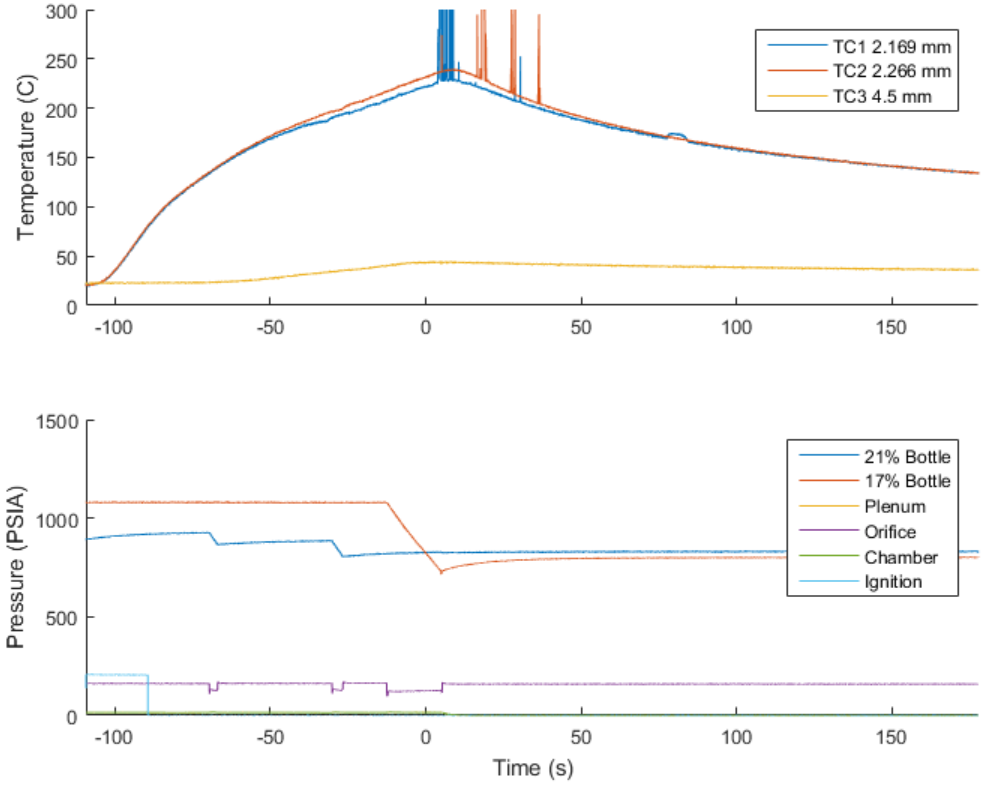

Figure 6.39. Drop Test 9 thermocouple temperature measurements and Combustion Tunnel control parameters.

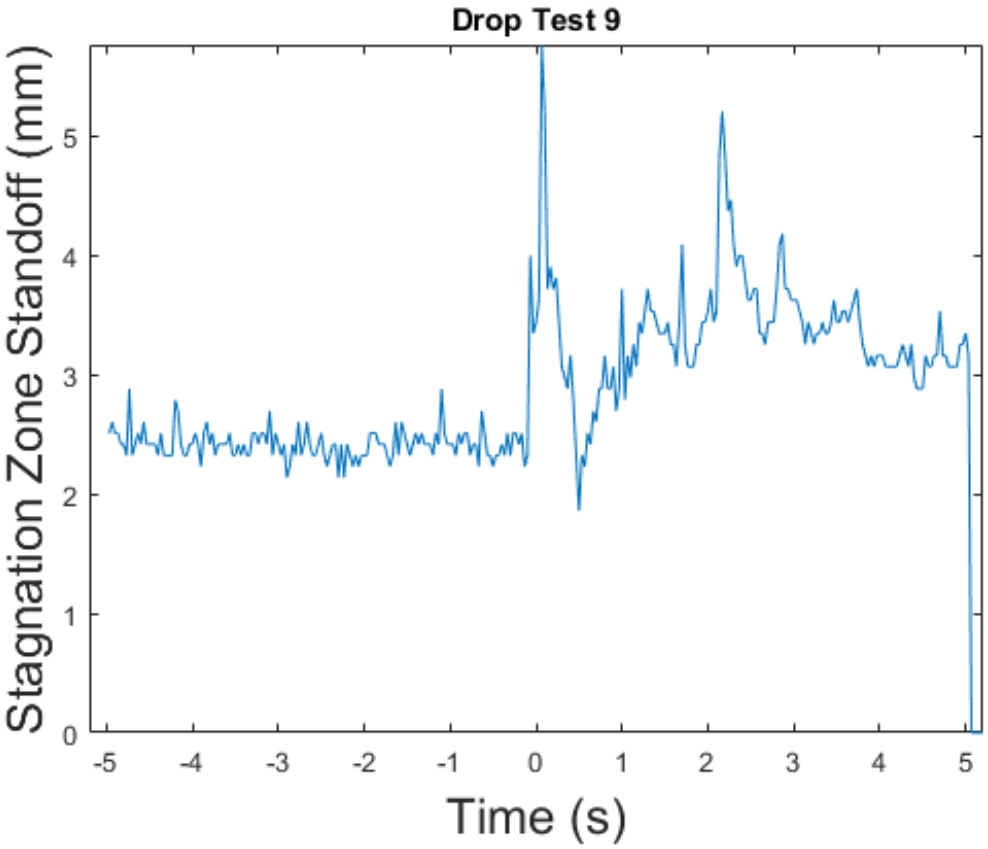

Figure 6.40. Drop Test 9 flame standoff distance and flame sheet thickness.

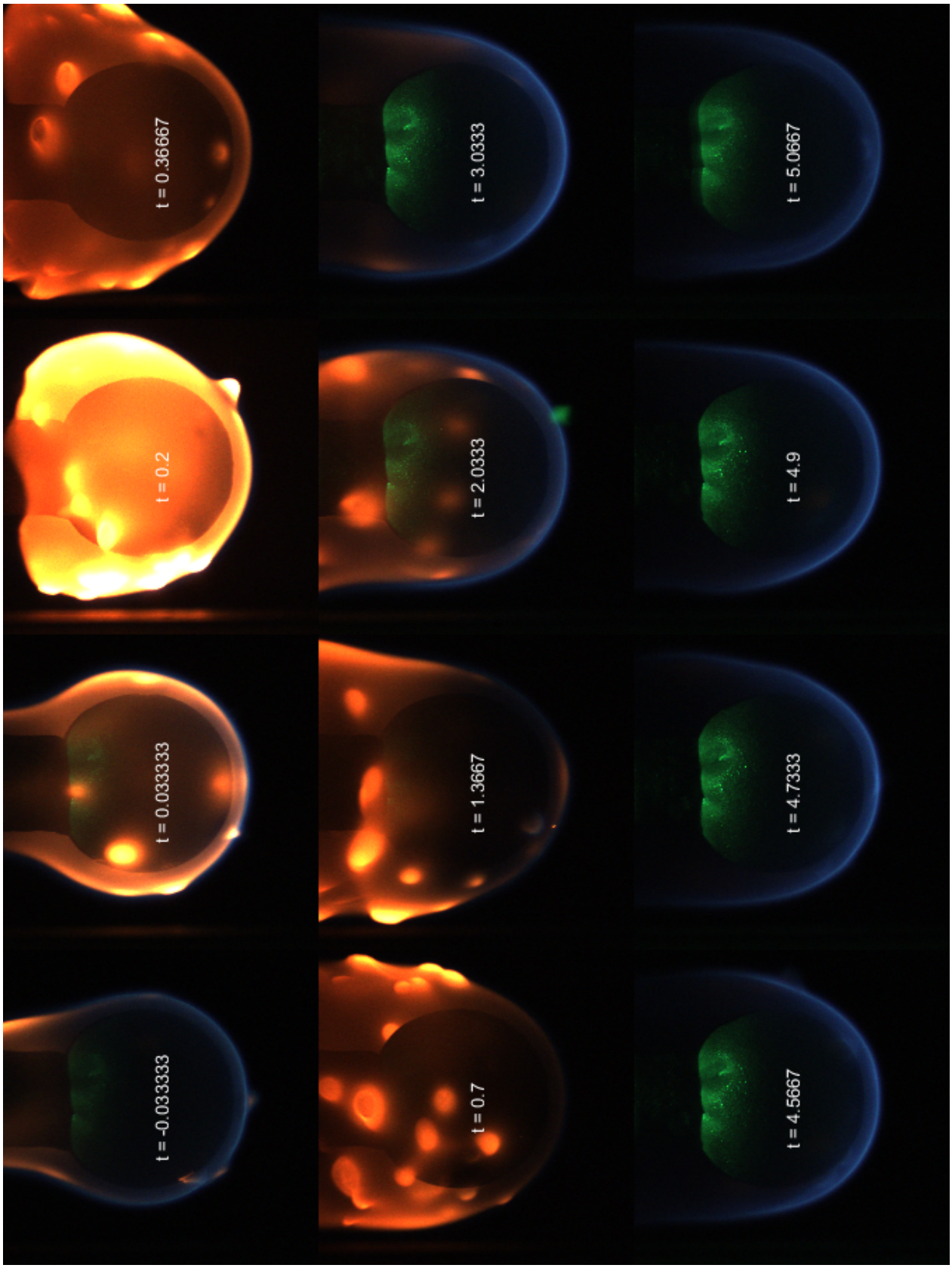

Figure 6.41. Drop Test 9 significant image frames

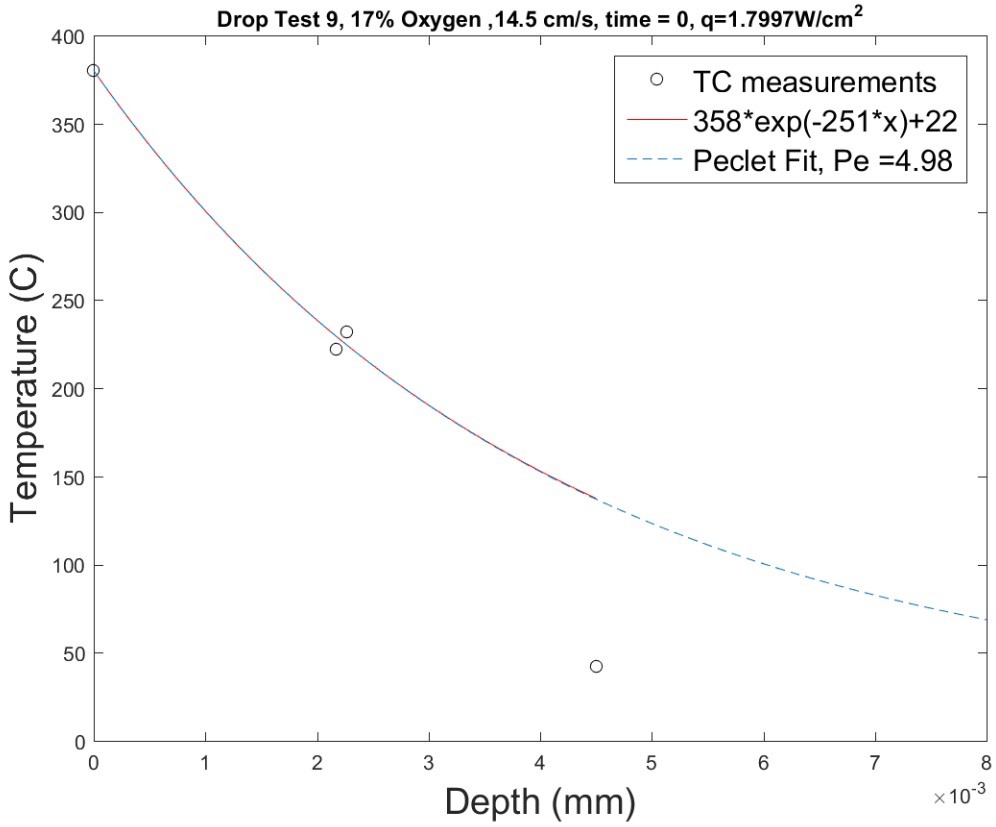

Figure 6.42. Fit of temperature profile at the time of the drop.

Drop Test 10, X-16-147

Drop Test 10 was conducted at the same conditions as Drop Test 4 with a higher level of preheat. Ignition was for 20 seconds in quiescent 21% oxygen concentration by volume. 17% oxygen gas was burped into the quiescent chamber during preheating, but it was not enough to overcome the oxygen consumption by the flame. The flame extinguished and had trouble reigniting. There were a total of 4 ignition cycles to establish the flame before the drop leading to a very high preheating value. After

Pre Drop Test #10 thermocouple locations	
TC1	2.016 mm on axis
TC2	4.006 mm on axis
TC3	6.354 mm on axis
Post Drop Test #10 thermocouple locations	
TC1	1.716 mm on axis
TC2	3.706 mm on axis
TC3	6.054 mm off axis

Table 6.11. Thermocouple locations for Drop Test #10.

reestablishing the flame, 17% oxygen flow at 6 cm/s was set before the drop. The drop was when thermocouple 1 read 283^oC.

This test reused sample sphere0005 and thermocouple locations for CT scans are shown in Table 6.11. All of the thermocouples were damaged, but thermocouples 1 and 2 appear to show an accurate temperature on average despite a large amount of noise.

Test Conditions.

- 6 cm/s flow, $a_b \approx 19s^{-1}$, $a_f \approx 4.5s^{-1}$
- Ignition in quiescent 21% oxygen by volume starting at -200.42 s
- 20 second reignition starting at -90.05 s
- 20 second reignition starting at -68.42 s
- 20 second reignition starting at -30.82 s
- Started 17% O_2 flow at 6 cm/s at -14.15 s
- Dropped when TC1 temperature is 283^oC
- Heat loss to the solid in the stagnation zone the drop time is estimated at $1.30W/cm^2$

Results. This test was ignited in quiescent 21% oxygen by volume, but was switched to 17% oxygen early in the preheating stage. New gas was burped in occasionally,

but oxygen consumption caused the flame to extinguish. The dimming of the flame was a slow process as oxygen was consumed, but extinction was very sudden from the full envelope flame. The igniter was brought back in to reignite as in the previous extinguished tests, however there still was not enough oxygen to reestablish a self sustaining flame without the hot igniter present. 21% oxygen was burped back in, and then the flame was re-established. The gas was switched back to 17% oxygen by volume at 6 cm/s flow before the drop.

Response to the drop was similar to the other high preheat cases (i.e. Drop Test #9). Figure 6.45 Frame 1 shows the established flame at t=-0.33 s before the drop. The blue flame in the stagnation zone is very dim due to the automatic camera shutter speed adjustment from the bright soot in the wake region. After the drop is triggered, the amount of soot increases very quickly in Frame 2. The flame tips then begin to open up between Frame 3 at t=0.2 s and Frame 4 at t=0.37 s. Vapor jetting was intense and marked by very bright circles of soot starting in the stagnation region and propagating downstream with the forced flow. Sooting begins to decrease after Frame 5 at t=0.7 s and the flame becomes blue as the reduced heat feedback decreases the excess pyrolyzate. The flame tip on the right side of the sphere at t=3.7 s retreats slightly, but the flame remains stable with continued waviness from fuel jetting from the surface. The flame survived the 5.18 s drop.

Figure 6.44 shows an initial flame standoff distance of about 1.6 mm in 1 g. The flame reaches a standoff distance of about 3.5 mm by the end of the drop, but it is unknown if this would be the psuedosteady value, due to the limited about of time in microgravity.

Figure 6.43 shows the temperature data recorded by the thermocouples and the gas flow conditions within the Combustion Tunnel. Thermocouple TC3 is known to have failed completely. Thermocouples TC1 and TC2 exhibit a lot of noise marked as sharp upward spikes throughout the test, but it is assumed that they are still reading the correct temperatures on average. The exponential fit temperature curve is plotted with the temperature data at the time of the drop in Fig. 6.46, and shows good agreement when discarding thermocouple TC3.

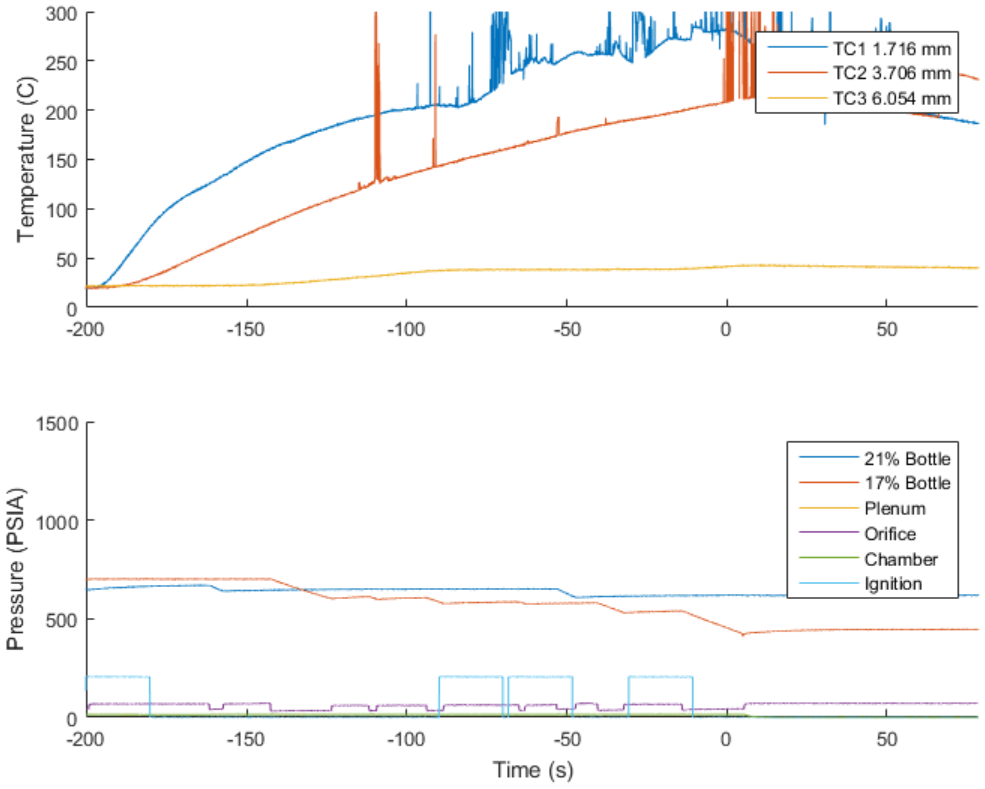

Figure 6.43. Drop Test 10 thermocouple temperature measurements and Combustion Tunnel control parameters.

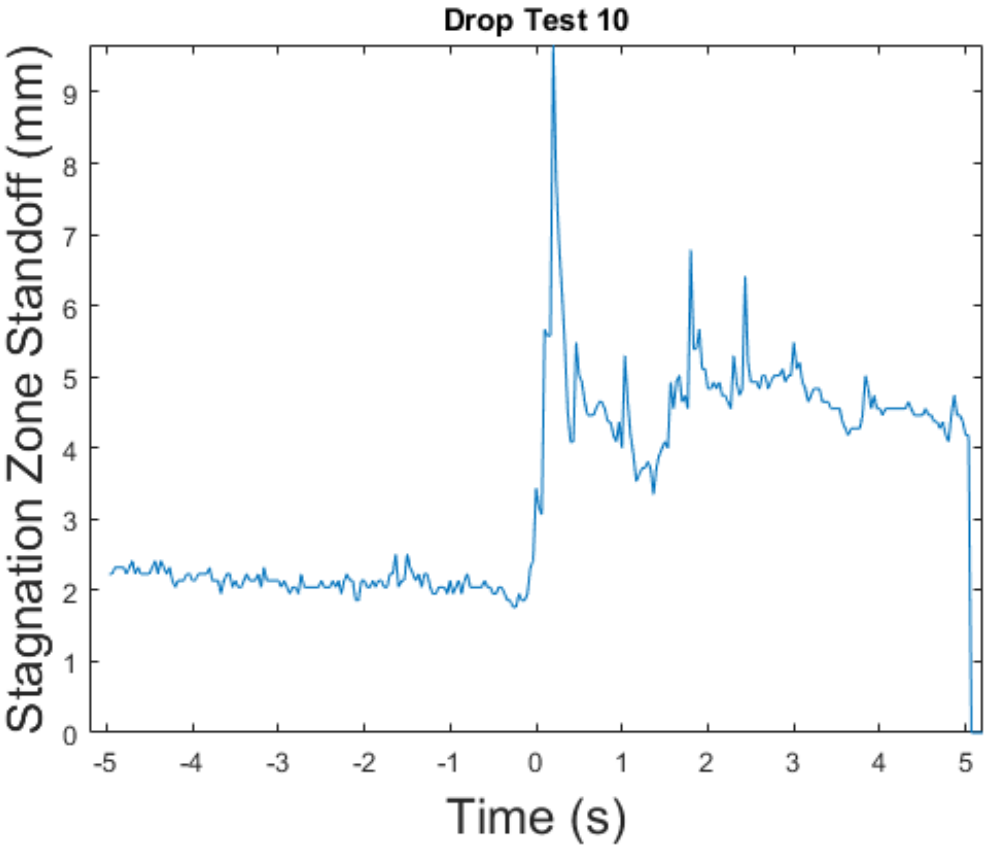

Figure 6.44. Drop Test 10 flame standoff distance and flame sheet thickness.

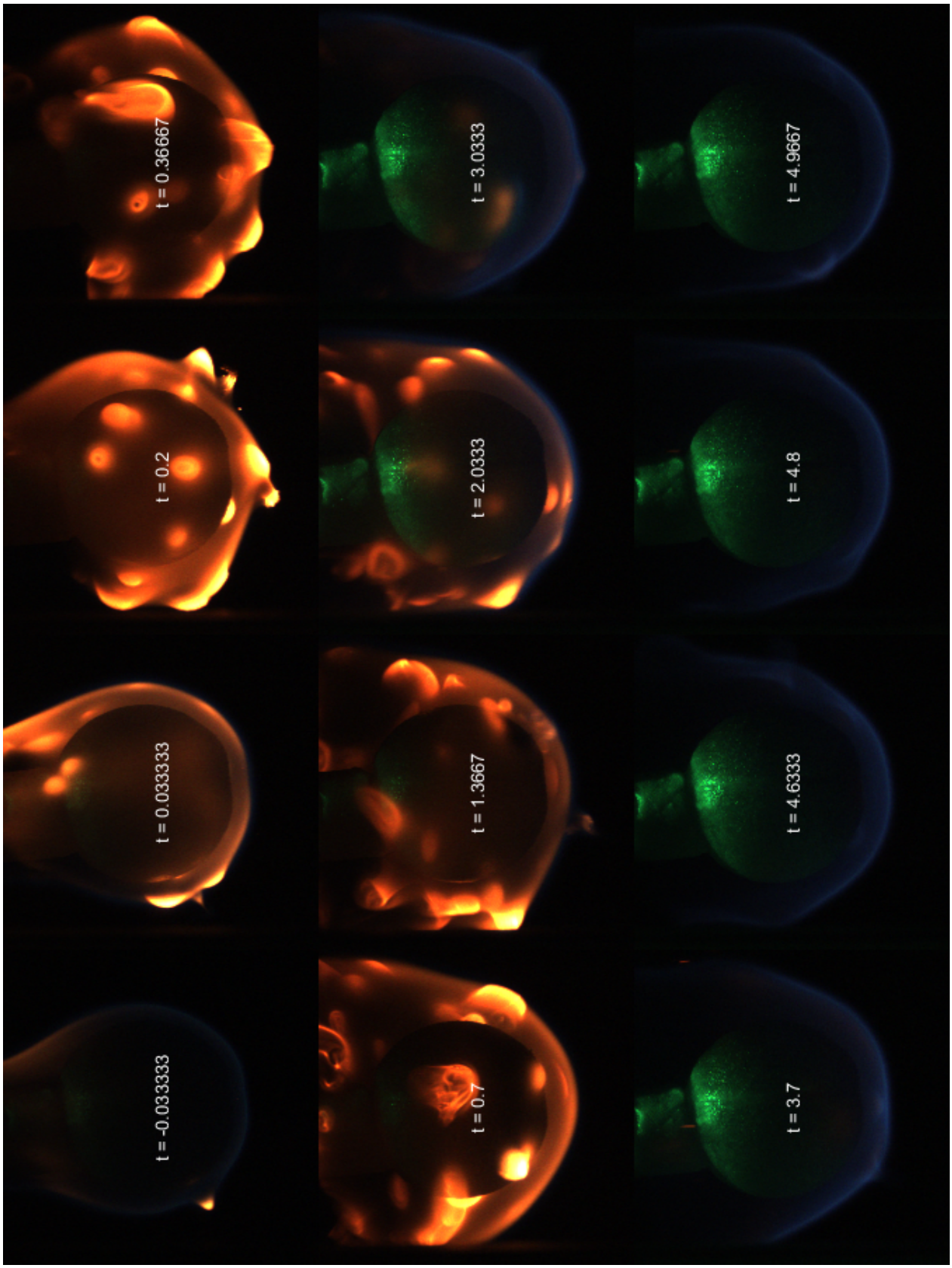

Figure 6.45. Drop Test 10 significant image frames

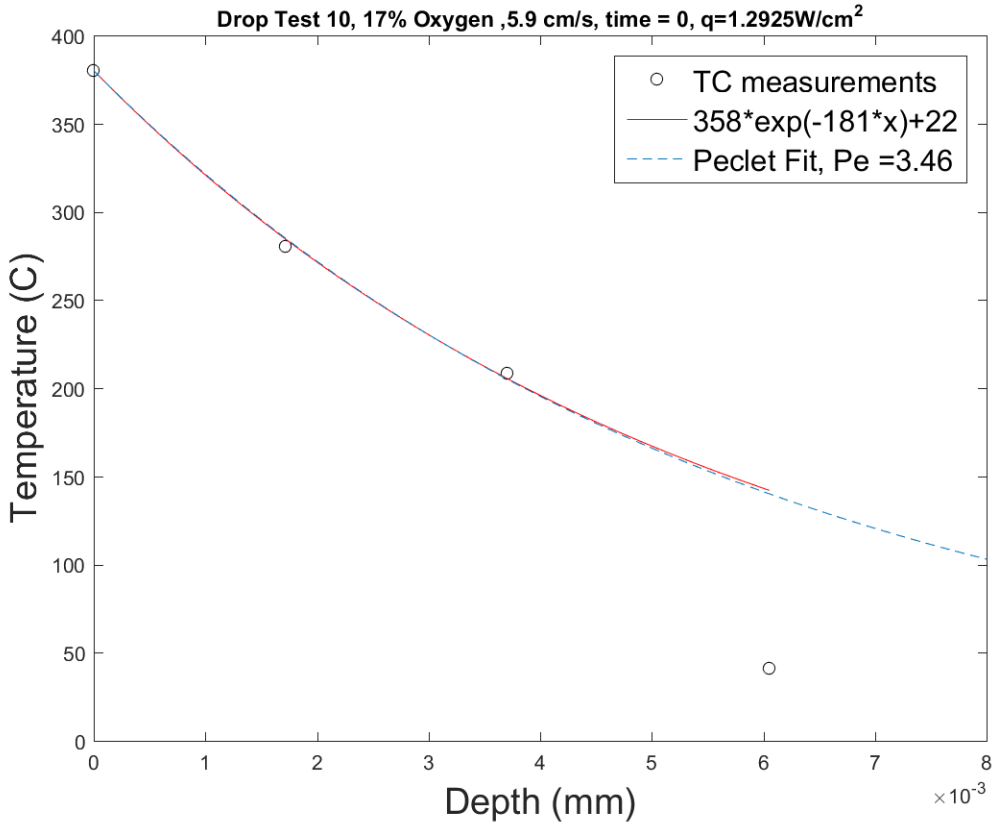

Figure 6.46. Fit of temperature profile at the time of the drop.

Drop Test 11, X-16-148

Drop Test 11 was intended to be run at heat loss conditions between Drop Test 4 and 10 and as a companion test to Drop Test 2, which was conducted at a lower stretch rate, to help narrow down the flammability boundaries. The test was ignited for 20 seconds in quiescent 21% oxygen by volume. Fresh oxygen was burped into the chamber a few times during preheating. The gas was switched to 17% oxygen at 6 cm/s before the drop. The drop was triggered when thermocouple TC1 read 252^oC.

Pre Drop Test #11 thermocouple locations	
TC1	1.579 mm on axis
TC2	5.205 mm on axis
TC3	6.773 mm on axis
Post Drop Test #11 thermocouple locations	
TC1	0.837 mm on axis
TC2	3.518 mm on axis
TC3	5.057 mm on axis

Table 6.12. Thermocouple locations for Drop Test #11.

The test reused sample sphere0003. The thermocouple locations from CT scans before and after the test are shown in Table 6.12.

Test Conditions.

- 6 cm/s flow, $a_b \approx 19s^{-1}$, $a_f \approx 4.5s^{-1}$
- Ignition in quiescent 21% oxygen by volume starting at -82.94 s
- Started 17% O_2 at 6 cm/s at -35.74 s
- Dropped when TC1 temperature is 252^oC
- Heat loss to the solid in the stagnation zone the drop time is estimated at $1.98W/cm^2$

Results. A bright sooty full envelope flame was established over the entire sphere in quiescent 21% oxygen, after switching to 17% oxygen by volume, the flame dimmed and turned blue in color except some orange streaks in the wake region before the drop. The pre-drop flame can be seen in Fig. 6.49 Frame 1 at t=-0.03 s before the drop. Some light orange sooting can already be seen in Frame 2 at t=0.03 s after the drop. The standoff distance then increased with high sooting between the flame sheet and material surface in Frames 3 and 4. As the flame sheet relaxed back towards the surface, vapor jet bubbles bulged through the flame sheet and propagated downstream as bright orange sooty spots as seen in Frame 5 at t=0.7 s. As sooting subsided, the

vapor jets became visible as blue ripples in the flame sheet. The flame survived the 5.18 second drop.

Figure 6.47 shows the temperature data recorded by the thermocouples and the flow conditions within the Combustion Tunnel. Thermocouple TC3 is again expected to have broken in the previous test. The exponential temperature profile is plotted against the known experimental temperatures in Fig. 6.50. Discarding thermocouple TC3 data leads to an acceptable fit.

Figure 6.48 shows the stagnation flame standoff distance of about 1.4 mm in 1 g and about 3.1 mm by the end of the drop.

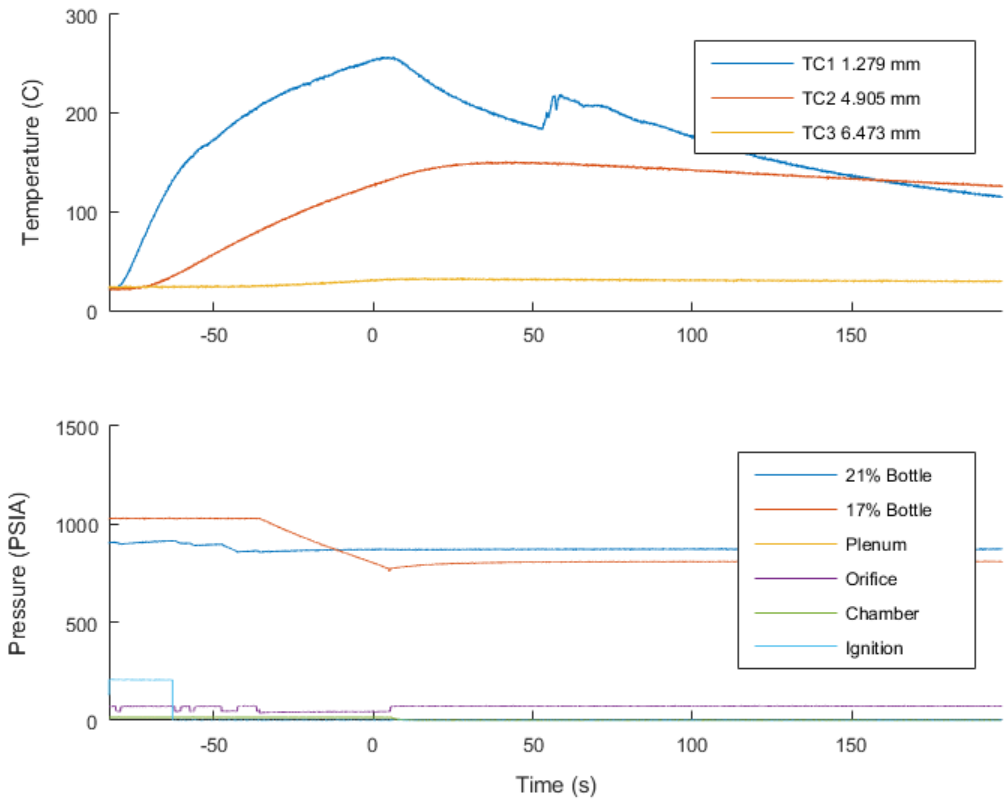

Figure 6.47. Drop Test 11 thermocouple temperature measurements and Combustion Tunnel control parameters.

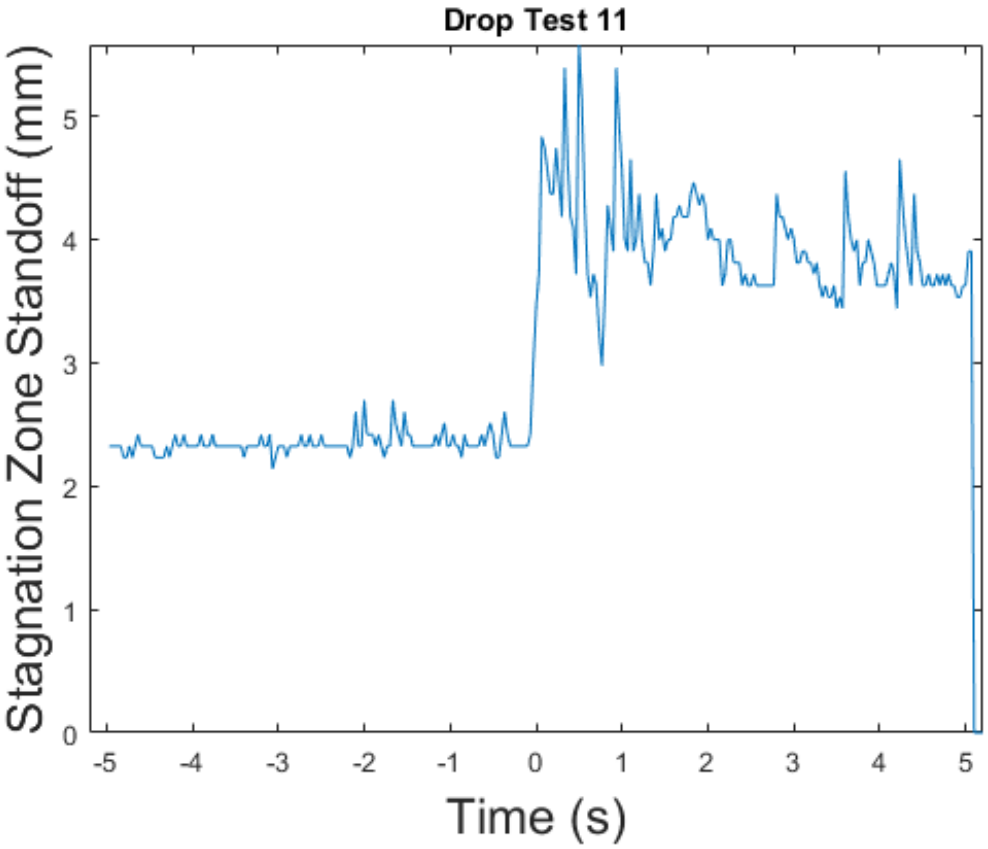

Figure 6.48. Drop Test 11 flame standoff distance and flame sheet thickness.

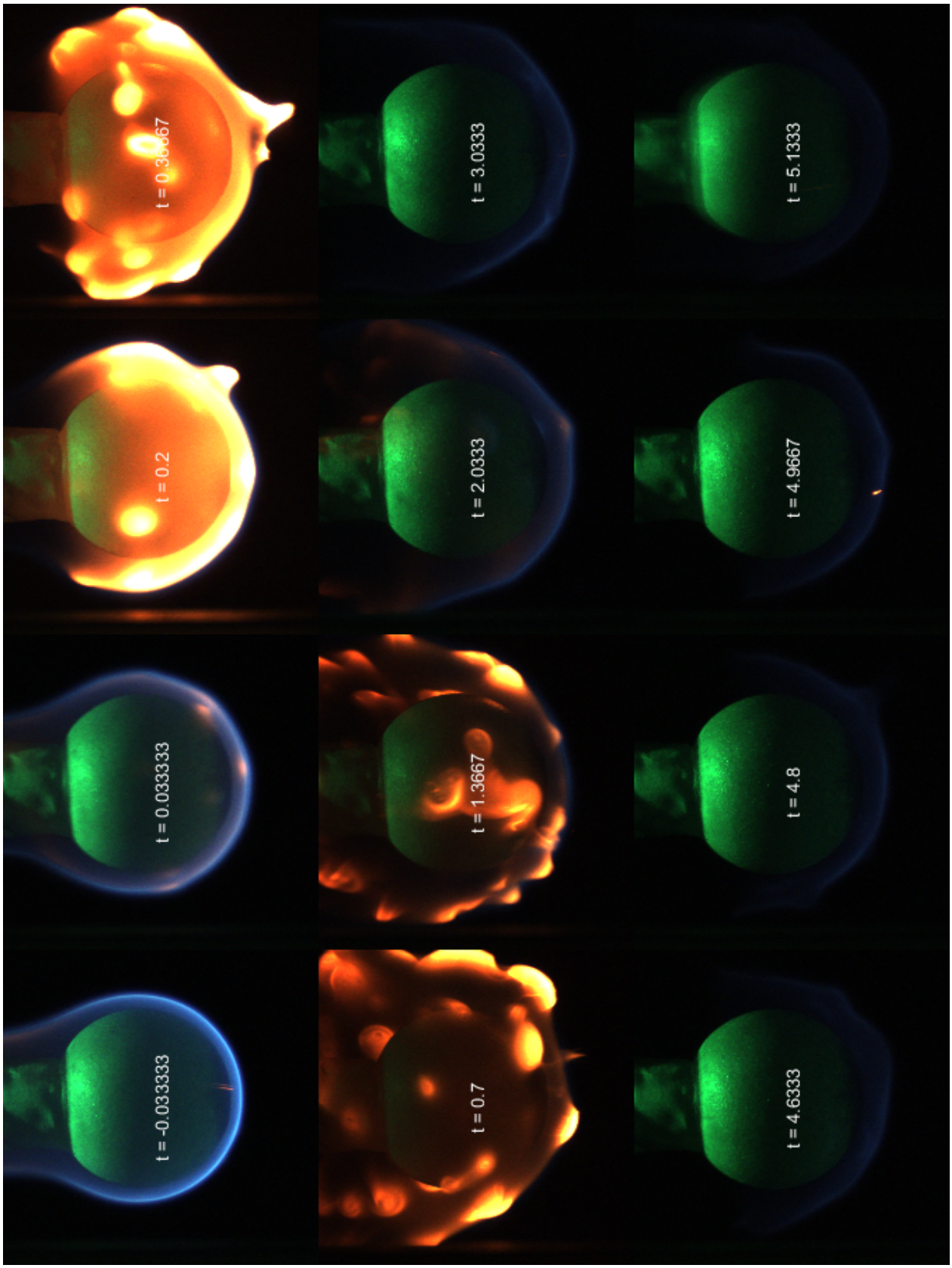

Figure 6.49. Drop Test 11 significant image frames

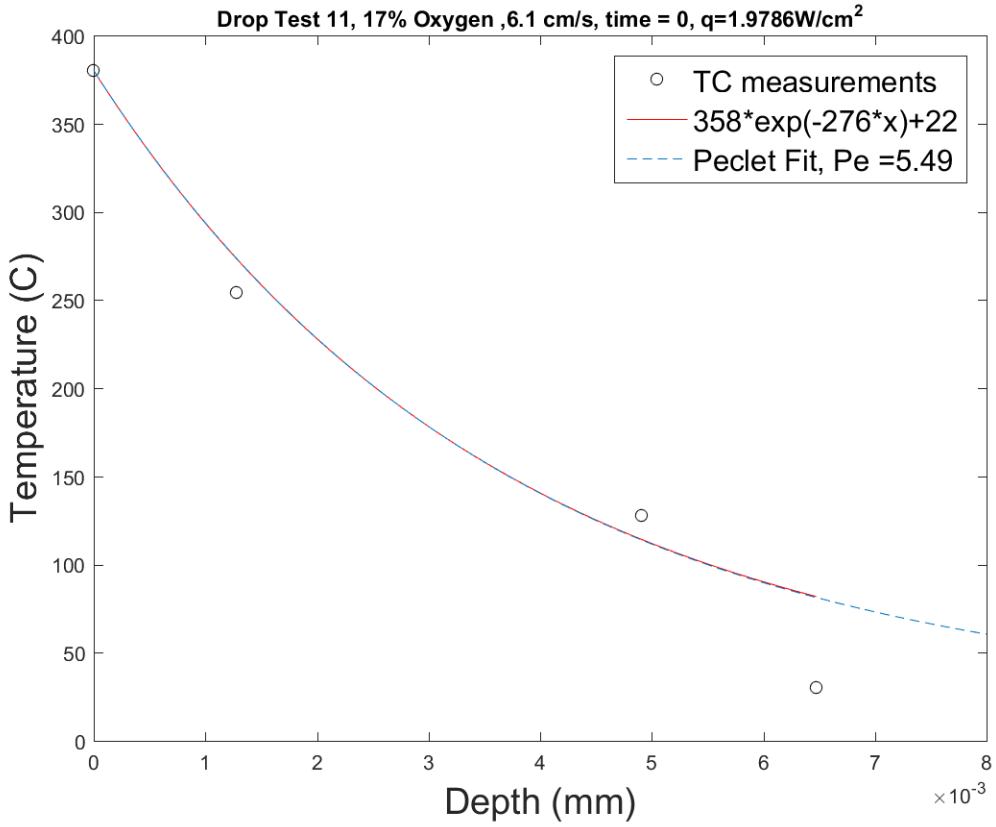

Figure 6.50. Fit of temperature profile at the time of the drop.

Drop Test 12, X-16-149

Drop Test 12 was conducted at 17% oxygen by volume at 4 cm/s. Ignition was for 20 seconds in quiescent 21% oxygen concentration by volume. The gas was changed to 17% oxygen by volume at 4 cm/s before the drop. The drop was triggered when thermocouple 1 reached 185^oC.

The test reused sample sphere0004. Thermocouple locations from CT scans are shown in Table 6.13.

Pre Drop Test 12 thermocouple locations	
TC1	2.249 mm on axis
TC2	4.914 mm on axis
TC3	6.859 mm on axis
Post Drop Test 12 thermocouple locations	
TC1	2.090 mm on axis
TC2	4.294 mm on axis
TC3	6.334 mm on axis

Table 6.13. Thermocouple locations for Drop Test #12.

Test Conditions.

- 17% Oxygen at 4 cm/s flow, $a_b \approx 19s^{-1}$, $a_f \approx 3s^{-1}$
- Ignition in quiescent 21% oxygen by volume starting at -64.86 s
- Switched to 17% oxygen at 4 cm/s at -32.46 s
- Dropped when TC1 temperature is 185^oC
- Heat loss to the solid in the stagnation zone the drop time is estimated at $2.89W/cm^2$

Results. The image sequence displayed in Fig. 6.53 looks very similar to the the sequence in Drop Test 11. A full envelope flame is established in Frame 1 at t=-0.033 s before the drop, with some sparking and vapor jetting in the stagnation zone, and some soot developing in the wake region. The standoff distance begins to increase in Frame 2 at t=0.033 seconds after the drop and continues moving outward until Frame 6 at 0.7 s. Sooting increases between the flame sheet and sample surface and vapor jetting increases across the sphere surface. After Frame 6, the sooting blows off downstream and the flame turns blue. Waviness continues in the upstream region because of vapor jetting. The flame survives the 5.18 second drop.

Figure 6.51 shows the temperature measurements recorded by the thermocouples and the flow conditions within the Combustion Tunnel. It is unclear whether thermocouple TC3 (shown in yellow) is responding correctly due to the extreme depth of 6.559 mm. The exponential fit temperature profile is shown in Fig. 6.54 with the known experimental temperature points.

Figure 6.52 shows the stagnation zone flame standoff distance measurements of about 1.3 mm in 1 g and around 3.2 mm near the end of the available drop time.

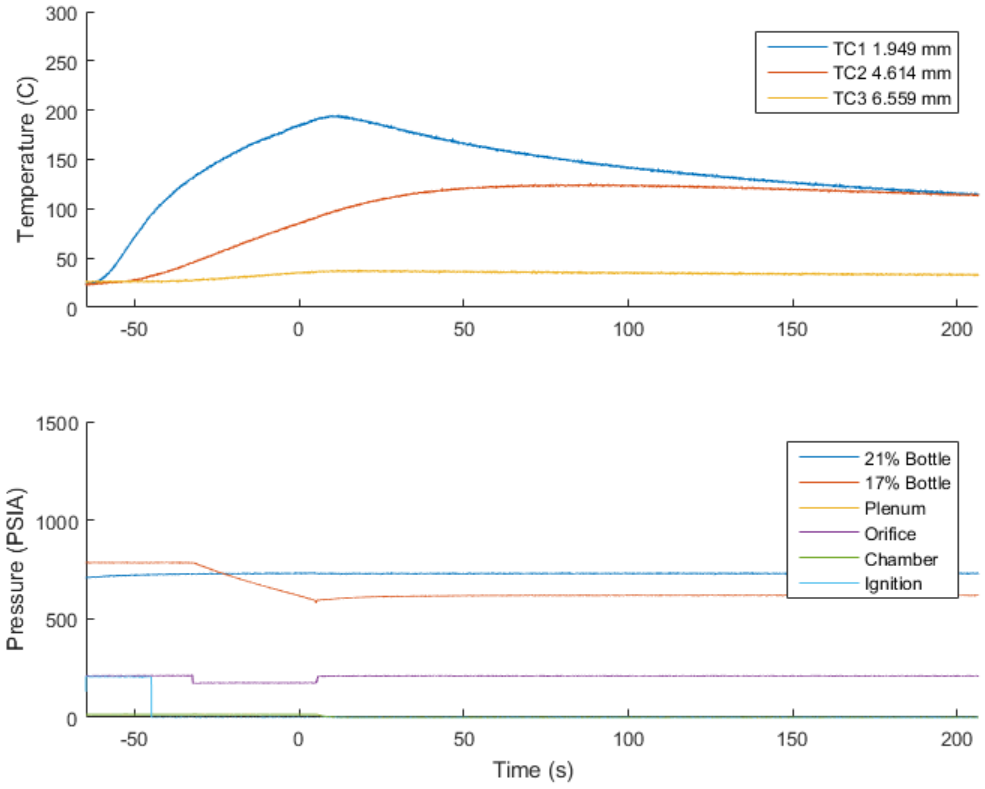

Figure 6.51. Drop Test 12 thermocouple temperature measurements and Combustion Tunnel control parameters.

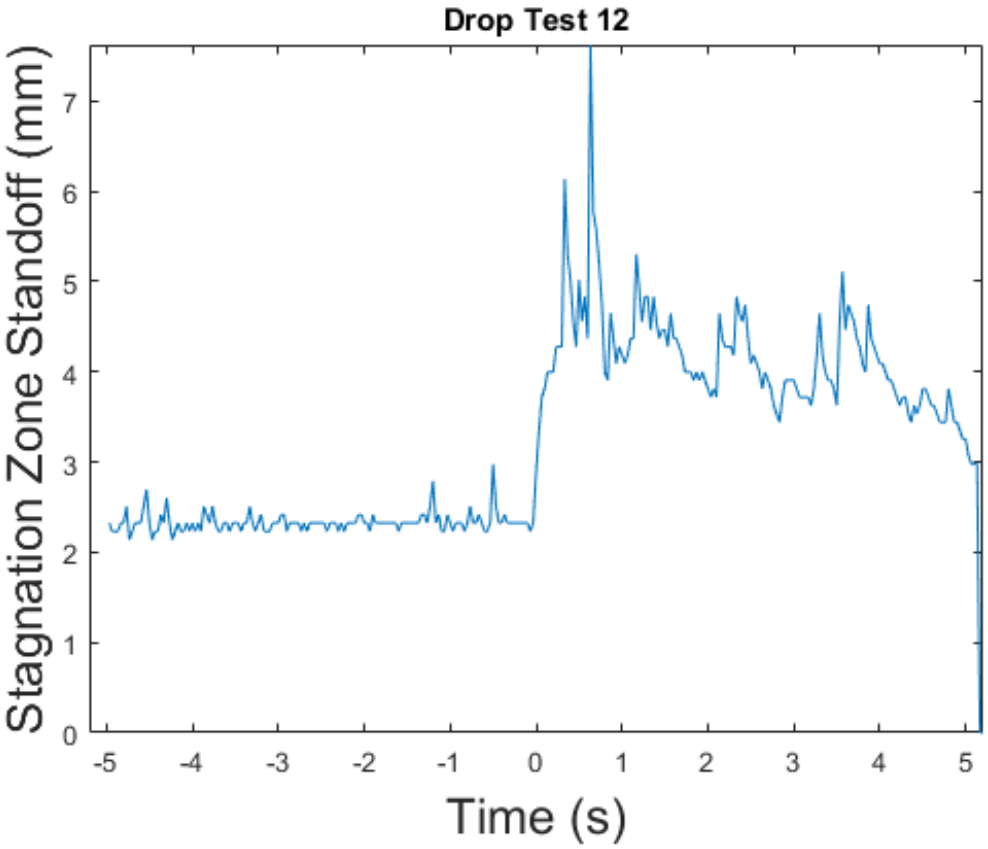

Figure 6.52. Drop Test 12 flame standoff distance and flame sheet thickness.

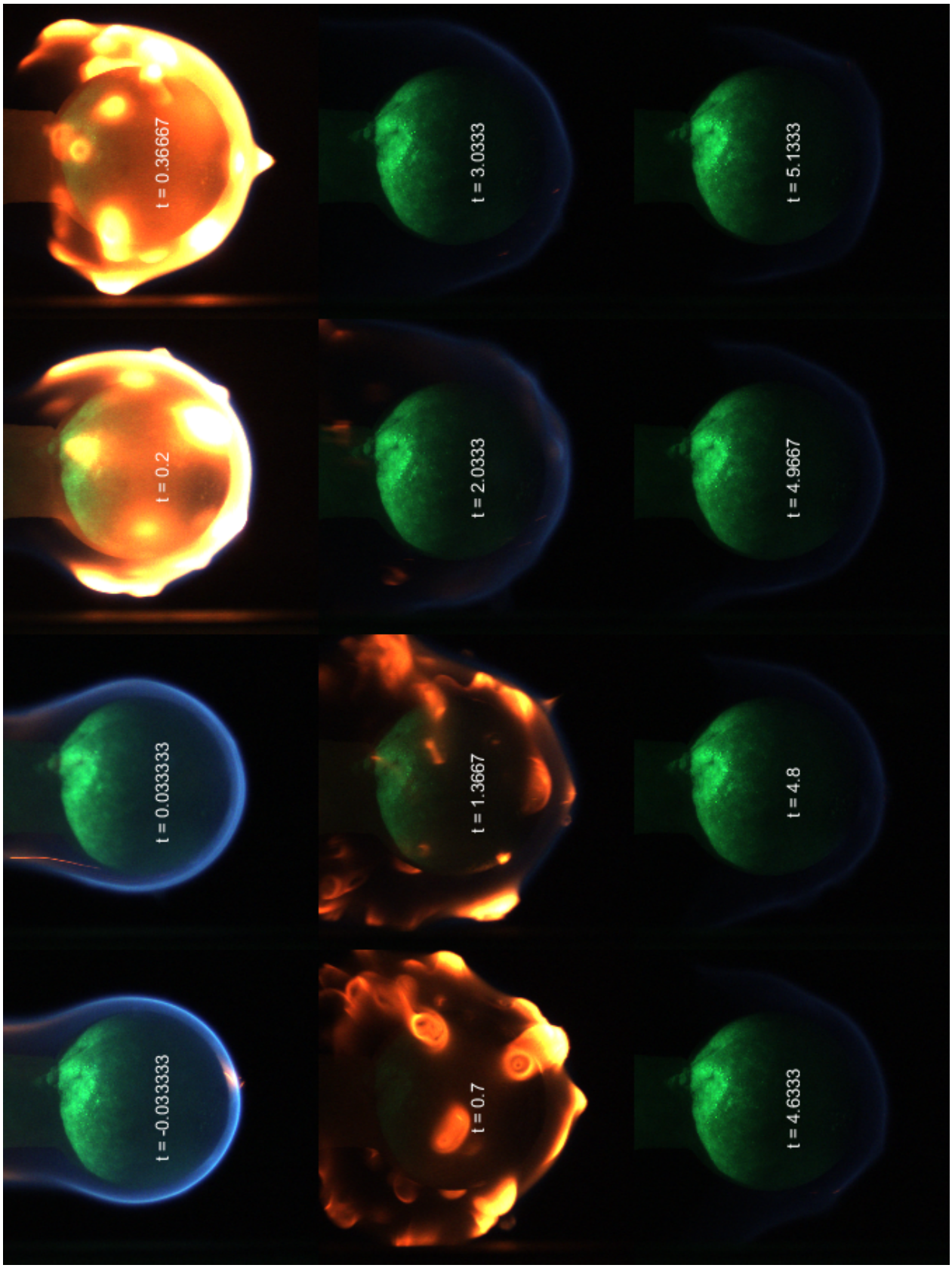

Figure 6.53. Drop Test 12 significant image frames

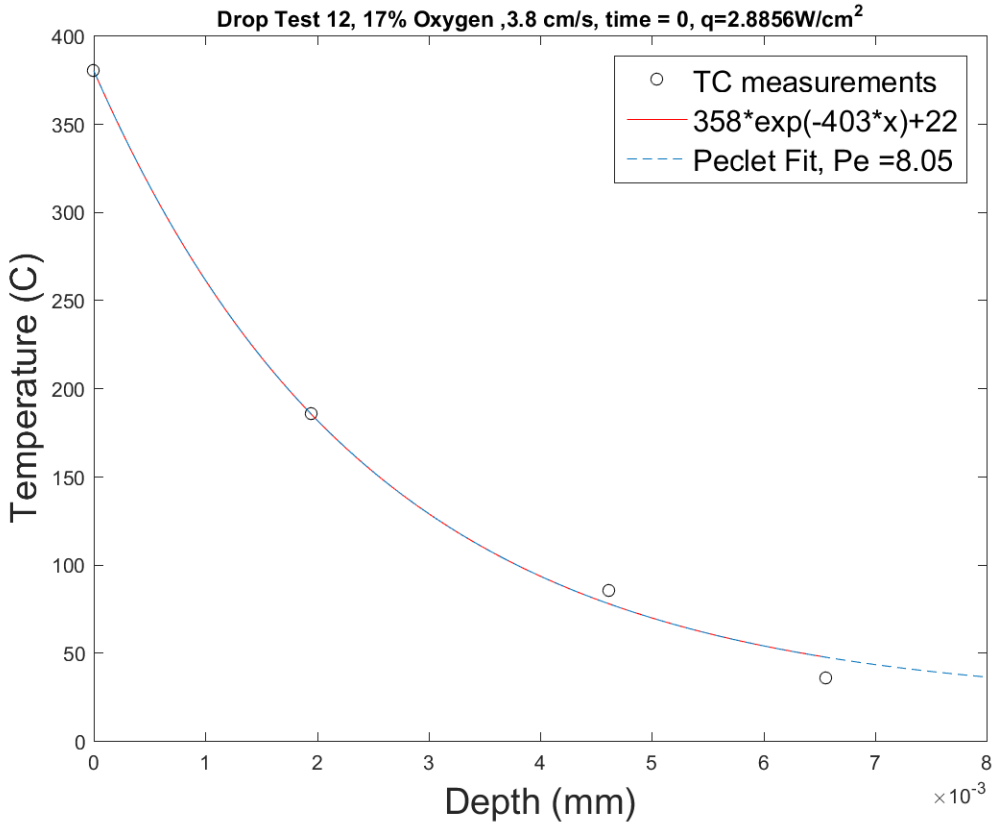

Figure 6.54. Fit of temperature profile at the time of the drop.

Drop Test 13, X-16-150b

The igniter circuit failed in Drop Test 13 due to cumulative damage from overloading the current limit of the circuit (facility's test number X-16-150a). Repairs were made and Drop Test 13 was reset as X-16-150b. The test was planned to be at a high level of preheating. Because of previous thermocouple failures due to heat, the downstream support tube was insulated with a layer of ceramic foam and an outer coating of black anodized aluminum foil to reflect thermal radiation and minimize stray visible light reflection.

Pre Drop Test 13 thermocouple locations	
TC1	2.090 mm on axis
TC2	4.294 mm on axis
TC3	6.334 mm on axis
Post Drop Test 13 thermocouple locations	
TC1	1.790 mm on axis
TC2	3.994 mm on axis
TC3	6.034 mm on axis

Table 6.14. Thermocouple locations for Drop Test #13.

Ignition was for 20 seconds in quiescent 21% oxygen concentration by volume. Fresh oxygen was burped in occasionally throughout the preheating. The gas was switched to 17% oxygen concentration at 2 cm/s flow before the drop. The drop was triggered when thermocouple 1 reached 280^oC.

Test Conditions.

- 17% oxygen, 2 cm/s flow, $a_b \approx 19s^{-1}$, $a_f \approx 1.5s^{-1}$
- Ignition in quiescent 21% oxygen by volume starting at -111.43 s
- Changed to 17% oxygen by volume at 2 cm/s at -37.89 s
- Dropped when TC1 temperature is 280^oC
- Heat loss to the solid in the stagnation zone the drop time is estimated at $1.54W/cm^2$

Results. Figure 6.57 shows the significant image frames during the drop test. This test was very different in appearance compared to the other drop tests because of the very slow forced flow and very high level of preheating. In Frame 1, after the change to 17% oxygen at 2 cm/s in 1g, the flame was bluish purple with light orange streaks starting at the stagnation zone and extending to the wake. An orange color propagates around as a sort of wave in the blue flame in the stagnation region. Occasional sparking is present from vapor jetting. In Frame 2 at t=0.033 s after the drop was

triggered, the flame standoff distance increases with the increase in sooting between the flame sheet and surface. Vapor jetting protrudes through the flame sheet increasing measurable stand off distance by about 50% intermittently. The flame sheet itself is difficult to define as the sheet thickness is very thick and wavy in nature. After Frame 5, as the sheet relaxes back towards the surface it begins pulsing. After the flame tips retreat to around the equator of the sphere, a slow deflagration reignites the downstream wake and then blows off. Just after this occurs, the flame in the stagnation region begins to extinguish on one side of the sphere. Impact occurs just before the flame extinguishes completely. This is marked on Figure 6.59 as an extinction case as this flame is not expected to be self sustaining and likely would have died if one more frame of video was available.

Figure 6.55 shows the temperatures measured by the thermocouples and the flow conditions in the Combustion Tunnel throughout the test. Thermocouple TC2 seems to have broken during the test, exhibiting large unexplained peaks in temperature before the drop. Discarding thermocouple TC2, the exponential temperature profile fit is shown in Fig. 6.58 plotted against the known temperatures.

Figure 6.56 shows the measured stand off distance of about 1.45 mm in 1 g. It is difficult to determine an accurate standoff distance in 0 g since the vapor jetting is so prevalent. The maximum flame standoff from a vapor jet bursting goes to 10.78 mm from the solid surface, but this is by no means steady and the flame position can best be described as fluid.

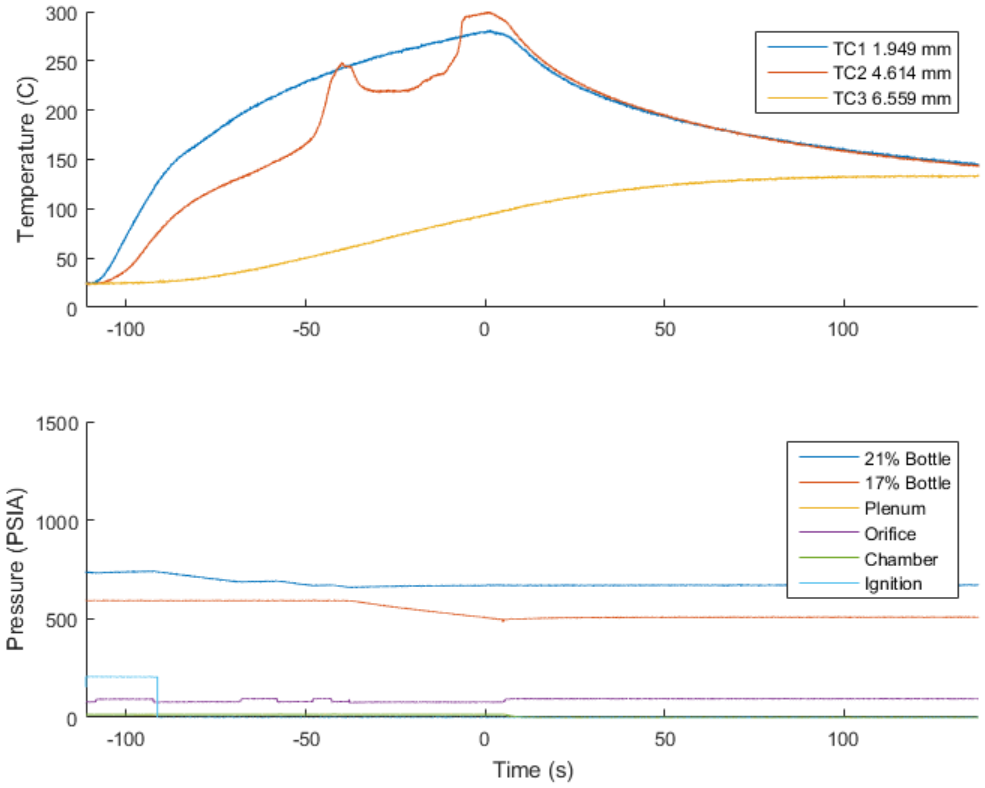

Figure 6.55. Drop Test 13 thermocouple temperature measurements and Combustion Tunnel control parameters.

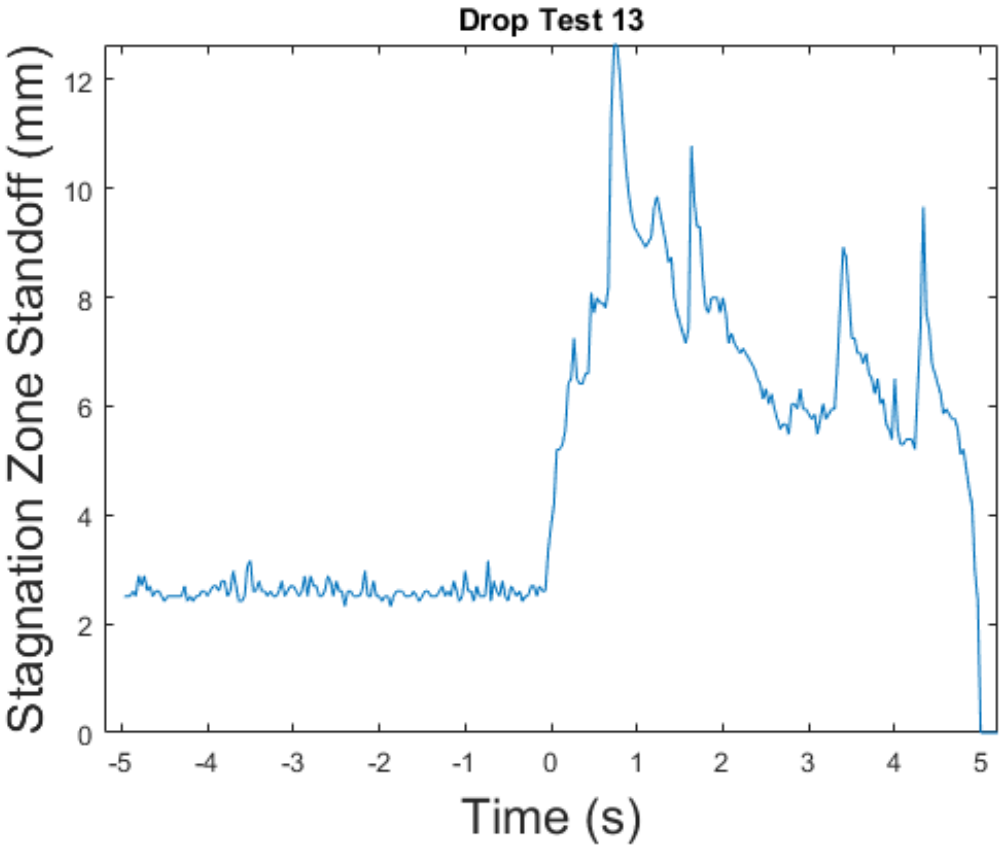

Figure 6.56. Drop Test 13 flame standoff distance and flame sheet thickness.

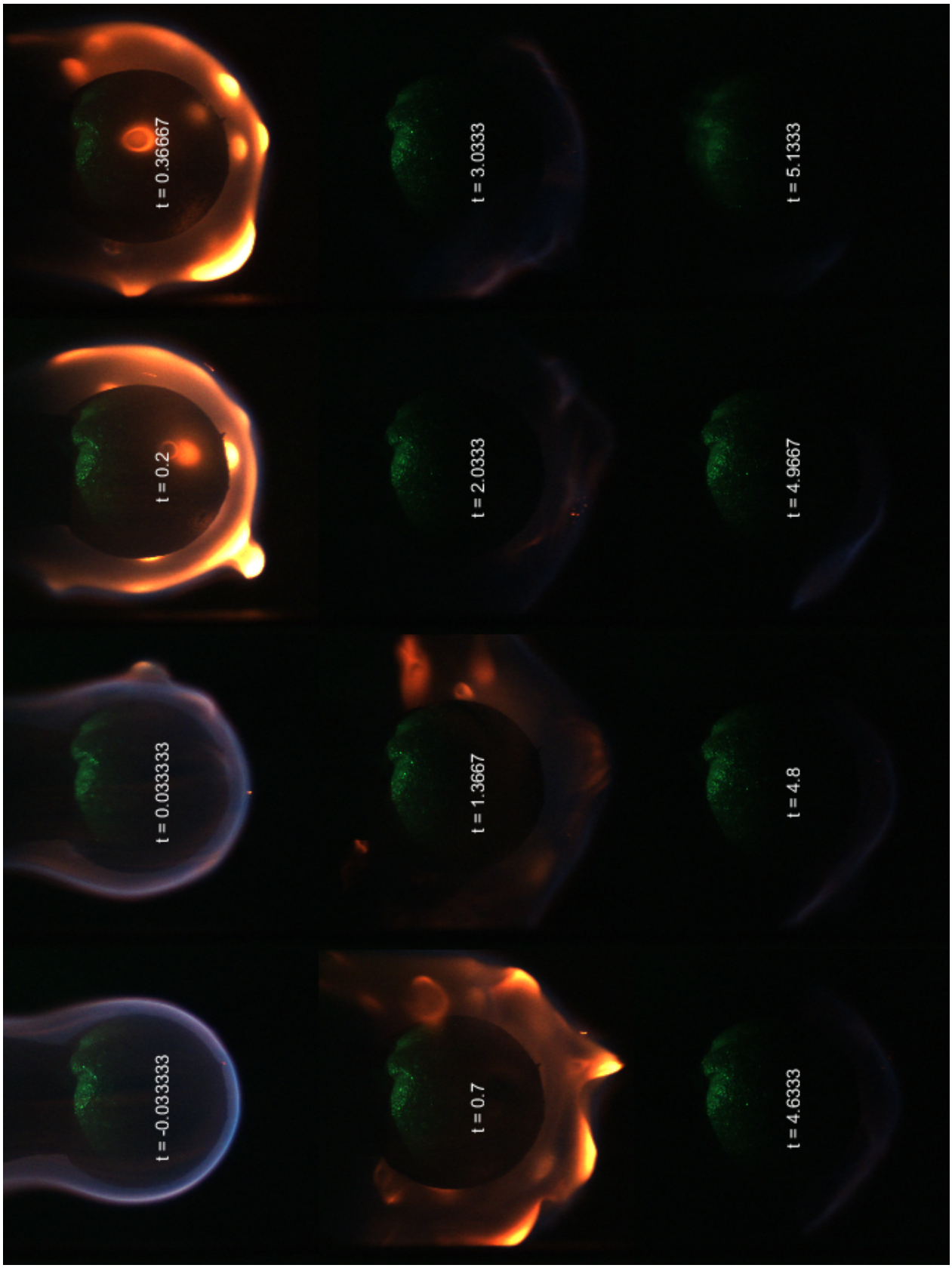

Figure 6.57. Drop Test 13 significant image frames

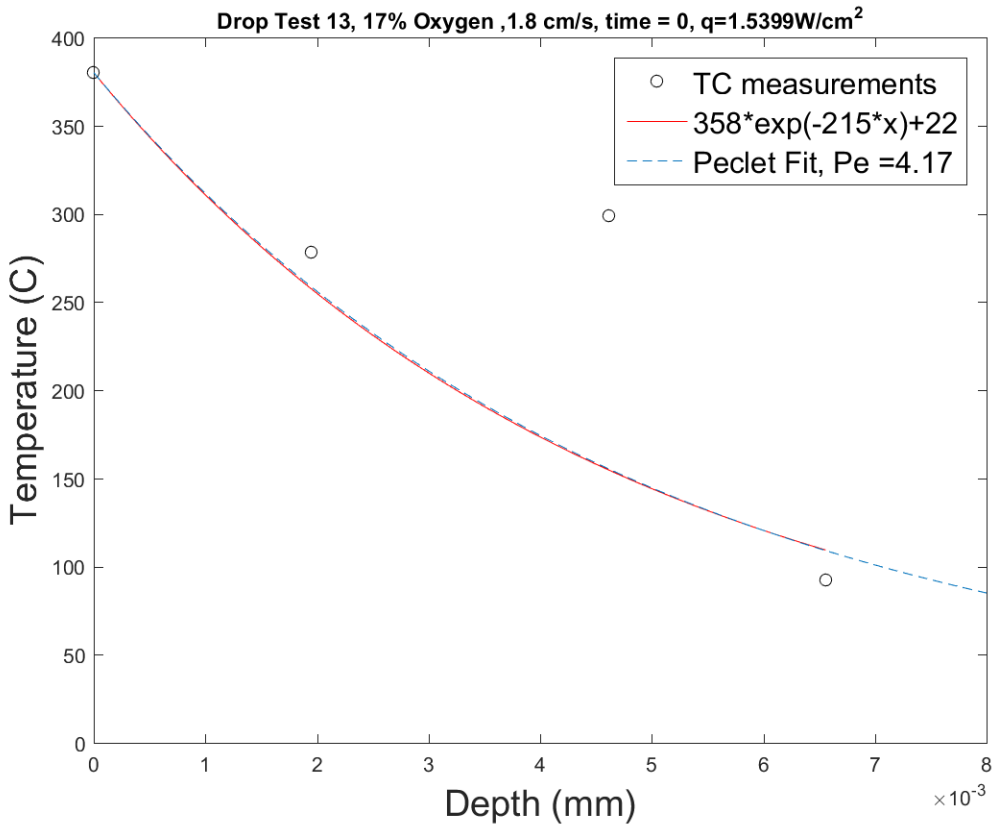

Figure 6.58. Fit of temperature profile at the time of the drop.

6.4 Discussion

The drop test campaign is summarized in Table 6.15 which tabulates the independent test parameter of *Freestream Velocity* and the measured test parameter of *Heat Loss to Solid*. Other vital measurements are shown in the table including *buoyant standoff distance*, *peak standoff distance* after the drop is initiated, *peak time* when peak standoff occurs, *final standoff distance*, defined as the last trackable flame standoff distance either before self extinguishment or before the end of the drop, and the

Extinction Time is listed in the final column, with an *X* if the flame survives the 5.18 second drop.

6.4.1 Extinction Boundary

Figure 6.59 charts the heat loss to the solid interior, as estimated by the spacial derivative of an exponential temperature fit at the surface with respect to depth, and stagnation region stretch rate estimated from the purely forced free stream velocity. Alternatively, the x-axis can be considered to be the free stream flow velocity in the purely forced environment by reversing the expression for forced stretch rate. The surviving cases are plotted as filled circles and the cases which extinguished in the 5.18 seconds of zero gravity are plotted as open circles.

An approximate qualitative flammability boundary was superimposed over the graph which separates the surviving and extinction cases. There are not enough near limit cases to enable a more precise termination of the boundary, but it must lay between the two types of data points. This flammability map says little about the ability of the solid to hold a flame in a steady state, it only suggests that in this snap shot of conditions, i.e. flow velocity (stretch rate) and heat loss to the interior, the flame either can or can not survive for 5.18 seconds.

The Drop Test 13 flame survived the drop time. However, due to the extremely small size of the flame and its position outside of the stagnation zone, this point was marked as an extinction case. It was expected to extinguish if one more frame of video was available.

The slope of the flammability map between a stretch of 5 and 20 is not well established and is plotted here only for demonstration. More test points are needed

in this range of stretch. A purely forced flow stretch rate of 20 1/s is the maximum available stretch rate with a 4 cm sphere inside the Combustion Tunnel. At a higher stretch rate, a blow off boundary would be approached, and the flammability map would curve back downwards.

6.4.2 Effect of heat loss into the solid interior

Two groups of tests are marked with red dotted boxes in Fig. 6.59. Summary Series 1 marked on the graph varies the heat loss to the solid interior as a parameter across three tests. Time series photographs of these drop tests are shown side by side in Fig. 6.60 with Drop Test 4, 11, and 10 from left to right. Time advances from top to bottom. At 3.8 seconds, Drop Test 4 is well on its way to extinction, with the flame retreating towards the stagnation region. The flame extinguishes for Drop Test 4 between 3.90 and 3.93 seconds. The slightly off center extinction was not uncommon in testing. Drop Test 11, shown in the center column survives the 5.18 second drop. The same time period is shown. The flame front has some ripples near the stagnation region, but the flame envelops past the boundary layer separation point. Drop Test 10 in the right column shows similar results to Drop Test 11, but with a stronger flame with occasional fuel jetting which is visible as orange sparks. This test had higher solid fuel preheating prior to the drop and therefore lower heat loss to the solid interior, the flame can then use more energy for fuel pyrolysis. Drop Test 11 had a standoff distance of about 3.2 mm in zero g, the higher preheat Drop Test 10 had a stand off distance of about 3.6 mm because of the higher vaporization rate.

Test Number	Freestream Velocity (cm/s)	Heat Loss to Solid (W/cm^2)	Buoyant Standoff (mm)	Peak Standoff (mm)	Peak Time (s)	Final Standoff (mm)	Extinction Time (s)
1	1.95	3.76	2.23	4.368	1.17	2.78	4.13
2	1.98	2.19	2.323	6.134	0.70	3.625	4.267
3	3.8	3.72	2.045	4.089	0.33	2.788	2.4
4	5.8	3.72	2.14	4.089	0.23	2.695	3.8
5	25.1	3.62	2.416	3.532	0.03	2.602	X
6	14.6	3.58	2.323	3.625	0.90	2.509	3.367
7	19.5	3.54	2.230	3.439	0.23	2.695	X
8	19.6	3.98	2.138	3.346	0.50	2.323	2.367
9	14.5	1.8	2.416	5.762	0.70	3.160	X
10	5.9	1.29	2.138	9.670	0.20	4.182	X
11	6.1	1.98	2.323	5.576	0.50	3.90	X
12	3.8	2.89	2.323	7.621	0.63	2.974	X
13	1.8	1.54	2.602	12.64	0.73	5.204	4.8*

Table 6.15. Drop Test Summary Graph. All tests are ignited at 21% oxygen by volume, all drops at 17% oxygen by volume. (*) Time when flame leaves stagnation zone.

6.4.3 Effect of Flow Velocity (Stretch Rate)

Summary Series 2 labeled in Fig. 6.59 varies stretch rate as a parameter with the zero-g drop starting when heat loss to the solid is approximately the same value. A time series is shown in Fig. 6.61 with Drop Tests 2, 11, and 9 shown from left to right and time advancing from top to bottom. Drop Test 2 on the left shows a quenching process with the flame retreating towards the stagnation region and extinguishing slightly off center between 4.40 and 4.43 seconds after the drop. Surviving case Drop Test 11 is shown in the center column with a full envelope flame, persisting beyond the available 5.18 seconds. Drop Test 9 in the right column shows a larger envelope flame with a brighter blue flame intensity and well defined flame sheet extending further downstream. The flame stand off distance in Drop Test 9 is around 2 mm, and is considerably closer to the fuel surface than Drop Test 11 at about 3.2 mm due to the faster flow velocity pushing it towards the sample in the stagnation zone.

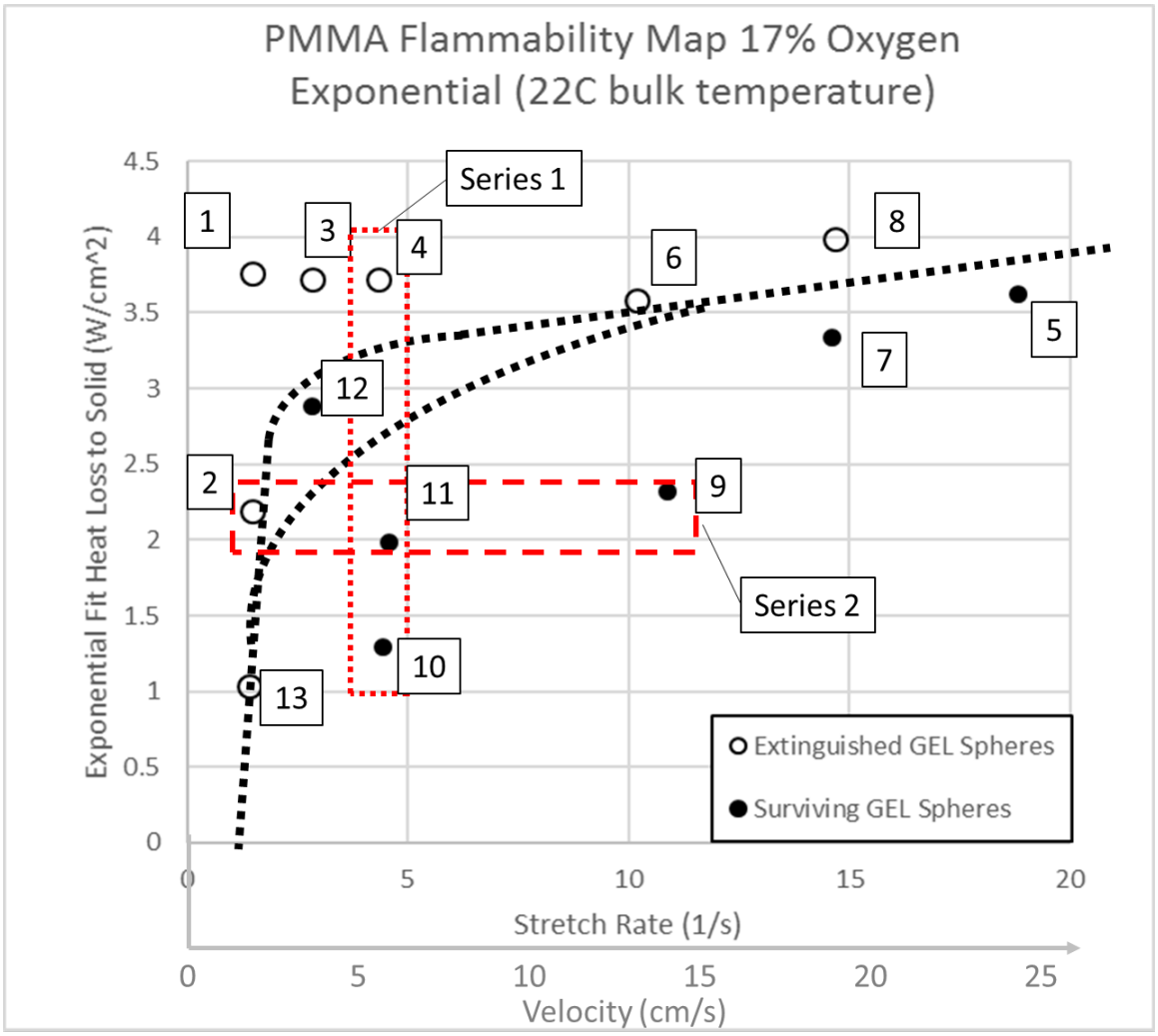

Figure 6.59. Drop Test Summary Graph

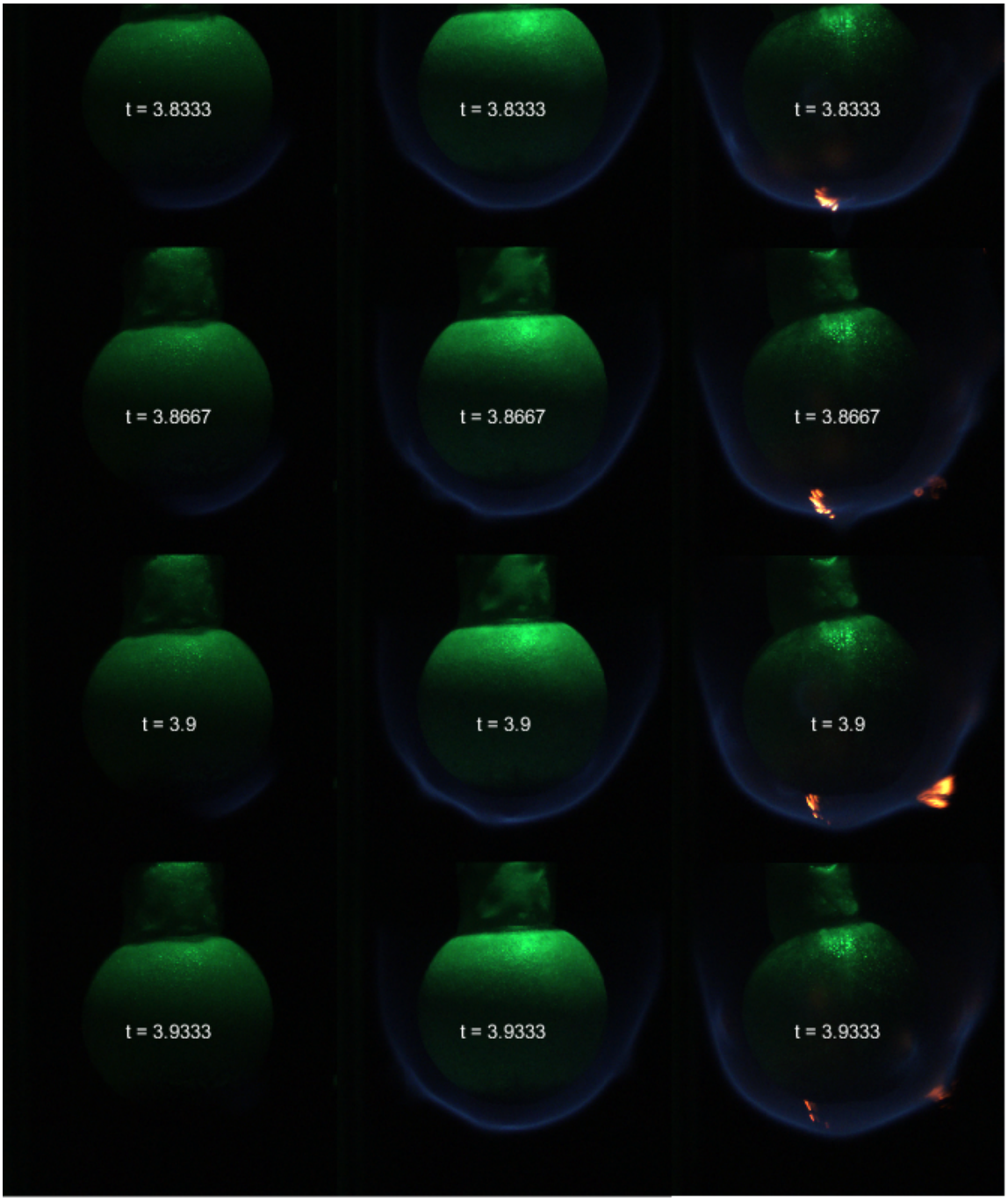

Figure 6.60. Summary Series 1 varying heat loss to the solid interior (at stagnation region) at stretch rate of $a_b = 4.5s^{-1}$, velocity = 6 cm/s. Left Column $q = 3.72W/cm^2$ (Drop Test 4), Middle Column $q = 1.98W/cm^2$ (Drop Test 11), Right Column $1.30W/cm^2$ (Drop Test 10)

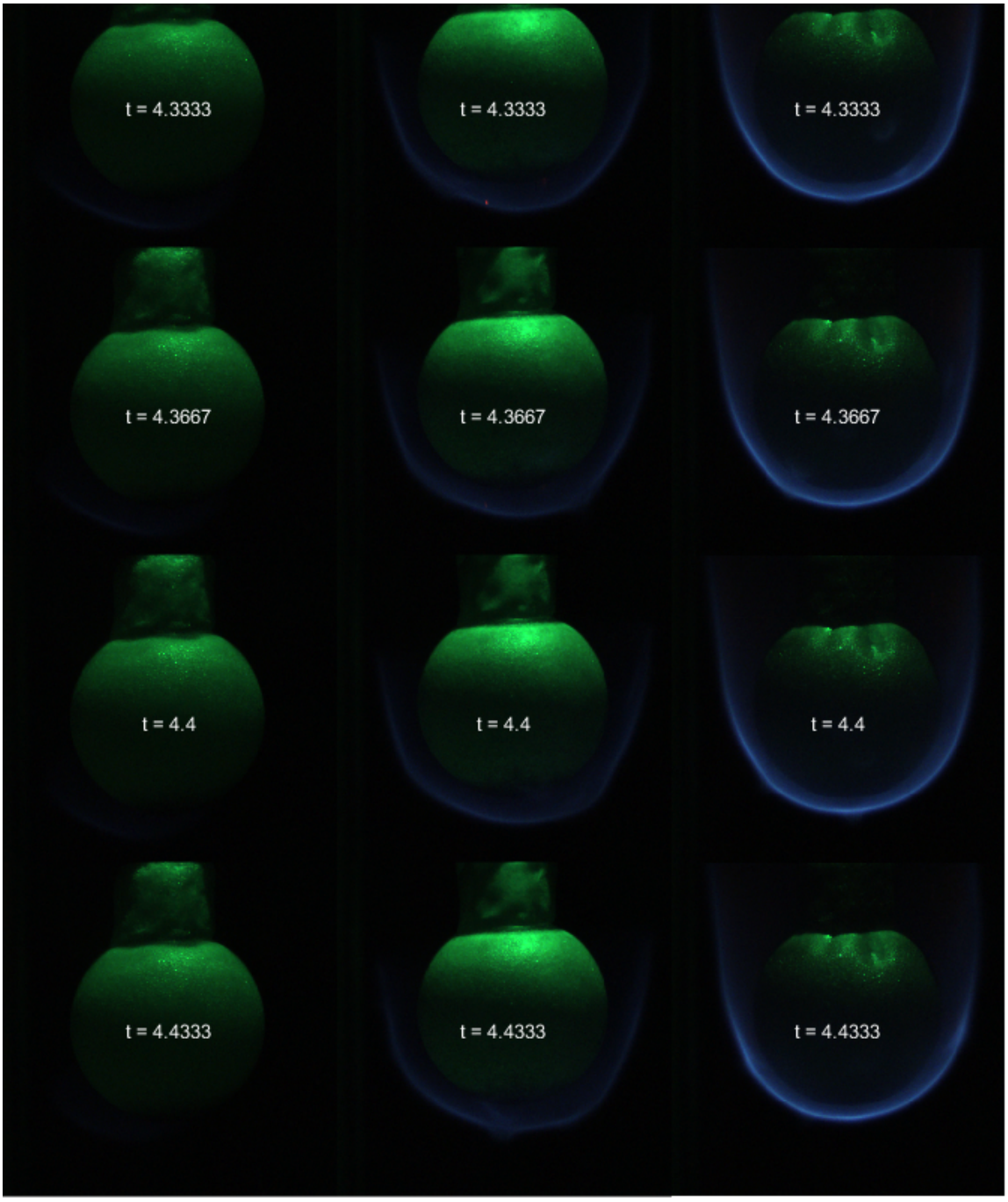

Figure 6.61. Summary Series 2 varying stretch rate (velocity) at a heat loss to the solid of $q \approx 2.25 W/cm^2$. Left Column $a \approx 1.461/s$ (Drop Test 2), Middle Column $a \approx 4.51/s$ (Drop Test 11), Right Column $a \approx 111/s$ (Drop Test 9)

6.4.4 Stagnation Zone Stretch Rate Equivalence

According to stagnation flame theory and Foutch and T'ien [5], there should be an equivalence between the 1 g and 0 g flame if proper stretch rates are defined. Equation 2.2 from Foutch and T'ien [5] describes the stretch rate for buoyant, forced, and combined flow conditions. Manipulating the equation with the proper input parameters of a_f and ϕ from Eq. 2.1 provides equations 6.6 and 6.7. This was the founding principle of the tests on spherical shells described in a previous chapter.

$$a_b = \sqrt{\frac{T^* - T_\infty}{T^*}\frac{g}{R}} \tag{6.6}$$

$$a_f = \frac{3}{2}\frac{U_\infty}{R} \tag{6.7}$$

On the spherical samples where the radius R is fixed as $R = 2cm$, U_∞ becomes the only parameter to match the pure forced flow stretch rate to the buoyant stretch rate. Setting Eqs. 6.6 and 6.7 equal, estimating $T^* \approx 1200K$ and solving for U_∞:

$$U_\infty = \frac{2R}{3}\sqrt{\frac{T^* - T_\infty}{T^*}\frac{g}{R}} = 25.6cm/s \tag{6.8}$$

Drop Test 5 was conducted with 25 cm/s purely forced flow. This gives a forced flow stretch rate of $a_f = 18.75s^{-1}$ according to Eq. 6.7. This is approximately the same stretch as given by Eq. 6.6 in a 1 g environment from purely buoyancy induced flow. Figure 6.62 shows a comparison of Drop Test 1 in 1 g just before the drop was triggered, this was a nearly pure buoyancy flame with a 2 cm/s trickle flow to replenish oxygen vs Drop Test 5 when the flame had stabilized after the drop transition with the solid sample surfaces aligned vertically. The buoyant flame standoff distance measures

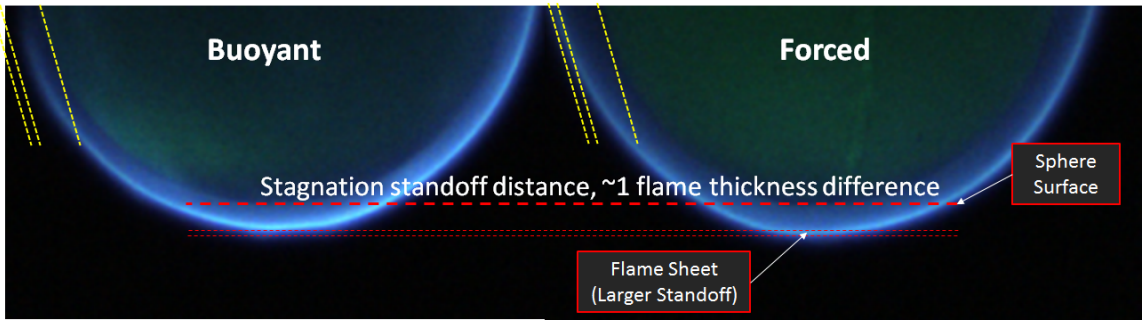

Figure 6.62. Comparison of buoyant stagnation zone to purely forced flow stagnation zone on 4 cm diameter GEL spheres.

about 1.3 mm, and the forced flow flame standoff distance (after initial transient) of about 1.7 mm. This is a difference of about one flame thickness. The thin red dotted lines in Fig. 6.62 are set at the boundaries of the flame thickness for the forced flow case and are extended into the picture of the buoyant case. The buoyant flame sheet is well inside the standoff distance of the forced flow case. A similar set of lines is shown in yellow at the same arbitrary location along the sphere. Although stagnation flame theory says little about the flame outside the stagnation zone, it is illustrated here that the boundary layer in the buoyant case is significantly closer to the surface in this region outside the stagnation zone due to upward acceleration and entrained air pushing the boundary layer back against the sphere's surface.

The comparison of the 1 g buoyant standoff in Drop Test 1 and the purely forced flow standoff in Drop Test 5 were made when the heat loss to the solids were as close as possible; $3.96 W/cm^2$ in Drop Test 1 and $3.74 W/cm^2$ in Drop Test 5. This small deviation is not expected to cause the difference in standoff distance.

Figure 6.63 shows a similar comparison of stagnation zone standoff at identical purely forced flow velocities at t=+3.83 s after the drop for the tests in Series 1 (Fig. 6.59). Drop Tests 10 ($1.3 W/cm^2$) and 11 ($2.4 W/cm^2$) show similar stable standoff

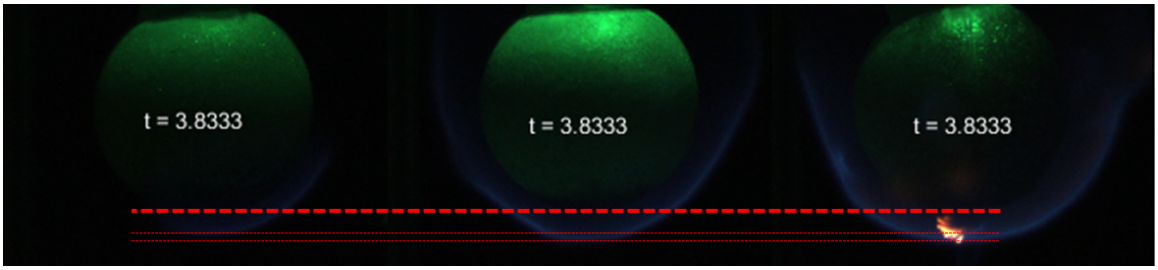

Figure 6.63. Comparison of standoff distances in zero g for Series 1: Drop Test 4 (Left), Drop Test 11 (Middle), Drop Test 10 (Right)

distance, but Drop Test 10 on the right hand side has increased surface jetting beyond the flame zone. The colder solid sample with increased heat loss to the solid in Drop Test 4 ($3.7W/cm^2$) exhibits a smaller stand off distance about one flame sheet width closer to the surface. This test extinguished at about t=+3.9s after the drop.

6.4.5 Final standoff distance

The *final standoff distance*, the last trackable standoff distance before the flame either self extinguishes or before the 5.18 second drop ends is charted against the measured heat loss to the solid interior in Fig. 6.64. Cases that self extinguish are shown as red bubbles, and cases that survived the 5.18 seconds are shown as blue bubbles. Bubble diameter represents the freestream velocity in cm/s. An inverse linear trend is formed. This is likely due to the inverse linear dependence of the fuel vaporization rate on heat loss to the solid interior (last term) shown in the surface energy balance equation Eq. 5.2.

The *final standoff distance* is also plotted against the freestream velocity in Fig. 6.65. Cases that self extinguished are shown as open circles, and cases that survived the drop are shown as closed circles. The extinction cases form a flammability boundary which describes the flame quenching distance and all surviving cases fall to one

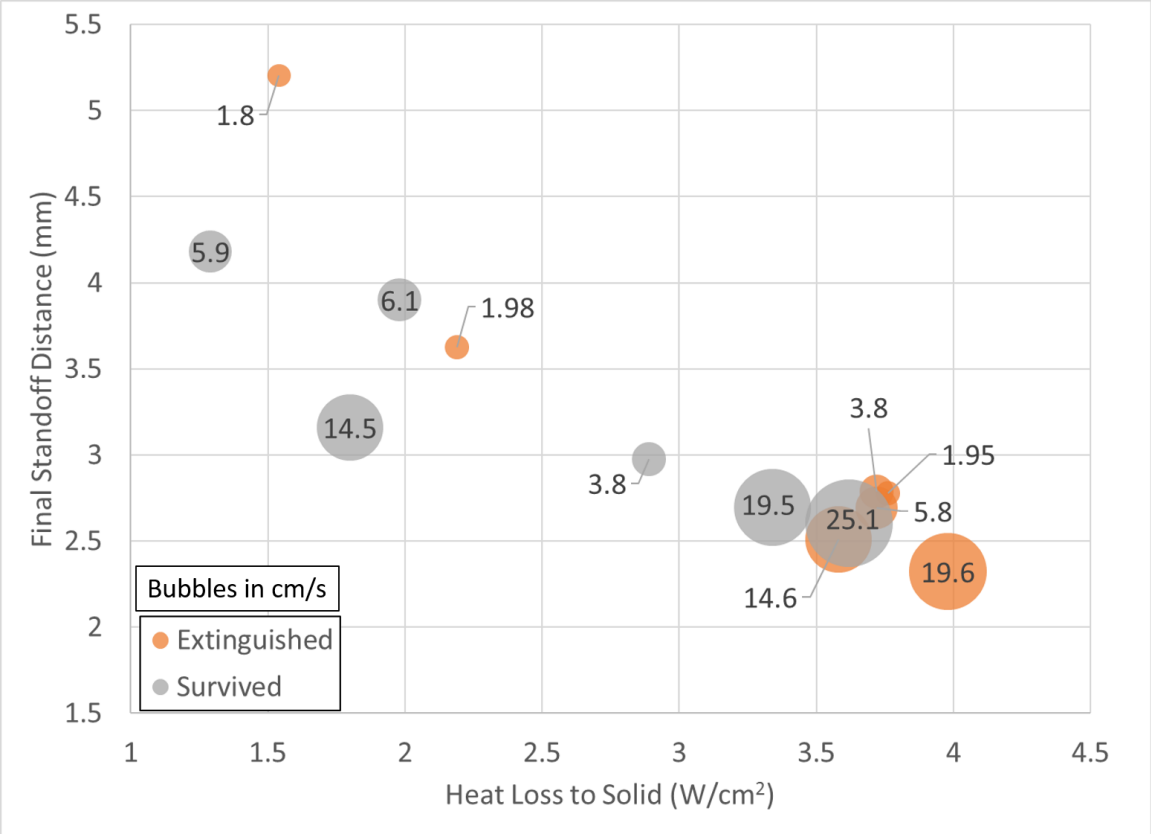

Figure 6.64. The final standoff distance for each drop test is plotted with respect to the heat loss to the solid interior. Freestream velocity is shown as bubble diameter.

side of this line. This quenching boundary, presented without exact mathematical form, takes a similar shape to the flammability boundary in 6.59 excepted inverted vertically. The boundary is very steep on the low velocity side and shallows out towards higher velocities, with the probed tests ending at 25 cm/s. When transitioning to microgravity, the flame would overshoot its final standoff distance, moving well into the flammable region in Fig. 6.65, then the flame would relax back towards the solid surface until it reaches it reaches its stable final standoff distance in the flammable region, touches the quenching distance boundary line and extinguishes, or the 5.18 second test ends.

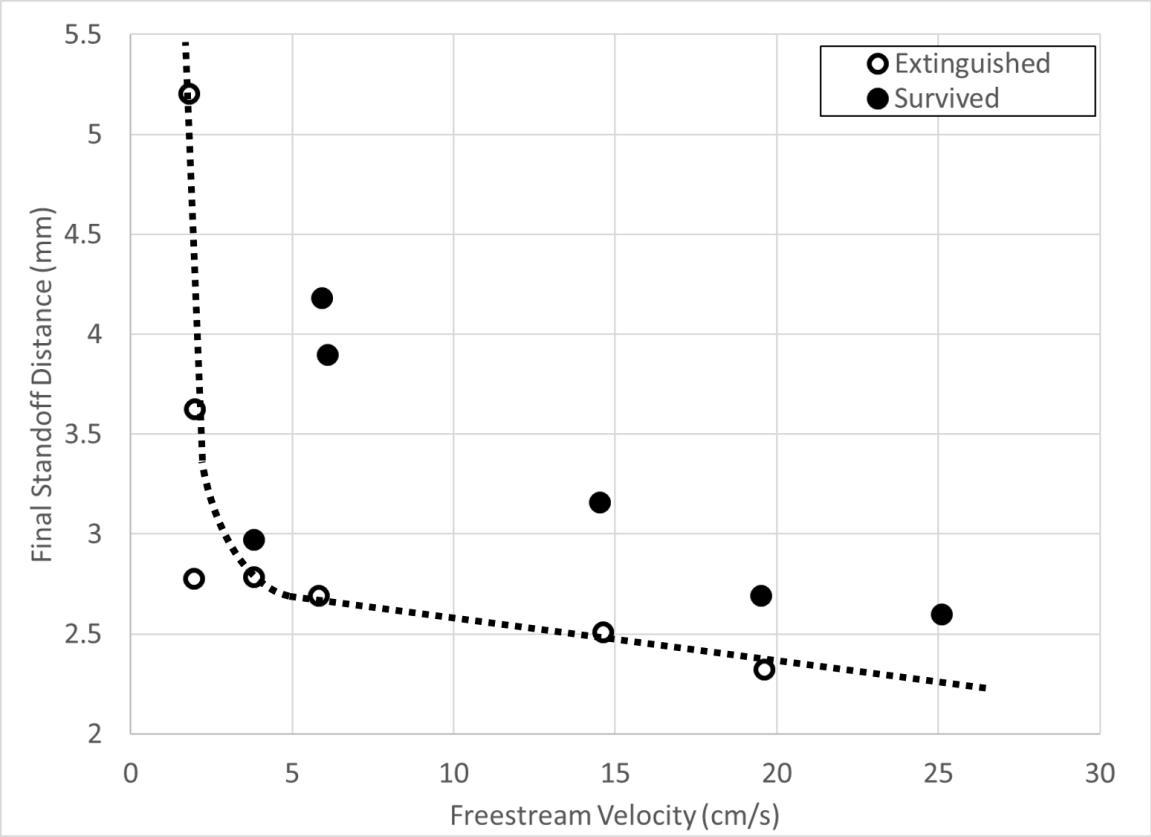

Figure 6.65. The final standoff distance for each drop test is plotted with respect to freestream velocity. A quenching distance extinction boundary is formed by the extinguished cases.

6.4.6 Summary

The series of experiments presented in this chapter have helped to refine the GEL space flight test matrix which will be presented in the next section. Because the extinction behavior at flow conditions and level of preheating had to be predicted prior to each discrete test in the ZGRF, reproducing these results and extending them further aboard ISS should be considerably easier since the SoFIE tunnel will be capable of sweeping a wide range of flow speeds towards extinction over the course of a single long duration burn of approximately 1-2 minutes. Because of this, the

GEL flight test matrix can accommodate a wider range of conditions varying oxygen percentage and chamber pressure.

The summary graph plotting the flammability map of heat loss to the solid vs stretch rate could use more test points to help define the extinction curve which was plotted in 6.59. The change of the curve from very steep to very shallow where test point 12 sets a 'knee' was unexpected. It will be interesting to see if this test point can truly sustain (grow as the sphere continues to heat up) a flame when burn times longer than 5.18 seconds are available.

After measuring stand off distance between a 1 g flame and 0 g flame with similar levels of preheating, these tests have shown that the equation for estimating buoyant stretch rate may need some adjustment. Because only one comparison was conducted between the counterpart test of purely forced and purely buoyant stretch, this should be investigated in future work in a series of drops involving various preheat values or in the flight experiment. Ideally, this would also include different radii of curvature.

7 Growth and Extinction Limits (GEL) Space Flight Experiment.

The works described in previous chapters are intended to help support and determine the parameters and test conditions for the long duration microgravity experiment Growth and Extinction Limits to be conducted onboard the International Space Station (ISS) as part of the Solid Fuel Ignition and Extinction (SoFIE) project. The hardware is currently under development as a modular insert for the Combustion Integrated Rack already aboard ISS. The Growth and Extinction Limits experiment will be described in this chapter to help set a road map for the future work.

7.1 Hardware Development

The combined use SoFIE tunnel insert is under development by ZIN Technologies as a module for the Combustion Integrated Rack (CIR) already aboard the International Space Station (ISS) [82, 83], and the information in this chapter may change as the hardware is built. The SoFIE apparatus must satisfy the needs of a multiple users and combustion investigations. These other users utilize a wide array of different

sample geometries and/or materials and require different diagnostics. The simplified design requirements for GEL are summarized below:

- Smooth uniform flow in the stagnation region of the spherical sample, controllable between 0-80 cm/s.
- Controllable oxygen concentration between 0 and 35% oxygen.
- High resolution video with two cameras at orthogonal views.
- Real time ground monitoring of standard definition or higher quality video during testing.
- Real time ground control of oxygen concentration, chamber pressure, and flow velocity
- Real time ground control of ignition
- Real time controllable chamber illumination to view sample surface.
- 10 Hz measurement of 5 thermocouples internal to the GEL sample.

The CIR facility, shown in Fig. 7.1 is currently operational and occupied by the Multi-user Droplet Combustion Apparatus (MDCA) investigating combustion on liquid fuel droplets. It will then be used by the Advanced Combustion via Microgravity Experiments (ACME) apparatus, investigating laminar gaseous flames, before a vacancy is available for SoFIE. It is an approximately 100 Liter self contained atmospheric chamber capable of internal pressures between near vacuum and 3 atmospheres. It is designed with windows for external optical diagnostics, electrical power and sensor feedthroughs, supply gas mixtures from pressurized cylinders, and water capture and CO2 scrubbing devices to remove unwanted products.

The SOFIE design concept is shown in Fig. 7.2. Flow is generated on the right hand side by a calibrated fan combined with flow conditioning such as honeycomb

and screens, shown in purple. The gas travels through the square channel 10 cm x 10 cm flow duct from right to left. The GEL spherical samples are shown on the left in a retracted position away from the flow duct. Three instrumented spherical samples will be installed on a rotating indexing assembly to reduce the astronaut time necessary for sample installation. A sample will be rotated into position, centered with the duct cross section. The igniter arm is shown forward of the center GEL sample. The arm can move in multiple directions for the fine control of alignment by the ground crew. The igniter can be extended into the sample stagnation region, and then retracted out of the way of the flame during the test.

Figure 7.3 shows an orthogonal view of the SoFIE apparatus with a GEL sphere sample indexed in place and extended into position within the flow duct with the igniter arm positioned forward of the stagnation region. The alternate samples installed in the duct are protected from the flame outside of the duct. This picture represents the furthest insertion into the duct. Ideally, the GEL sphere should be positioned just at the tunnel exit, to prevent flow confinement and acceleration between the 4 cm diameter sphere and the 10 cm wide duct.

The GEL samples themselves are described in the Samples chapter of this document. Each sample will be used multiple times. We hope to achieve 50 tests on 15 samples which will be described in the the Test Matrix section below.

7.2 Ignition

The exact method of ignition was not listed as a requirement for the design of the SoFIE hardware, instead it was left open ended provided the ignition method of

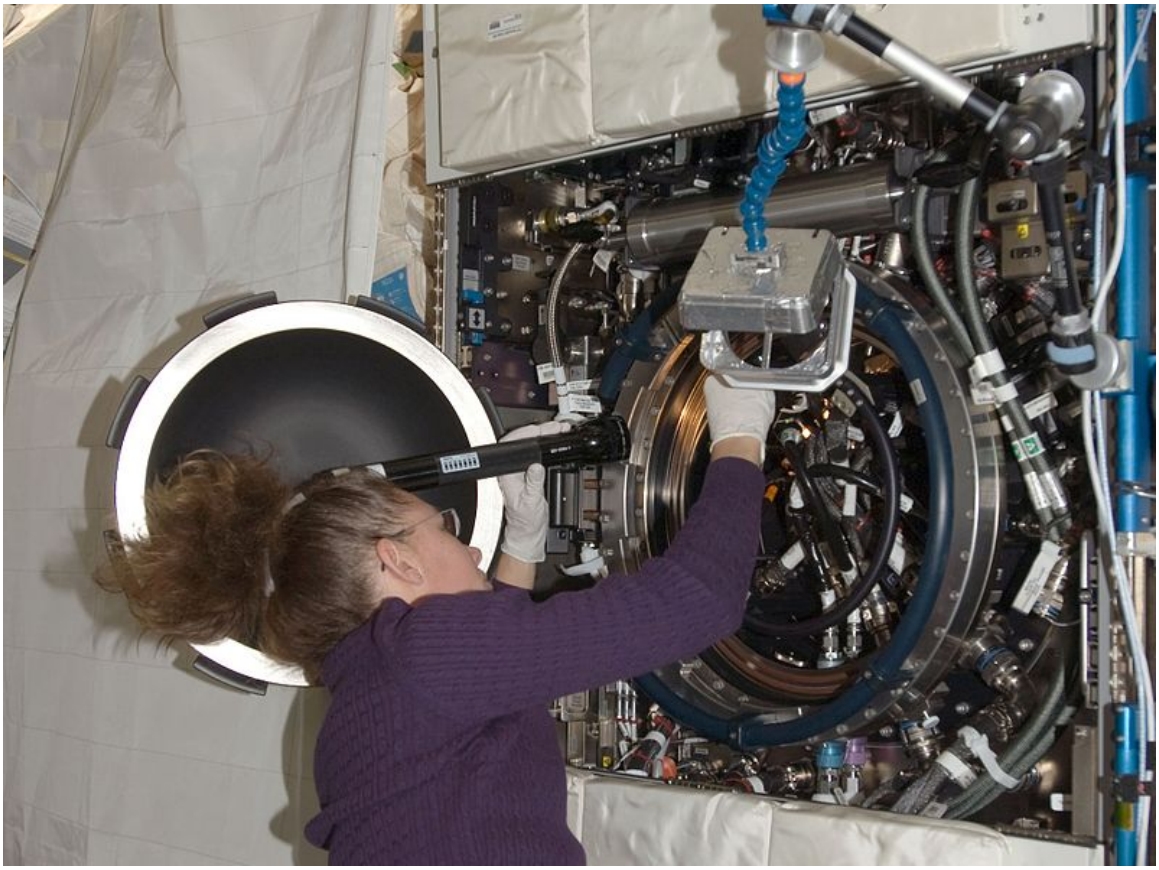

Figure 7.1. Astronaut Sandra Magnus installing an experiment module into the Combustion Integrated Rack aboard ISS (Stock NASA Image ISS018E35752)

choice can provide enough energy to ignite the sample in a reasonable amount of time (approximately 30 seconds). Currently, a resistive coil Kanthal A-1 hotwire is planned, similar to that used in the Zero Gravity Research Facility and the Burning and Suppression of Solids (BASS) experiment. The ignition of the sphere is typically satisfactory with this method, however the reliability of such a design during the BASS operations was poor. Because BASS was conducted in the Microgravity Science Glovebox (MSG) with constant hands on interaction from the ISS crew, a broken igniter could be swapped relatively quickly without straining the crew time resources from other projects. During the primarily automated and ground controlled SoFIE

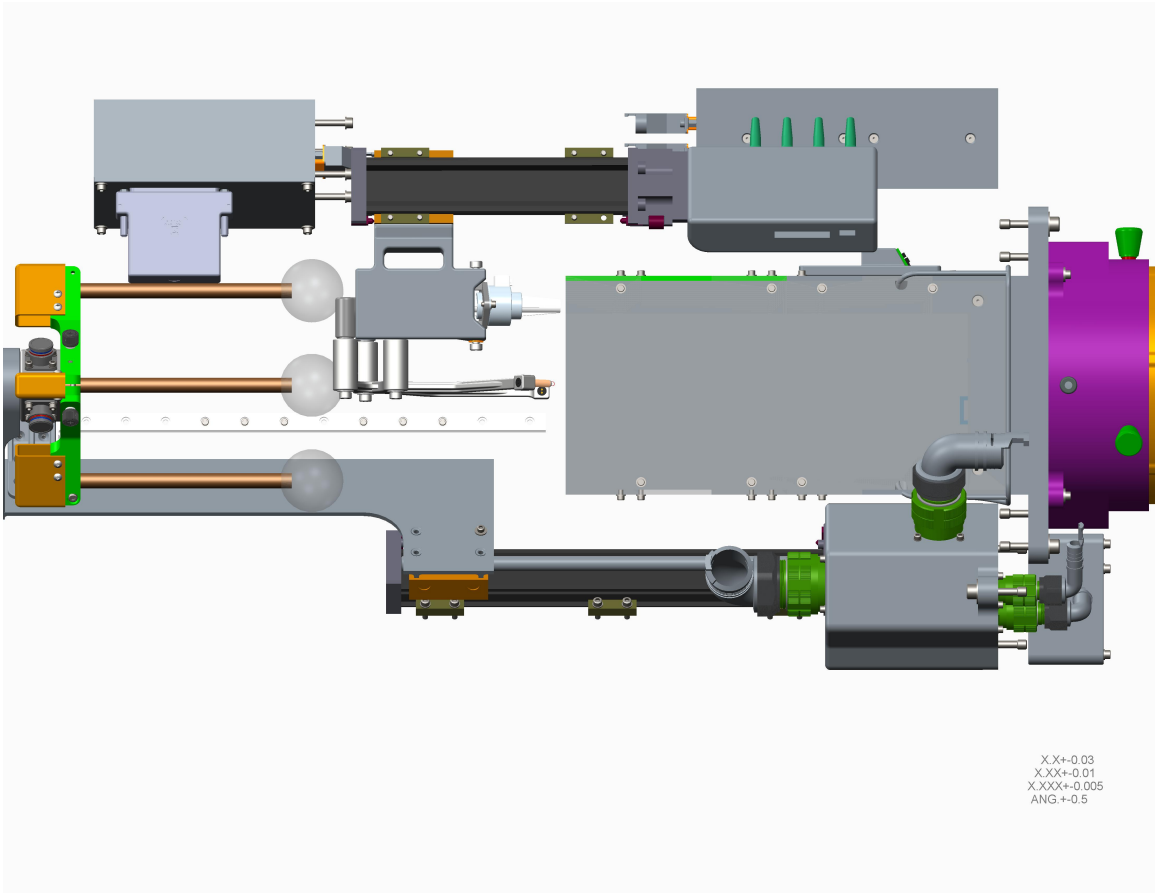

Figure 7.2. Front view of the SoFIE hardware concept from ZIN Technologies., with the GEL samples retracted.

investigations, this will not be the case. Igniter failures may take hours of crew time to open the CIR chamber, partially remove the SoFIE insert, and replace the hotwire igniter on the igniter arm. Multiple igniter failures could be devastating to GEL and SoFIE in general.

Because of the critical nature of the igniter survivability, some experimentation was conducted in the laboratory and the information sent to ZIN Technologies to consider in their prototyping. In prior experiments, we have had good success with a Kanthal A-1 coil igniter of about 3 to 3-1/2 wire turns with a diameter of 1/4". These can be made by turning a wire over a 1/4"-20 bolt as shown in Fig 7.4. The

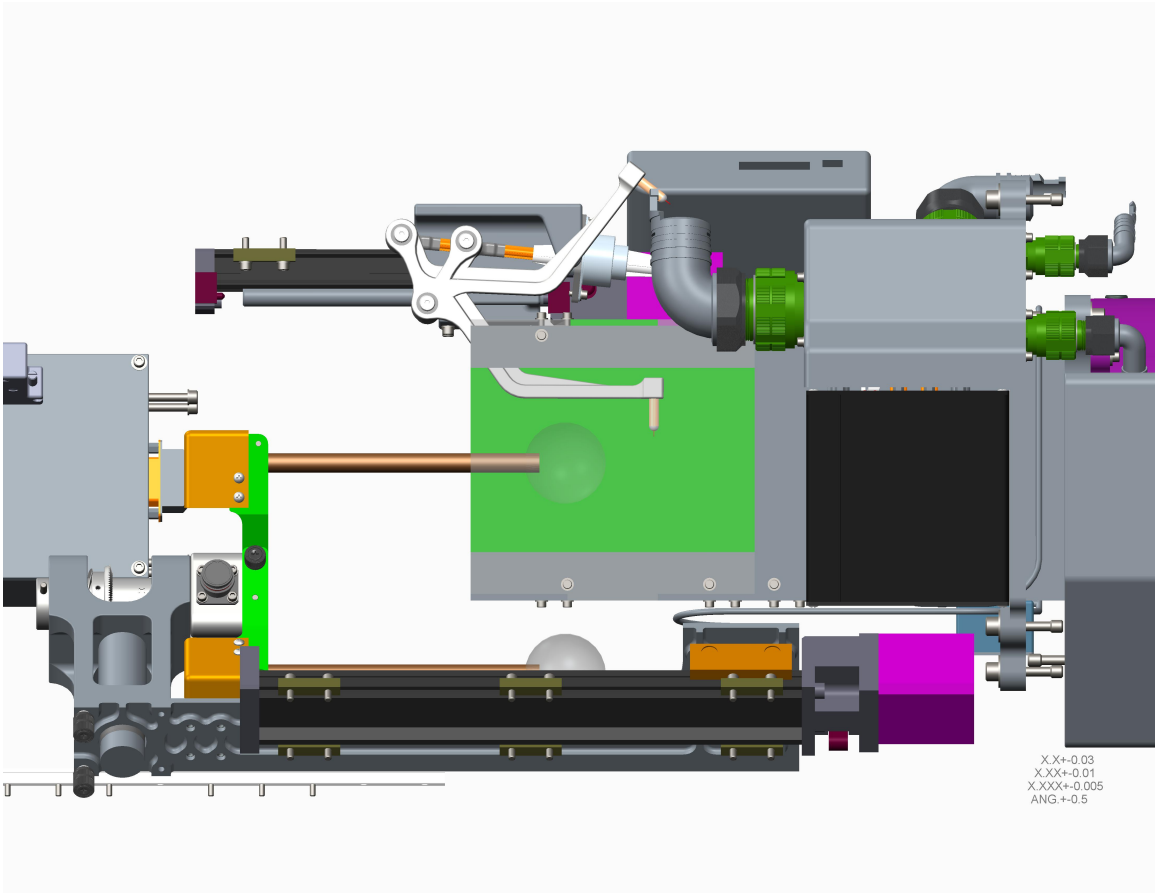

Figure 7.3. Side view of the SoFIE hardware concept from ZIN Technologies Inc., with a GEL sample inserted into the flow duct

bolt is then just rotated free from the igniter coil. The legs are trimmed to length and crimped onto gold plated barrel pin connectors (part # 205089-1) with a M22520/1-01 crimping tool with a M22520/2-08 positioner. This allows the wire to interface with a gold plated barrel socket (part # 205090-1). The finished coil is shown in Fig. 7.5.

Kanthal A-1 wire is chosen because of its resistance to high temperature and extremely flat resistivity temperature coefficient. After initial oxidation, Kanthal becomes stiff and resists sagging and shape change unless overheated. The properties of Kanthal A-1 in various gauges from a few suppliers are shown in Table 7.1. Temco

was found to be consistent with the published properties of the Kanthal brand. A supplier this work refers to as 'LV' was likely selling B stock wire which had a deviation of resistance values up to 14%.

A series of 3 turn coil igniters were made in progressively increasing diameter from 29 gauge to 16 gauge to test for ruggedness. The igniters were subjected to 100 thermal cycles, powered up for 30 seconds and then powered off for 60 seconds. Testing was conducted with either power dissipation held constant around .318 W/mm, or surface loading held constant around .317 W/mm^2. An energized coil is shown in Fig 7.6. The color of the main coil is just on the transition from glowing orange to glowing white hot. The wire legs of the coil are a dim orange. The hot coil can be seen through the inspection port of the gold plated in contact, the contact itself is beginning to oxidize and turn brownish from the heat. In this case, the coil itself is physically collapsing either because of stress induced from the internal temperature differentials from the heating and cooling cycling or from gravity itself causing the upper leg to sag slightly.

An extreme case of igniter failure can be seen in Fig. 7.7. The 22 AWG wire failed on the 69th thermal cycle. It is unclear what causes the failure compared to the smaller gauge wires, but the result is a liquification of the Kanthal which flows towards the pin which remains hot longer due to thermal inertia after the circuit has failed like a fuse. As a comparison, a 27 AWG wire which has underwent 100 thermal cycles is shown in Fig. 7.8. The surface of the Kanthal still looks clean and fairly unoxidized. The coil may have collapsed slightly under its own weight, but from appearance, it looks relatively new.

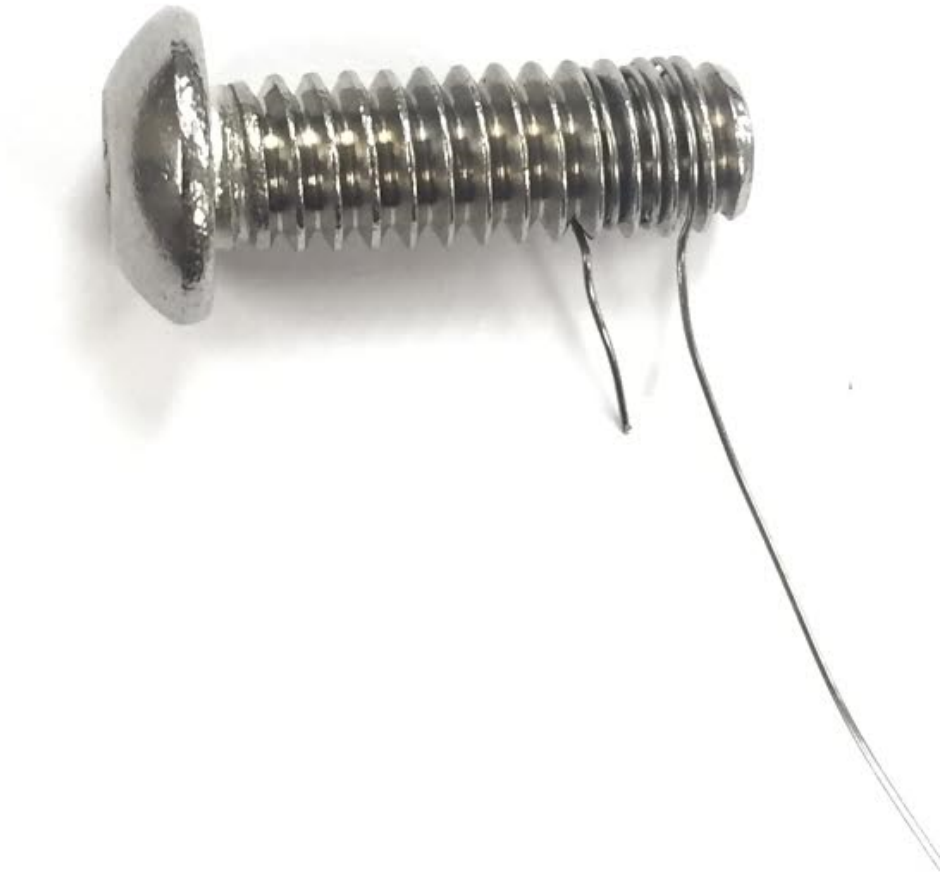

Figure 7.4. A Kanthal A-1 wire turned into shape in the threads of a 1/4-20" bolt.

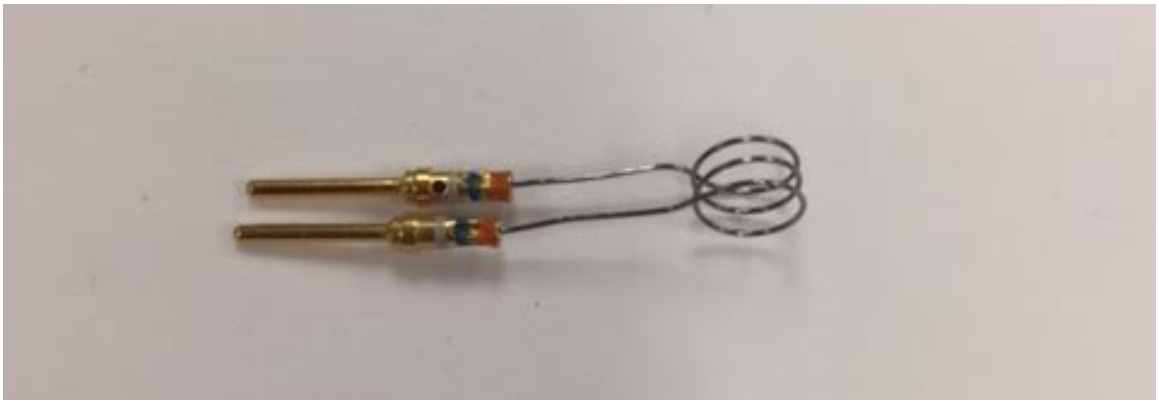

Figure 7.5. A finished igniter coil.

Wire (AWG)	Manufacturer	Published Cold Resistance	Measured Cold Resistance	%difference	Diameter (mm)	c ($2\pi D$)	Area (mm^2)
29	Kanthal	.224			.29	.90	.06
29	LV	.224			.29	.90	.06
29	Temco	.224			.29	.90	.06
28	LV	.180	.154	14.67%	.32	1.01	.08
28	Temco	.180	.174	3.411%	.32	1.01	.08
27	Temco	.142	.139	1.98%	.36	1.13	.10
26	Temco	.113	.112	1.14%	.40	1.27	.13
24	Temco	.071	.073	2.49%	.51	1.60	.20
22	Temco	.044	.044	0.12%	.65	2.03	.33
20	LV	.028	.029	2.70%	.81	2.55	.52
16	LV	.011	.010	6.21%	1.29	4.05	1.31

Table 7.1. Properties of Kanthal A-1 resistive wire

Wire (AWG)	Hot R (ohm/m)	Current (A)	Power (W/mm)	Surface Loading (W/mm^2)	100 Thermal Cycles	Ignites PMMA
29	23.54					
28	18.94	4.1	.328	.317	PASS	PASS
27	14.90	4.7	.329	.291	PASS	PASS
27	14.90	4.9	.358	.316	PASS	PASS
26	11.89	5.2	.321	.256	PASS	PASS
24	7.44	6.6	.324	.202	PASS	PASS
24	7.44	7.5	.418	.261	PASS	PASS
24	7.44	8.3	.512	.319	PASS	PASS
22	4.66	8.3	.321	.158	PASS	PASS
22	4.66	10.0	4.66	.230	69- FAIL	PASS
22	4.66	11.7	.638	.315	26-FAIL	PASS

Table 7.2. Thermal cycle testing of a 3 turn Kanthal A-1 hotwire coil. All wire shown supplied by Temco.

7.3 Proposed Test Matrix

Fifteen 4 cm diameter instrumented spherical samples will be provided for the experiment with two additional spheres to serve as hardware backups. Currently, fifty tests are planned. This is a rough number depending on resource utilization of available compressed gas reserves, amount of sample regression and shape change, and survivability of the fragile thermocouple instrumentation. The GEL experiment is broken into multiple test series tiers to help prioritize the efforts of the limited resources of expense, crew time, and occupancy time in the shared use facility as follows: normal pressure conditions, reduced pressure and normoxic conditions, and blowoff. The test

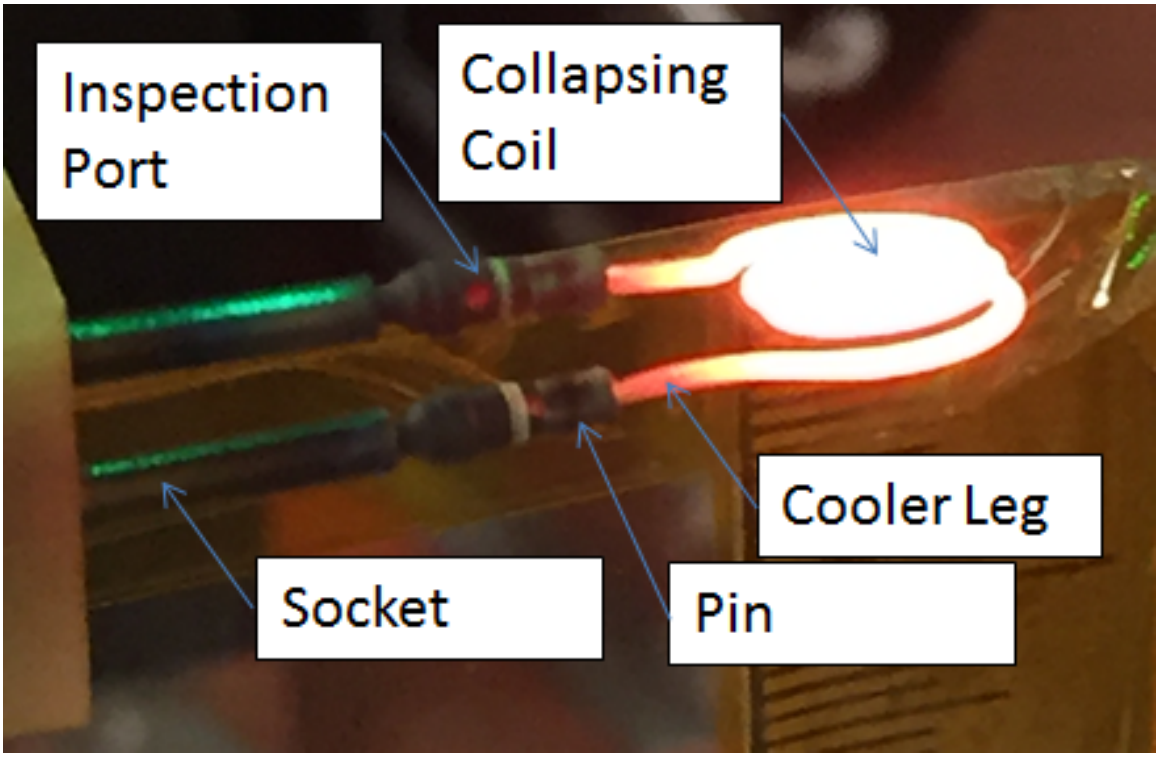

Figure 7.6. A test igniter collapsing under as it cycles through 100 thermal cycles

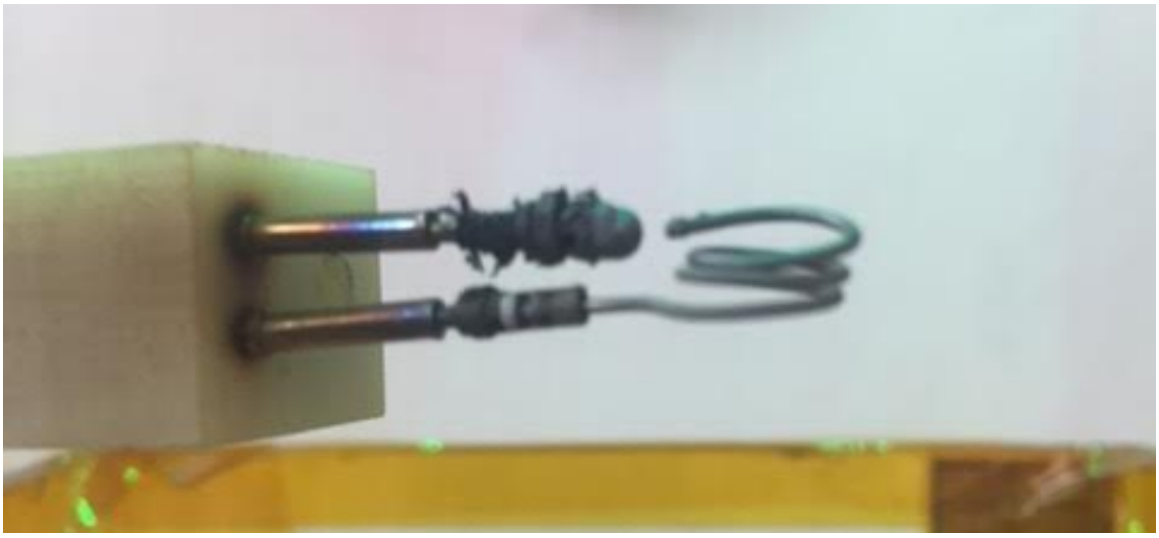

Figure 7.7. An extreme case of igniter failure. 22 AWG.

matrices outlined below account for 40 of the planned tests. This leaves 10 available tests of the original 50 proposed for repeatability or exploring any unforeseen phenomenon of interest.

Figure 7.8. A 27 AWG Kanthal A-1 coil igniter which has survived 100 thermal cycles.

The tests proposed below are merely suggestions. The test matrix can, and should, deviate from the planned conditions depending on experimental results.

7.3.1 Test Series 1: Normal Pressure

GEL flight Test Series 1 should follow the quenching experiments laid out in the Earth based ZGRF facility described in Chapter 6. The low velocity quenching limit will be approached at multiple oxygen concentrations (including 17% previously explored) by slowly decreasing nozzle forced flow velocity until the flame extinguishes. The same procedure will be repeated by holding flow velocity constant and slowly decreasing oxygen concentration by nitrogen dilution within the chamber or by vitiation of the atmosphere by oxygen consumption from the flame. These low speed quenching velocities will be mapped for at least three different values of heat loss to the solid interior.

In the long duration microgravity of the flight experiment, measurement of flame spread rate across the sphere surface from ignition at the forward stagnation point to

Test Number	Pressure	Oxygen Concentration	Preheat Level	Nozzle Velocity
1	1 atm	17%	#1	Decrease until extinction
2	1 atm	17%	#2	Decrease until extinction
3	1 atm	17%	#3	Decrease until extinction
4	1 atm	21%	#1	Decrease until extinction
5	1 atm	21%	#2	Decrease until extinction
6	1 atm	21%	#3	Decrease until extinction
7	1 atm	19%	#1	Decrease until extinction
8	1 atm	19%	#2	Decrease until extinction
9	1 atm	19%	#3	Decrease until extinction
10	1 atm	Decrease until extinction	#1	Velocity 1
11	1 atm	Decrease until extinction	#2	Velocity 1
12	1 atm	Decrease until extinction	#3	Velocity 1
13	1 atm	Decrease until extinction	#1	Velocity 2
14	1 atm	Decrease until extinction	#2	Velocity 2
15	1 atm	Decrease until extinction	#3	Velocity 2
16	1 atm	Decrease until extinction	#1	Velocity 3
17	1 atm	Decrease until extinction	#2	Velocity 3
18	1 atm	Decrease until extinction	#3	Velocity 3

Table 7.3. Growth and Extinction Limits *Test Series 1: Normal Pressure* suggested test matrix

the fully established envelope flame is possible. This is a key visual result for comparison with the computer model developed by Endo [1], but could not be performed in ZGRF.

7.3.2 Test Series 2: Reduced Pressure

In a second test series, GEL intends to probe the low oxygen concentration limit of combustion as a function of the level of preheating in the following manner: The oxygen concentration of the CIR chamber will be set, the flame established on the sphere, the sphere will continue to burn until near the intended level of preheating, then the CIR chamber pressure will be vented slowly to reduce total pressure until extinction occurs. The oxygen concentration limit at three flow velocities should

Test Number	Pressure	Oxygen Concentration	Preheat Level	Nozzle Velocity
19	0.6 atm	17%	#1	Decrease until extinction
20	0.6 atm	17%	#2	Decrease until extinction
21	0.6 atm	17%	#3	Decrease until extinction
22	0.8 atm	17%	#1	Decrease until extinction
23	0.8 atm	17%	#2	Decrease until extinction
24	0.8 atm	17%	#3	Decrease until extinction
25	0.7 atm	24.3%	#1	Decrease until extinction
26	0.7 atm	24.3%	#2	Decrease until extinction
27	0.7 atm	24.3%	#3	Decrease until extinction
28	0.5 atm	34%	#1	Decrease until extinction
29	0.5 atm	34%	#2	Decrease until extinction
30	0.5 atm	34%	#3	Decrease until extinction
31	0.5 atm	21%	#1	Decrease until extinction
32	0.5 atm	21%	#2	Decrease until extinction
33	0.5 atm	21%	#3	Decrease until extinction

Table 7.4. Growth and Extinction Limits *Test Series 2: Reduced Pressure* suggested test matrix

already be established at 1 atmosphere from the minimum requirements. This series of tests will establish the same results for proposed space exploration atmospheres which lie along the normoxic curve. Namely, since biological systems tend to be dependent upon the proper oxygen partial pressure, the partial pressure of oxygen is held fixed and the total pressure is reduced by decreasing the balance of the nitrogen diluent. Testing would include the 100% oxygen concentration possible in the space suits used for extravehicular activities, but is bound by the safe limits of the CIR hardware.

7.3.3 Test Series 3: Blowoff

The final GEL flight test series focuses on finding the maximum velocity to sustain combustion on the GEL sample in the purely forced flow microgravity environment.

Test Number	Pressure	Oxygen Concentration	Preheat Level	Nozzle Velocity
34	1 atm	17%	#1	Increase until extinction
35	1 atm	17%	#2	Increase until extinction
36	1 atm	17%	#3	Increase until extinction
37	0.6 atm	17%	#0	Increase until extinction
38	0.6 atm	18%	#0	Increase until extinction
39	0.6 atm	19%	#0	Increase until extinction
40	0.8 atm	17%	#0	Increase until extinction

Table 7.5. Growth and Extinction Limits *Test Series 3: Blowoff* suggested test matrix

This is often referred to as the blowoff limit. The flame will be established with a fixed chamber pressure and oxygen concentration, the nozzle velocity will then be increased until blow off occurs. Because blow off is primarily related to either the gas phase chemical residence time and/or gaseous upstream heat diffusion, it is thought that the amount of preheating of the solid will have little effect on the high velocity blow off limits. This will be confirmed in testing.

7.4 Compressed Gas Resources

The amount of compressed gas is the most important limited resource after ISS crew time and consumption needs to be carefully planned. The 100 liter CIR chamber is expected to have a free volume of about 85 liters after the SoFIE hardware is installed. The chamber will need to be filled with the desired oxygen/nitrogen blend before each test and oxygen may need to be added as the experiment progresses to replenish the amount consumed by the flame. Depending on the ability of the CIR hardware to scrub CO2 and water from the atmosphere during combustion, some of the gas may need to be vented during a test and then refilled with fresh oxygen and nitrogen. The

rate at which CIR can scrub these products is currently unknown. It should be noted that filling and venting operations can not be conducted simultaneously due to safety concerns, but the chamber can be repeatedly vented and refilled in the vicinity of the desired chamber pressure.

A rough estimate of the compressed gas resources necessary for the test campaign is necessary. Nitrogen gas is considered 'free' from the standpoint of CIR operations, as it is available as a byproduct the space station's liquid nitrogen cryogenic systems. Compressed oxygen will have to be supplied specifically for each experiment in SoFIE. For safety reasons, a blend of oxygen and nitrogen is typically provided to reduce the fire hazard. According to the original CIR user's manual for principal investigators [84], gas cylinders are pressurized to 2000 psig, and are available in sizes 1.0 L (capable of 85% oxygen), 2.25 L (capable of 50% oxygen), and 3.8 L (capable of 30% oxygen). A newer technical memorandum lists the maximum oxygen percentage as 80% [85], this may be an error. Previously, cylinders have been provided for CIR as 85% oxygen mixed with 15% nitrogen, and 30% oxygen mixed with 70% nitrogen. The maximum oxidizer flow rate is 30 standard liters per minute (SLM) per manifold and 90 SLM total.

The 85% oxygen, 15% nitrogen 1L cylinders should be used when possible for oxygen replenishment in order to prevent unnecessary pressure rise within the combustion chamber, which may require venting. At 2000 psi, each compressed gas cylinder will hold about 150.5 g of oxygen and 23.2 g of nitrogen. Three of these cylinders can be installed simultaneously for a total of 451.5 g of oxygen and 69.6 g of nitrogen.

Typically, the CIR chamber will be drawn to vacuum to evacuate products from the previous experiment. Nitrogen will then be added from the station supply, then

the high concentration oxygen/nitrogen blend will be added until the CIR oxygen concentration reaches the desired value.

In the combustion field, flammability is often reported in terms of volumetric oxygen concentration. For a pressure vessel, it can be convenient to think of oxygen concentrations within the chamber in terms of partial pressures, and resource consumption from pressurized cylinders in terms of mass. To fill the CIR chamber to the desired volumetric oxygen concentration, the necessary partial pressure of oxygen can be related to the desired parameters of chamber total pressure $P_{Chamber}$ and volumetric oxygen concentration C_{O_2} by Eq. 7.1.

$$P_{O_2} = C_{O_2} P_{Chamber} \tag{7.1}$$

This oxygen partial pressure be related to mass by Eq. 7.2. This is the amount of oxygen by mass necessary to achieve the desired volumetric oxygen concentration at the desired pressure and temperature.

$$M_{O_2} = X_{O_2} \frac{P_{O_2} V_{Chamber}}{R T_{Chamber}} \tag{7.2}$$

Where $V_{Chamber}$ is the chamber volume, $T_{Chamber}$ is the chamber temperature, and X_{O_2} is the molar mass of gaseous oxygen. When filling the chamber, the total pressure will be related to:

$$P_{Chamber} = P_{O_2 Cylinder} + P_{N_2 Cylinder} + P_{N_2 Station} \tag{7.3}$$

Where the partial pressure from the compressed gas cylinder will take the form of:

$$P_{O_2Cylinder} = aC_{cylinder} \tag{7.4}$$

$$P_{N_2Cylinder} = a(1 - C_{cylinder}) \tag{7.5}$$

where $C_{cylinder}$ is the volumetric oxygen concentration of the supply gas cylinder, a is the amount of gas, expressed in partial pressure, added from the cylinder.

$$P_{Chamber} = a[C_{cylinder} + (1 - C_{cylinder})] + P_{N_2Station} \tag{7.6}$$

The volumetric oxygen concentration of the chamber is then:

$$C_{Chamber} = \frac{aC_{cylinder}}{P_{Chamber}} \tag{7.7}$$

then a, the partial pressure needed from the compressed gas cylinder is:

$$a = \frac{C_{Chamber}P_{Chamber}}{C_{Cylinder}} \tag{7.8}$$

The station nitrogen supply will be filled first, a partial pressure mixing can be very accurate. This means the station nitrogen will fill the chamber until the chamber pressure transducer reads:

$$P_{N_2Station} = P_{Chamber} - a \tag{7.9}$$

The amount of mass consumed by the experiment from the station nitrogen supply, nitrogen from the compressed gas cylinder, and oxygen from the compressed gas cylinder, is respectively Eq. 7.10, 7.12, 7.11:

$$M_{N_2Station} = X_{N_2} \frac{P_{N_2Station} V_{Chamber}}{RT_{Chamber}} \tag{7.10}$$

$$M_{O_2Cylinder} = X_{O_2} \frac{a(C_{Cylinder}) V_{Chamber}}{RT_{Chamber}} \tag{7.11}$$

$$M_{N_2Cylinder} = X_{N_2} \frac{a(1 - C_{Cylinder}) V_{Chamber}}{RT_{Chamber}} \tag{7.12}$$

7.4.1 Setting Initial Chamber Conditions

The CIR chamber can be drawn to vacuum and refilled completely to ensure a consistent and repeatable starting condition of a known gas concentration and pressure. However, if compressed gas resources become too scarce, the chamber may be started at the conditions of a previous test, venting to an intermediate pressure, and then refilling with additional oxygen or nitrogen as necessary. The equations from the section above apply, but are rearranged here for convenience. When changing the atmosphere of the CIR chamber, there are multiple independent parameters which can be adjusted: the chamber can be vented, pure nitrogen can be added, and the oxygen/nitrogen blend can be added from the gas cylinder.

The pre test chamber filling strategies can be summarized in the four graphs in Fig. 7.9. The chamber oxygen concentration vs chamber total pressure is shown. In the upper left, the gas already within the chamber from the previous test is first vented and then filled with the ISS nitrogen supply. In the upper right, the chamber is first vented and then filled with the oxygen/nitrogen blend from the gas cylinder. In the bottom of the figure, when increasing pressure beyond the limits of the light

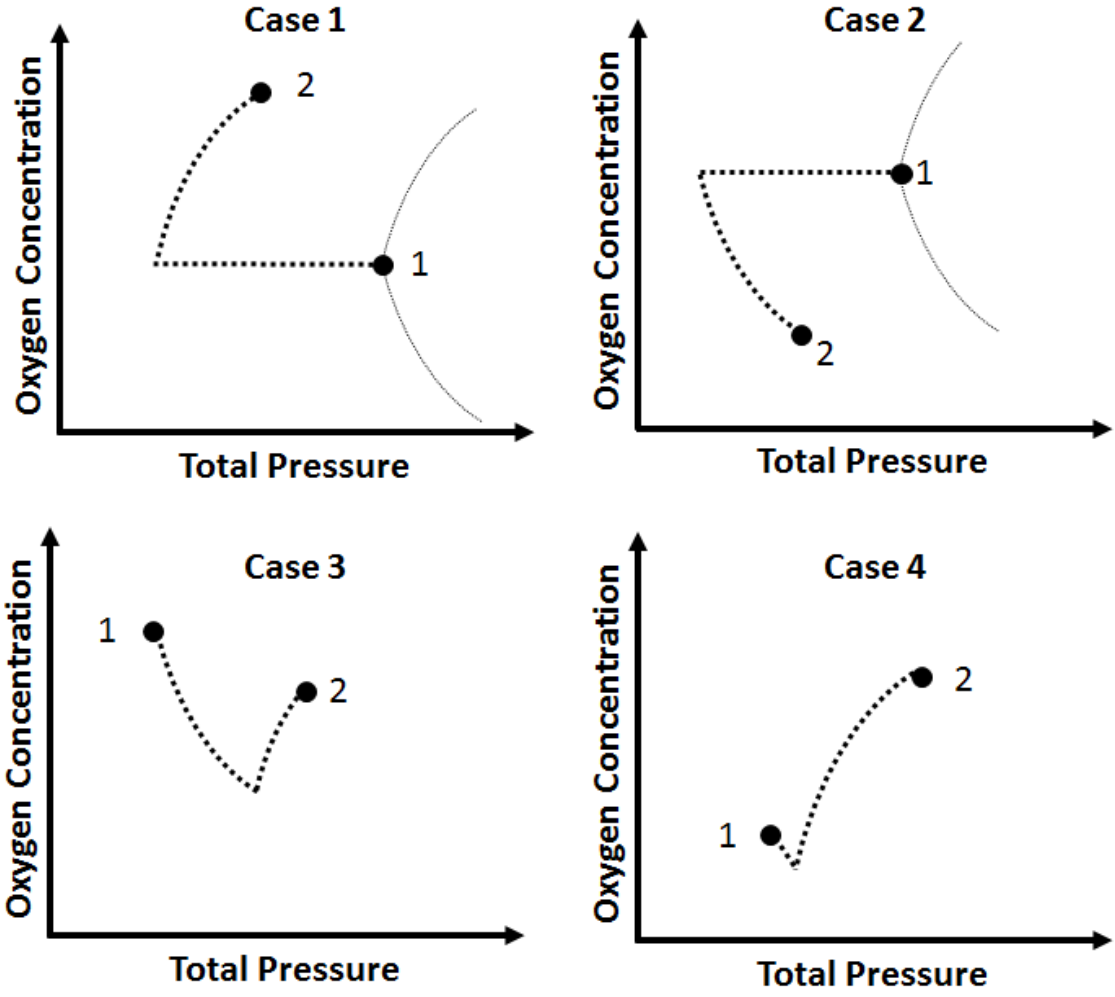

Figure 7.9. The operations necessary for four distinct chamber filling operations.

dotted lines shown in the top figure, no chamber venting is necessary, nitrogen is first added, then the oxygen concentration is increased with the oxygen/nitrogen blend.

Case 1: Vent Chamber, Increase Oxygen Concentration. Fill Case 1 occurs when the chamber must be vented before oxygen is added. This means the desired pressure and oxygen concentration point lies to the left of the light dotted outline shown in Fig. 7.9. Specifically, the desired oxygen concentration can not be reached by filling from the oxygen/nitrogen cylinder or the ISS nitrogen supply before exceeding

the desired target pressure, the chamber needs to be vented first to an intermediate pressure calculated in Eq. . The chamber is then filled with the oxygen nitrogen blend until reaching the desired chamber pressure.

$$P_{intermediate} = \frac{P_{target}}{1 + \frac{C_{initial} - C_{target}}{C_{target} - C_{cylinder}}} \tag{7.13}$$

The partial pressure contributed by the cylinder gas is then computed in Eq. 7.14. This can be expressed in terms of oxygen and nitrogen mass consumption form the cylinder as Eqs. 7.15 and 7.16

$$P_{cylinder} = \frac{C_{initial} - C_{target}}{C_{initial} - C_{cylinder}} P_{target} \tag{7.14}$$

$$M_{O_2 Cylinder} = X_{O_2} \frac{P_{cylinder}(C_{Cylinder}) V_{Chamber}}{R T_{Chamber}} \tag{7.15}$$

$$M_{N_2 Cylinder} = X_{N_2} \frac{P_{cylinder}(1 - C_{Cylinder}) V_{Chamber}}{R T_{Chamber}} \tag{7.16}$$

Case 2: Vent Chamber, Decrease Oxygen Concentration. Case 2 involves venting the CIR chamber and then refilling with ISS supplied nitrogen to lower oxygen concentration. The chamber will be vented to the intermediate pressure is calculated by Eq. 7.17. It will then be refilled to the desired P_{target} with the ISS supplied nitrogen gas. The amount of station nitrogen used is not as critical as the resource consumption of the oxygen mixture cylinder, but is calculated in Eq. 7.18.

$$P_{intermediate} = \frac{C_{target}}{C_{initial}} P_{target} \tag{7.17}$$

$$M_{N_2Station} = X_{N_2} \frac{P_{N_2Station} V_{Chamber}}{RT_{Chamber}} \tag{7.18}$$

Case 3: Increase Pressure, Decrease Oxygen Concentration. Case 3 can be reached without venting the chamber. Nitrogen gas from the station supply is added first to bring the chamber to the intermediate pressure according to Eq. 7.19. The pressure is then raised form this intermediate pressure to the final chamber pressure by adding partial pressure of Eq. 7.20 from the oxygen/nitrogen blend cylinder.

$$P_{intermediate} = P_{target} - \frac{C_{target}P_{target} - P_{initial}C_{initial}}{C_{cylinder}} \tag{7.19}$$

$$P_{cylinder} = \frac{C_{target}P_{target} - C_{initial}P_{initial}}{C_{cylinder}} \tag{7.20}$$

$$M_{O_2Cylinder} = X_{O_2} \frac{P_{cylinder}(C_{Cylinder}) V_{Chamber}}{RT_{Chamber}} \tag{7.21}$$

$$M_{N_2Cylinder} = X_{N_2} \frac{P_{cylinder}(1 - C_{Cylinder}) V_{Chamber}}{RT_{Chamber}} \tag{7.22}$$

Case 4: Increase Pressure, Increase Oxygen Concentration. The chamber filling operations for Case 4 are the same as Case 3, although the overall oxygen concentration is increased. The equations will below will be the same.

$$P_{intermediate} = P_{target} - \frac{C_{target}P_{target} - P_{initial}C_{initial}}{C_{cylinder}} \tag{7.23}$$

$$P_{cylinder} = \frac{C_{target}P_{target} - C_{initial}P_{initial}}{C_{cylinder}} \tag{7.24}$$

$$M_{O_2Cylinder} = X_{O_2} \frac{P_{cylinder}(C_{Cylinder})V_{Chamber}}{RT_{Chamber}} \tag{7.25}$$

$$M_{N_2Cylinder} = X_{N_2} \frac{P_{cylinder}(1 - C_{Cylinder})V_{Chamber}}{RT_{Chamber}} \tag{7.26}$$

It should be noted that from the standpoint of compressed gas resource consumption, low oxygen cases should be prioritized first. If the CIR atmosphere is recycled with an oxygen partial pressure that is too high, the excess oxygen is vented into space and lost forever.

7.4.2 Examples

Examples of how to apply the above calculations are shown here.

Case 1 Example. $P_{initial}$**=1 atm,** $C_{initial}$**=21%** $\rightarrow$ P_{target}**=0.5 atm,** C_{target}**=34%.** Assuming the oxygen concentration of the compressed gas cylinder is $C_{cylinder} = 0.85$, using Eq. 7.13 for the intermediate pressure of Case 1, the chamber is vented to:

$$P_{intermediate} = \frac{0.5atm}{1 + \frac{.21-.34}{.34-.85}} = 0.398atm \tag{7.27}$$

The chamber is then refilled to the target pressure $P_{target} = 0.5$ atm using the 85% oxygen compressed gas cylinder. In this operation, the resources consumed are given by Eqs. 7.14, 7.15, 7.16:

$$P_{cylinder} = \frac{.21 - .34}{.21 - .85}(0.5atm) = .1016atm \tag{7.28}$$

$$M_{O_2Cylinder} = (32\frac{g}{mol})\frac{(.1016atm)(85)(85L)}{(0.08206\frac{L*atm}{K*mol})(300K)} = 9.542g \tag{7.29}$$

$$M_{N_2Cylinder} = (28\frac{g}{mol})\frac{(.1016atm)(1-.85)(85L)}{(0.08206\frac{L*atm}{K*mol})(300K)} = 1.473g \tag{7.30}$$

Case 2 Example. $P_{initial}$**=1 atm,** $C_{initial}$**=21%** $\rightarrow$ P_{target}**=0.6 atm,** C_{target}**=17%.** Assuming the oxygen concentration of the compressed gas cylinder is $C_{cylinder} = 0.85$, using Eq. 7.17 for the intermediate pressure of Case 2, the chamber is vented to:

$$P_{intermediate} = \frac{.17}{.21}(0.6atm) = 0.486atm \tag{7.31}$$

The chamber is then refilled with station supplied nitrogen gas to the desired target pressure $P_{target} = 0.6$ atm. The amount of station nitrogen used is given by Eq. 7.18:

$$M_{N_2Station} = (28\frac{g}{mol})\frac{(0.6atm - 0.486atm)(85L)}{(0.08206\frac{L*atm}{K*mol})(300K)} = 11.021g \tag{7.32}$$

Case 3 Example. $P_{initial}$**=0.02 atm,** $C_{initial}$**=21%** $\rightarrow$ P_{target}**=1.0 atm,** C_{target}**=17%.** This example estimates the gas consumption to evacuate the chamber to its minimum pressure, and refill completely with oxygen and nitrogen. Assuming the oxygen concentration of the compressed gas cylinder is $C_{cylinder} = 0.85$, the chamber is filled with station supplied pure nitrogen until the intermediate pressure is reached according to Eq. 7.19. The chamber is then filled from the oxygen/nitrogen blend cylinder until reaching P_{target}.

$$P_{intermediate} = (1.0atm) - \frac{.17(1.0atm) - .21(0.02atm)}{.85} = 0.8049atm \tag{7.33}$$

$$M_{O_2Cylinder} = (32\frac{g}{mol})\frac{(.1951atm)(.85)(85L)}{(0.08206\frac{L*atm}{K*mol})(300K)} = 18.32g \tag{7.34}$$

$$M_{N_2Cylinder} = (28\frac{g}{mol})\frac{(.1951atm)(1-.85)(85L)}{(0.08206\frac{L*atm}{K*mol})(300K)} = 2.83g \tag{7.35}$$

$$M_{N_2Station} = (28\frac{g}{mol})\frac{(.8049atm - .02atm)(85L)}{(0.08206\frac{L*atm}{K*mol})(300K)} = 47.21g \tag{7.36}$$

Case 4 Example. $P_{initial}$**=0.02 atm,** $C_{initial}$**=17%** $\rightarrow$ P_{target}**=1.0 atm,** C_{target}**=21%.** This example estimates the gas consumption to evacuate the chamber to its minimum pressure after a low oxygen test, and refill completely with oxygen and nitrogen. Assuming the oxygen concentration of the compressed gas cylinder is $C_{cylinder} = 0.85$, the chamber is filled with station supplied pure nitrogen until the intermediate pressure is reached according to Eq. 7.19. The chamber is then filled from the oxygen/nitrogen blend cylinder until reaching P_{target}.

$$P_{intermediate} = (1.0atm) - \frac{.21(1.0atm) - .17(0.02atm)}{.85} = 0.7569atm \tag{7.37}$$

$$M_{O_2Cylinder} = (32\frac{g}{mol})\frac{(.2431atm)(.85)(85L)}{(0.08206\frac{L*atm}{K*mol})(300K)} = 22.83g \tag{7.38}$$

$$M_{N_2Cylinder} = (28\frac{g}{mol})\frac{(.2431atm)(1-.85)(85L)}{(0.08206\frac{L*atm}{K*mol})(300K)} = 3.53g \tag{7.39}$$

$$M_{N_2Station} = (28\frac{g}{mol})\frac{(.7569atm-.02atm)(85L)}{(0.08206\frac{L*atm}{K*mol})(300K)} = 71.24g \tag{7.40}$$

7.4.3 Maintaining Chamber Conditions

Because of the oxygen consumption and the generation of carbon dioxide, water, and heat, the atmosphere within the CIR chamber needs to be maintained throughout long duration testing. The chamber can be vented, and new oxygen from the compressed gas cylinders can be added. Heat will be removed by the CIR cooling loop which cycles coolant through a cold plate inside the chamber, and carbon dioxide and water will be scrubbed during testing. Oxygen and carbon dioxide sensors will be present, and can help to determine the rate at which oxygen is depleting in real time.

Species Production. In the gas flow estimates made here, a best guess at burning rate is needed. For example, a GEL sphere burning in 17% oxygen in the Vertical Oxygen Tunnel (VOT), which was described in a previous chapter, has a burning rate on the order of $\dot{m} = 0.01g/s$. Upon first approximation, complete combustion is assumed, specifically, all the mass loss from the sphere will become gaseous fuel vapor and will be converted completely to water and carbon dioxide in the flame zone. A more accurate description of the reaction products will be left to the computer modelers and measured during the experiment. The global gas phase chemical reaction is written in 7.41 in terms of moles, which can be converted more conveniently to mass in Eqs. 7.42,7.43, 7.44. where X is the respective molar mass of each component.

$$C_5H_8O_2 + 6O_2 \rightarrow 5CO_2 + 4H_2O + \Delta H_{MMA} \tag{7.41}$$

In terms of mass consumed, the products are:

$$\dot{M}_{CO_2} = 5\frac{molCO_2}{molC_5H_8O_2 consumed}\frac{X_{CO_2}}{X_{MMA}}\dot{m} = 2.2\frac{gCO_2}{gC_5H_8O_2}(0.01\frac{gC_5H_8O_2}{s}) = 0.022\frac{gCO_2}{s} \tag{7.42}$$

$$\dot{M}_{H_2O} = 4\frac{molH_2O}{molC_5H_8O_2 consumed}\frac{X_{H_2O}}{X_{MMA}}\dot{m} = 0.721\frac{gH_2O}{gC_5H_8O_2}(0.01\frac{gC_5H_8O_2}{s}) = 0.00721\frac{gH_2O}{s} \tag{7.43}$$

$$\dot{M}_{O_2} = -6\frac{molO_2}{molC_5H_8O_2 consumed}\frac{X_{O_2}}{X_{MMA}}\dot{m} = -1.92\frac{gO_2}{gC_5H_8O_2}(0.01\frac{gC_5H_8O_2}{s}) = 0.0192\frac{gO_2}{s} \tag{7.44}$$

The method and rates at which the CIR chamber can scrub carbon dioxide and water are currently unknown. An 'advertised rate' should be made available in the near future as the hardware is being developed, but ultimately these values will have to be confirmed experimentally. It should be noted that some methods of scrubbing carbon dioxide generate a large amount of heat and/or water. This will be ignored until further information is made available. If scrubbing of products can not occur fast enough, the chamber will need to be vented intermittently and throughout a test, especially to remove water before reaching saturation where condensation on cold surfaces such as the cold plate or windows can occur.

Considering the maximum burn time of $t_{burn} = 5$ minutes is suggested in the science requirements document [86], the combustion products for a 5 minute burn can be estimated as:

$$M_{CO_2Produced} = \dot{M}_{CO_2} t_{burn} = 0.022 \frac{gCO_2}{s}(300s) = 6.6g \tag{7.45}$$

$$M_{H_2OProduced} = \dot{M}_{H_2O} t_{burn} = 0.00721 \frac{gH_2O}{s}(300s) = 2.16g \tag{7.46}$$

$$M_{O_2Consumed} = \dot{M}_{O_2} t_{burn} = 0.0192 \frac{gO_2}{s}(300s) = 5.76g \tag{7.47}$$

There will be a pressure rise in the chamber due to the pyrolysis process. Under complete combustion conditions, this can be accounted for by considering the partial pressure of the reaction products. These can be calculated as:

$$P_{CO_2} = M_{CO_2Produced} \frac{RT_{chamber}}{V_{chamber} X_{CO_2}} = (6.6g) \frac{0.08206 \frac{L*atm}{K*mol}(300K)}{(85L)(44\frac{g}{mol})} = .0434atm \tag{7.48}$$

$$P_{H_2O} = M_{H_2OProduced} \frac{RT_{chamber}}{V_{chamber} X_{H_2O}} = (2.16g) \frac{0.08206 \frac{L*atm}{K*mol}(300K)}{(85L)(18\frac{g}{mol})} = .0348atm \tag{7.49}$$

Replenishing Oxygen. In order to replenish the oxygen consumed in the chemical reaction, an oxygen mass equivalent to Eq. 7.47 must be added to the chamber. Since this happens through a oxygen/nitrogen blend from the compressed gas cylinder, some nitrogen must come with the oxidizer. The partial pressure rise due to oxygen

addition is calculated in Eq. 7.50 the total pressure rise due to the addition from the oxygen cylinder is then Eq. 7.51.

$$P_{O_2 cylinder} = M_{O_2 Consumed} \frac{RT_{chamber}}{V_{chamber} X_{O_2}} = (5.76g) \frac{0.08206 \frac{L*atm}{K*mol} (300K)}{(85L)(32 \frac{g}{mol})} = 0.0521atm \tag{7.50}$$

$$P_{cylinder} = P_{O_2 cylinder} / C_{cylinder} = \frac{0.0521atm}{.85} = 0.0613atm \tag{7.51}$$

This added pressure rise scales with the concentration of the compressed oxygen nitrogen blend. The highest oxygen percentage cylinders should be used to minimize this, as the excess pressure will have to be vented from the chamber and lost to space forever. If the CO_2 and H_2O are not able to be scrubbed, then the total pressure to vent will also rise, this will take the form:

$$P_{vent} = P_{CO_2} + P_{H_2O} + P_{cylinder} = .0434atm + 0.0348atm + 0.0613atm = 0.140atm \tag{7.52}$$

Removal of Water. Keeping the water concentration of the combustion chamber within acceptable limits is critical to the success of the long duration burns. The atmosphere can only hold a finite amount of water before condensation begins on the cold surfaces. The CIR coolant flows through the cold plate at 18.3^oC [84]. The Arden Buck Equation [87] in Eq 7.53 calculates the saturation vapor pressure of water vapor based on temperature at 1 atm. Temperature is in Celsius and pressure is in

atmospheres. The buck equation gives the maximum vapor pressure of water before condensation occurs.

$$P_{saturation} = 0.61121 exp((18.678 - \frac{T}{234.5})(\frac{T}{257.14 + T}))(0.009869) \tag{7.53}$$

For the surface of a cold plate that is at the coolant temperature, 18.3^oC, the saturation vapor pressure is then $P_{saturation} = 0.0208$ atm. In terms of water mass in the CIR chamber, this would be

$$M_{saturation} = X_{H_2O}\frac{P_{saturation}V_{chamber}}{RT_{chamber}} = (18.02\frac{g}{mol})\frac{(.0208atm)(85L)}{(0.08206\frac{L*atm}{K*mol})(300K)} = 1.29g \tag{7.54}$$

Note that for the saturation vapor pressure, the cold plate temperature is used to estimate the saturation pressure, when the water will condense. When converting to the equally distributed mass in the chamber, the bulk chamber temperature is used, since most of this water mass is far from the coldest condensing surface. If the amount of water in the chamber goes above 1.29 g, condensation of liquid water will occur on the cold plate.

In the section on combustion products, Eq 7.46 estimates a water production of 2.16 g throughout the test. At least 0.87 g of this needs to be removed by scrubbers. Ideally, all of the water will be removed. Air recirculates through the CIR filters at 20 SLM [85]. It is unknown how effective filtration will be, but at this rate, the amount of water passing through the filter will be:

$$\dot{M}_{filteredwater} = X_{H_2O}\frac{P_{H_2O}V_{FilterLoop}}{RT_{chamber}} = P_{H_2O}\frac{(18g/mol)(20\frac{L}{Min})}{.08206\frac{L*atm}{K*mol}(300K)} = 14.62P_{H_2O}g/min \tag{7.55}$$

The speed of filtration is partially dependent on the partial pressure of water. At saturation, the maximum rate of filtration would be $\dot{M}_{filteredwater} = 0.304$ g/min. A more realistic estimate would be to use about half of the saturation partial pressure. Since the chamber will not be at the water saturation vapor pressure all the time, a conservative estimate would be to use about 1/2 of this value. This means that about $\dot{M}_{filteredwater} = 0.152$ g/min can be removed. This is 0.76 g of water removed over a 5 minutes test. This is just short of the 0.87 g needed.

Removal of Heat. The heat generated during the chemical reaction, $\Delta H_{MMA} = -2748.7kJ/mol = -27.5kJ/g$ is the heat of combustion of methyl methacrylate, the gaseous monomer of the pyrolyzed poly(methyl methacrylate) solid material. Because of the close proximity of the flame to the fuel, much of this heat will be lost to the thick solid fuel surface and to the latent heat of sublimation to maintain fuel vaporization. Some heat will be lost to the chamber walls and equipment within the chamber, but the majority of the heat will have to be removed by the CIR cooling loop. The cooling water flows through a cold plate inside the chamber at an inlet temperature of 65^oF [84], but the actual cooling capability of the plate will need to be determined experimentally.

The amount of excess from the flame can be estimated as the heat of combustion minus the heat conduction into the solid interior and latent heat of vaporization:

$$\dot{Q} = \dot{Q}_{flame} - \dot{Q}_{fuelinterior} - \dot{Q}_{pyrolysis} \tag{7.56}$$

where $\dot{Q}_{flame}$ is the heat generated by the flame, $\dot{Q}_{fuelinterior}$ is the loss of energy to the interior of the solid, $\dot{Q}_{pyrolysis}$ is the loss of energy to the phase change of the fuel

$$\dot{Q}_{flame} = \Delta H_{MMA}\dot{M}_{MMA} = (27.5\frac{kJ}{g})(0.01\frac{g}{s}) = 275W \tag{7.57}$$

$$\dot{Q}_{fuelinterior} = \dot{Q}''A_{fuel} = 2.5\frac{W}{cm^2}\frac{4}{3}\pi(2cm)^2 = 125W \tag{7.58}$$

$$\dot{Q}_{pyrolysis} = L_v\dot{M}_{MMA} = (1000\frac{J}{g})(0.01\frac{g}{s}) = 10W \tag{7.59}$$

Then the excess heat according to Eq. 7.56 is $\dot{Q}$ = 140 W. This will have to be removed by the cold plate or absorbed by the chamber walls and equipment to keep the temperature constant.

7.4.4 Estimated Gas Consumption

A conservative baseline estimate of gas resource consumption for initial chamber fills can be made by multiplying example case 4 by 50 tests. This would give the resources consumed by venting the combustion chamber to its minimum pressure and refilling to 21% oxygen at 1 atm. This would consume $M_{O_2Cylinder}$=1141.5 g, $M_{N_2Cylinder}$=176.5 g, $M_{N_2Station}$=3562.0 g. Note that this 21% concentration at 1 atmosphere is also accurate for the oxygen/nitrogen blend usage for all chamber fills along the normoxic

curve. Only the station supplied nitrogen would be different. All other tests at reduced oxygen would consume less than this conservative value.

A conservative estimate of the amount of gas needed to counterbalance the oxygen consumption by the flame during each burn can also be made by multiplying $M_{O_2Consumed}$ from Eq. 7.47 by 50 tests. This gives 288 g of oxygen consumed from the oxygen/nitrogen blend cylinder.

Total oxygen consumption is then 1429.5 g needed throughout the GEL experiment campaign. This requires a quantity of ten 1 L bottles of 85% oxygen and 15% nitrogen charged to 2000 psig.

7.5 Discussion

The science requirements have already been agreed upon with hardware vender, ZIN Technologies, who will design and build the final SoFIE flight hardware. The design phase is currently ongoing, and actual fabrication will begin in the near future. Hopefully this chapter can help to guide their development and outline any known pitfalls moving forward. As mentioned above, the main peril for GEL is the possibility of igniter system failure, and ZIN is working on methods to ruggedize the hotwire scheme to survive multiple ignitions.

Equations and examples have also been worked out to estimate resource gas consumption in the GEL project. They have also been couched in a manner which can be referenced when conducting operations in the future. Fill procedures have been outlined for filling the combustion chamber with new gas before an experiment and

for conserving gasses by recycling previously used atmospheric conditions if resources become scarce.

The section on water production and condensation constrains the GEL maximum burn time if other methods for water removal can not be implemented.

This section also refines the originally proposed test matrix based on the results of previous chapters of this work and ranks the experiments in order of importance. Specifically, the results of the experiment campaign in Chapter 6 in the NASA Zero Gravity Research Facility have helped to resolve many of the "To Be Determined" conditions in the original proposal.

8 Closing Summary

This work explored the effect of material preheating and heat loss to the interior on solid fuel combustion in the low speed microgravity conditions that are common in spacecraft. Two related experimental configurations were used, the bottom stagnation zone of large diameter spherical shells in buoyant flow, and the forward stagnation zone of smaller diameter spheres tested in purely forced flow in the NASA Zero Gravity Research Facility (ZGRF). The correspondence between these two configurations was related via the stretch rate parameter which was fixed at approximately 7.9 1/s for the spherical shells and varied across a range of 1.5-20 1/s for the spheres.

Heat loss to the interior of spherical shells was controlled by choice of shell thickness between 2.5-12 mm and a 0^oC ice bath in contact with the back surface. The nearly constant nature of the pyrolysis temperature lends itself to a constant in depth temperature profile and heat conduction away from the pyrolyzing surface can be established independent of flow conditions. The reaction of the flame to progressively decreasing oxidizer concentration was observed. Because the experiments were performed in a buoyant field, real time gravimetric measurement of mass loss was possible. Burning rate is uniform in a stagnation flame, so local burning rate was

calculated by dividing mass loss rate by exposed surface area for each oxygen concentration and heat loss. Local burning rate decreased approximately linearly with decreasing oxygen concentration. Local burning rate increased with decreased heat loss to the solid interior since more energy is available for pyrolysis.

The transient flame response on 4 cm diameter PMMA spheres after a step change from 1g to microgravity was observed in NASA ZGRF in a flow range from 2 cm/s to 25 cm/s at 17% oxygen concentration by volume. Heat loss to the solid interior was calculated from the realtime temperature profile near the stagnation region as measured by thermocopules embedded in the sample. Precise thermocouple locations were measured before and after each experiment with computed tomography. A flammability boundary was mapped on the axis of heat loss to the solid interior and freestream flow velocity. The microgravity flame was qualitatively different in the wake region of the sphere, but the stagnation zone displays the similarity with the shell experiments as expected from previous works. The flame standoff distances were measured in the stagnation region during each test. The last measurable flame standoff distance (before self extinction or before the drop test ended) was shown to inversely vary with increased heat loss to the sold interior over the range tested. The standoff distance measured before extinction plotted against freestream velocity forms a boundary which describes flame quenching distance. Surviving flames must have a larger standoff than the quenching distance. Future work in the NASA ZGRF should be expanded to include the proposed future space exploration atmospheres at reduced pressure along the normoxic curve.

Some of this work focused on preparing for the Growth and Extinction Limits (GEL) flight experiment which is scheduled to go the International Space Station in

a few years as a part of the Solid Flammability, Ignition, and Extinction (SoFIE) investigation. The proposed test conditions were refined in response to the ground experiments conducted and major pitfalls were outlined. With the test campaign in the ZGRF, the GEL sample prototypes have been tested in actual microgravity conditions.

To facilitate 1g testing in reduced oxygen, a vertical variable oxygen tunnel was designed and built with dimensions similar to the wind tunnel proposed for SoFIE. The apparatus is capable of measuring burning rate in real time and changing gas conditions via computer control. The device has found much use with other combustion researchers.

As a closing remark, much of the progress on solid fuel combustion in microgravity environments was made in the 1990's either as featured research aboard the Space Shuttle Orbiter or as ground based support of those experiments, but they had just scratched the surface of progress. After the International Space Station (ISS) construction was considered complete, there was a transition to prioritizing the use as a science facility. With this came a resurgence of interest in microgravity combustion science with the Combustion Integrated Rack becoming operational and combustion experiments occupying the Microgravity Science Glovebox over the last few years. At the time of this writing, the SoFIE project is the last microgravity combustion experiment planned aboard the ISS before it is decommissioned around 2024. The Space Shuttle Program was decommissioned with the promise of a replacement transport which has not yet come to fruition. There has been no serious effort for a replacement for the ISS. Microgravity research could conceivably end if interest and investment in space exploration is not renewed.

Appendix A: Variable Oxygen Tunnel: Flow System Parts List

The parts used in the Variable Oxygen Tunnel flow system are listed below. Parts are made from 316L stainless steel unless listed otherwise.

Item #	Part #	Manuf.	Description
N-1	NI300	Airgas	Nitrogen K-cylinder (2400 psi MAX)
N-2	Y11-215D	Airgas	Nitrogen regulator valve, 3500 psi MAX
N-3	Y11-215D	Airgas	High pressure gauge 0-400 psi
N-4	Y11-215D	Airgas	Low pressure gauge 0-200 psi
N-5	Y11-215D	Airgas	Needle valve
N-6	SS-FL4TA4TA4-36	Swagelok	1/4" stainless steel braided stainless steel hose - 36" long
N-7	SS-400-3-4TTF	Swagelok	1/4" tube x 1/4" tube x 1/4" FNPT tee
N-8	SS-RL3M4A-F4	Swagelok	1/4" MNPT Relief Valve 50-350 psi
N-9	SS-400-3	Swagelok	1/4" tube tee
N-10	SS-810-6-4	Swagelok	1/2" x 1/4" reducing union (tube)
N-11	SS-8-WVCO-6-810	Swagelok	1/2" FVCO to 1/2" tube adapter
N-12	1559A00451LG1BV	mks Insruments	50,000 SCCM argon mass flow controller
N-13	SS-8-WVCO-6-810	Swagelok	1/2" FVCO to 1/2" tube
N-14	SS-4-WVCR-6-400	Swagelok	VCR face seal 1/4" wvcr to 1/4" tube
N-15	1179AX13CR14V26	mks Instruments	1,000 SCCM nitrogen mass flow controller, Viton
N-16	SS-4WVCR-6-400	Swagelok	Face seal VCR 1/4" WVCR to 1/4" tube
N-17	SS-810-9	Swagelok	1/2" elbow
N-18	SS-810-3-8-4	Swagelok	1/2" x 1/2" x 1/4" tee
A-1	AI300	Airgas	Air K-cylinder (2400 psi MAX)
A-2	Y11215D590	Airgas	Air regulator 0-100 psi CGA-590
A-3	Y11215D590	Airgas	High pressure gauge
A-4	Y11215D590	Airgas	Low pressure gauge
A-5	Y11215D590	Airgas	Needle valve
A-6	SS-FL4TA4TA4-36	Swagelok	1/4" stainless steel braided stainless steel hose - 36" long
A-7	SS-400-3-4TTF	Swagelok	1/4" tube x 1/4" tube x 1/4" FNPT tee
A-8	SS-RL3M4A-F4	Swagelok	1/4" MNPT relief valve 10-225 psig
A-9	SS-810-6-4	Swagelok	1/2" x 1/4" reducing union
A-10	SS-8-WVCO-6-810	Swagelok	1/2" FVCO to 1/2" tube
A-11	1559A00451LG1BV	Swagelok	50,000 SCCM argon mass flow controller
A-12	SS-8-WVCO-6-810	Swagelok	1/2" FVCO to 1/2" tube
O-1	OI300	Airgas	Oxygen k-cylinder (2400 psi MAX)
O-2	3121-540	Matheson	Oxygen regulator valve, 3500 psi max CGA-540
O-3	3121-540	Matheson	High pressure gauge 0-3000 psi
O-4	3121-540	Matheson	Low pressure gauge 0-60 psi
O-5	3121-540	Matheson	Needle valve
O-6	SS-FL4TA4TA4-36	Swagelok	1/4" stainless steel braided stainless steel hose - 36" long
O-7	SS-400-3-4TTF	Swagelok	1/4" tube x 1/4" tube x 1/4" FNPT tee
O-8	CRN08314410	Kingston	Safety relief valve - set at 40 psi
O-9	6L-CW454	Swagelok	proportional check valve
O-10	SS-400-3	Swagelok	1/4" tube tee
O-11	SS-810-6-4	Swagelok	1/2" x 1/4" reducing union (tube)
O-12	SS-8-WVCO-6-810	Swagelok	1/2" FVCO x 1/2" tube
O-13	1559A00451LG1BV	mks Instruments	50,000 SCCM argon mass flow controller
O-14	SS-8-WVCO-6-810	Swagelok	1/2" FVCO x 1/2" tube
O-15	SS-4-WVCR-6-400	Swagelok	VCR face seal 1/4" WVCR to 1/4" tube
O-16	1179AX13CR14V26	mks Instruments	1,000 SCCM nitrogen mass flow controller, viton
O-17	SS-4-WVCR-6-400	Swagelok	VCR face seal 1/4" WVCR to 1/4" tube
O-18	SS-810-9	Swagelok	1/2" elbow
O-19	SS-810-3-8-4	Swagelok	1/2" x 1/2" x 1/4" tee (tube)
M-1	SS-810-4	Swagelok	Stainless steel 1/2" union (cross)
M-2	SS-810-1-8	Swagelok	1/2" tube x 1/2" MNPT union
M-3	SS-QF8-S-8PF	Swagelok	stainless steel full flow quick connect stem 1/2" FNPT
M-4	SS-QF8-B-810	Swagelok	stainless steel full flow quick connect body 1/2" tube
M-5	SS-FL8-TA8TA8-12	Swagelok	stainless steel braided stainless steel hose 1/2" tube - 12"
M-6	SS-QF8-B-810	Swagelok	stainless steel full flow quick connect body 1/2" tube
M-7	SS-QF8-S-8PM	Swagelok	stainless steel quick connect stem 1/2" MPNT

Table 8.1. Table of Variable Oxygen Tunnel Flow Parts

Appendix B: Variable Oxygen Tunnel: Wiring Chart

The wiring of the Variable Oxygen Tunnel is described below.

Terminal #	Type	Connection 1	Color 1	Connection 2	Color 2	Bridge
1	SETPOINT	AO ACH0-0	BLU	O1-8	GRN/WHT	
2	SETPOINT	AO ACH1-0	RED/BLK	O2-6	GRN/WHT	
3	SETPOINT	AO ACH2-0	WHT/BLK	A-8	GRN/WHT	
4	SETPOINT	AO ACH3-0	OR	N1-8	GRN/WHT	
5	SETPOINT	AO ACH4-0	WHT	N2-6	GRN/WHT	
6	FLOWRATE	AI ACH0-0	GRN/BLK	O1-2	GRN/BLK	
7	FLOWRATE	AI ACH1-0	OR/BLK	O2-2	GRN/BLK	
8	FLOWRATE	AI ACH2-0	BLU/BLK	A-2	GRN/BLK	
9	FLOWRATE	AI ACH3-0	RED	N1-2	GRN/BLK	
10	FLOWRATE	AI ACH4-0	BLU/WHT	N2-2	GRN/BLK	
11	SIGNAL GND	DAQ	GRN	01-11	BLU	1
11				O1-12	BLU/WHT	1
12	SIGNAL GND	DAQ	GRN/WHT	02-7	BLU	1
12				O2-8	BLU/WHT	1
13	SIGNAL GND	DAQ	RED/WHT	A-11	BLU	1
13				A-12	BLU/WHT	1
14	SIGNAL GND	DAQ	BLK	N1-11	BLU	1
14				N1-12	BLU/WHT	1
15	SIGNAL GND	DAQ	BLU/WHT	N2-7	BLU	1
15				N2-8	BLU/WHT	1
16	EARTH GND	DAQ	BLU	01-5	RED	1
16				O1-15	BLK	1
17	+/-15VDC GND	+/-15VDC SUPPLY	GRN	O2-4	RED	1
17				O2-SHLD	BLK	1
18	+/- 12VDC GND	+/- 12VDC SUPPLY	BLK	A-5	RED	1
18				A-15	BLK	1
19	E-STOP GND	E-STOP	OR	N1-5	RED	1
19				N1-15	BLK	1
20	GND			N2-4	RED	1
20		TRMNL33-LED	BLU	N2-SHLD	BLK	1
21	+15VDC	NC		O1-7	RED/BLK	2
21				O2-3	RED/BLK	2
22	+15VDC	NC	NC	A-7	RED/BLK	2
22				N1-7	RED/BLK	2
23	+15VDC	+15VDC PWR SUPPLY	WHT	N2-3	RED/BLK	2
24	-15VDC	-15VDC PWR SUPPLY	BLK	O1-6	RED/WHT	3
24				O2-5	RED/WHT	3
25	-15VDC	NC	NC	A-6	RED/WHT	3
25				N1-6	RED/WHT	3
26	-15VDC	NC	NC	N2-5	RED/WHT	3
27						
28	E-STOP	NC	NC	O1-3	OR	4
29	E-STOP	NC	NC	O2-1	OR	4
30	E-STOP	NC	NC	A-3	OR	4
31	E-STOP	NC	NC	N1-4	OR/BLK	4
32	E-STOP	E-STOP	RED	N2-1	OR	4
33	GND	TMNL20-LED	BLU	LED-GND	BLK	
34	+12VDC	+12VDC-LED	RED	LED-POS	RED	
35	IGNITER	RELAY-0A	RED	VAR PWR	RED	
36	IGNITER	RELAY-0B	BLK	IGN HOT	RED	
37		RELAY-1A	WHT			
38		RELAY-1B	GRN			

Table 8.2. Variable Oxygen Tunnel Wiring Chart

Appendix C: Zero-G Facility Tests: Time Codes

The information contained in the timestamps for the two high resolution cameras aboard the Zero-G drop rig and the data acquisition system are not precisely synchronized. The data below can be used as a key to align information in the raw data files if they are to be analyzed further in the future. It was obtained from writing down the time code from each significant video frame from the GigE front view camera and GigE side view camera and from the excel output file of the Zero-G facility. The time listed in "Zeroed Time" synchornizes 0s with the drop trigger command. Note that due to frame rate and data sampling rate, there is some error in time synchronization of less than 10 ms.

9/9/16	GigE Front	GigE Side	Kinetics	Zeroed Time
Ignition Start			10:07:44.1	-39.553
Ignition Stop			10:08:03.9	-19.787
Flow Change Start			10:07:57.8	-25.853
Flow Change at Sample				
Drop	10:06:09.451	10:06:09.449	10:08:223.6	-0.053
Extinction	10:06:13.687	10:06:13.682		
Impact	10:06:14.597	10:06:14:615		

Table 8.3. Drop test 1 time synchronization

9/28/16	GigE Front	GigE Side	Kinetics	Zeroed Time
Ignition Start			9:57:28.5	-120.73
Ignition Stop			9:57:48.4	-100.8
Flow Change Start			9:57:45.6	-103.57
Flow Change at Sample				
Drop	9:58:36.139	9:58.36.175	9:59:29.2	-0.00057
Extinction	9:58:40.615	9:58:40.642		
Impact	9:58:41.323	9:58:41.342		

Table 8.4. Drop test 2 time synchronization

10/4/16	GigE Front	GigE Side	Kinetics	Zeroed Time
Ignition 1 Start			9:58:32.5	-54.96
Ignition 1 Stop			9:58:52.4	-35.02
Ignition 2 Start			9:59:02.4	-24.99
Ignition 2 Stop			9:59:16.7	-10.76
Flow Change Start			9:58:50.1	-37.32
Flow Change at Sample				
Drop	9:57:45.481	9:57:45.510	9:57:27.4	.011
Extinction	9:57:48.010	9:57:48.010		
Impact	9:57:50.673	9:57:50.676		

Table 8.5. Drop test 3 time synchronization

10/13/16	GigE Front	GigE Side	Kinetics	Zeroed Time
Ignition Start			10:06:52.2	-57.21
Ignition Stop			10:07:12.1	-37.27
Flow Change Start			10:07:21.6	-27.81
Flow Change at Sample				
Drop	10:06:30.446	10:06:30.452	10:07:49.4	-.0064
Extinction	10:06:34.380	10:06:34.385		
Impact	10:06:35.584	10:06:35.618		

Table 8.6. Drop test 4 time synchronization

4/18/17	GigE Front	GigE Side	Kinetics	Zeroed Time
Ignition Start			11:35:54	-51.03
Ignition Stop			11:36:14	-31.10
21% 25 cm/s			11:36:26	-19.63
17% 25 cm/s			11:36:32	-12.86
Drop	11:39:03.236	11:49:03.227	11:36:45	.0035
Impact	11:49:08.359	11:49:08.360		

Table 8.7. Drop test 5 time synchronization

4/19/17	GigE Front	GigE Side	Kinetics	Zeroed Time
Ignition Start			10:45:44	-47.86
Ignition Stop			10:46:04	-27.96
21% 15 cm/s			10:46:12	-19.89
17% 15 cm/s			10:46:17	-15.49
Drop	10:58:53.808	10:58:53.816	10:46:32	.006
Extinction	10:58:57.291	10:58:57.313		3.497
Impact	10:58:58.943	10:58:58.947		

Table 8.8. Drop test 6 time synchronization

5/2/17	GigE Front	GigE Side	Kinetics	Zeroed Time
Ignition 1 Start			10:30:26	-73.29
Ignition 1 Stop				-53.36
21% 20 cm/s				-45.39
17% 20 cm/s				-41.05
Ignition 2 Start			10:31:09	-30.35
Ignition 2 Stop			10:31:29	-10.39
Drop	10:44:57.505	10:44:57.487	10:31:39	-.053
Impact	10:45:02.649	10:45:02.653		5.144

Table 8.9. Drop test 7 time synchronization

5/3/17	GigE Front	GigE Side	Kinetics	Zeroed Time
Ignition Start			9:58:47.5	-50.00
Ignition Stop			9:59:07.4	-30.10
21% 20 cm/s			9:59:26.1	-11.40
17% 19.6 cm/s			9:59:28.7	-8.73
Drop	10:13:00.458	10:13:00.483	9:59:37.4	-.032
Extinction	10:13:03.020	10:13:02.983		2.532
Impact	10:13:05.615	10:13:05.616	9:59:42.4	4.935

Table 8.10. Drop test 8 time synchronization

5/9/17	GigE Front	GigE Side	Kinetics	Zeroed Time
Ignition Start			12:04:14.9	-109.39
Ignition Stop			12:04:34.8	-89.46
17% 15 cm/s			12:05:51.7	-12.66
Drop	13:53:37.517	13:53:37.528	12:06:04.2	-0.02
Impact	13:53:42.674	13:53:42.678	12:06:09.2	4.88

Table 8.11. Drop test 9 time synchronization

5/10/17	GigE Front	GigE Side	Kinetics	Zeroed Time
Ignition 1 Start			12:03:47.1	-200.42
Ignition 1 Stop			12:04:07.1	-180.42
Ignition 2 Start			12:05:37.5	-90.05
Ignition 2 Stop			12:05:57.4	-70.15
Ignition 3 Start			12:05:59.1	-68.42
Ignition 3 Stop			12:06:19.1	-48.42
Ignition 4 Start			12:06:36.7	-30.82
Ignition 4 Stop			12:06:56.7	-10.82
17% 6 cm/s			12:06:53.4	-14.15
Drop	10:43:30.053	10:43:30.067	12:07:07.3	-0.188
Impact	10:43:35.251	10:43:35.258	12:07:12.3	4.81

Table 8.12. Drop test 10 time synchronization

5/16/17	GigE Front	GigE Side	Kinetics	Zeroed Time
Ignition Start			12:03:55.0	-82.94
Ignition Stop			12:04:14.9	-63.00
17% 6 cm/s			12:04:42.2	-35.74
Drop	10:14:10.726	10:14:10.724	12:05:17.9	-0.069
Impact	10:14:15.878	10:14.15.890	12:05:22.8	4.90

Table 8.13. Drop test 11 time synchronization

5/17/17	GigE Front	GigE Side	Kinetics	Zeroed Time
Ignition Start			12:03:36.8	-64.86
Ignition Stop			12:03:56.7	-44.93
17% 4 cm/s			12:04:09.2	-32.46
Drop			12:04:41.6	-0.06
Impact			12:04:46.6	4.94

Table 8.14. Drop test 12 time synchronization

5/23/17	GigE Front	GigE Side	Kinetics	Zeroed Time
Ignition 1 Start			12:04:05.1	-111.43
Ignition 1 Stop			12:04:25.1	-91.46
17% 2 cm/s			12:05:18.7	-37.89
Drop	13:20:57.947	13:20:57.932	12:05:56.4	-0.13
Impact	13:21:03.102	13:21:03.098	12:05:56.4	4.84

Table 8.15. Drop test 13 time synchronization

References

[1] Makoto Endo. Numerical modeling of flame spread over spherical solid fuel under low speed flow in microgravity: Model development and comparison to space flight experiments. PhD thesis, Case Western Reserve University, 2016.

[2] Sandra L Olson. Buoyant low stretch stagnation point diffusion flames over a solid fuel. PhD thesis, Case Western Reserve University, 1997.

[3] JS T'ien. The possibility of a reversal of material flammability ranking from normal gravity to microgravity. Combustion and Flame, 80(3-4):355–357, 1990.

[4] Paul V Ferkul and Sandra L Olson. Zero-gravity centrifuge used for the evaluation of material flammability in lunar gravity. Journal of Thermophysics and Heat Transfer, 25(3):457–461, 2011.

[5] David W. Foutch and James S. T'ien. Extinction of a stagnation-point diffusion flame at reduced gravity. AIAA journal, 25(7):972–976, 1987.

[6] Paul Ferkul, Julie Kleinhenz, Hsin-Yi Shih, Richard Pettegrew, Kurt Sacksteder, and James Tien. Solid fuel combustion experiments in microgravity using a continuous fuel dispenser and related numerical simulations. Microgravity Science and Technology, 15(2):3–12, 2004.

[7] Vedha Nayagam, Daniel L Dietrich, Paul V Ferkul, Michael C Hicks, and Forman A Williams. Can cool flames support quasi-steady alkane droplet burning? Combustion and Flame, 159(12):3583–3588, 2012.

[8] Sandra L Olson. Mechanisms of microgravity flame spread over a thin solid fuel: oxygen and opposed flow effects. Combustion Science and Technology, 76(4-6): 233–249, 1991.

[9] Fumiaki Takahashi and Viswanath R Katta. Reaction kernel structure and stabilizing mechanisms of jet diffusion flames in microgravity. Proceedings of the Combustion Institute, 29(2):2509–2518, 2002.

[10] John Kuhlman and Kyle Phillips. Development of the wvu 1.25 s reduced-gravity drop tower. In 53rd AIAA Aerospace Sciences Meeting, page 2018, 2015.

[11] William A Dittrich. Drop tower physics. The Physics Teacher, 52(7):415–417, 2014.

[12] SL Olson and FJ Miller. Experimental comparison of opposed and concurrent flame spread in a forced convective microgravity environment. Proceedings of the Combustion Institute, 32(2):2445–2452, 2009.

[13] SL Olson, FJ Miller, S Jahangirian, and IS Wichman. Flame spread over thin fuels in actual and simulated microgravity conditions. Combustion and Flame, 156(6):1214–1226, 2009.

[14] Richard Dale Pettegrew. An experimental study of ignition effects and flame growth over a thin solid fuel in low-speed concurrent flow using drop-tower facilities. PhD thesis, Case Western Reserve University, 1996.

[15] SL Olson, MC Johnston, SY Hsu, JS T'ien, and PV Ferkul. Experiments and modeling of normal gravity ignition and transition to microgravity of a pmma sphere in a forced convective flow. In 7th US National Meeting of the Combustion Institute, 2011.

[16] JB Armstrong, SL Olson, and JS T'ien. Transient model and experimental validation of low-stretch solid-fuel flame extinction and stabilization in response to a step change in gravity. Combustion and Flame, 147(4):262–277, 2006.

[17] T Kashiwagi, KB McGrattan, SL Olson, O Fujita, M Kikuchi, and K Ito. Effects of slow wind on localied radiative ignition and transition to flame spread in microgravity. Proceedings of the Combustion Institute, 26(1):1345–1352, 1996.

[18] Osamu Fujita, Katsuhiro Nishizawa, and Kenichi Ito. Effect of low external flow on flame spread over polyethylene-insulated wire in microgravity. Proceedings of the Combustion Institute, 29(2):2545–2552, 2002.

[19] Kurt R Sacksteder, Ioan I Feier, Hsin-Yi Shih, and James S T'ien. Three-dimensional upward flame spreading in partial-gravity buoyant flows. Technical report, Sixth international microgravity combustion workshop, NASA/CP-2001-210826, 2001.

[20] Ioan I Feier, Hsin-Yi Shih, Kurt R Sacksteder, and James S T'ien. Upward flame spread over thin solids in partial gravity. Proceedings of the Combustion Institute, 29(2):2569–2577, 2002.

[21] Jiann C Yang, Anthony Hamins, and Michelle K Donnelly. Reduced gravity combustion of thermoplastic spheres. Combustion and Flame, 120(1):61–74, 2000.

[22] S Rouvreau, P Cordeiro, JL Torero, and P Joulain. Influence of g-jitter on a laminar boundary layer type diffusion flame. Proceedings of the Combustion Institute, 30(1):519–526, 2005.

[23] Pierre Joulain, Pierre Cordeiro, Sébastien Rouvreau, Guillaume Legros, Andres Fuentes, and José L Torero. Influence of g-jitter on the characteristics of a non-premixed flame: Experimental approach. Microgravity Science and Technology, 16(1):328–332, 2005.

[24] Thomas Vietoris, Janet L Ellzey, Pierre Joulain, Shivani N Mehta, and José L Torero. Laminar diffusion flame in microgravity: the results of the minitexus 6 sounding rocket experiment. Proceedings of the Combustion Institute, 28(2): 2883–2889, 2000.

[25] Sandra L Olson, U Hegde, S Bhattacharjee, JL Deering, L Tang, and RA Altenkirch. Sounding rocket microgravity experiments elucidating diffusive and radiative transport effects on flame spread over thermally thick solids. Combustion Science and Technology, 176(4):557–584, 2004.

[26] C. Sanchez Tarifa and B. Lazaro. Experiments conducted on combustion of a solid at microgravity in the texus-38 sounding rocket. results and conclusions. In O. Minster and B. Schürmann, editors, Microgravity Research and Aplications in Physical Sciences and Biotechnology, volume 454 of ESA Special Publication, page 267, 2001.

[27] JH Kimzey. Skylab results: Proceedings of the 3rd space processing symposium, vol. 1. Technical report, NASA TM-X-70752: Marshall Space Flight Center, 1974.

[28] Prashant A Ramachandra, Robert A Altenkirch, Subrata Bhattacharjee, Lin Tang, Kurt Sacksteder, and M Katherine Wolverton. The behavior of flames spreading over thin solids in microgravity. Combustion and Flame, 100(1):71–84, 1995.

[29] Jeff West, Lin Tang, Robert A Altenkirch, Subrata Bhattacharjee, Kurt Sacksteder, and Michael A Delichatsions. Quiescent flame spread over thick fuels in microgravity. Proceedings of the Combustion Institute, 26(1):1335–1343, 1996.

[30] Robert A Altenkirch, Lin Tang, Kurt Sacksteder, Subrata Bhattacharjee, and Michael A Delichatsios. Inherently unsteady flame spread to extinction over thick fuels in microgravity. Proceedings of the Combustion Institute, 27(2):2515–2524, 1998.

[31] RA Altenkirch, MF Bundy, L Tang, S Bhattacharjee, K Sacksteder, and MA Delichatsios. Reflight of the solid surface combustion experiment: Flame radiation near extinction. Technical report, Fifth international microgravity combustion workshop, NASA/CP-19990053971, 1999.

[32] Takashi Kashiwagi and Sandra L Olson. Radiative ignition and transition to spread investigation (ritsi). In United States Microgravity Payload: One Year Report, pages 97–118. NASA/CP-1998-207891, 1998.

[33] AV Ivanov, Ye V Balashov, TV Andreeva, and AS Melikhov. Experimental verification of material flammability in space. Technical report, NASA/CR-1999-209405, 1999.

[34] David L Urban, Peter B Sunderland, and Zeng-Guang Yuan. Smoke point in co-flow experiment. Technical report, NASA JSC-17962-41, 2009.

[35] Keenan T Dotson, Peter B Sunderland, Zeng-Guang Yuan, and David L Urban. Laminar smoke points in coflow measured aboard the international space station. In 48th AIAA Aerospace Sciences Meeting, Orlando, FL, pages 4–7, 2010.

[36] Bin Ma, Su Cao, Davide Giassi, Dennis P Stocker, Fumiaki Takahashi, Beth Anne V Bennett, Mitchell D Smooke, and Marshall B Long. An experimental and computational study of soot formation in a coflow jet flame under microgravity and normal gravity. Proceedings of the Combustion Institute, 35(1):839–846, 2015.

[37] Paul V Ferkul, Sandra L Olson, Fumiaki Takahashi, Makoto Endo, Michael C Johnson, and James S T'ien. Thickness and fuel preheating effects on material flammability in microgravity from the bass experiment. In American Society for Gravitational and Space Research (ASGSR) Annual Meeting. 3-8 Nov. 2013; Orlando, FL; United States, 2013.

[38] Xiaoyang Zhao, Ya-Ting T Liao, Michael C Johnston, James S. T'ien, Paul V Ferkul, and Sandra L Olson. Concurrent flame growth, spread, and quenching over composite fabric samples in low speed purely forced flow in microgravity. Proceedings of the Combustion Institute, 36(2):2971–2978, 2017.

[39] Paul V Ferkul, Sandra Olson, Michael C Johnston, and James T'ien. Flammability aspects of a cotton-fiberglass fabric in opposed and concurrent airflow in microgravity. In American Society for Gravitational and Space Research (ASGSR) Annual Meeting. 28 Nov. 2012; New Orleans, LA; United States, 2012.

[40] Paul V Ferkul, Subrata Bhattacharjee, Carlos Fernandez-Pello, Fletcher Miller, Sandra L Olson, Fumiaki Takahashi, and James S T'ien. Combustion of solids in microgravity: Results from the bass-ii experiment. In American Society for Gravitational and Space Research (ASGSR) Annual Meeting. 23-26 Oct. 2014; Pasadena, CA; United States, 2014.

[41] Subrata Bhattacharjee, Matthew Laue, Luca Carmignani, Paul Ferkul, and Sandra Olson. Opposed-flow flame spread: A comparison of microgravity and normal gravity experiments to establish the thermal regime. Fire Safety Journal, 79:111–118, 2016.

[42] Sandra L Olson and Paul V Ferkul. Microgravity flammability boundary for pmma rods in axial stagnation flow: Experimental results and energy balance analyses. Combustion and Flame, 180:217–229, 2017.

[43] Paul Ferkul, Sandra Olson, David L Urban, Gary A Ruff, John Easton, James S T'ien, Ta-Ting T Liao, A Carlos Fernandez-Pello, Jose L Torero, Christian Eigenbrand, et al. Results of large-scale spacecraft flammability tests. In International Conference on Environmental Systems (ICES). 16-20 Jul. 2017; Charleston, SC; United States, 2017.

[44] J. S. T'ien, S. N. Singhal, D. P. Harrold, and J. M. Prahl. Combustion and extinction in the stagnation-point boundary layer of a condensed fuel. Combustion and Flame, 33:55–68, 1978.

[45] Jennifer L Rhatigan, Hasan Bedir, and James S T'ien. Gas-phase radiative effects on the burning and extinction of a solid fuel. Combustion and Flame, 112(1): 231–241, 1998.

[46] Hideo Ohtani, Kazuo Akita, and Toshisuke Hirano. An analysis of bottom stagnation region combustion of polymeric material pieces under natural convection. Combustion and Flame, 53(1-3):33–40, 1983.

[47] James S. T'ien and Makoto Endo. Material flammability: A combustion science perspective. Procedia Engineering, pages 120–129, 2013.

[48] Sandra L. Olson and James S. T'ien. Buoyant low-stretch diffusion flames beneath cylindrical pmma samples. Combustion and Flame, 121(3):439–452, 2000.

[49] MJ Gollner, X Huang, J Cobian, AS Rangwala, and FA Williams. Experimental study of upward flame spread of an inclined fuel surface. Proceedings of the Combustion Institute, 34(2):2531–2538, 2013.

[50] Hideo Ohtani, Toshisuke Hirano, and Kazuo Akita. Experimental study of bottom surface combustion of polymethylmethacrylate. Proceedings of the Combustion Institute, 18,1:591–599, 1981.

[51] Y Pizzo, JL Consalvi, P Querre, M Coutin, L Audouin, B Porterie, and JL Torero. Experimental observations on the steady-state burning rate of a vertically oriented pmma slab. Combustion and Flame, 152(3):451–460, 2008.

[52] DD Drysdale and HE Thomson. Flammability of plastics ii: Critical mass flux at the firepoint. Fire Safety Journal, 14(3):179–188, 1989.

[53] David Rich, Chris Lautenberger, Jose L Torero, James G Quintiere, and Carlos Fernandez-Pello. Mass flux of combustible solids at piloted ignition. Proceedings of the Combustion Institute, 31(2):2653–2660, 2007.

[54] Sonia Fereres, Chris Lautenberger, Carlos Fernandez-Pello, David Urban, and Gary Ruff. Mass flux at ignition in reduced pressure environments. Combustion and Flame, 158(7):1301–1306, 2011.

[55] Linton K Honda and Paul D Ronney. Mechanisms of concurrent-flow flame spread over solid fuel beds. Proceedings of the Combustion Institute, 28(2):2793–2801, 2000.

[56] Ali S Rangwala, Steven G Buckley, and Jose L Torero. Upward flame spread on a vertically oriented fuel surface: The effect of finite width. Proceedings of the Combustion Institute, 31(2):2607–2615, 2007.

[57] Amit Kumar and James S. T'ien. Numerical modeling of limiting oxygen index apparatus for film type fuels. International Journal of Spray and Combustion Dynamics, 4(4):299–322, 2012.

[58] Mathieu Suzanne, MA Delichatsios, and JP Zhang. Flame extinction properties of solids obtained from limiting oxygen index tests. Combustion and Flame, 161 (1):288–294, 2014.

[59] International Organization for Standardization. Determination of burning behavior by oxygen index, plastic test standard. ISO 4859, 1996.

[60] Limiting Oxygen Index. Standard test method for measuring minimum oxygen concentration to support candle-like combustion of plastics. ASTM D, 2863, 2009.

[61] SL Olson, FJ Miller, and IS Wichman. Characterizing fingering flamelets using the logistic model. Combustion Theory and Modelling, 10(2):323–347, 2006.

[62] James S. T'ien. Diffusion flame extinction at small stretch rates: the mechanism of radiative loss. Combustion and Flame, 65(1):31–34, 1986.

[63] Bai Han, Alfonso F Ibarreta, Chih-Jen Sung, and James S. T'ien. Experimental low-stretch gaseous diffusion flames in buoyancy-induced flowfields. Proceedings of the Combustion Institute, 30(1):527–535, 2005.

[64] Chin Tien Yang and James S. T'ien. Numerical simulation of combustion and extinction of a solid cylinder in low-speed cross flow. Journal of Heat Transfer, 120(4):1055–1063, 1998.

[65] S. L. Olson and J. S. T'ien. Near-surface vapour bubble layers in buoyant low stretch burning of polymethylmethacrylate. Fire and Materials, 23(5):227–237, 1999. ISSN 1099-1018.

[66] Michael C Johnston and James S T'ien. Gravimetric measurement of solid and liquid fuel burning rate near and at the low oxygen extinction limit. Fire Safety Journal, 91:140–146, 2017.

[67] Wei Shang. Laboratory-scale evaluation of aramid blend material as a fire barrier for flexible polyurethane foam, 2016.

[68] Limiting Oxygen Index. Standard test method for measuring minimum oxygen concentration to support candle-like combustion of plastics. ASTM D, 2863, 1983.

[69] James S. T'ien, Jonathan Jordan, Zhengxuan Wu, and Gabriel. Nastac. An experimental study of upward flame spread over wavy thin solids. In 10th US National Meeting of the Combustion Institute, 2017.

[70] Ammar Alsairafi, Shih-Tuen Lee, and James S. T'ien. Modeling gravity effect on diffusion flames stabilized around a cylindrical wick saturated with liquid fuel. Combustion Science and Technology, 176(12):2165–2191, 2004.

[71] M. P. Raju and J. S. T'ien. Modelling of candle burning with a self-trimmed wick. Combustion Theory and Modelling, 12(2):367–388, 2008.

[72] P. B. Sunderland, J. G. Quintiere, G. A. Tabaka, D. Lian, and C.-W. Chiu. Analysis and measurement of candle flame shapes. Proceedings of the Combustion Institute, 33(2):2489–2496, 2011.

[73] F. G. Roper. The prediction of laminar jet diffusion flame sizes: Part i. theoretical model. Combustion and Flame, 29:219–226, 1977.

[74] F. G. Roper, C. Smith, and A. C. Cunningham. The prediction of laminar jet diffusion flame sizes: Part ii. experimental verification. Combustion and Flame, 29:227–234, 1977.

[75] William Y. Chan and James S. T'ien. An experiment on spontaneous flame oscillation prior to extinction. Combustion Science and Technology, 18(3-4):139–143, 1978.

[76] Y. Shu, J. T'ien, D. Dietrich, and H. D. Ross. Modeling of candle flame and near-extinction oscillation in microgravity. J. Jpn. Soc. Microgravity Appl, 15: 272–277, 1988.

[77] Sally Cheatham and Moshe Matalon. A general asymptotic theory of diffusion flames with application to cellular instability. Journal of Fluid Mechanics, 414: 105–144, 2000.

[78] J. Buckmaster. Edge-flames and their stability. Combustion Science and Technology, 115(1-3):41–68, 1996.

[79] Howard D. Ross. Ignition of and flame spread over laboratory-scale pools of pure liquid fuels. Progress in Energy and Combustion Science, 20(1):17–63, 1994.

[80] Amit Kumar and James S. T'ien. A computational study of low oxygen flammability limit for thick solid slabs. Combustion and Flame, 146(1):366–378, 2006.

[81] P. J. Pagni and T. M. Shih. Excess pyrolyzate. Proceedings of the Combustion Institute, 16:1329–1343, 1977.

[82] NASA. Combustion integrated rack - fluids and combustion facility (cir) - 07.19.17, 2017. URL https://www.nasa.gov/mission_pages/station/research/experiments/326.html.

[83] NASA. Cir, 2016. URL https://spaceflightsystems.grc.nasa.gov/sopo/ihho/psrp/fcf/cir/.

[84] Robert L Zurawski and Nora G Bozzolo. ISS Fluids and Combustion Facility Combustion Integrated Rack Payload Acommodations, Principal Investigator's Guide. National Aeronautics and Space Administration, 2000.

[85] Terence F O'Mally and Karen J Weiland. The fcf combustion integrated rack: Microgravity combustion science onboard the international space station. Technical report, NASA/TM-2002-210981, 2002.

[86] James S. T'ien, Paul V Ferkul, Sandra L Olson, and Makoto Endo. Science requirements document for growth and extinction limit of solid fuels (gel). 2013.

[87] Arden L Buck. New equations for computing vapor pressure and enhancement factor. Journal of Applied Meteorology, 20(12):1527–1532, 1981.